The Higgs boson as a probe for new physics: Investigation of CP properties and search for associated dark matter production with ATLAS Run 2 data

Erlend Aakvaag

A thesis presented for the degree of

Doctor of Philosophy

University of Bergen

Institute of Physics and Technology

The Higgs boson as a probe for new physics: Investigation of CP properties and search for associated dark matter production with ATLAS Run 2 data

Erlend Aakvaag

Abstract

This thesis presents studies of the Higgs boson using the full Run 2 proton–proton collision dataset collected by the ATLAS experiment at the LHC at a centre-of-mass energy of $\sqrt{s} = 13$ TeV, corresponding to an integrated luminosity of 140 fb^{-1}. The CP properties of the Higgs boson are investigated in the vector-boson fusion production mode, using its decay into τ-leptons. To probe potential CP-violating interactions between the Higgs boson and electroweak gauge bosons, the Optimal Observable method is employed in the framework of effective field theory. No significant deviations from the Standard Model are observed, and constraints are placed on CP-odd parameters, interpreted both in the HISZ basis via $\tilde{d}$ and in the Warsaw basis via the Wilson coefficient $c_{H\tilde{W}}$. The stand-alone result from the fully leptonic channel yields a 95% confidence interval of $\tilde{d} \in [-0.078, 0.091]$ and $c_{H\tilde{W}} \in [-1.38, 1.71]$. Further enhancement is obtained by statistically combining all three decay modes of the τ-lepton pair, with combined measurements of $\tilde{d} \in [-0.012, 0.049]$ and $c_{H\tilde{W}} \in [-0.24, 0.84]$ at 95% confidence level. The latter represents one of the strongest limits on the $c_{H\tilde{W}}$ Wilson coefficient to date.

Additionally, dark matter production in association with a Higgs boson decaying into hadronically decaying τ-leptons is investigated, using the same dataset. No evidence of new physics is observed, and the results are interpreted in the context of a two-Higgs-doublet model with an additional pseudoscalar mediator (2HDM+a), with exclusion limits set at 95% confidence level on the model parameters. Model-independent upper limits on the visible cross-section of new physics in the $E_{\mathrm{T}}^{\mathrm{miss}} + h(\tau\tau)$ final state are also provided, ranging from 0.04 to 0.08 fb depending on the signal region.

Supervisors: Bjarne Stugu and Anna Lipniacka

Leting etter ny fysikk med Higgs-bosonet: Studier av CP-egenskaper og assosiert mørk materie produksjon med ATLAS Run 2-data

Erlend Aakvaag

Abstract

Denne avhandlingen presenterer studier av Higgs-bosonet ved bruk av hele Run 2 datasettet fra proton–proton-kollisjoner samlet inn av ATLAS-eksperimentet ved LHC, med $\sqrt{s} = 13$ TeV og en integrert luminositet på 140 fb^{-1}. CP-egenskapene til Higgs-bosonet undersøkes i vektor-boson-fusjon produksjon, med henfall til τ-leptoner. For å studere mulige CP-brytende interaksjoner mellom Higgs-bosonet og elektrosvake vektor-bosoner benyttes en matrise-basert variabel som sensitiv til avvik som kommer fra CP brudd. Ingen signifikante avvik fra standardmodellen har blitt observert, og det settes begrensinger på CP-odd parametere, tolket både i HISZ-basen via $\tilde{d}$ og i Warszawa-basen via Wilson-koeffisienten $c_{H\tilde{W}}$. Resultatet fra den fullt leptoniske kanalen gir alene et 95% konfidensintervall på $\tilde{d} \in [-0.078, 0.091]$ og $\tilde{c}_{HW} \in [-1.38, 1.71]$. Videre forbedring oppnås gjennom en statistisk kombinasjon av alle tre henfallskanaler til τ-leptonparet, med kombinerte målinger som gir 95% konfidensintervall på $\tilde{d} \in [-0.012, 0.049]$ og $c_{H\tilde{W}} \in [-0.24, 0.84]$. Sistnevnte representerer en av de mest sensetive målingene av Wilson-koeffisienten $c_{H\tilde{W}}$ til dags dato.

I tillegg undersøkes produksjon av mørk materie i assosiasjon med et Higgs-boson som henfaller til hadroniske τ-leptoner ved bruk av det samme datasettet. Ingen tegn til ny fysikk har blitt observert, og resultatene tolkes innenfor en To-Higgs-Doublet modell med en ekstra pseudoskalar mediator (2HDM+a), hvor eksklusjonsgrenser ved 95% konfidensnivå settes på modell-parameterne. Modell-uavhengige øvre grenser for det synlige tverrsnittet for ny fysikk i topologien $E_{\mathrm{T}}^{\mathrm{miss}} + h(\tau\tau)$ presenteres også, og varierer mellom 0.04 til 0.08 fb avhengig av signal-regionen.

Veiledere: Bjarne Stugu and Anna Lipniacka

Acknowledgements

I would like to thank my supervisors Bjarne Stugu and Anna Lipniacka for guidance and support during these last years, allowing me to pursue my research interest with great freedom and not demanding rent for my a bit longer than expected stay in the Saint Genis apartment. Thanks to the rest of the Bergen group, especially Bertrand Martin dit Latour for keeping the computing resources alive, Nikolai Fomin for his patience during the early stages of my PhD, and Tarje for sharing many enjoyable indulgent meals.

I have also had the pleasure of working with the Freiburg ATLAS group. Thank you to Ogul, Daniel and Lorenzo for welcoming me into the team. It has been a valuable experience, with many lessons learned. I also extend my thanks to the conveners and members of the ATLAS HIGP and tau CP groups. Special thanks to Serhat for help with ID scale factors, and to Antonio for his general technical support.

I would also like to thank my family for their unconditional support. Special and extra big thanks goes out to Seulgi Kim, 너와 함께여서 행복해.

Declaration

The research leading to the results presented in this this thesis have received funding from the Norwegian Financial Mechanism for years 2014-2021, grant no DEC-2019/34/H/ST2/00707.

The next page summarises publications and ATLAS notes where the author has contributed, and selected talks given by the author during the PhD. ATLAS notes and workshops are internal. The VBF CP anlysis is still undergoing final approval within the ALTAS collaboration, with public results expected later this spring. The target journal is Journal for High Energy Physics (JHEP).

Research

Journal Articles

1. E. Aakvaag, N. Fomin, A. Lipniacka, S. Pokorski, J. Rosiek, and D. Sahoo, "Exploring CP violation in $H \to \tau^+ \tau^- \gamma$," *Eur. Phys. J. C*, vol. 84, no. 3, p. 341, 2024. DOI: `10.1140/epjc/s10052-024-12691-z`. arXiv: `2311.16211 [hep-ph]`.
2. G. Aad *et al.*, "Search for dark matter produced in association with a Higgs boson decaying to tau leptons at $\sqrt{s}$ = 13 TeV with the ATLAS detector," *JHEP*, vol. 09, p. 189, 2023. DOI: `10.1007/JHEP09(2023)189`. arXiv: `2305.12938 [hep-ex]`.

Selected public conference talks

1. E. Aakvaag, Test of CP invariance in the Higgs VBF production vertex with the ATLAS detector using the $H \to \tau\tau$ channel, Spåtind - Nordic Conference on Particle Physics, Skeikampen, Norway, 2025. URL: `https://indico.cern.ch/event/1422718/contributions/6280620/`.
2. E. Aakvaag, New ATLAS results in monoHiggs to tau tau and combination for DM limits, Conference of Norwegian Financial Mechanism Early Universe project, Bergen, Norway, 2023. URL: `https://indico.global/event/10596/contributions/101226/`.

ATLAS internal notes

1. D. Bahner, E. Aakvaag, M. Schumacher, *et al.*, "Probing the Higgs boson CP properties in Vector-Boson Fusion production in the ditau channel in proton-proton collisions at 13 TeV using the full ATLAS Run 2 data sample – Internal Note," CERN, Geneva, 2024. URL: `https://cds.cern.ch/record/2891741`.
2. E. Aakvaag, "Measurment of Tau ID efficiencies using $W \to \tau\nu$ events with the ATLAS detector in LHC Run 2," CERN, Geneva, 2023. URL: `https://cds.cern.ch/record/2866467`.
3. N. Fomin, T. Buanes, E. Aakvaag, J. I. Djuvsland, and A. Lipniacka, "Search for Dark Matter produced in association with a Higgs boson decaying to tau leptons at $\sqrt{s}$ = 13 TeV with the ATLAS detector," CERN, Geneva, 2020. URL: `https://cds.cern.ch/record/2707037`.

Selected ATLAS workshop talks

1. E. Aakvaag, "Tau Identification SF measurement in Wtaunu Signal region (Run2 + Run3)," Tau CP Workshop, CERN, Switzerland, 2024. URL: `https://indico.cern.ch/event/1372592/contributions/5810750/`.
2. E. Aakvaag, "VBF CP: Analysis overview + combination plan," HLepton Workshop 2024, CERN, Switzerland, 2024. URL: `https://indico.cern.ch/event/1372592/contributions/5778422/`.
3. E. Aakvaag, "Overview of VBF CP studies in $H \to \tau\tau$," Higgs Workshop, Tokyo, Japan, 2023. URL: `https://indico.cern.ch/event/1280531/contributions/5564961/`.

Contents

Chapter 1

Introduction

The Standard Model (SM) represents the current understanding of the fundamental constituents of matter and the interactions that govern their behaviour. It incorporates all known elementary particles and describes their interactions through the strong, electromagnetic, and weak forces. The formulation of the model reached its present form in the 1970s and has since undergone extensive experimental scrutiny. Remarkably, its predictions have consistently demonstrated exceptional agreement with experimental observations. With the discovery of the Higgs boson in 2012 by the ATLAS and CMS collaborations [1, 2], all particles predicted by the SM have been experimentally verified.

Despite its success, however, the SM is known to be incomplete. One of the key shortcomings is its inability to account for the observed baryon–antibaryon asymmetry in the universe. The level of asymmetry predicted by the SM is several orders of magnitude smaller than what is required to explain the observed imbalance [3–5]. According to the Sakharov conditions [6], generating such an asymmetry requires the presence of processes that violate charge conjugation (C) and the combined charge-parity (CP) symmetry. While the SM does contain a source of CP violation through quark mixing in the electroweak sector [7, 8], it is insufficient to explain the observed baryon asymmetry, suggesting the existence of additional CP-violating interactions beyond the SM.

Given that CP violation in the SM arises in the electroweak sector, it is natural to search for additional sources of CP violation in other electroweak processes. The couplings of the Higgs boson to vector bosons (HVV couplings) are particularly well-suited for such studies. This thesis presents an analysis that probes the CP structure of the HVV vertex via Higgs boson production through vector boson fusion (VBF) in final states containing a pair of τ-leptons and two jets. CP-violating interactions are introduced by extending the SM Lagrangian to include anomalous couplings arising from higher-dimensional operators within the framework of effective field theory. These additional terms can modify the SM Higgs couplings to gauge bosons, leading to measurable deviations in observables that are sensitive to CP-violating effects. In this thesis, a matrix-element-based Optimal Observable is used, where the presence of CP-violating interactions gives rise to asymmetries in the distribution, offering direct sensitivity to such contributions.

Another major shortcoming of the SM is the nature of dark matter (DM), which constitutes approximately 27% of the energy content of the universe [9, 10]. The SM does not provide a viable DM candidate, motivating new theories beyond the SM. Collider-based searches for DM typically target signatures with large missing transverse momentum ($E_{\mathrm{T}}^{\mathrm{miss}}$) arising from weakly interacting particles escaping detection. One promising class of searches is the mono-Higgs signature, where DM is produced in association with a Higgs boson. This topology is targeted by the analysis in this thesis, where a search is performed in final states with a τ-lepton pair and large $E_{\mathrm{T}}^{\mathrm{miss}}$. This signature can be incorporated into a simplified model that extends the Higgs sector. The search in this thesis is interpreted in the context of the Two-Higgs-Doublet Model extended by a pseudoscalar mediator (2HDM+a) [11]. The model provides a minimal, renormalisable framework that allows the Higgs sector to couple to DM particles.

To provide context for the analyses presented, this thesis begins a the theoretical motivation, followed by a description of the experimental tools, and concludes with the analysis strategies and results. It is organised into three main parts:

Part I: The first part covers the relevant theoretical concepts for the analyses described in this thesis. Chapter 2 provides an overview of the SM, with particular focus on the Higgs boson and its properties. Chapter 3 discusses the theory of CP violation both within and beyond the SM, and outlines potential search strategies based on the framework of effective field theory. Chapter 4 presents the evidence for DM and explores search techniques for DM candidates arising in extended Higgs sector theories.

Part II: The second part describes the experimental infrastructure and methodology underlying the results presented in this thesis. Chapter 5 introduces the LHC accelerator, the main components of the ATLAS detector, and the simulation of theoretical predictions for physics processes. Chapter 6 details the algorithms used to reconstruct physics objects employed in ATLAS analyses. Chapter 7 covers the statistical methods used in LHC measurements and the procedures for setting limits on new physics models.

Part III: The third and final part presents the analysis strategies and results of the two studies conducted in this thesis. Chapter 8 describes the strategy for measuring CP violation in the VBF production vertex using $H \to \tau\tau$ decays, with special emphasis on the fully leptonic channel. Chapter 9 outlines the strategy and results of the mono-Higgs $E_{\mathrm{T}}^{\mathrm{miss}} + h(\tau\tau)$ DM search with hadronically decaying τ-leptons.

Part I

Theory

Chapter **2**

The Standard Model

This chapter provides a brief introduction to the theoretical foundations of the Standard Model. An overview is first presented, followed by a discussion of the underlying symmetry principles and the physical theories that arise from them. The chapter concludes with a discussion of the Brout–Englert–Higgs mechanism and the Higgs boson, which is of particular interest in this thesis. Experimental signatures and measurements of Higgs properties are also briefly summarised.

2.1 Particle Content of the Standard Model

All elementary particles observed to date are incorporated into the Standard Model (SM) framework. Based on their intrinsic spin, they are categorised into two fundamental classes: fermions, which are spin-$\frac{1}{2}$ particles that constitute matter, and bosons, which are integer-spin (0, 1) particles that mediate the fundamental interactions or, in the case of the Higgs boson, are responsible for the generation of particle masses through electroweak symmetry breaking.

There are twelve elementary fermions, divided equally into leptons and quarks, each grouped into three generations based on their quantum numbers and masses. Leptons consist of the electron (e), muon (μ), and tau (τ), each carrying an electric charge $Q = -1$, together with their associated electrically neutral neutrinos (ν_e, ν_μ, ν_τ). Charged leptons participate in both electromagnetic and weak interactions, whereas neutrinos interact only via the weak interaction. In the SM, each generation of leptons is organised into a left-handed $SU(2)_L$ doublet, comprising a charged lepton and its associated neutrino, and a right-handed $SU(2)_L$ singlet corresponding to the charged lepton. The weak interaction couples to leptons via the weak isospin, which distinguishes the members of the doublet, and the hypercharge Y, which is related to the electric charge through the Gell–Mann–Nishijima relation[12]:

$$Q = T_3 + \frac{Y}{2}, \tag{2.1}$$

where T_3 is the third component of the weak isospin. Additionally, each lepton has an associated antiparticle with identical mass but opposite electric charge and lepton number. The leptons and their properties are summarised in Table 2.1.

Generation	Particle	Mass [MeV]	Charge [e]	Weak isospin T_3	Antiparticle
I	e	0.511	-1	$+\frac{1}{2}$	$\bar{e}$
	ν_e	$< 0.8 \times 10^{-8}$	0	$-\frac{1}{2}$	$\bar{\nu}_e$
II	μ	105.7	-1	$+\frac{1}{2}$	$\bar{\mu}$
	ν_μ	<0.19	0	$-\frac{1}{2}$	$\bar{\nu}_\mu$
III	τ	1777	-1	$+\frac{1}{2}$	$\bar{\tau}$
	ν_τ	<18.2	0	$-\frac{1}{2}$	$\bar{\nu}_\tau$

Table 2.1: Properties of left-handed leptons in the SM. Values taken from PDG [13].

Quarks similarly form three generations, each containing one up-type quark (up, charm, top) with electric charge $Q = +\frac{2}{3}$ and one down-type quark (down, strange, bottom) with electric charge $Q = -\frac{1}{3}$. Like leptons, quarks form left-handed doublets and right-handed singlets under the $SU(2)_L$ symmetry group, and have both weak isospin and hypercharge. In addition to weak and electromagnetic interactions, quarks carry colour charge and interact via the strong force, which binds them into colour-neutral hadrons such as protons, neutrons, and mesons. The properties of the quarks are summarised in Table 2.2.

Generation	Particle	Mass [MeV]	Charge [e]	Weak isospin T_3	Antiparticle
I	u	$2.2^{+0.5}_{-0.4}$	$+\frac{2}{3}$	$+\frac{1}{2}$	$\bar{u}$
	d	$4.7^{+0.5}_{-0.3}$	$-\frac{1}{3}$	$-\frac{1}{2}$	$\bar{d}$
II	c	1275^{+25}_{-35}	$+\frac{2}{3}$	$+\frac{1}{2}$	$\bar{c}$
	s	95^{+9}_{-3}	$-\frac{1}{3}$	$-\frac{1}{2}$	$\bar{s}$
III	t	$(173 \pm 0.4) \times 10^3$	$+\frac{2}{3}$	$+\frac{1}{2}$	$\bar{t}$
	b	4180^{+40}_{-30}	$-\frac{1}{3}$	$-\frac{1}{2}$	$\bar{b}$

Table 2.2: Properties of quarks in the SM. Values taken from PDG [13]

The SM describes three of the four fundamental interactions in the universe: the strong, electromagnetic, and weak interactions. These interactions are mediated by spin-1 gauge bosons.

The strong interaction, mediated by gluons (g), operates at short distances and is responsible for binding quarks together to form hadrons, such as protons and neutrons, which in turn bind into atomic nuclei. The electromagnetic interaction, mediated by photons (γ), governs the interaction between electrically charged particles, leading to the formation of atoms, molecules, and larger chemical structures. The weak interaction, mediated by the massive $W^{\pm}$ and Z^0 bosons, enables processes such as β-decay, which are essential for radioactive decays.

Additionally, the SM includes a spin-0 scalar particle, the Higgs boson (H). The Higgs boson arises through the Brout-Englert-Higgs mechanism, which spontaneously breaks the $SU(2)_L \times U(1)_Y$ electroweak symmetry and give rise to mass terms for the $W^{\pm}$ and Z^0 gauge bosons, as well as fermions through additional Yukawa couplings. The strength of interaction with the Higgs field determines particle masses, while massless particles like photons remain unaffected. The properties of the Higgs and gauge bosons are summarised in Table 2.3.

Interaction	Mediator	Mass [GeV]	Spin	Charge [e]
Electromagnetic	γ	0	1	0
Weak (neutral)	Z^0	91.1876 ± 0.0021	1	0
Weak (charged)	$W^{\pm}$	80.379 ± 0.012	1	± 1
Strong	g	0	1	0
Higgs boson	H	125.25 ± 0.17	0	0

Table 2.3: Properties of the vector and scalar bosons in the SM [13].

2.2 Gauge theories and symmetries

Gauge theories are quantum field theories characterised by local gauge symmetries. Their dynamics are described using the Lagrangian formalism, with the Lagrangian density $\mathcal{L}(\phi, \partial_\mu \phi)$ expressed in terms of fields ϕ and their derivatives $\partial_\mu \phi$. Integrating the Lagrangian density over space-time yields the action:

$$S = \int d^4x \, \mathcal{L}(\phi, \partial_\mu \phi). \tag{2.2}$$

Hamilton's principle states that physical systems evolve to make the action stationary, leading to the Euler–Lagrange equations of motion:

$$\frac{\partial \mathcal{L}}{\partial \phi} - \partial_\mu \left(\frac{\partial \mathcal{L}}{\partial(\partial_\mu \phi)} \right) = 0, \tag{2.3}$$

This equation can be applied to any field to obtain the dynamics of a system from the Lagrangian.

Symmetry plays a central role in physics, underpinning conservation laws. A continuous symmetry transformation, represented by an infinitesimal phase shift ϵ, can be expressed as:

$$\phi \to e^{i\epsilon}\phi \approx \phi + i\epsilon\phi. \tag{2.4}$$

If the Lagrangian remains invariant under a continuous global transformation, Noether's theorem implies the existence of a conserved current j^μ:

$$\partial_\mu j^\mu = 0, \quad \text{where} \quad j^\mu = \frac{\partial \mathcal{L}}{\partial(\partial_\mu \phi)} \delta\phi. \tag{2.5}$$

Integrating the time component of this current over all space yields the associated conserved charge:

$$Q = \int d^3x \, j^0. \tag{2.6}$$

For instance, if the Lagrangian is invariant under a global $U(1)$ symmetry, the conserved charge can be identified with the electric charge. More complicated transformations also exists, where the infinitesimal changes are done in multiple dimensions. The $SU(2)$ and $SU(3)$ Lie groups are defined by phase rotations in two or three dimensions respectively. The associated conserved charges under $SU(2)$ can be identified with the weak isospin, while for $SU(3)$ its colour charge.

The SM itself is built upon gauge symmetries, and enforcing invariance under local phase transformations leads to the introduction of gauge fields mediating the fundamental interactions. Specifically, the SM Lagrangian is required to be invariant under local transformations of the following three gauge groups:

$$SU(3)_C \times SU(2)_L \times U(1)_Y. \tag{2.7}$$

Each symmetry group has a corresponding set of generators: $U(1)_Y$ has a single generator associated with phase rotations, $SU(2)_L$ has three generators corresponding to the Pauli matrices, and $SU(3)_C$ has eight generators corresponding to the Gell-Mann matrices. The number of generators determines the number of gauge boson mediators in the theory.

2.2.1 Quantum electrodynamics

Quantum Electrodynamics (QED) is the quantum field theory describing electromagnetic interactions, formulated by quantising the classical electromagnetic field. Classically, this field is represented by the scalar potential $\phi(\mathbf{x})$ and the vector potential $\mathbf{A}(\mathbf{x})$, combined into a four-vector potential $A_\mu(\mathbf{x}) = (\phi, \mathbf{A})$. The dynamics of these potentials are described by the Maxwell equations, which in terms of potentials give rise to the electromagnetic field tensor:

$$F_{\mu\nu} = \partial_\mu A_\nu - \partial_\nu A_\mu. \tag{2.8}$$

The free photon Lagrangian is given by:

$$\mathcal{L}_{\text{photon}} = -\frac{1}{4} F_{\mu\nu} F^{\mu\nu}, \tag{2.9}$$

and remains invariant under gauge transformations of the form:

$$A_\mu \to A_\mu + \partial_\mu f(x), \tag{2.10}$$

where $f(x)$ is an arbitrary scalar function.

Fermions, described by spinor fields $\psi(x)$, follow the Dirac equation derived from the Dirac Lagrangian:

$$\mathcal{L}_{\text{fermion}} = \bar{\psi}(x)(i\gamma^\mu \partial_\mu - m)\psi(x) \tag{2.11}$$

where γ^μ represents the Dirac gamma matrices. This Lagrangian is invariant under global $U(1)$ phase transformations, but enforcing invariance under local gauge transformations requires replacing the partial derivative ∂_μ with the covariant derivative $D_\mu = \partial_\mu + iqeA_\mu(x)$. This replacement introduces an interaction term between photons and fermions:

$$\mathcal{L}_{\text{QED}} = \bar{\psi}(i\gamma^\mu D_\mu - m)\psi - \frac{1}{4}F_{\mu\nu}F^{\mu\nu}. \tag{2.12}$$

2.2.2 Quantum Chromodynamics

Quantum Chromodynamics (QCD) is the quantum field theory describing the strong interaction between quarks, mediated by gluons. Quarks are fermions carrying both electric charge and an additional quantum number called colour, which exists in three types conventionally labelled as red, green, and blue. QCD is formulated as a non-Abelian gauge theory, meaning that the generators of its symmetry group $SU(3)_C$ do not commute.

Each quark field with flavour f is represented by a three-component spinor Ψ in colour space, and the dynamics of free quarks are described by the Lagrangian:

$$\mathcal{L}_0 = \bar{\Psi}(i\gamma^\mu\partial_\mu - m_f)\Psi. \tag{2.13}$$

Enforcing invariance under local $SU(3)_C$ gauge transformations requires the introduction of a covariant derivative D_μ:

$$D_\mu = \partial_\mu + \frac{ig_s}{2}\lambda_j A^j_\mu, \quad j = 1, \ldots, 8, \tag{2.14}$$

where g_s is the strong coupling constant, λ_j are the Gell-Mann matrices and A^j_μ are the gluon fields.

This leads to an interaction term between quarks and gluons:

$$\mathcal{L}_{\text{int}} = -\frac{g_s}{2}\bar{\Psi}\gamma^\mu\lambda_j\Psi A^j_\mu. \tag{2.15}$$

Adding a kinetic term for the gluon fields gives the full QCD Lagrangian:

$$\mathcal{L}_{\text{QCD}} = \bar{\Psi}(i\gamma^\mu D_\mu - m_f)\Psi - \frac{1}{4}G^j_{\mu\nu}G^{\mu\nu}_j, \tag{2.16}$$

where the gluon field strength tensor $G^j_{\mu\nu}$ is defined as:

$$G^j_{\mu\nu} = \partial_\mu A^j_\nu - \partial_\nu A^j_\mu + g_s f_{jkl}A^k_\mu A^l_\nu. \tag{2.17}$$

The prefactor f_{jkl} denotes the structure constants of $SU(3)$. The non-Abelian nature of QCD, reflected in the non-linear structure of $G^j_{\mu\nu}$, leads to gluon self-interactions. These interactions are responsible for the phenomenon of confinement, whereby quarks and gluons cannot be observed as free particles but instead form colour-neutral bound states such as baryons and mesons. Experimental studies of quarks and gluons are carried out indirectly via high-energy collisions, where collimated sprays of hadrons known as jets offer insight into the underlying parton dynamics.

2.2.3 Electroweak Theory

Electroweak theory unifies the electromagnetic and weak interactions into a single gauge theory based on the symmetry group $SU(2)_L \times U(1)_Y$. Originally formulated by Glashow, Weinberg, and Salam [14–16], the theory predicts the existence of three gauge fields, W_j^μ $(j = 1, 2, 3)$ associated with the $SU(2)_L$ symmetry group, and one gauge field B^μ associated with $U(1)_Y$ symmetry group.

The electroweak interaction is chiral, meaning that it couples differently to left-handed and right-handed fermions. The chiral components of the fermion fields can be obtained with projection operators:

$$P_{L/R}\psi = \frac{1}{2}(1 \mp \gamma^5)\psi_{L/R}, \tag{2.18}$$

where the chirality matrix γ^5 is defined from the four Dirac matrices. The resulting left-handed components form a doublet Ψ_L that transform under the combined operation of $SU(2)_L \times U(1)_Y$, while the right-handed components ψ_R are singlets under $SU(2)_L$ and only transform under $U(1)_Y$. For leptons, the left-handed doublet consists of a charged lepton and its associated neutrino, while the right-handed singlet is only defined for the charged lepton. Similarly, for quarks, each left-handed doublet contains one up-type and one down-type quark, accompanied by separate right-handed singlets for both the up- and down-type components.

To maintain invariance under local gauge transformations, covariant derivatives must be introduced for the left- and right-handed fermion fields:

$$D^\mu \Psi_L = \left(\partial^\mu + i g_W \frac{\sigma_j}{2} W_j^\mu + i g' \frac{Y}{2} B^\mu\right) \Psi_L, \quad D^\mu \psi_R = \left(\partial^\mu + i g' \frac{Y}{2} B^\mu\right) \psi_R, \tag{2.19}$$

where g_W and g' are the coupling constants associated with $SU(2)_L$ and $U(1)_Y$, respectively, σ_j are the Pauli matrices, and Y denotes the hypercharge of the fermion field.

The charged weak fields $W_\mu^\pm$ couple to left-handed fermions with strength g_W and arise from linear combinations of W_μ^1 and W_μ^2:

$$W_\mu^\pm = \frac{1}{\sqrt{2}} \left(W_\mu^1 \mp i W_\mu^2\right). \tag{2.20}$$

The photon field A_μ and the neutral weak field Z_μ emerge from a rotation of the $U(1)_Y$ gauge field B_μ and the

$SU(2)_L$ gauge field W_μ^3 by the weak mixing angle θ_W, defined as $\theta_W = \tan^{-1}(g'/g_W)$:

$$\begin{pmatrix} A_\mu \\ Z_\mu \end{pmatrix} = \begin{pmatrix} \cos\theta_W & \sin\theta_W \\ -\sin\theta_W & \cos\theta_W \end{pmatrix} \begin{pmatrix} B_\mu \\ W_\mu^3 \end{pmatrix}. \tag{2.21}$$

Both A_μ and Z_μ couple to left- and right-handed fermion fields with coupling strengths:

$$\begin{aligned} e &= g_W \sin\theta_W = g' \cos\theta_W, \\ g_Z &= \frac{g_W}{\cos\theta_W} = \frac{g'}{\sin\theta_W}, \end{aligned} \tag{2.22}$$

where e is the coupling constant from QED. The $SU(2)_L$ symmetry group is also non-Abelian, leading to self-interactions among the charged electroweak gauge bosons, as well as interactions between the charged bosons, the neutral Z boson, and the photon.

Electroweak theory provides a comprehensive theoretical description of the unified electroweak interaction. It does however rely on massless gauge bosons and fermions since adding corresponding mass terms to the Lagrangian breaks local gauge invariance. This is in conflict with experimental observations that the $W^\pm$ and Z^0 gauge bosons are massive [17, 18]. To resolve this, an additional mechanism is required.

2.2.4 Electroweak symmetry breaking and gauge boson mass terms

The first approaches to solve the zero-mass constraint of the electroweak model were introduced in 1964 [19–21]. The first step requires the introduction of a $SU(2)_L$ doublet Φ of complex scalar fields ϕ:

$$\Phi = \begin{pmatrix} \phi^+ \\ \phi^0 \end{pmatrix} = \frac{1}{\sqrt{2}} \begin{pmatrix} \phi_1 + i\phi_2 \\ \phi_3 + i\phi_4 \end{pmatrix}, \tag{2.23}$$

where ϕ^+ has charge $Q = +1$ and ϕ^0 is neutral. The corresponding Lagrangian, which remains invariant under global $SU(2)_L \times U(1)_Y$ transformations acting on Φ, is given by:

$$\mathcal{L} = (\partial_\mu \Phi)^\dagger (\partial^\mu \Phi) - V(\Phi), \tag{2.24}$$

with the potential:

$$V(\Phi) = \mu^2 \Phi i^\dagger \Phi + \lambda \left(\Phi^\dagger \Phi\right)^2. \tag{2.25}$$

In the case where $\mu^2 < 0$, the potential has an infinite set of degenerate minima. Every field configuration that satisfies:

$$\Phi^\dagger \Phi = \frac{1}{2}\left(\phi_1^2 + \phi_2^2 + \phi_3^2 + \phi_4^2\right) = -\frac{\mu^2}{2\lambda} = \frac{v^2}{2}, \tag{2.26}$$

minimises the potential at a non-zero value. The quantity $v \approx 246$ GeV [13] is referred to as the vacuum expectation value (vev) of Φ, arising when the potential has a non-zero ground state. Spontaneous symmetry breaking of the global $SU(2)_L \times U(1)_Y$ symmetry occurs when the field settles into a specific minimum. A convenient choice, referred to as the unitary gauge, sets the doublet components to the following:

$$\begin{aligned} \phi_1 = \phi_2 = \phi_4 = 0, \\ \phi_3 = \sqrt{\frac{-\mu^2}{\lambda}} = v. \end{aligned} \tag{2.27}$$

Due to the choice $\phi = \phi_2 = 0$ the charged scalar field component of Φ vanishes and leads to an electrically neutral ground state:

$$\Phi = \frac{1}{\sqrt{2}}\begin{pmatrix} 0 \\ v \end{pmatrix}. \tag{2.28}$$

By choosing this minimum, the global $SU(2)_L \times U(1)_Y$ symmetry get spontaneously broken. This reduces the number of degrees of freedom from four to one. The three seemingly vanishing degrees of freedom reappear as longitudinal degrees of freedom for the massive gauge bosons when they acquire mass. Expanding the field around the ground state yields:

$$\Phi = \frac{1}{\sqrt{2}}\begin{pmatrix} 0 \\ v + H \end{pmatrix}, \tag{2.29}$$

where H represents the physical Higgs field. Inserting Eq. 2.29 into Eq. 2.24 and replacing the derivative ∂_μ with the following covariant derivative:

$$D^\mu = \partial^\mu + i g_W \frac{\sigma_j}{2} W_j^\mu + i \frac{g'}{2} B^\mu, \tag{2.30}$$

keeps the Lagrangian invariant under local $SU(2)_L \times U(1)_Y$ gauge transformations. Explicitly this yields:

$$\begin{aligned} \left(D_\mu \Phi\right)^\dagger \left(D^\mu \Phi\right) = \frac{1}{2}\left(\partial_\mu H\right)^\dagger \left(\partial^\mu H\right) + \frac{1}{8} g_W^2 \left(W_\mu^1 + i W_\mu^2\right)\left(W^{1\mu} - i W^{2\mu}\right)(v+H)^2 \\ + \frac{1}{8}\left(g_W W_\mu^3 - g' B_\mu\right)\left(g_W W^{3\mu} - g' B^\mu\right)(v+H)^2. \end{aligned} \tag{2.31}$$

The mass terms arise from the terms proportional to v^2. Using the identities from Eq. 2.20–2.22, they can be re-expressed in the basis of the physical gauge bosons:

$$\mathcal{L}_{\text{mass}} = \frac{1}{2}\left(\frac{v g_W}{2}\right)^2 \left(W_\mu^- W^{-\mu} + W_\mu^+ W^{+\mu}\right) + \frac{1}{2}\left(\frac{v\sqrt{g_W^2 + g'^2}}{2}\right)^2 Z_\mu Z^\mu. \tag{2.32}$$

This demonstrates that, by introducing a complex scalar $SU(2)_L$ doublet with a non-zero vacuum expectation value, and coupling it to the $SU(2)_L$ and $U(1)_Y$ gauge fields, it is possible to generate mass terms for the corresponding gauge bosons while preserving local gauge invariance. This procedure is referred to as the Brout–Englert–Higgs (BEH) mechanism, or the Higgs mechanism for short. Through this mechanism, both the $W^\pm$ and Z^0 bosons acquire mass, while the photon remains massless. The masses of the electroweak gauge bosons are given by:

$$m_W = \frac{1}{2} v g_W \quad m_Z = \frac{1}{2} v \sqrt{g_W^2 + g'^2}. \tag{2.33}$$

The terms in Eq. 2.31 proportional to H and H^2 give rise to interactions between the Higgs boson and the $W^{\pm}$ gauge bosons:

$$\mathcal{L}_{\text{int}} \supset \frac{1}{2} g_W^2 v W_\mu^- W^{+\mu} H + \frac{1}{4} g_W^2 W_\mu^- W^{+\mu} H^2, \tag{2.34}$$

with coupling strength $\frac{g_W^2 v}{2} = g_W m_W$ proportional to the mass. Similarly the coupling strength for the HZZ interaction is given by $\frac{1}{2} v(g_W^2 + g'^2) = \frac{2m_Z^2}{v}$. The form of the potential in Eq. 2.25 also changes to:

$$V(H) = \lambda v^2 H^2 + \lambda v H^3 + \frac{\lambda}{4} H^4, \tag{2.35}$$

where the first term represents the mass of the Higgs boson $m_H = \sqrt{2\lambda v^2}$. The second and third term give rise to Higgs self-coupling.

2.2.5 Yukawa couplings and fermion mass terms

In the SM, fermions are initially massless due to the chiral structure of the theory. Left-handed fermions transform as doublets under $SU(2)_L$, whereas right-handed fermions transform as singlets. This distinction prevents the inclusion of explicit fermion mass terms in the Lagrangian, as such terms would not be invariant under local $SU(2)_L \times U(1)_Y$ gauge transformations. To regain the symmetry, Yukawa couplings between the scalar field Φ and fermion fields are introduced. For leptons they take the following form:

$$\mathcal{L}_Y^\ell = -y_\ell \, \bar{L}_\ell \, \Phi \, \ell_R + \text{h.c.}, \tag{2.36}$$

where $L_\ell = (\nu_\ell, \ell)_L^{\mathrm{T}}$ is the left-handed lepton doublet, ℓ_R is the right-handed charged lepton, Φ is the scalar doublet, and y_ℓ is the Yukawa coupling for lepton flavour $\ell = e, \mu, \tau$. Inserting Eq. 2.29 into the expression for the Yukawa interaction yields:

$$\mathcal{L}_Y^\ell = -\frac{y_\ell v}{\sqrt{2}} \bar{\ell}\ell - \frac{y_\ell}{\sqrt{2}} \bar{\ell}\ell \, H, \tag{2.37}$$

where H is the Higgs boson. The first term generates masses for the leptons:

$$m_\ell = \frac{y_\ell v}{\sqrt{2}}. \tag{2.38}$$

The second term describes interactions between the leptons and the Higgs boson, which, like the gauge bosons, have a coupling strength proportional to the mass (or equivalently, a mass proportional to the coupling strength). In the minimal SM, neutrinos remain massless. This follows from the absence of right-handed neutrino fields ν_R, which are required to form gauge-invariant Yukawa terms similar to those of the charged leptons.

Quark masses are generated in a similar way as the charged leptons, though the construction requires the use of both the Higgs doublet and its charge-conjugate. The Yukawa Lagrangian for a single quark generation can be written as:

$$\mathcal{L}_Y^q = -y_d\,\bar{Q}_L\,\Phi\,d_R - y_u\,\bar{Q}_L\,\tilde{\Phi}\,u_R + \text{h.c.}, \tag{2.39}$$

where $Q_L = (u, d)_L^{\mathrm{T}}$ is the left-handed quark doublet, u_R and d_R are the right-handed up-type and down-type quarks, and $\tilde{\Phi}$ is defined as:

$$\tilde{\Phi} = i\sigma_2\Phi^* = \begin{pmatrix} \phi^{0*} \\ -\phi^- \end{pmatrix}, \tag{2.40}$$

where σ_2 is the second Pauli matrix, ϕ^- is the conjugate of ϕ^+, and ϕ^{0*} is the conjugate of the neutral scalar field ϕ^0.

After symmetry breaking, the quarks acquire masses:

$$m_u = \frac{y_u v}{\sqrt{2}}, \qquad m_d = \frac{y_d v}{\sqrt{2}}, \tag{2.41}$$

with additional interaction terms coupling them to the Higgs boson. Extending this to all three generations introduces Yukawa matrices, which after diagonalization lead to the CKM matrix. This matrix describes flavour mixing and plays a central role in weak interaction processes involving quarks and violation of charge conjugation parity (CP) symmetry in the SM. This will be covered in more detail in Chapter 3.

2.3 Success and limitations of the Standard Model

The SM has successfully predicted the existence of several elementary particles prior to their experimental discovery. These include the $W^\pm$ and Z^0 bosons [17, 18], the gluon [22–25], as well as the top and bottom quarks [26–28]. The final missing component of the theory, the Higgs boson, was discovered in 2012 by the ATLAS and CMS collaborations at the LHC [1, 2].

In addition to the discovery of individual particles, the SM provides precise predictions for the production cross-sections for a wide range of processes. These predictions have been confirmed by numerous measurements at high-energy colliders. Figure 2.1 summarises selected cross-section measurements from the ATLAS experiment, showing excellent agreement with the SM predictions over several orders of magnitude.

However, despite its many successes, the SM does not offer a complete description of fundamental physics. Both experimental observations and theoretical considerations point towards the need for a more comprehensive framework. Selected key phenomena that cannot be explained within the SM are listed below:

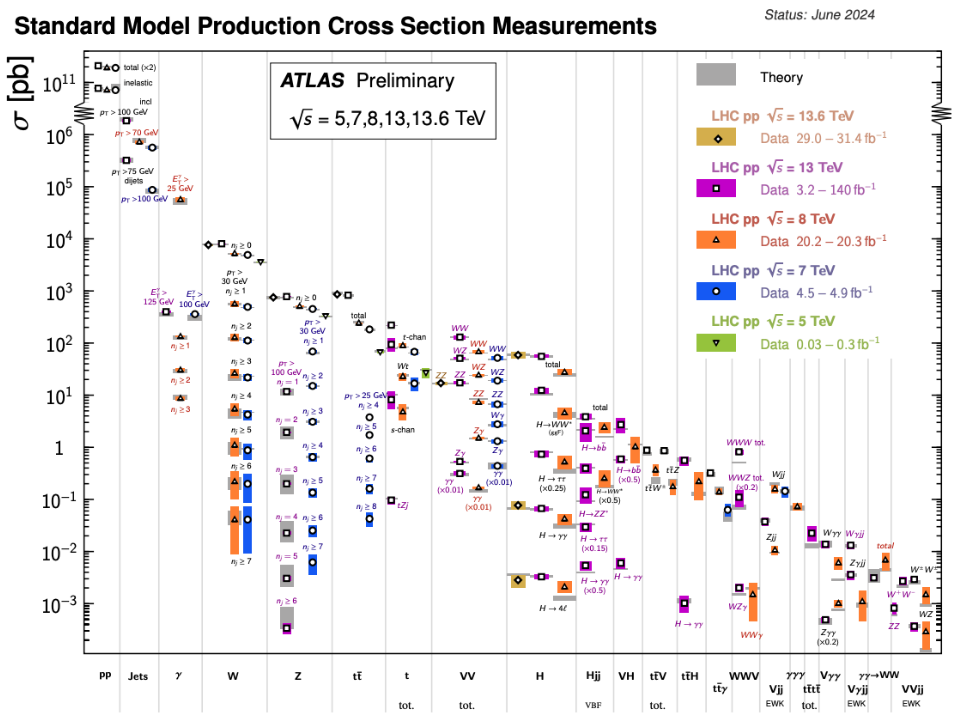

Figure 2.1: Measured production cross-sections for various SM processes as a function of process type, compared with theoretical predictions. The measurements are based on data collected by the ATLAS experiment up to 2024. The coloured bands represent the experimental measurements at different energies, while the grey band indicates the theoretical prediction uncertainties [29].

Gravity: Gravitational interactions are not included in the SM. Introducing the hypothesised spin-2 graviton as the mediator of gravity leads to a non-renormalisable theory, with ultraviolet divergences that cannot be consistently removed [30]. Efforts to develop a quantum theory of gravity include proposals such as string theory [31, 32] and loop quantum gravity [33].

Neutrino Masses: In the SM, neutrinos are massless due to the absence of right-handed neutrino states and the requirement of gauge invariance. However, the observation of neutrino oscillations [34–36], which involve changes in flavour during propagation, implies that at least two neutrino species must have non-zero masses. The mixing of neutrino flavour and mass eigenstates is described by the Pontecorvo–Maki–Nakagawa–Sakata (PMNS) matrix [37, 38].

Matter–Antimatter Asymmetry: The SM predicts that matter and antimatter should have been produced in equal amounts in the early universe. However, observations show that the present-day universe consists almost entirely of matter. This imbalance implies the need for a dynamical process known as baryogenesis, which must satisfy the three Sakharov conditions [6]: violation of baryon number, violation of C and CP symmetries, and a departure from thermal equilibrium. Although the SM exhibits features that partially satisfy these conditions, such as non-perturbative baryon number violation via sphaleron processes at high temperatures and CP violation in the quark sector via the CKM matrix, it is insufficient to quantitatively account for the observed asymmetry. A discussion of CP violation within the SM, as well as potential sources of additional CP violating couplings beyond the SM in the Higgs sector, is presented in Chapter 3.

Dark Matter: Observational evidence from galactic rotation curves [39], gravitational lensing [40], and measurements of the cosmic microwave background (CMB) [10] strongly indicates the existence of a non-visible, non-baryonic form of matter, commonly referred to as dark matter. The SM does not contain any viable dark matter candidate. Dark matter appears to interact predominantly through gravity, with no confirmed evidence for non-gravitational interactions via the electromagnetic, weak, or strong forces. According to CMB observations [10], dark matter constitutes approximately 27% of the total energy density of the universe, while baryonic matter accounts for about 5%. The remaining 69% is attributed to dark energy. Models and experimental approaches aiming to explain and detect dark matter will be discussed in more detail in Chapter 4.

Dark Energy: The accelerated expansion of the universe, observed through supernovae surveys [41, 42], provides strong evidence for the existence of dark energy. The SM does not account for this phenomenon. Dark energy is postulated to be uniformly distributed throughout space and to possess negative pressure, thereby influencing the dynamics of cosmic expansion. Within the ΛCDM framework, dark energy is often modelled as a non-zero cosmological constant Λ, corresponding to a vacuum energy density [43]. However, theoretical estimates of the vacuum energy based on quantum field theory exceed the observed value by many orders of magnitude, highlighting a profound theoretical challenge. The nature and origin of dark energy therefore remain unknown.

2.4 The Higgs boson

As discussed in the previous sections, electroweak symmetry breaking predicts the existence of a scalar particle, the Higgs boson. Since its discovery in 2012, the Higgs boson has been extensively studied at the LHC. The measured properties of the Higgs boson are in good agreement with the predictions of the SM. This section provides an overview of the Higgs boson properties relevant to the studies presented in this thesis.

2.4.1 Production and decay

There are several mechanisms by which a Higgs boson can be produced in proton–proton collisions at the LHC. The leading-order Feynman diagrams corresponding to the main production modes are shown in Figure 2.2. The production cross sections at a different centre-of-mass energies have been computed in Ref. [44] and are summarised in Figure 2.3.

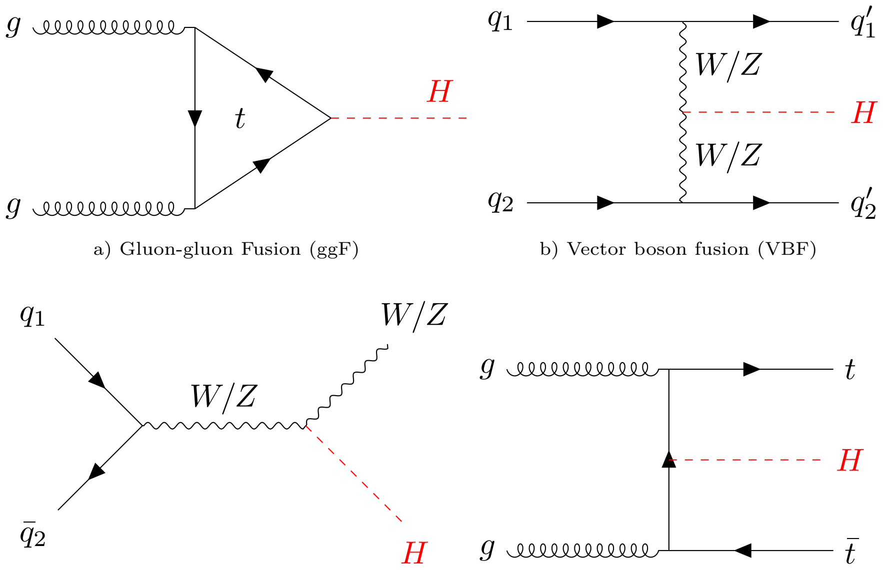

a) Gluon-gluon Fusion (ggF) b) Vector boson fusion (VBF)

c) Higgs-strahlung (VH) d) Associated production (ttH)

Figure 2.2: Leading order Feynman diagrams of the top four Higgs boson production modes at the LHC: gluon-gluon fusion (top left), vector-boson-fusion (top right), Higgs-Strahlung (bottom left) and associated production with a top-antitop quark pair (bottom left).

The dominant Higgs boson production mode is gluon–gluon fusion (ggF), in which two gluons interact through a virtual loop of heavy quarks, primarily the top quark, to produce a Higgs boson. This dominance arises because, at the energies probed by the LHC, gluon interactions from proton–proton collisions are highly probable and abundant, and because the Higgs–fermion coupling strength, given by the Yukawa interaction in Eq. 2.37, is proportional to the fermion mass.

The second most common production mechanism is vector boson fusion (VBF), where two incoming quarks emit W or Z bosons that fuse to form a Higgs boson. In addition to the Higgs, this process typically produces two high-momentum jets in the forward regions of the detector. These jets are well separated in pseudorapidity and form a distinctive topology, which helps to discriminate VBF events from background.

Associated production with a vector boson (VH) or a top quark pair ($t\bar{t}H$) also contribute to the overall Higgs boson production rate. While their cross sections are smaller, these processes offer different event topologies

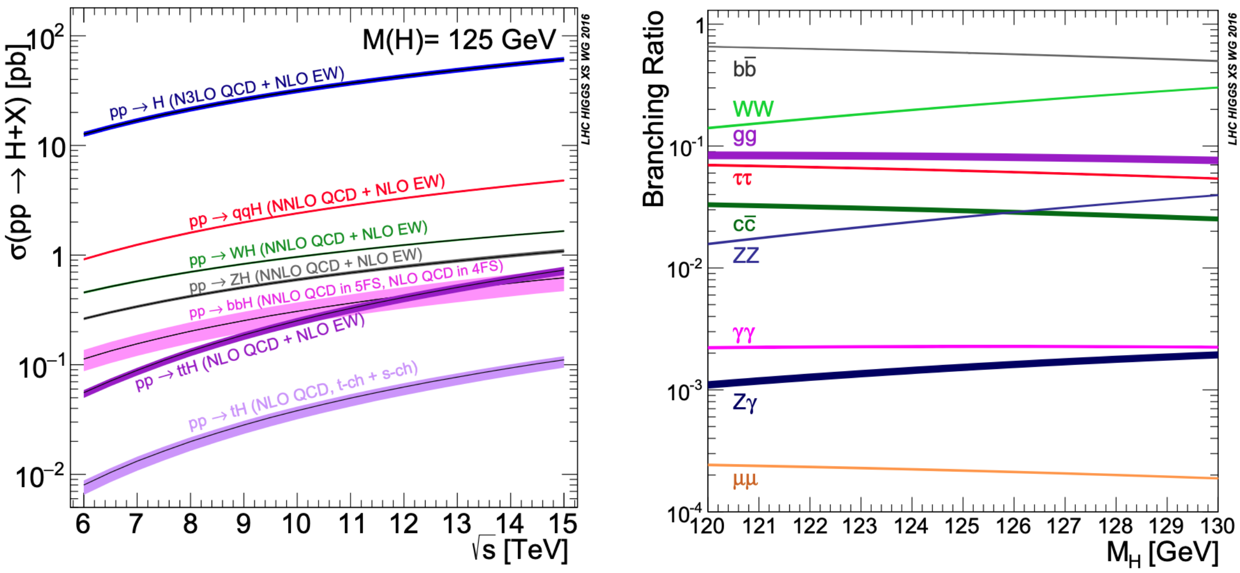

a) Higgs production b) Higgs decay

Figure 2.3: Higgs production cross section (left) as a function of $\sqrt{s}$ for proton-proton collisions. The VBF process is indicated here as qqH. Higgs decay branching ratios (right) as a function of m_H near $m_H = 125$ GeV [44].

that can be exploited in dedicated analyses.

The Higgs boson is not a stable particle and is therefore inferred through the reconstruction of its decay products. As it couples to all massive SM particles, it can decay via multiple channels. The hierarchy of the Higgs boson decays is closely related to particle masses. Decays to heavier particles are generally favoured. Since the top quark is heavier than the Higgs boson, on-shell $H \to t\bar{t}$ decays are kinematically forbidden. Consequently, the largest branching ratio comes from $H \to b\bar{b}$ decays, followed by WW, and gg. The latter arises from loop-mediated processes involving top or bottom quarks, and can be considered the reverse analogue of the ggF production mechanism. The fourth largest branching ratio comes from the decay studied in both analyses in this thesis, namely $H \to \tau\tau$. A summary of the expected Higgs boson branching ratios is shown in Figure 2.3. The branching ratios are calculated from comparing the partial decay width from each mode with the total Higgs decay width Γ. At leading order in perturbation theory, the partial decay width for the $H \to \tau\tau$ process is given by:

$$\Gamma(H \to \tau\tau) = \frac{g_W^2 m_H m_\tau^2}{32\pi m_W^2}\left(1 - \frac{4m_\tau^2}{m_H^2}\right)^{\frac{3}{2}}. \tag{2.42}$$

The most precise predictions for the branching ratios are obtained using the PROPHECY4F [45, 46] and HDECAY [47] programs. Based on these calculations, the branching ratio for $H \to \tau\tau$ is estimated to be [44]:

$$\mathrm{BR}(H \to \tau\tau) = 0.0627 \pm 0.0014, \tag{2.43}$$

where the uncertainty includes theoretical uncertainties due to missing higher order corrections, and parametric uncertainties.

2.4.2 Spin and CP properties

The SM predicts the Higgs boson to be a spin-0 particle with even parity. From the Landau-Yang theorem [48] it is forbidden for a massive spin-1 particle to decay into two photons. Since the decay $H \to \gamma\gamma$ has been observed experimentally (mediated via loop diagrams involving $W^{\pm}$ bosons or heavy quarks), it follows that the Higgs boson cannot be a spin-1 state.

Alternative spin and parity hypotheses have been tested by ATLAS, primarily using bosonic final states during Run 1 [49]. The results, summarised in Figure 2.4, provide strong support for the SM prediction and exclude several alternative scenarios at 99% confidence level. Among the excluded models is a pure CP-odd Higgs state. However, no definitive conclusion could be drawn regarding a mixed CP state with a predominantly CP-even component.

Studies of a potential CP-mixed Higgs boson state were initiated during Run 1 [50] and have been extended with more comprehensive analyses in Run 2 [51–53]. To date, no significant indication of a CP-odd component has been observed. However, the sensitivity of these measurements remains limited by statistical uncertainties, and the possibility of a CP-mixed state is not yet fully excluded. This possibility is the subject of the central analysis presented in this thesis and will be covered in the next section.

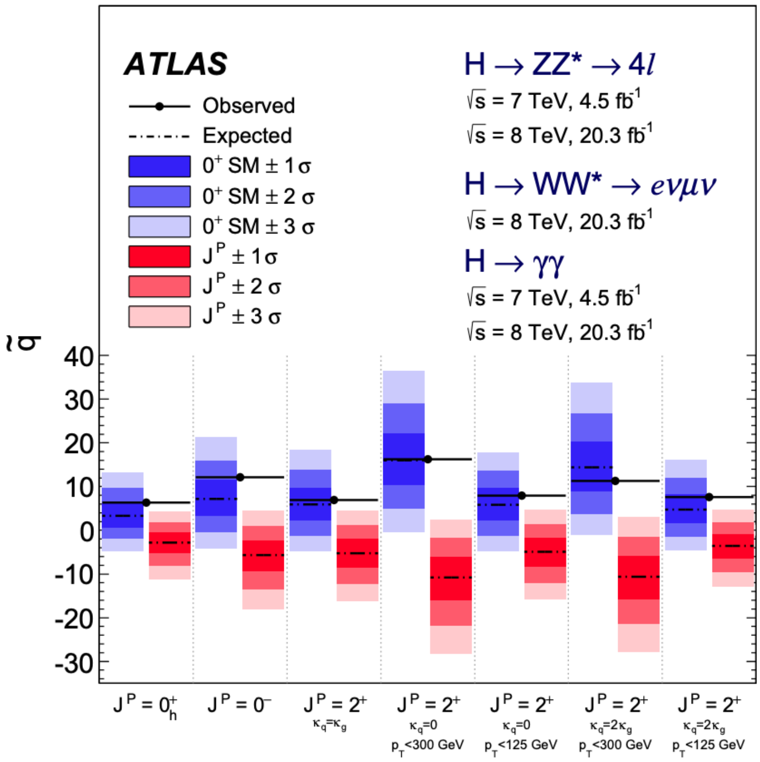

Figure 2.4: Distribution of the test statistic $\tilde{q}$ (Obtained from the profile likelihood ratio) for different spin and CP hypotheses of the Higgs boson. Observed values is indicated in black. The SM expectation is shown in blue, while alternative hypotheses are shown in red. Associated uncertainties are represented by corresponding error bands ($\pm 1\sigma$, $\pm 2\sigma$, $\pm 3\sigma$). Results are from the ATLAS experiment with Run 1 data and combine measurements from the $H \to ZZ^* \to 4\ell$, $H \to WW^* \to e\nu\mu\nu$, and $H \to \gamma\gamma$ decay channels [54].

Chapter 3

CP Violation and Anomalous HVV Couplings

In 1932, Carl Anderson discovered particles identical in mass to electrons but with opposite electric charge [55]. This marked the first experimental evidence of antimatter, as predicted by the Dirac equation. Antimatter has the same properties as matter, except for reversed additive quantum numbers. CP symmetry asserts that the behaviour of a physical system remains unchanged when particles are replaced with their antiparticles (charge conjugation, C) and the system is mirrored (parity, P). Furthermore, CP symmetry implies that any process involving the creation or annihilation of matter must involve an equal amount of antimatter. This is in conflict with the observation that the universe contains almost no antimatter.

The first and major project of this thesis is a search for CP violation in the coupling of the Higgs boson to vector bosons, often referred to as the HVV couplings. The search is performed using the VBF Higgs production mode, utilising Higgs decays to τ-lepton pairs. The Feynman diagram for this process is illustrated in Figure 3.1, with the red circle indicating the HVV vertex.

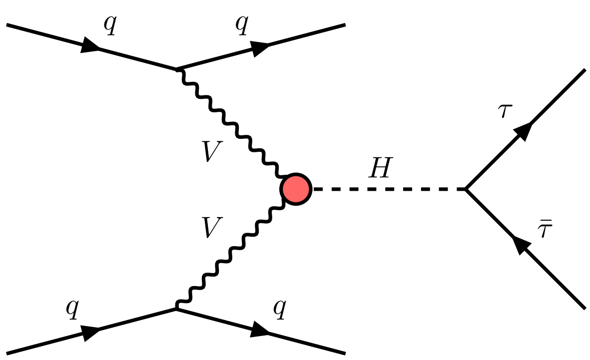

Figure 3.1: Higgs VBF production with the red dot indicating the HVV vertex. The topology consists of two tagging jets and the Higgs decay.

This chapter covers CP-violating processes within the SM, explores how additional CP-violating effects can arise in theories beyond the SM, and outlines methods for testing CP invariance in a framework based on effective field theory, with a specific focus on VBF Higgs production.

3.1 CKM matrix and CP violation in the Standard Model

In the SM, the only interaction known to violate CP symmetry is the in the weak interaction of quarks. The first evidence of CP violation was discovered in 1964 through the decay of neutral kaons [56]. To account for this phenomenon, the Cabibbo-Kobayashi-Maskawa (CKM) matrix was introduced [7, 8]. The CKM matrix arises from the fact that the mass eigenstates of quarks do not align with the weak eigenstates, which govern how quarks couple to the $W^\pm$ boson. This misalignment give rise a unitary 3×3 matrix, expressed as:

$$V_{\mathrm{CKM}} = \begin{pmatrix} V_{ud} & V_{us} & V_{ub} \\ V_{cd} & V_{cs} & V_{cb} \\ V_{td} & V_{ts} & V_{tb} \end{pmatrix}, \tag{3.1}$$

where the subscripts correspond to the different quark flavours. The CKM matrix describes the probability of a transition from one quark flavour j to another quark flavour i through the exchange of a weak boson $W^\pm$. These transitions are proportional to $|V_{ij}|^2$. CP violation can be made manifest by choosing an explicit parametrisation. The Wolfenstein parametrisation is an expansion of the CKM matrix in terms of $\lambda = |V_{us}|$ (approximately 0.22) that expresses the matrix using four mixing parameters: λ, A, ρ, and η. Neglecting higher order terms proportional to λ^4, this parametrisation gives:

$$V_{\mathrm{CKM}} = \begin{pmatrix} 1 - \frac{\lambda^2}{2} & \lambda & A\lambda^3(\rho - i\eta) \\ -\lambda & 1 - \frac{\lambda^2}{2} & A\lambda^2 \\ A\lambda^3(1 - \rho - i\eta) & -A\lambda^2 & 1 \end{pmatrix} + \mathcal{O}\left(\lambda^4\right). \tag{3.2}$$

For CP symmetry to be violated, it is necessary that $V_{ij} \neq V_{ij}^*$, which requires the presence of a complex phase in the CKM matrix. From the Wolfenstein parametrisation, this condition is satisfied if $\eta \neq 0$. The parameters of the matrix are experimentally accessible from flavour decays, with global fits performed by the CKMFitter [57] and UTFit [58] collaborations. The current global fit results for the four mixing parameters [13] gives:

$$\begin{aligned} &\lambda = 0.22501 \pm 0.00068, \quad &A = 0.826^{+0.016}_{-0.015} \\ &\bar{\rho} = 0.1591 \pm 0.0094, \quad &\bar{\eta} = 0.3523^{+0.0073}_{-0.0071}, \end{aligned} \tag{3.3}$$

with $\bar{\rho} = \rho\left(1 - \lambda^2/2 + \ldots\right)$ and $\bar{\eta} = \eta\left(1 - \lambda^2/2 + \ldots\right)$. From these measurements, the 9 CKM elements can be explicitly written out, revealing the hierarchy of transition amplitudes for quarks in the SM [13]:

$$|V_{\mathrm{CKM}}| = \begin{pmatrix} 0.97435 \pm 0.00016 & 0.22501 \pm 0.00068 & 0.003732^{+0.000090}_{-0.000085} \\ 0.22487 \pm 0.00068 & 0.97349 \pm 0.00016 & 0.04183^{+0.0069}_{-0.000069} \\ 0.00858^{+0.0019}_{-0.00017} & 0.04111^{+0.00077}_{-0.00068} & 0.999118^{+0.00009}_{-0.000034}. \end{pmatrix} \tag{3.4}$$

How the complex phase arise in the CKM matrix depends on the parametrisation. One can however define a CP-violating quantity in V_{CKM} that is independent of the parametrisation [59]. This quantity, called the Jarlskog invariant, relates the amount CP violation directly to the elements of the CKM matrix, but can also be written out in terms of the Wolfenstein mixing parameters:

$$J \simeq \lambda^6 A^2 \eta. \tag{3.5}$$

CP violation requires $J \neq 0$, which naturally follows from $\eta \neq 0$. Current best measurement of the Jarlskog invariant yields [13]:

$$J = \left(3.12^{+0.13}_{-0.12}\right) \times 10^{-5} \tag{3.6}$$

These measurements show that CP violation is an intrinsic property of the SM that arise within the electroweak quark sector. While analogous mechanisms exist in the neutrino sector, where CP violation can arise through the mixing of neutrinos as described by the PMNS matrix [37, 38], such topics will not be covered in this thesis. The only confirmed and established source of CP violation within the SM arises from the complex phase in the CKM matrix. Consequently, its implications for baryogenesis have been studied extensively [3–5]. The baryon asymmetry in the universe, usually expressed as the ratio of baryon to photon number densities, has been measured through observations of the Cosmic Microwave Background (CMB) at the time of Big Bang Nucleosynthesis (BBN) to be [60]:

$$\frac{n_b - n_{\bar{b}}}{n_\gamma} \approx \frac{n_b}{n_\gamma} = (6.10 \pm 0.04) \times 10^{-10}. \tag{3.7}$$

The necessary conditions for generating such an asymmetry were first formulated by Andrei Sakharov in 1967 [6], who identified three key requirements: baryon number violation, C and CP violation, and a departure from thermal equilibrium. While the SM satisfies these conditions in principle, its quantitative contributions fall far short of explaining the observed asymmetry. The net baryon asymmetry produced within the SM is estimated to be of order 10^{-20} [61], many orders of magnitude below the observed value, rendering the amount of CP violation in the SM effectively negligible for baryogenesis.

Following the discovery of the Higgs boson, its interactions with fermions and gauge bosons have been recognised as possible sources of CP violation beyond those present in the SM. While a purely CP-odd Higgs state has been excluded at the 99% confidence level, current experimental results still have not fully excluded the possibility of a CP-mixed state dominated by a CP-even component. The observation of such a state would constitute direct evidence of CP violation in the Higgs sector and point to physics beyond the the SM (BSM).

The following sections will therefore provide an overview of how CP-violating effects in the coupling between the Higgs and gauge boson can be described within the framework of effective field theory. In addition, strategies for probing such effects at the LHC will be discussed.

3.2 Effective Field Theories

BSM physics may introduce new particles that are too massive to be directly produced at the LHC. In such cases, direct observation is not feasible, and the effects of these heavy particles must be studied indirectly. Effective field theories (EFTs) provide a framework to describe the impact of heavy particles with mass M at an energy scale Λ on observables at much lower energy scales $E \ll \Lambda$. This approach allows physics at the infrared (IR) scale to be described without requiring detailed knowledge of the full ultraviolet (UV) theory, as enabled by the decoupling theorem [62].

The key advantage of EFTs is that they do not require knowledge of the field content of the UV theory, enabling model-independent tests at lower energy scales. A well-known example of an EFT is Fermi's theory of weak interactions [63]. This framework describes charged-current processes of the weak interaction at energy scales below the mass of the W boson. For instance, the β decay of a neutron, $n \to p + e^- + \bar{\nu}_e$, and the muon decay, $\mu^- \to e^- + \bar{\nu}_e + \nu_\mu$, can be effectively described as direct couplings with strength, G_F (the Fermi coupling constant), between four fermions. The four-fermion interaction for the muon decay is illustrated in Figure 3.2a.

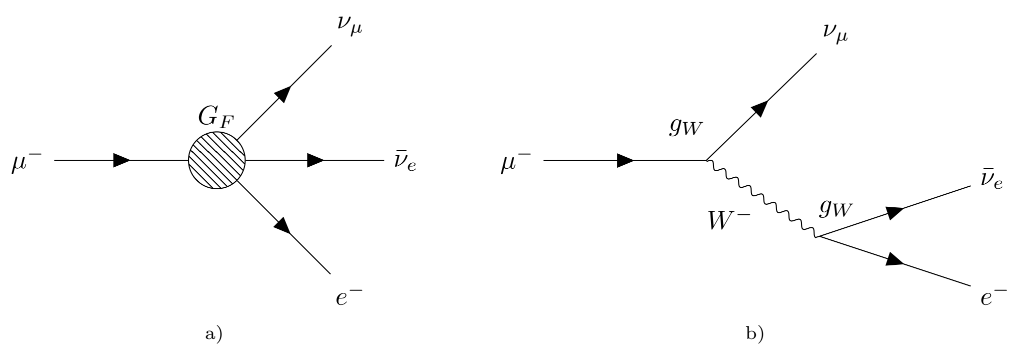

Figure 3.2: Comparison of muon decay interactions: (a) Four-fermion interaction with an effective Fermi coupling G_F. (b) SM description via the exchange of a W^- boson with weak coupling g_W.

At low energies, this effective interaction provides an reliable approximation, successfully capturing the phenomenology of weak decays without requiring the explicit presence of a mediator. However, this effective description breaks down at energies approaching 80 GeV. At these energy scales, the exchanged particle in the interaction, the W boson, must be explicitly included in the theory. The W boson, with a mass of $m_W \approx 80.4$ GeV, mediates the weak interaction as shown in Figure 3.2b. The relation between the Fermi coupling constant G_F and the weak coupling strength g_W is given by:

$$G_F = \frac{\sqrt{2} g_W^2}{8 m_W^2}. \tag{3.8}$$

The same procedure can be applied to the entire SM, treating it as a low-energy effective theory in which the effects of BSM physics are encoded in higher-dimensional operators. The Standard Model Effective Field Theory (SMEFT) framework [64] extends the SM Lagrangian by including additional Lorentz-invariant operators constructed from SM fields. These operators capture the effects of new physics without requiring explicit assumptions about the nature of the underlying theory.

Each operator has a dimensionless prefactor f, known as the Wilson coefficient, and is suppressed by a power of the energy scale Λ, which represents the characteristic scale of new physics. This scale can be interpreted as the mass scale where new particles and interactions, beyond those included in the EFT, become important and need to be explicitly accounted for. The structure of an EFT Lagrangian can be expressed as:

$$\mathcal{L}_{\text{EFT}} = \mathcal{L}_{\text{SM}} + \sum_i \frac{f_i^5}{\Lambda} \mathcal{O}_i^5 + \sum_i \frac{f_i^6}{\Lambda^2} \mathcal{O}_i^6 + \dots \tag{3.9}$$

The superscript of the operators $\mathcal{O}_i$ denotes their mass dimension. Since Lagrangians have a mass dimension of 4, dimension-5 operators are suppressed by a factor of $1/\Lambda$, dimension-6 operators by $1/\Lambda^2$, and so on. Λ is typically assumed to be of order 1 TeV or higher, as current experimental results have not indicated the presence of new particles below this scale.

The Wilson coefficients serve as the coupling constants in the EFT and are determined by the couplings and masses of the full theory, analogous to how G_F is defined in terms of g_W and m_W in the Fermi theory according to Eq. 3.8. Measuring values for the Wilson coefficient that deviate from zero, would be a sign of new physics. Any UV-complete BSM theory that reduces to the SM at low energies can be described within this framework. Consequently, constraining the Wilson coefficients of the SMEFT operators imposes simultaneous constraints on a wide range of potential UV-complete models.

In the SMEFT framework, the large number of possible higher-dimensional operators can make calculations and interpretations challenging. Not all operators that can be constructed from the SM fields are permitted, only combinations of fields that respect the SM symmetries can be consistently incorporated into the SMEFT

Lagrangian. It is also common to organize the operators into well-defined bases. A basis is a complete, non-redundant set of operators that can be used to express any possible effective interaction in the SMEFT framework. Different bases provide alternative ways of organizing the same underlying physics, often tailored to specific theoretical or experimental considerations, simplifying the study of BSM interactions.

At dimension-5, the only allowed operator is the Weinberg operator [65], which introduces Majorana neutrino masses and violates lepton number. While this operator is important for understanding neutrino physics, it is typically neglected in studies of Higgs physics. Operators of dimension greater than six are increasingly suppressed by higher powers of Λ, making dimension-6 terms the primary focus of most SMEFT analyses. The dimension-6 operators can be expressed in several bases, the most commonly used being the Warsaw [66], HISZ [67], and SILH [68] bases. These bases are related through mappings derived from the equations of motion [69]. In the context of CP violation and the studies presented in this thesis, results are interpreted within both the HISZ and Warsaw basis.

3.2.1 HISZ basis

The HISZ basis [67], introduced by Hagiwara, Ishihara, Szalapski, and Zeppenfeld, is a restricted set of dimension-6 operators that modify gauge boson couplings while respecting $\mathrm{SU}(2)_L \times \mathrm{U}(1)_Y$ symmetry. Although it stems from the broader SMEFT, the HISZ basis focuses specifically on electroweak gauge boson sector. One simplification is that the scope of the EFT used in this thesis is limited to CP-odd extensions of HVV couplings. In this framework, the effective Lagrangian is the SM Lagrangian extended by CP-violating operators of mass dimension-6. These operators are constructed from the Higgs doublet Φ and the $U(1)$ and $SU(2)$ electroweak gauge fields B_μ and W_μ^j ($j = 1, 2, 3$), respectively. CP-conserving dimension-6 operators formed from these fields are not considered. All interactions between the Higgs boson and other SM particles (fermions and gluons) are assumed to follow the predictions from the SM. The simplified EFT Lagangian can be written as [64, 70]:

$$\mathcal{L}_{\text{eff}} = \mathcal{L}_{\text{SM}} + \frac{f_{\tilde{B}B}}{\Lambda^2}\mathcal{O}_{\tilde{B}B} + \frac{f_{\tilde{W}W}}{\Lambda^2}\mathcal{O}_{\tilde{W}W} + \frac{f_{\tilde{B}}}{\Lambda^2}\mathcal{O}_{\tilde{B}}. \tag{3.10}$$

In terms of the SM fields the three dimension-6 operators are defined as:

$$\mathcal{O}_{\tilde{B}B} = \Phi^\dagger \hat{\tilde{B}}_{\mu\nu}\hat{B}^{\mu\nu}\Phi, \quad \mathcal{O}_{\tilde{W}W} = \Phi^\dagger \hat{\tilde{W}}_{\mu\nu}\hat{W}^{\mu\nu}\Phi, \quad \mathcal{O}_{\tilde{B}} = (D_\mu\Phi)^\dagger \, \hat{\tilde{B}}^{\mu\nu} D_\nu\Phi. \tag{3.11}$$

Here, $\hat{B}_{\mu\nu} = i\frac{g'}{2}B_{\mu\nu}$ and $\hat{W}_{\mu\nu} = \frac{ig_W}{2}\sigma_j W^j_{\mu\nu}$ with σ_j being the Pauli matrices. The last operator $\mathcal{O}_{\tilde{B}}$ contributes to the CP-violating charged triple gauge couplings via the relation $\tilde{\kappa} = \cot 2\theta_W \frac{\kappa}{2} = -\frac{m_W^2}{\Lambda^2} f_{\gamma WZ}\tilde{B}$. CP-violating charged triple gauge couplings have been constrained by the ALEPH [71] and OPAL [72] experiments. The contribution from $\mathcal{O}_{\tilde{B}}$ is therefore neglected in the following, and only contributions from $\mathcal{O}_{\tilde{B}B}$ and $\mathcal{O}_{\tilde{W}W}$ are taken into account. These two operators can be written in the in terms of the Higgs boson, photon and the Z boson after electroweak symmetry breaking. Following the notation in Ref. [73] this gives:

$$\mathcal{L}_{\text{eff}} = \mathcal{L}_{\text{SM}} + \tilde{g}_{HAA} H \tilde{A}_{\mu\nu} A^{\mu\nu} + \tilde{g}_{HAZ} H \tilde{A}_{\mu\nu} Z^{\mu\nu} + \tilde{g}_{HZZ} H \tilde{Z}_{\mu\nu} Z^{\mu\nu} + \tilde{g}_{HWW} H \tilde{W}^{+}_{\mu\nu} W^{\mu\nu}_{-}. \tag{3.12}$$

Only two out of the four couplings, g_i, are independent due to constraints imposed by the $U(1)_Y \times SU(2)_L$ invariance on the Lagrangian in Eq. 3.10. They can therefore be expressed in terms of two dimensionless parameters, $\tilde{d}$ and $\tilde{d}_B$:

$$\tilde{g}_{HAA} = \frac{g}{2m_W}(\tilde{d}\sin^2\theta_W + \tilde{d}_B\cos^2\theta_W) \qquad \tilde{g}_{HAZ} = \frac{g}{2m_W}\sin 2\theta_W(\tilde{d} - \tilde{d}_B) \tag{3.13}$$

$$\tilde{g}_{HZZ} = \frac{g}{2m_W}(\tilde{d}\cos^2\theta_W + \tilde{d}_B\sin^2\theta_W) \qquad \tilde{g}_{HWW} = \frac{g}{m_W}\tilde{d} \tag{3.14}$$

Relating the parameters $\tilde{d}$ and $\tilde{d}_B$ to the corresponding Wilson coefficients, yields the following expressions:

$$\tilde{d} = -\frac{m_W^2}{\Lambda^2} f_{\tilde{W}W} \quad \tilde{d}_B = -\frac{m_W^2}{\Lambda^2}\tan^2\theta_W f_{\tilde{B}B}, \tag{3.15}$$

where $\tilde{d}$ and $\tilde{d}_B$ represent contributions from different vector bosons to the CP-odd HVV coupling. However, in practice, the different electroweak gauge boson fusion processes cannot be distinguished experimentally. Therefore, for simplicity, the assumption $\tilde{d} = \tilde{d}_B$ is made. This yields the following relations:

$$\tilde{g}_{HAA} = \tilde{g}_{HZZ} = \frac{1}{2}\tilde{g}_{HWW} = \frac{g}{2m_W}\tilde{d} \quad \text{and} \quad \tilde{g}_{HAZ} = 0, \tag{3.16}$$

enabling the characterization of CP violation in the HVV vertex with a single parameter $\tilde{d}$. The matrix element for the HVV interaction receives a CP-even contribution, $\mathcal{M}_{\text{SM}}$, from the SM and a CP-odd contribution, $\mathcal{M}_{\text{CP-odd}}$, from the considered dimension-6 operators:

$$\mathcal{M} = \mathcal{M}_{\text{SM}} + \tilde{d} \cdot \mathcal{M}_{\text{CP-odd}}. \tag{3.17}$$

The cross-section is proportional to the squared matrix element which can be separated into three terms:

$$|\mathcal{M}|^2 = |\mathcal{M}_{\text{SM}}|^2 + \tilde{d} \cdot 2\,\text{Re}(\mathcal{M}^*_{\text{SM}}\mathcal{M}_{\text{CP-odd}}) + \tilde{d}^2 \cdot |\mathcal{M}_{\text{CP-odd}}|^2. \tag{3.18}$$

The first and third term are both CP-even and do not contribute to CP violation. The interference term however, $\tilde{d} \cdot 2\,\text{Re}(\mathcal{M}^*_{\text{SM}}\mathcal{M}_{\text{CP-odd}})$, is CP-odd and results in CP violation in the HVV vertex. This term does not contribute to the total cross-section, since it vanishes when integrated over a CP-symmetric phase space. The third term leads to an increase in the cross-section quadratically in $\tilde{d}$. Although this term depends on $\tilde{d}$, this features is not exploited in the analysis described in Chapter 8, since an increase in the total cross-section with respect to the SM can also arise from additional CP-even contributions.

3.2.2 Warsaw basis

The Warsaw basis [66] is the most widely used basis for dimension-6 operators and is the main basis used by ATLAS for combination efforts. In total there are 59 gauge and Lorentz invariant operators in the Warsaw basis, 6 of which are related to the HVV vertex: 3 being CP-even and 3 being CP-odd. The CP-odd operators can be written in a similar way as in the HISZ basis:

$$\mathcal{L}_{\text{Warsaw}} \supset \frac{c_{H\tilde{B}}}{\Lambda^2}\mathcal{O}_{\tilde{B}B} + \frac{c_{H\tilde{W}}}{\Lambda^2}\mathcal{O}_{\tilde{W}W} + \frac{c_{H\tilde{W}B}}{\Lambda^2}\mathcal{O}_{\tilde{B}}. \tag{3.19}$$

However, while in the HISZ basis certain assumptions are made by relating the coefficients of these operators, in the Warsaw basis they are treated as separate and independent. Since VBF production is predominantly mediated by the HWW vertex, analyses targeting this production mode are primarily sensitive to $c_{H\tilde{W}}$, with significantly reduced sensitivity to $\tilde{c}_{HB}$ and $c_{H\tilde{W}B}$.

Similar to Eq. 3.18, the contributions of each operator to the squared matrix element can be separated into SM, BSM and SM–BSM interference terms:

$$|\mathcal{M}|^2 = |\mathcal{M}_{\text{SM}}|^2 + 2\sum_i \frac{c_i}{\Lambda^2}\operatorname{Re}\left(\mathcal{M}^*_{\text{SM}}\mathcal{M}_i\right) + \sum_{i,j}\frac{c_i c_j}{\Lambda^4}\operatorname{Re}\left(\mathcal{M}^*_i\mathcal{M}_j\right), \tag{3.20}$$

where c_i and c_j are the Wilson coefficient for each of the considered Warsaw basis operators. Like in the HISZ basis, only the interference term is CP-odd and probed in the analysis in Chapter 8. The SM and quadratic BSM term are both CP-even and only contribute to the total cross section.

A conversion between the Warsaw basis and the HISZ basis is possible if certain conditions are satisfied. If the Wilson coefficient $c_{H\tilde{W}B}$ and $f_{\tilde{B}}$ are both set to zero, and it is assumed that $c_{H\tilde{W}} = c_{H\tilde{B}}$, it is possible to show that:

$$\tilde{d} = \frac{v^2}{\Lambda^2}c_{H\tilde{W}} = \frac{v^2}{\Lambda^2}c_{H\tilde{B}}. \tag{3.21}$$

These assumptions are equivalent to setting $\tilde{d} = \tilde{d}_B$ in the HISZ basis. As a result, they do not permit independent measurements of the corresponding Warsaw basis parameters, and is therefore not used in the analysis in this thesis. Nevertheless, it provides a useful illustration of how the parametrisations in the two bases scale relative to one another.

3.3 CP-odd observables and the Optimal Observable

Testing CP invariance involves selecting an observable that is sensitive to CP-mixing. If the initial state $|i\rangle$ and final state $|f\rangle$ of a process $|i\rangle \to |f\rangle$ are eigenstates under the CP transformation with different eigenvalues, CP invariance is violated. Following the description in Ref. [74], an observable can be constructed such that:

$$\mathcal{O}(CP|i\rangle \to CP|f\rangle) = \pm\mathcal{O}(|i\rangle \to |f\rangle), \tag{3.22}$$

which is a CP-odd observable if it changes sign under CP transformation. If the initial state is an eigenstate under CP and the underlying theory is CP-symmetric, the expectation value of a CP-odd observable will be 0. Consequently, a symmetric distribution of $\mathcal{O}$ around zero implies CP conservation, with $\langle\mathcal{O}\rangle = 0$. In contrast, any asymmetry, where $\langle\mathcal{O}\rangle \neq 0$, provides evidence for CP violation [74].

It is worth noting that the initial qq' state in VBF production is not a CP eigenstate [74, 75]. This prevents the construction of genuinely CP-odd observables in the strict sense. Nonetheless, the initial state is invariant under parity and under the so-called naive time-reversal (T_N) transformation [75, 76], defined as reversing the momenta and spins of all particles without exchanging the initial and final states. As a result, one can construct T_N-odd observables to probe CP violation.

The distinction between a CP-odd and T_N-odd observables only becomes important when considering particles with masses below the EFT cutoff scale Λ that can lead to additional BSM contributions to the VBF process through loop corrections. Such on-shell loop corrections are also referred to as rescattering. These contributions can break the T_N symmetry of the VBF transition amplitude, leading to a non-zero mean value of $\mathcal{O}$, even in the absence of CP violation. A significantly asymmetric $\mathcal{O}$ distribution would therefore indicate either CP violation or rescattering, both of which are evidence for new physics. In this analysis, the considered observables are treated as CP-odd under the assumption that rescattering effects are negligible, which is well motivated given the lack of evidence for such phenomena.

Many CP-odd observables exist and they can be constructed from the VBF topology shown in Figure 3.1, where the final state consist of two quarks that hadronise into two jets alongside the Higgs boson decay. The most straightforward CP-odd observable is the signed azimuthal angle between the tagging two jets, $\Delta\phi_{jj}^{\mathrm{signed}}$ [77], defined as:

$$\Delta\phi_{jj}^{\mathrm{signed}} = \phi_{j_1} - \phi_{j_2}, \tag{3.23}$$

where j_1 and j_2 are the VBF tagging jets ordered such that $\eta_{j_1} > \eta_{j_2}$. The sensitivity of $\Delta\phi_{jj}^{\mathrm{signed}}$ to CP violation originates from the structure of the Higgs interactions in the VBF process. In the SM, these interactions lead to a parity-symmetric angular distributions of the jets. However, in a CP-mixed scenario, where both CP-even and CP-odd contributions interfere, P-violating effects induced by the CP-odd component alter the angular distributions of the jets, breaking the symmetry of $\Delta\phi_{jj}^{\mathrm{signed}}$. This asymmetry manifests as a shift in the signed angle distribution, resulting in $\langle\Delta\phi_{jj}^{\mathrm{signed}}\rangle \neq 0$.

The expression can also be expanded by incorporating information about the transverse momenta of the two jets and taking the sine of $\Delta\phi_{jj}^{\text{signed}}$. As shown in Ref. [78] the following observable can be defined:

$$\mathcal{O} \;=\; p_T^{j_1}\, p_T^{j_2}\, \sin\!\left(\Delta\phi_{jj}^{\text{signed}}\right), \tag{3.24}$$

which in addition to the signed azimuthal angle also effectively captures the cross-product nature of the two jets.

Distributions for the two angular observables can be seen in Figure 3.3, showing simulated VBF $H \to \tau\tau$ events for the SM ($\tilde{d} = 0$) and two CP-violating scenarios with $\tilde{d} = 0.1$ and $\tilde{d} = -0.02$. The SM distribution is symmetric, whereas the BSM distributions are shifted to the right and left for positive and negative values of $\tilde{d}$, respectively. The degree of CP violation is related to the amount asymmetry which is directly proportional to the magnitude of $\tilde{d}$ defined in Eq. 3.15.

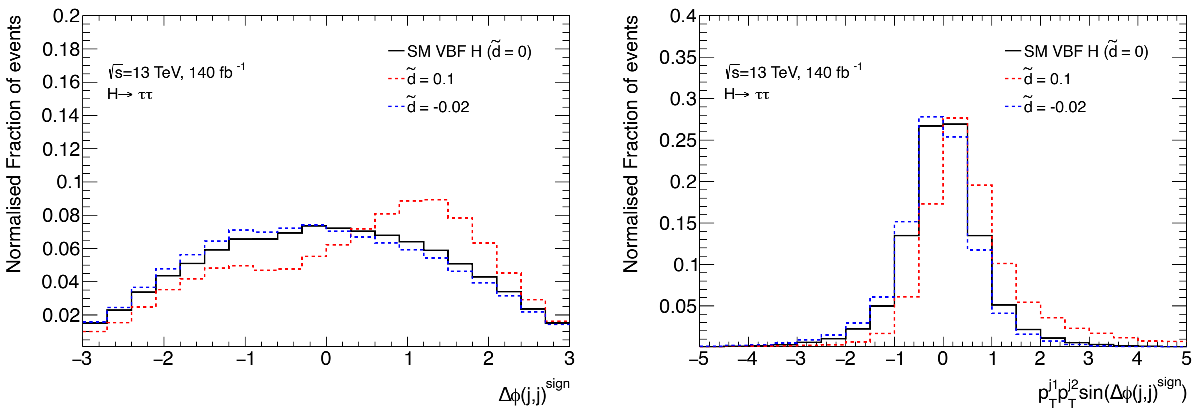

Figure 3.3: Simulated distributions for $\Delta\phi_{jj}^{\text{signed}}$ (left) and $p_T^{j_1}\, p_T^{j_2}\, \sin\!\left(\Delta\phi_{jj}^{\text{signed}}\right)$ (right) in VBF $H \to \tau\tau$ showing the SM case (black) and two CP-violating scenarios with $\tilde{d} = 0.1$ (red) and $\tilde{d} = -0.02$ (blue).

3.3.1 The Optimal Observable

The interference term in Eq. 3.18 can be used to construct a CP-odd observable, known as the Optimal Observable (OO) [79–81]. It is defined as the ratio of the interference term between the BSM and SM matrix elements to the squared SM matrix element:

$$\mathrm{OO} = \frac{2\,\mathrm{Re}\left(\mathcal{M}_{\mathrm{SM}}^{*}\mathcal{M}_{\mathrm{CP-odd}}\right)}{\left|\mathcal{M}_{\mathrm{SM}}\right|^{2}}. \tag{3.25}$$

This CP-odd observable characterizes the full phase space of the VBF final state, condensing high-dimensional information into a single quantity. It was demonstrated in Run 1 to have the highest sensitivity to $\tilde{d}$, compared to $\Delta\phi_{jj}^{\text{signed}}$ [50]. This is also demonstrated in Chapter 8.

Simulated distributions of the Optimal Observable are shown in Figure 3.4 for the SM ($\tilde{d} = 0$) and two CP-violating scenarios with $\tilde{d} = 0.1$ and $\tilde{d} = -0.02$. As with other CP-odd observables, the SM distribution is symmetric with $\langle OO \rangle = 0$, while the presence of CP violation shifts the distribution toward negative or positive values, depending on the sign and magnitude of $\tilde{d}$.

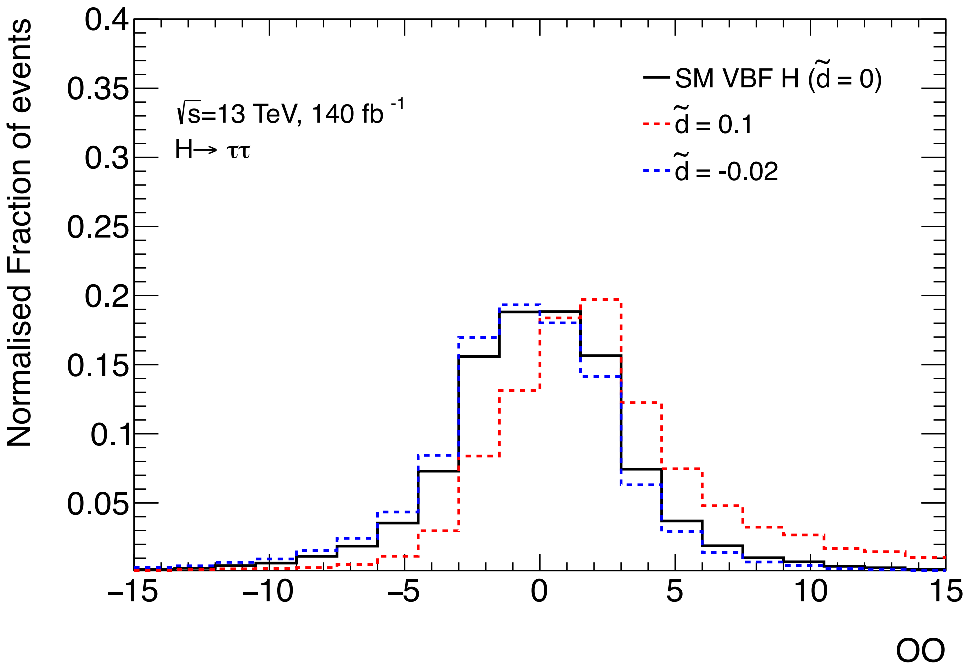

Figure 3.4: Simulated distributions for the Optimal Observable in $VBF \to \tau\tau$ showing the SM case (black) and two CP-violating scenarios with $\tilde{d} = 0.1$ (red) and $\tilde{d} = -0.02$ (blue).

The matrix elements are computed at leading order using HAWK [82–84], requiring the four-momentum of the Higgs boson and the two tagging jets. The momentum fractions of the initial-state partons are determined via energy-momentum conservation:

$$x_{1/2}^{\text{reco}} = \frac{M_{Hjj}}{\sqrt{s}} e^{\pm y_{Hjj}}, \tag{3.26}$$

where x_1 (x_2) is the momentum fraction of the parton travelling in the positive (negative) z-direction. M_{Hjj} and y_{Hjj} denote the mass and rapidity of the final state, obtained from the vectorial sum of the tagging jets and the Higgs boson four-momentum.

Since the four-momentum of the Higgs decay products is needed for the computation of the Optimal Observable, any analysis that can reliably reconstruct the Higgs boson can also apply this method. In this thesis, the analysis is performed in the $H \to \tau\tau$ channel, where the Higgs four-momentum is reconstructed using the Missing Mass Calculator [85].

The matrix element calculation depends on the flavour of the incoming and outgoing partons, which cannot be determined experimentally. Instead, the matrix elements for all possible parton-flavour combinations are computed and summed, weighted by the corresponding CT10 [86] parton distribution function values for the initial-state partons.

The Optimal Observable is an established observable for probing CP violation in gauge boson interactions and has been used across a wide range of analyses [49–53, 87, 88]. More recently, in the context of VBF Higgs production and HVV couplings, ATLAS has performed measurements using the Optimal Observable in three Higgs final states during Run 2. The ΔNLL curve for these measurements can be seen in Figure 3.5.

The partial Run $H \to \tau\tau$ [51] analysis interpreted results only in terms of $\tilde{d}$ in the HISZ basis, while both the $H \to \gamma\gamma$ [53] and $H \to ZZ \to 4\ell$ [52] full Run 2 analyses provided additional interpretations in the Warsaw basis. The analysis described in Chapter 8 is an enhancement of the partial Run 2 study with the full Run 2 dataset, placing constraints on parameters in both the HISZ and Warsaw bases through maximum likelihood fits to the shape of the Optimal Observable. An additional check is also performed to evaluate the sensitivity of the Optimal Observable with respect to the angular observables.

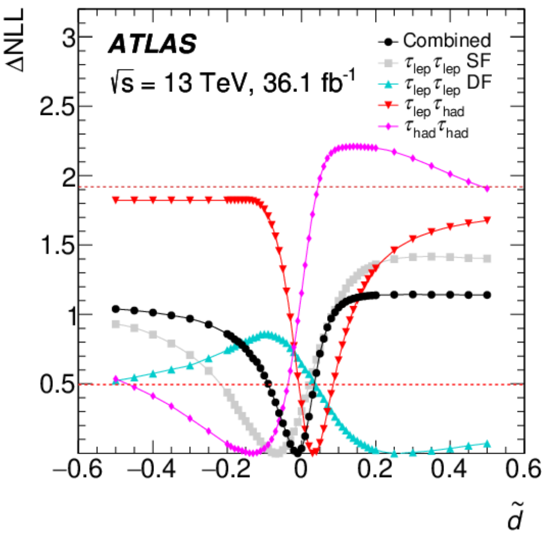

a) $H \to \tau\tau$

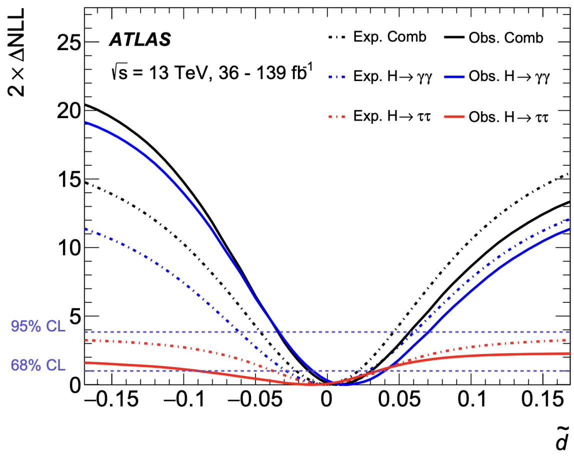

b) $H \to \gamma\gamma$

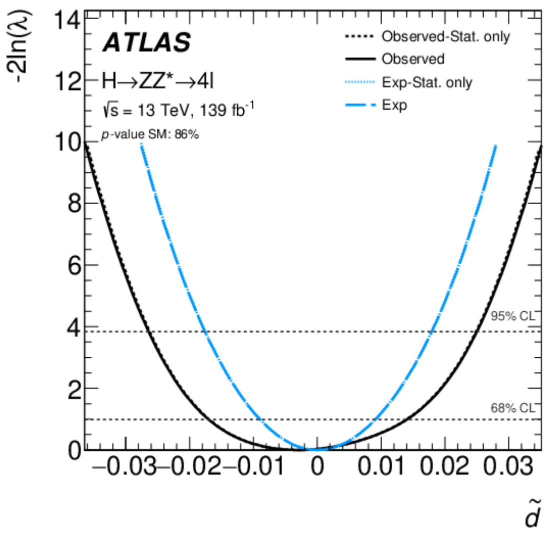

c) $H \to ZZ \to 4\ell$

Figure 3.5: Constraints on $\tilde{d}$ from the partial Run 2 (36.1 fb^{-1}) $H \to \tau\tau$ analysis [51] (top left), the full Run 2 (140.1 fb^{-1}) $H \to \gamma\gamma$ analysis [53] (top right) and $H \to ZZ \to 4\ell$ analysis [52] (bottom). The middle plot also shows a comparison of the partial Run 2 $H \to \tau\tau$ (red) and the $H \to \gamma\gamma$ (blue) analyses. All three results are obtained by maximum likelihood fits to the Optimal Observable.

Chapter 4

Dark matter

Observations of the motions of stars and galaxies in the early twentieth century suggested the presence of gravitational effects that could not be attributed to visible matter alone. These findings led to the formulation of the concept of dark matter (DM): a form of matter that interacts gravitationally, but not electromagnetically, and is therefore invisible to direct observation. The nature of DM is not explained by the SM and remains a mystery. As such, DM candidates are a central focus in many BSM theories. This chapter outlines the most compelling and well-known evidence for DM, followed by a discussion of a particular class of theoretical particle candidates and the detection techniques employed to search for them at the LHC.

4.1 Evidence for dark matter

The first evidence for DM was proposed by Fritz Zwicky in 1933 [89, 90], who observed that the velocities of galaxies within the Coma cluster were significantly higher than what would be expected based on the visible mass alone. This implied the presence of additional source non-visible matter required to gravitationally bind the cluster. Decades later, this conclusion was further supported by the work of Vera Rubin and collaborators in the 1970s [39, 91], through their measurements of galactic rotation curves. Their results demonstrated that the rotational velocities of stars remained constant at large radii from galactic centres, a behaviour that cannot be explained by the distribution of visible matter alone. The stellar rotation curve for the NGC 3198 galaxy [92] is shown in Figure 4.1. In galaxies, most of the visible matter is clustered in the centre. Assuming Newtonian mechanics the velocity of a stellar object at distance r from the centre should have the following velocity profile:

$$v = \sqrt{\frac{G_N M(r)}{r}}, \tag{4.1}$$

where G_N is the gravitational constant, and $M(r) = 4\pi \int \rho(r) r^2 dr$ is the total mass within a sphere of radius r from the galactic centre. The mass density, $\rho(r)$, of visible matter decreases with increasing distance from the centre, and as a result, $M(r)$ tends towards a constant value at large radii. Consequently, the expected rotational velocity is predicted to decrease with distance by $1/\sqrt{r}$, what is referred to as the "disk" in Figure 4.1. It can be seen that this velocity curve does model the data very well at small radius, but deviates largely as one moves further from the galactic centre. This deviation can be explained if there is a halo of DM around the galactic centre.

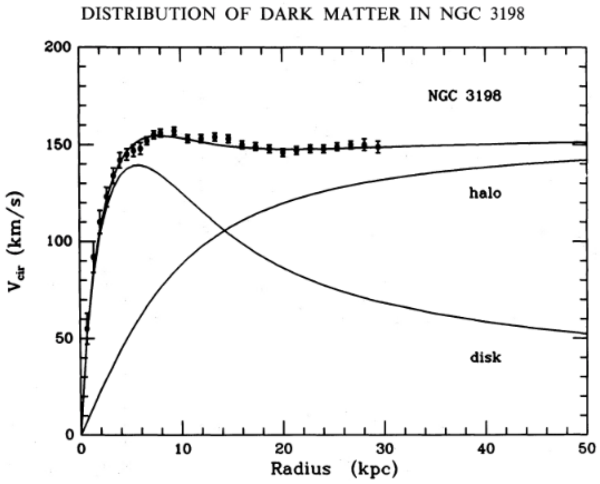

Figure 4.1: Rotation curve of NGC 3198, illustrating the agreement between observational data and the combined model fit, which includes the velocity distribution of visible matter (the "disk") and dark matter (the "halo") [92].

While a model that incorporates a DM halo can explain the stellar velocity distributions of galaxies, it is not the only possible explanation. Alternative models, which do not require the introduction of new forms of matter, include various modified theories of gravity [93]. These models achieve some success when describing stellar rotation curves in galaxies, but fail in explaining other compelling DM evidence coming from galaxy clusters.

Figure 4.2 shows a composite image of the galaxy cluster 1E 0657-556, also known as the Bullet Cluster. This cluster was formed after the collision of two large clusters of galaxies, and the image is constructed by overlaying X-ray observations of hot gas (pink) from the Chandra X-ray Observatory [40] with optical images of galaxies (orange and white) from the Magellan [94] and Hubble [94] telescopes. Gravitational lensing, where the light from distant background galaxies is bent according to the gravitational potential of the cluster, is used to infer the mass distribution (blue). The image shows that during the collision, the gaseous (visible) matter of the two clusters interacts and slows down due to friction. However, the majority of the mass in the clusters passes through without interacting. This behaviour is consistent with the expected properties of DM, which interacts gravitationally but does not significantly interact with itself or with baryonic matter.

Figure 4.2: Observation from the Chandra X-ray Observatory showing the Bullet cluster. The pink region corresponds to hot gas observed with X−rays. The total matter distribution inferred by gravitational lensing is highlighted in blue [40].

The Standard Model of cosmology (ΛCDM) also relies on the existence of DM in order to account for the uniformity of the photons in the CMB [95]. The ΛCDM model can be parametrised in terms of the energy densities of different components of the universe, namely Ω_b, Ω_{DM}, and Ω_Λ, which correspond to baryonic matter, dark matter, and dark energy, respectively. These parameters are constrained by measurements of temperature fluctuations in the CMB. Observations from the WMAP [9] and Planck [10] experiments when fitted to the ΛCDM model, indicate that less than 5% of the total energy content of the universe consists of baryonic matter as described by the SM, with approximately 27% attributed to DM and the remaining 69% to dark energy.

4.2 Weakly Interacting Massive Particles (WIMPs)

As discussed in the previous section, there is strong experimental evidence in favour of the existence of DM through its gravitational influence. However, these observations do not provide any insight into the underlying nature of DM. One hypothetical class of DM candidates are so-called Weakly Interacting Massive Particles (WIMPs) [96], denoted by χ. These are hypothetical BSM particles whose motivation arises from a paradigm known as the WIMP miracle [97]. That is, if the temperature in the early universe was sufficiently high, WIMPs could have been in thermal equilibrium with SM particles through annihilation and pair-production processes of the form $\chi\chi \leftrightarrow \text{SM}$. The corresponding DM annihilation rate can then be given as:

$$\Gamma_{\text{ann}} = n_\chi \langle \sigma(\chi\chi \to \text{SM}) v_\chi \rangle, \tag{4.2}$$

where n_χ is the WIMP number density, σ is the annihilation cross section, v_χ is the relative velocity between WIMPs, and the angle brackets $\langle \cdots \rangle$ denote thermal averaging.

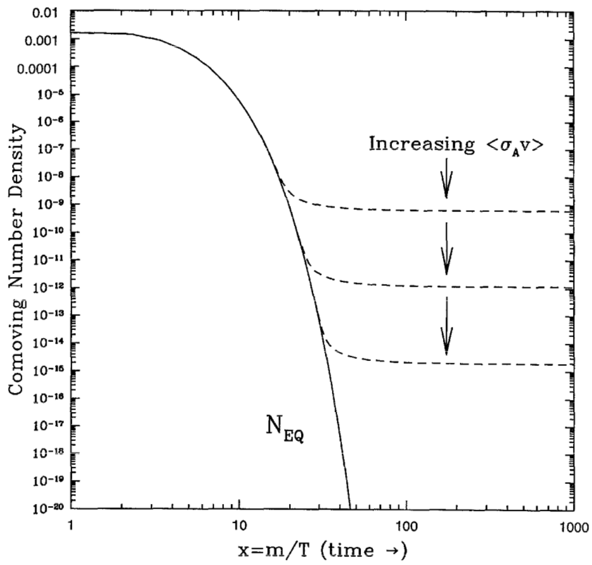

Figure 4.3: DM abundance as a function of the ratio between WIMP mass and temperature, m_χ/T. Decreasing temperature reflects the direction of time. The solid and dashed lines correspond to the WIMP abundance before and after freeze-out, respectively, where the abundance is deceasing with increasing annihilation cross section [98].

As the universe expanded and cooled, the WIMP number density decreased exponentially, making interactions increasingly rare as the average separation between WIMPs grew. Eventually, the annihilation rate Γ_{ann} dropped below the Hubble expansion rate H, and WIMPs fell out of thermal equilibrium. From this point onward, their number density remained essentially constant, fixing the DM abundance as illustrated in Figure 4.3. By applying the freeze-out condition $\Gamma_{\text{ann}} < H$ to Eq. 4.2, one can estimate the present-day DM abundance, known as the relic abundance. Measurements from WMAP [9] yield:

$$\Omega_c h^2 = 0.1131 \pm 0.0034, \tag{4.3}$$

while theoretical predictions from the freeze-out scenario give [99]:

$$\Omega_c h^2 \approx \frac{3 \times 10^{-27}\ \text{cm}^3\text{s}^{-1}}{\langle \sigma_{\text{ann}} v_\chi \rangle}. \tag{4.4}$$

This expression reproduces the observed relic density if the thermally averaged annihilation cross section satisfies $\langle \sigma_{\text{ann}} v \rangle \approx 3 \times 10^{-26}$ cm^{3}s^{-1}, which can be achieved for a DM particle with mass near the electroweak scale that couples to SM particles with a strength of the order of the weak interaction. Consequently, WIMPs could potentially be produced and studied at the LHC experiments.

Its is however important to note that WIMPs represent only one among several theoretically well-motivated DM scenarios [96]. Alternatives include axions [100], sterile neutrinos [101] and feebly interacting massive particles (FIMPs) [102]. In this thesis, however, the DM candidate is assumed to be of WIMP nature, following the thermal freeze-out paradigm.

4.3 DM Detection Techniques

If DM particles interact with SM particles, it might be possible to produce and study them within a laboratory setting. Figure 4.4 presents a schematic diagram illustrating the three principal approaches to DM detection.

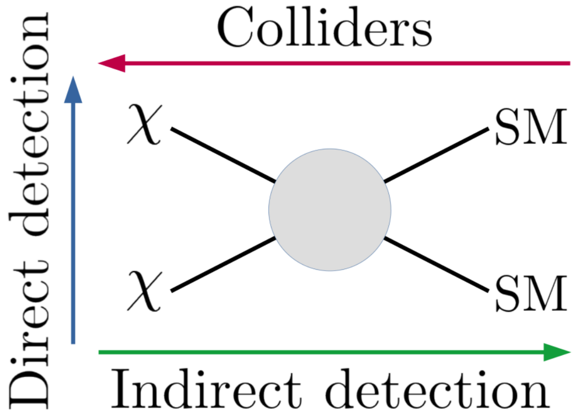

Figure 4.4: Schematic diagram illustrating potential interactions between the dark and SM sector and corresponding detection techniques [103] .

Indirect detection: Interpreting the time axis from left to right corresponds to DM annihilation into SM particles. Such processes are anticipated in regions with high DM density, like the Galactic Centre or dwarf spheroidal galaxies. These scenarios are explored through indirect detection methods, which search for excesses in cosmic rays, gamma rays, or neutrinos resulting from DM annihilation or decay [104].

Direct detection: Viewing the diagram with the time axis oriented vertically represents a scattering process, where DM particles interact with SM particles, similar to neutrino-nucleus scattering. These interactions are the focus of direct detection experiments, which aim to observe the recoil of nuclei resulting from collisions with DM particles. These experiments are conducted in deep underground laboratories to shield against cosmic ray backgrounds [104].

Colliders: Interpreting the time axis from right to left corresponds to the production of DM particles from SM particle collisions, a process investigated through collider searches. High-energy colliders, like the LHC, could produce DM particles if kinematically accessible. This category of DM detection is the focus in this thesis.

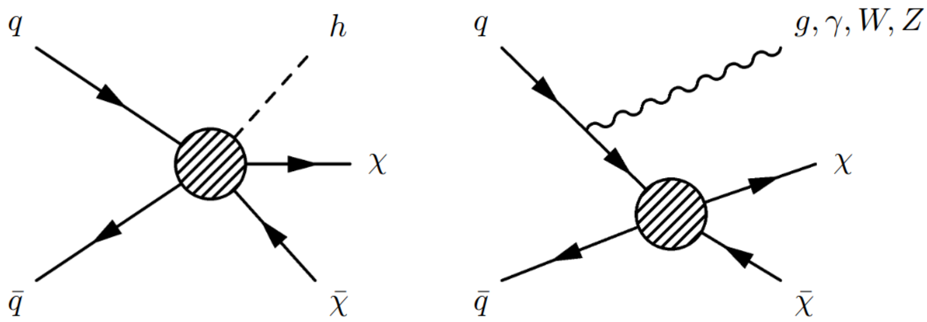

Figure 4.5: Feynman diagrams depicting DM production in association with initial state radiation (ISR) of a gluon, photon, Z, W, or Higgs boson.

Figure 4.4 provides a conceptual overview of DM interactions but does not detail the detection strategies employed in collider experiments. Since particle detectors primarily rely on electromagnetic interactions, DM particles themselves are invisible to the detector. However, if DM production is accompanied by a visible SM particle, such as a jet or photon from initial-state radiation (ISR), the event can be identified through a characteristic imbalance in transverse momentum associated with the visible SM final state. This leads to so-called mono-X signatures, where X denotes the associated SM particle [105]. Representative Feynman diagrams illustrating potential mono-X production mechanisms are shown in Figure 4.5.

Among these, the mono-Higgs signature, where DM is produced in association with a Higgs boson, offers a unique probe. Unlike other mono-X signatures, the Higgs boson is less likely to be emitted as ISR due to its substantial mass and coupling structure. Consequently, mono-Higgs signatures can arise from direct interactions between the Higgs boson and the DM sector, providing insights into the nature of the mediator and the coupling mechanisms [106].

In this thesis, the focus is placed on the mono-Higgs signature. To realise this signature, extensions of the Higgs sector are considered. One such extension is the Two-Higgs-Doublet Model with an additional pseudoscalar mediator (2HDM+a), which is discussed in detail in Section 4.5. This model provides a theoretical framework that enhances the mono-Higgs production rate, thereby making it a promising channel for DM searches at the LHC.

4.4 Effective Field Theories and simplified models

Chapter 3 discussed how EFTs can be used to describe new physics in a model-independent way, without specifying the high-energy degrees of freedom. In principle, the interactions illustrated in Figure 4.5 can be described by contact operators within an EFT framework. However, the validity of this approach in the context of LHC searches for DM has been critically re-evaluated, particularly since the end of Run 1 [107].

EFTs assume that the mediator particles responsible for interactions between the SM and DM sectors are much heavier than the energies probed at the collider, allowing their effects to be encoded in higher-dimensional operators suppressed by the cutoff scale Λ. This approximation is valid when the momentum transfer Q involved in the process satisfies $Q \ll \Lambda$. However, if the mediator mass lies within the kinematic reach of the LHC, it may be produced on-shell, in which case the EFT description becomes invalid. In such scenarios, EFTs fail to reproduce the correct kinematic distributions and can significantly overestimate event rates, leading to overly strong and potentially misleading constraints on the DM parameter space.

This limitation, however, does not apply in the same way to EFTs used for describing anomalous couplings, such as those discussed in Chapter 3 to probe CP violation. In such cases, the EFT framework remains valid because the new physics effects are assumed to arise from integrating out heavy degrees of freedom at scales well above the energies probed at the LHC. The EFT is then used as a controlled expansion in higher-dimensional operators to describe subtle deviations from the SM, rather than a description of new on-shell particle production.

An alternative to EFTs is provided by simplified models. Simplified models are constructed to include the minimal set of particles and couplings necessary to capture the relevant collider phenomenology. Unlike EFTs, which integrate out all heavy states and describe interactions via higher-dimensional operators, simplified models can be interpreted as the low-energy limit of more complete theories, in which only the lightest degrees of freedom in the dark sector are retained. Typically, such models consist of one stable DM candidate and one mediator, often allowing for a full description of the process using tree-level Feynman diagrams.

A detailed overview of simplified models used in LHC Run 2 searches can be found in [108]. In this thesis, the focus is placed on a particular class of simplified models in which the mediator arises from an extended Higgs sector incorporating an additional spin-0 particle. This framework enables resonant production mechanisms and distinctive final-state signatures, such as the mono-Higgs topology discussed previously.

4.5 The Two-Higgs-Doublet-Model and 2HDM+a

A minimal extension of the Higgs sector, as introduced in Section 2.2.4, is the Two-Higgs-Doublet Model (2HDM), in which the SM is extended to include a second scalar doublet. The following provides a brief overview of this framework. For a comprehensive review, see Ref. [109]. The model introduces two complex $SU(2)_L$ doublets, Φ_1 and Φ_2:

$$\Phi_1 = \begin{pmatrix} \phi_1^+, \\ \phi_1^0 \end{pmatrix} \quad \Phi_2 = \begin{pmatrix} \phi_2^+ \\ \phi_2^0 \end{pmatrix}. \tag{4.5}$$

After electroweak symmetry breaking, the neutral components of both doublets acquire vacuum expectation values, denoted v_1 and v_2:

$$\Phi_1 = \begin{pmatrix} \phi_1^+ \\ (h_1 + v_1 + i\eta_1)/\sqrt{2} \end{pmatrix}, \quad \Phi_2 = \begin{pmatrix} \phi_2^+ \\ (h_2 + v_2 + i\eta_2)/\sqrt{2} \end{pmatrix}. \tag{4.6}$$

The two vacuum expectation values are related to the the vev from the SM Higgs sector by the following relation [109]:

$$v = \sqrt{v_1^2 + v_2^2} \approx 246.22 \text{ GeV} \tag{4.7}$$

The scalar content includes eight real fields: two charged scalars $\phi_1^\pm$, $\phi_2^\pm$, two CP-even neutral scalars h_1, h_2, and two CP-odd pseudoscalars η_1, η_2. After symmetry breaking, three degrees of freedom are absorbed by the $W^\pm$ and Z bosons, leaving five physical Higgs bosons[110]:

$$H^\pm = -\sin\beta\, \phi_1^\pm + \cos\beta\, \phi_2^\pm, \qquad A^0 = -\sin\beta\, \eta_1 + \cos\beta\, \eta_2 \tag{4.8}$$

$$h^0 = -\sin\alpha\, h_1 + \cos\alpha\, h_2, \qquad H^0 = \cos\alpha\, h_1 + \sin\alpha\, h_2 \tag{4.9}$$

The fields in Eq. 4.8 correspond to the CP-odd mass eigenstates: $H^\pm$ are charged scalars, and A^0 is a neutral pseudoscalar. The fields in Eq. 4.9 correspond to the CP-even mass eigenstates, with h^0 and H^0 both being electrically neutral scalar fields.

The mixing angle β is defined in terms of the vacuum expectation values of the two Higgs doublets:

$$\tan\beta = \frac{v_2}{v_1}. \tag{4.10}$$

In the so-called alignment limit, where the lighter scalar h^0 is identified with the observed SM Higgs boson, the mixing angles satisfy the relation:

$$\alpha = \beta - \frac{\pi}{2}. \tag{4.11}$$

There are multiple ways to construct the Yukawa sector in the 2HDM Model, depending on how the fermions couple to the two scalar doublets. In this thesis, a Type-II 2HDM [111] is considered, in which the doublet Φ_1 couples to down-type quarks and charged leptons, while Φ_2 couples to up-type quarks. The corresponding Yukawa interaction Lagrangian is given by:

$$\mathcal{L}_Y = -\left(\bar{Q}Y_u\tilde{\Phi}_2 u_R + \bar{Q}Y_d\Phi_1 d_R + \bar{L}Y_\ell\Phi_1\ell_R + \text{h.c.}\right), \tag{4.12}$$

where Y_f are the Yukawa matrices acting on the three fermion generations f. The fields Q and L denote the left-handed quark and lepton doublets, while u_R, d_R, and ℓ_R represent the corresponding right-handed fermion singlets. The field $\tilde{\Phi}_2$ is the charge-conjugate of Φ_2.

To obtain the 2HDM+a model, an additional pseudoscalar singlet field P is introduced. This field mediates interactions between the Higgs sector and a DM candidate χ. Following Ref. [11], the only renormalizable coupling between the pseudoscalar P and the dark Dirac fermion χ is given by:

$$\mathcal{L}_\chi = -iy_\chi P\,\bar{\chi}\gamma_5\chi, \tag{4.13}$$

where y_χ denotes the coupling strength. The scalar potential is extended and can be written as the sum of three components: the potential for the Higgs doublets, the interaction terms between the doublets and the pseudoscalar singlet, and the self-interaction of the pseudoscalar singlet:

$$V = V_\Phi + V_{\Phi P} + V_P. \tag{4.14}$$

These terms are explicitly given as [11]:

$$\begin{aligned} V_\Phi = {}& \mu_1\Phi_1^\dagger\Phi_1 + \mu_2\Phi_2^\dagger\Phi_2 + \left(\mu_3\Phi_1^\dagger\Phi_2 + \text{h.c.}\right) + \lambda_1(\Phi_1^\dagger\Phi_1)^2 + \lambda_2(\Phi_2^\dagger\Phi_2)^2 \\ & + \lambda_3(\Phi_1^\dagger\Phi_1)(\Phi_2^\dagger\Phi_2) + \lambda_4(\Phi_1^\dagger\Phi_2)(\Phi_2^\dagger\Phi_1) + \left[\lambda_5(\Phi_1^\dagger\Phi_2)^2 + \text{h.c.}\right], \end{aligned} \tag{4.15}$$

$$V_{\Phi P} = P\left(ib_P\,\Phi_1^\dagger\Phi_2 + \text{h.c.}\right) + P^2\left(\lambda_{P1}\Phi_1^\dagger\Phi_1 + \lambda_{P2}\Phi_2^\dagger\Phi_2\right), \tag{4.16}$$

$$V_P = \frac{1}{2}M_P^2P^2. \tag{4.17}$$

The parameters b_P and μ_i have dimension mass and mass squared, while the λ_i and λ_{Pi} are dimensionless quartic couplings. The parameter b_P determines the strength of the trilinear portal interaction between the pseudoscalar singlet and the Higgs doublets. After electroweak symmetry breaking, and upon rotation to the physical mass basis, the parameters M_P, μ_1, μ_2, μ_3, b_P, λ_1, λ_2, λ_4, and λ_5 can be re-expressed in terms of the physical masses, mixing angles, vacuum expectation values, and interaction strengths of the physical fields.

In addition to the physical mass eigenstates $H^{\pm}$, h^0, and H^0 from Eq. 4.8 and 4.9, the rotation to the mass basis also yields two pseudoscalar mass eigenstates, denoted a and A. These arise from the mixing of the CP-odd pseudoscalar A^0 from the Higgs sector and a singlet pseudoscalar P, with mixing angle θ:

$$\begin{aligned} A &= \cos\theta\, A^0 + \sin\theta\, P, \\ a &= \cos\theta\, P - \sin\theta\, A^0. \end{aligned} \tag{4.18}$$

These two pseudoscalar fields provide the connection between the dark sector and the extended Higgs sector. The couplings of a and A to SM fermions are obtained analogously to the Yukawa interactions defined in Eq. 4.12.

The physics of the 2HDM+a simplified model is therefore characterised by the mixing angles β, α, and θ, the vacuum expectation value v, the quartic couplings λ_3, λ_{P1}, and λ_{P2}, the DM coupling y_χ, and the masses m_h, m_H, $m_{H^\pm}$, m_A, m_a, and m_χ.

The values of several of these parameters are constrained by electroweak precision measurements, flavour physics, and theoretical considerations such as the requirement of vacuum stability [11, 112]. Additional parameter choices are motivated by the desire to simplify the model phenomenology and reduce the dimensionality of the parameter space to be probed by experimental searches. A summary of the parameter settings used for the benchmark scenarios studied in this thesis is presented below. A more detailed discussion of the 2HDM+a benchmarks recommended by the LHC Dark Matter Working Group can be found in Ref. [112].

The DM coupling is fixed to $g_\chi = 1$, which has negligible impact on the shapes of the kinematic distributions of interest. The alignment and decoupling limits are assumed, corresponding to $m_h = 125$ GeV, $v = 246$ GeV, and $\cos(\beta - \alpha) = 0$. The quartic coupling value $\lambda_3 = 3$ is chosen to ensure the stability of the Higgs potential for the selected values of the heavy Higgs boson masses. These are fixed to a common value, such that $m_A = m_H = m_{H^\pm}$. The relation $m_H = m_{H^\pm}$ is imposed to satisfy electroweak precision measurements [11], while the additional condition $m_A = m_H$ is chosen to reduce the number of free parameters [112]. The other quartic couplings, λ_{P1} and λ_{P2}, are also set to 3 to maximise the trilinear interactions between the CP-even and CP-odd neutral states. After these assumptions, five free parameters remain in the model:

- The common mass of the heavy Higgs bosons: $m_A = m_H = m_{H^\pm}$
- The mass of the pseudoscalar mediator: m_a

- The mass of the DM fermion: m_χ
- The sine of the mixing angle between a and A: $\sin\theta$
- The ratio of the vevs of the two Higgs doublets: $\tan\beta$

Constraints on the model are evaluated in ATLAS using two-dimensional parameter grids [113], where two of the free parameters are varied while the remaining ones are held fixed. The analysis presented in this thesis considers two such grids. One is the $m_A - m_a$ grid and another is the $m_A - \tan\beta$ grid, with all other parameters set according to the benchmark configurations listed in Table 4.1. Notably, setting $m_\chi = 10$ GeV ensures a sizeable branching ratio for the decay $a \to \chi\chi$ for $m_a > 100$ GeV. Studies in Ref. [113] show that, provided $m_\chi < m_a/2$, the choice of m_χ has a negligible impact on the sensitivity of 2HDM+a searches and can reproduce the observed relic density in Eq. 4.3, assuming the WIMP freeze-out paradigm.

Common parameters	
$m_H = m_A = m_{H^\pm}$	Heavy Higgs boson masses
$m_\chi = 10$ GeV	DM mass
$\cos(\beta - \alpha) = 0$	Alignment limit
$y_\chi = 1$	DM coupling strength
$\lambda_1 = \lambda_{P1} = \lambda_{P2} = 3$	Quartic coupling parameters
$v = 246$ GeV	Electroweak vacuum expectation value
$m_A - m_a$ parameter scan	
$\tan\beta = 1.0$	Ratio of the vacuum expectation values of the two Higgs doublets
$\sin\theta = 0.35$	Mixing angle between the pseudoscalar states A and a
$m_A - \tan\beta$ parameter scan	
$m_a = 250$ GeV	Pseudoscalar mediator mass
$\sin\theta = 0.7$	Mixing angle between the pseudoscalar states A and a

Table 4.1: Parameter configurations used in the 2HDM+a benchmark scenarios. The top section lists model parameters common to both scenarios. The lower sections define the settings for the two parameter scans explored in the analysis presented in this thesis.

The 2HDM+a model gives rise to a variety of mono-X signatures. One such signature occurs when the pseudoscalar mediator a is resonantly produced in association with a SM particle X, followed by the decay $a \to \chi\chi$, resulting in $E_{\mathrm{T}}^{\mathrm{miss}}$.

Several processes can lead to this to topology, including $h + E_{\mathrm{T}}^{\mathrm{miss}}$, $Z + E_{\mathrm{T}}^{\mathrm{miss}}$, and $tW + E_{\mathrm{T}}^{\mathrm{miss}}$ final states. Representative Feynman diagrams for these channels are shown in Figure 4.6. In the mono-Higgs topology, shown in the top-left diagram, the heavy pseudoscalar A can be produced on-shell if the mass condition $M_A > m_a + m_h$ is satisfied. This enables resonant mono-Higgs production, which typically dominates over non-resonant contributions such as the box diagram on the top right. Similar resonant behaviour can occur in the $Z + E_{\mathrm{T}}^{\mathrm{miss}}$

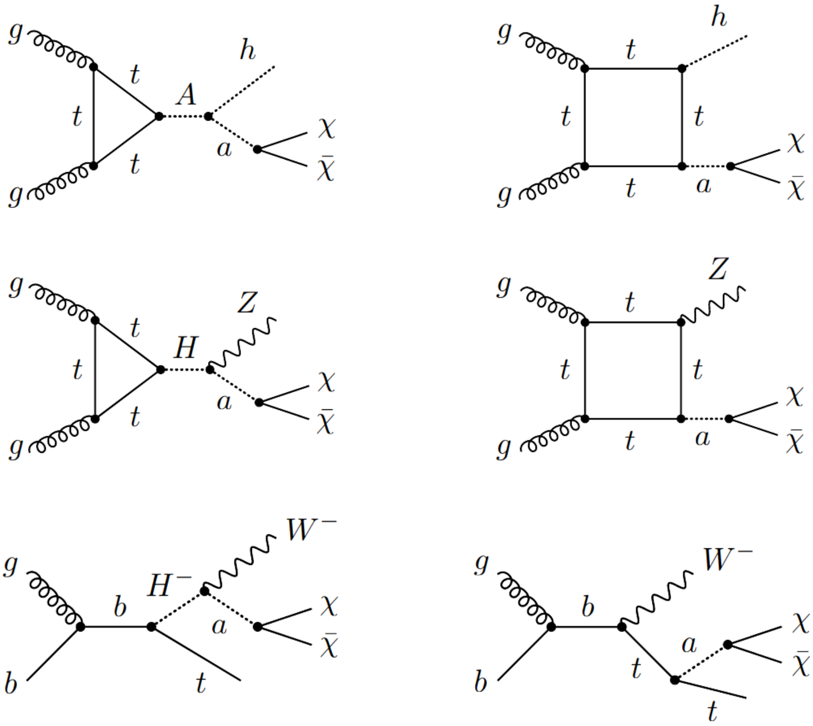

Figure 4.6: Feynman diagrams giving rise to $h+E_{\mathrm{T}}^{\mathrm{miss}}$ (top row), $Z+E_{\mathrm{T}}^{\mathrm{miss}}$ (second row), and $tW+E_{\mathrm{T}}^{\mathrm{miss}}$ (bottom row) signals via ggF production in the 2HDM+a model.

and $tW+E_{\mathrm{T}}^{\mathrm{miss}}$ channels when the mass of the corresponding heavy Higgs boson (H or $H^{\pm}$) exceeds the sum of m_a and the mass of the associated gauge boson.

For the mono-Higgs process, the resonant peak in the $E_{\mathrm{T}}^{\mathrm{miss}}$ distribution can be approximated by [112]:

$$E_{\mathrm{T,max}}^{\mathrm{miss}} = \frac{1}{2m_A}\sqrt{(m_A^2 - m_h^2 - m_a^2)^2 - 4m_h^2 m_a^2}. \tag{4.19}$$

Using the benchmark parameters defined in Table 4.1, Figure 4.7 shows the expected $E_{\mathrm{T}}^{\mathrm{miss}}$ distributions for different values of m_A and m_a for $\tan\beta = 1$ and $\sin\theta = 0.35$. Following from Eq. 4.19, increasing m_A shifts the peak of the distribution to higher $E_{\mathrm{T}}^{\mathrm{miss}}$ values, while increasing m_a shifts the peak to lower values. For large mass splitting, an additional tail at low $E_{\mathrm{T}}^{\mathrm{miss}}$ can be observed. This feature arises from interference between the two mono-Higgs diagrams shown in Figure 4.6, where the box diagram contributes predominantly in low-$E_{\mathrm{T}}^{\mathrm{miss}}$ region.

Scans of the 2HDM+a parameter space have been performed by both ATLAS [113] and CMS [114, 115] in multiple final states. In ATLAS the sensitivity to the model is mainly driven by the $E_{\mathrm{T}}^{\mathrm{miss}}+h(b\bar{b})$ mono-Higgs search [116] and the $E_{\mathrm{T}}^{\mathrm{miss}}+Z(\ell\ell)$ mono-Z search [117]. The exclusion contours in the $m_A - m_a$ parameter space from both analyses is shown in Figure 4.8. The model parameters are set according to corresponding the benchmark scenario in Table 4.1. Additionally, the exclusion contour from the $E_{\mathrm{T}}^{\mathrm{miss}}+Z(\ell\ell)$ analysis in the

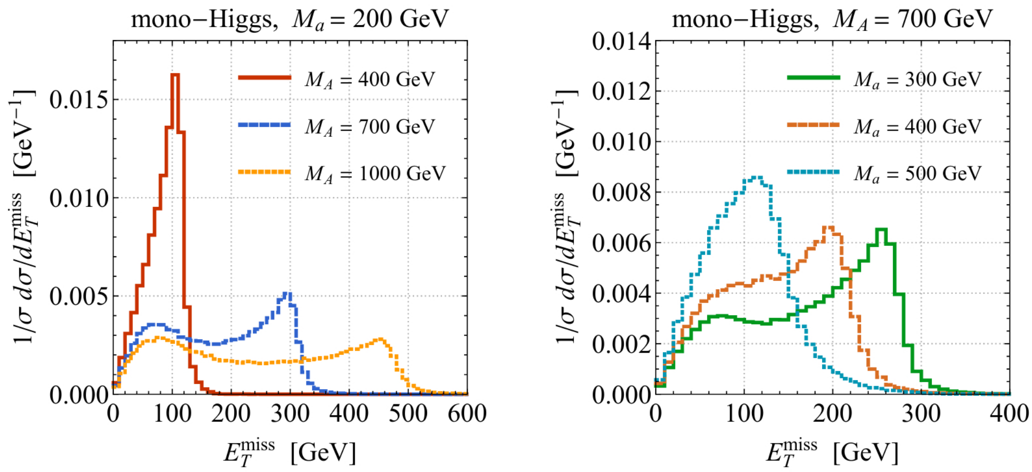

Figure 4.7: Normalised distributions for the mono-Higgs signal in the 2HDM+a model. The left panel shows the effect of varying m_A with fixed $m_a = 200$ GeV, while the right panel shows the effect of varying m_a with fixed $m_A = 700$ GeV. The distributions correspond to the benchmark parameters for the $m_A - m_a$ scan defined in Table 4.1 [112].

$m_A - \tan\beta$ parameter space is shown in Figure 4.9. This search was not included in the $E_{\mathrm{T}}^{\mathrm{miss}} + h(b\bar{b})$ publication, but results from this channel was provided later for the ATLAS statistical combination and summary paper and will be discussed when comparing the results to the analysis considered in this thesis.

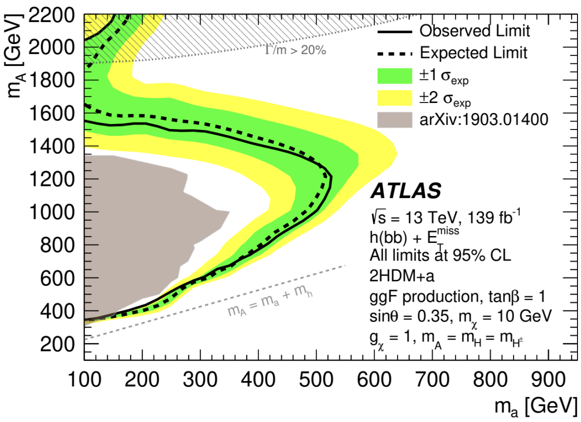

a) $E_{\mathrm{T}}^{\mathrm{miss}} + h(b\bar{b})$

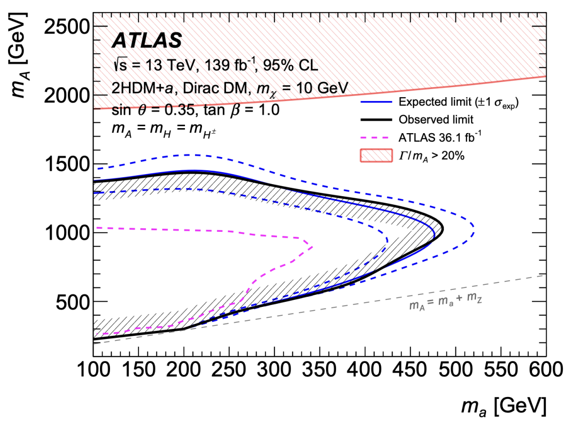

b) $E_{\mathrm{T}}^{\mathrm{miss}} + Z(\ell\ell)$

Figure 4.8: Observed (solid line) and expected (dashed lines) exclusion limits for the 2HDM+a model at 95% CL in the $m_A - m_a$ plane from the $E_{\mathrm{T}}^{\mathrm{miss}} + h(b\bar{b})$ [116] (left) and $E_{\mathrm{T}}^{\mathrm{miss}} + Z(\ell\ell)$ [117] (right) ATLAS searches. All points within the observed region are excluded at 95% confidence level. The dashed grey regions indicate the region where the width any Higgs bosons exceed 20% of its mass.

Both these analyses exclude large regions of the $m_A - m_a$ parameter space, with some overlap. The $E_{\mathrm{T}}^{\mathrm{miss}} + h(b\bar{b})$ exclude masses between $m_A = 400$ GeV and $m_A = 1500$ GeV with m_a excluded for masses up to 500 GeV depending on the region. At high values of m_A, the widths of the additional Higgs bosons increase substantially,

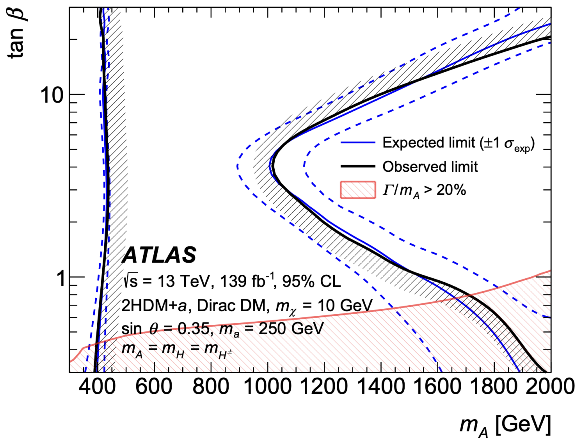

a) $E_{\mathrm{T}}^{\mathrm{miss}} + Z(\ell\ell)$

Figure 4.9: Observed (solid line) and expected (dashed lines) exclusion limits for the 2HDM+a model at 95% CL in the $m_A - \tan\beta$ plane from the $E_{\mathrm{T}}^{\mathrm{miss}} + Z(\ell\ell)$ [117] ATLAS search. All points within the observed region are excluded at 95% confidence level. The dashed grey regions indicate the region where the width any Higgs bosons exceed 20% of its mass.

and the theoretical predictions become subject to additional uncertainties associated with the treatment of the particle widths. As a result, exclusion limits are not shown in the region of large widths ($m_A > 2200$ GeV). The $E_{\mathrm{T}}^{\mathrm{miss}} + Z(\ell\ell)$ provide similar sensitivity in the $m_A - m_a$ parameter space, and exclude scenarios with $m_A \in [400, 1800]$ GeV at high and low $\tan\beta$ in the $m_A - \tan\beta$ parameter space. At large values of $\tan\beta$ ($\tan\beta \geq 10$) ggF production is heavily suppressed, with the main contribution coming from $b\bar{b}$ production. For small values ($\tan\beta \leq 1$) on the other hand , $b\bar{b}$ production is heavily suppressed, with ggF becoming the dominant production mode. In the intermediate region ($\tan\beta \in [1, 10]$), both production modes contribute with smaller cross sections, leading to the sensitivity drop in this part of the parameter space.

The analysis considered in this thesis is the same search in the $E_{\mathrm{T}}^{\mathrm{miss}} + h(\tau\tau)$ final state. This analysis also targets the mono-Higgs signature, although the branching ratio for $h \to \tau\tau$ is significantly smaller than for $h \to b\bar{b}$, making it challenging to achieve competitive sensitivity. This constitutes the first ATLAS search in the $E_{\mathrm{T}}^{\mathrm{miss}} + h(\tau\tau)$ topology. The analysis strategy, as well as measurements and limits on the 2HDM+a model will be covered in Chapter 9.

Part II

Experiment

Chapter **5**

LHC and ATLAS

This chapter provides an overview of the experimental setup used to collect the data analysed in this thesis. At the heart of this setup is the Large Hadron Collider (LHC), the world's most powerful high-energy particle accelerator, located at CERN near Geneva. Proton–proton collisions produced by the LHC are studied using general-purpose detectors designed to reconstruct the final-state particles emerging from these interactions. The analyses presented in this thesis are based on data recorded by the ATLAS detector. The design and function of both the LHC and the ATLAS detector will be described in the following. In addition, the simulation chain used to generate theoretical predictions at the LHC will be discussed.

5.1 The Large Hadron Collider

In the early 2000s, high-energy physics underwent a major shift. CERN's primary facility at the time, the Large Electron–Positron (LEP) Collider [118], was decommissioned in November 2000 after eleven years of operation. Designed to probe the electroweak scale, LEP operated at centre-of-mass energies ranging from 91 GeV (at the Z-pole) up to 209 GeV. It remains the most powerful electron–positron collider ever constructed. LEP enabled precision studies of the electroweak interaction, including strong experimental confirmation of the existence of exactly three light neutrino generations, based on measurements of the invisible decay width of the Z boson.

Towards the end of its operation, LEP also began to search for the Higgs boson. The dominant production mechanism at LEP was Higgsstrahlung ($e^+e^- \to HZ$), which becomes kinematically accessible only when the centre-of-mass energy exceeds the sum of the Higgs and Z boson masses. With a kinematic threshold of approximately 215 GeV, LEP fell just short of being able to fully explore this process. Nevertheless, results from the ALEPH experiment [119] indicated a modest excess compatible with a Higgs boson mass near 114 GeV. However, a conclusive discovery required access to significantly higher energies.

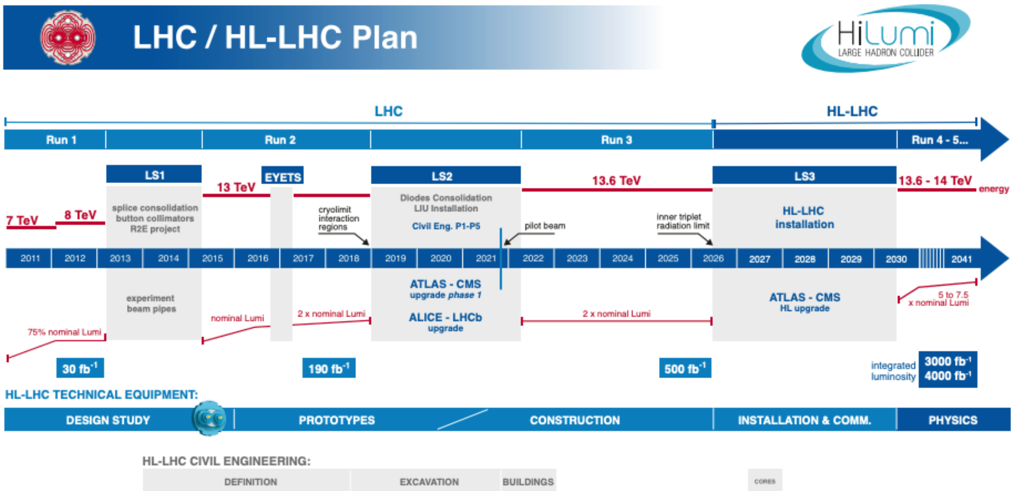

Figure 5.1: Overview of LHC operation periods and the planned schedule for the High-Luminosity LHC (HL-LHC) upgrade. Run 1 spanned 2010–2013, followed by Run 2 from 2015–2018. The ongoing Run 3 is expected to continue until 2026. A major upgrade is planned during Long Shutdown 3, after which the HL-LHC is scheduled to begin operation in 2030, with data-taking projected into the 2040s [123].

The machine that followed was the LHC [120, 121], approved by the CERN Council in December 1994. It was designed to reuse the existing LEP tunnel and infrastructure. Following LEP's decommissioning in 2000, installation of the LHC components began, leading to first beam injection in September 2008. After an initial technical incident delayed operations, the LHC achieved its first proton–proton collisions at a centre-of-mass energy of 7 TeV in March 2010. This marked the start of Run 1, which continued until early 2013 and culminated in the announcement of the Higgs boson discovery by the ATLAS and CMS experiments in July 2012 [1, 2].

Since then, the LHC has produced more than 8 million Higgs bosons [122] and continues to be a major discovery machine in particle physics. Its second operational period, Run 2, took place between 2015 and 2018 at a centre-of-mass energy of 13 TeV. This dataset forms the basis of the analysis presented in this thesis. After a long shutdown for significant upgrades to the accelerator and experiments, Run 3 began in July 2022, with proton–proton collisions still ongoing and expected to continue until the end of 2026.

Looking ahead, the next phase of the LHC's programme will focus not on increasing energy but on significantly increasing luminosity. The High-Luminosity LHC (HL-LHC) project aims to deliver an order of magnitude more collisions by enhancing the performance of both the accelerator and the detectors. Installation of the HL-LHC components is scheduled to begin during the Long Shutdown 3 (LS3), starting in 2026. The upgraded machine is expected to begin operations in 2030, with data-taking projected to continue into the 2040s. The proposed plan for HL-LHC schedule at the LHC (updated in January 2025) can be seen in Figure 5.1.

5.1.1 CERN accelerator chain and experiments

A schematic of the LHC accelerator chain can been seen in Figure 5.2. The LHC injection chain [124] begins with a standard cylinder of hydrogen gas, which is ionised to extract protons. These protons are initially accelerated by a linear accelerator (LINAC). From 2008 to 2020, LINAC 2 provided acceleration up to 50 MeV, after which it was replaced by LINAC 4 as part of the HL-LHC upgrade, increasing the output energy to 160 MeV. The protons are then further accelerated in the Proton Synchrotron Booster (PSB) to 1.4 GeV before entering the Proton Synchrotron (PS), where they reach 26 GeV. From the PS, the protons are transferred to the Super Proton Synchrotron (SPS), CERN's second-largest accelerator, which boosts their energy to 450 GeV. The SPS supplies protons to several experiments as well as to the LHC, where they are accelerated to their final energy of 6.8 TeV (6.5 TeV during Run 2), achieving a centre-of-mass energy of 13.6 TeV (13 TeV during Run 2). Superconducting dipole, quadrupole, and higher-order magnets guide and focus the beams, ensuring beam stability and precise collisions. Sixteen radio frequency (RF) cavities, operating at 400 MHz, provide the final acceleration while maintaining the proton bunch structure.

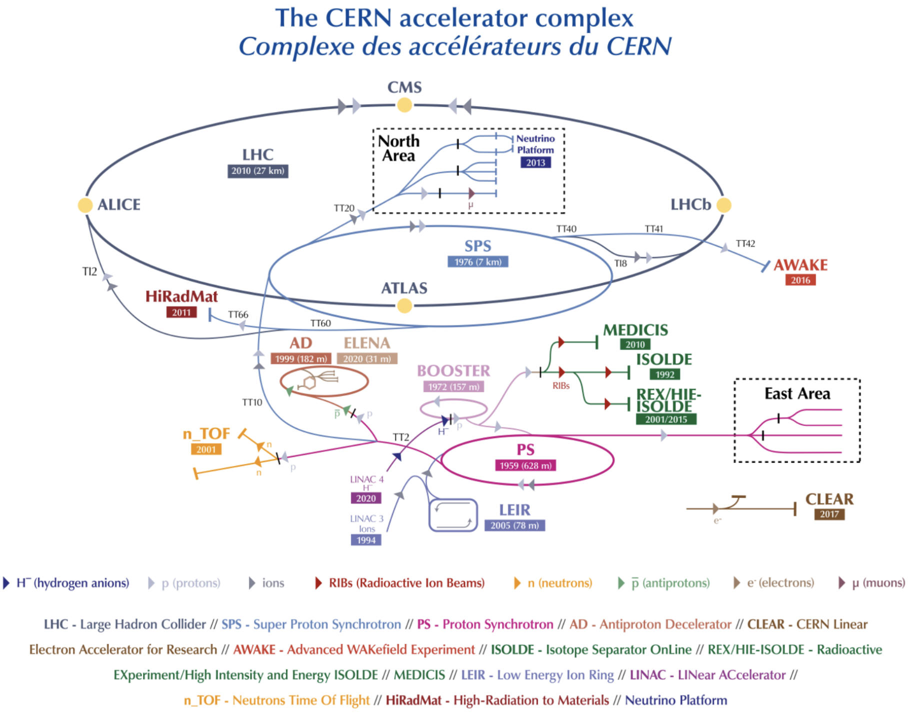

Figure 5.2: The CERN accelerator complex consists of a series of pre-accelerators culminating in the main LHC ring. The process begins in the Linac4 facility, where H^- ions are produced. These ions are stripped of their electrons, yielding bare protons, which are then sequentially accelerated through the pre-accelerator chain. Upon entering the LHC ring at an energy of 450 GeV, the protons are further accelerated to their final energy of 6.8 TeV (6.8 TeV during Run 2) over a period of approximately 20 minutes [125].

There are four primary interaction points along the LHC ring where the four main experiments are located: A Toroidal LHC Apparatus (ATLAS) [126], Compact Muon Solenoid (CMS) [127], A Large Ion Collider Experiment (ALICE) [128], and the Large Hadron Collider beauty experiment (LHCb) [129]. Among these, ATLAS and CMS are the largest experiments and serve as general-purpose detectors designed to explore a broad range of physics phenomena, including the search for new particles and interactions. The independent design and operation of these two detectors provide cross-confirmation of any potential discoveries.

The LHCb experiment is optimised for the study of heavy-flavour physics, particularly the decays of particles containing b quarks, to investigate the parameters of the CKM matrix and CP violation [129]. The ALICE experiment is dedicated to the study of heavy-ion collisions and the properties of strongly interacting matter at high energy densities. It aims to characterize the formation and behaviour of the quark–gluon plasma, a state of matter believed to have existed shortly after the Big Bang [128].

In addition to these main experiments, several smaller experiments are located at or near the interaction points and serve more specialized purposes. These include TOTEM (TOTal Elastic and diffractive cross-section Measurement) [130], LHCf (Large Hadron Collider forward) [131], FASER (Forward Search Experiment) [132], and MoEDAL (Monopole and Exotics Detector At the LHC) [133]. TOTEM is dedicated to the study of proton structure and measurements of total and inelastic cross-sections. LHCf measures particles produced at very small angles to the beamline to improve understanding of ultra-high-energy cosmic rays. FASER is designed to search for light, weakly interacting particles and study neutrinos produced in LHC collisions. MoEDAL focuses on the search for magnetic monopoles and other highly ionizing, stable, massive particles.

5.1.2 Luminosity

A large number of events is essential for all physics analyses, as it reduces statistical uncertainties and enables more precise measurements. The rate of expected events ($\Delta N/\Delta t$) for a specific process is determined by the product of its cross-section, σ, and the instantaneous luminosity $\mathcal{L}$:

$$\frac{\Delta N}{\Delta t} = \sigma \mathcal{L}. \tag{5.1}$$

The cross-section is determined by the nature of a specific process and can be predicted theoretically within a given model. In contrast, the luminosity is a quantity related to the performance of the collider and beam configuration. For proton–proton collisions at the LHC, under the assumption of head-on collisions between Gaussian-distributed bunches, the instantaneous luminosity can be approximated by:

$$\mathcal{L} = \frac{n^2 n_{\mathrm{b}} f_{\mathrm{rev}}}{2\pi \sigma_x \sigma_y}, \tag{5.2}$$

where n is the number of protons per bunch, n_{b} is the number of bunches per beam, and f_{rev} is the revolution frequency. The quantities σ_x and σ_y denote the horizontal and vertical transverse beam widths, respectively.

The target luminosity during the construction of the LHC was $\mathcal{L} = 10^{34}\,\mathrm{cm}^{-2}\mathrm{s}^{-1}$ [120]. This was achieved in 2016 and subsequently doubled in 2017. The size of a dataset is typically expressed using the integrated luminosity which represents the total number of proton-proton interactions over a given period of time. It is given in units of fb^{-1}, where $1\,\mathrm{b} = 10^{-28}\,\mathrm{m}^2$. The full Run 2 dataset available for physics analyses amounts to a integrated luminosity of 140 fb^{-1}. Operation at this level of luminosity can result in multiple protons colliding within the same bunch crossing. The average number of proton-proton interactions per bunch crossing is referred to as pile-up, μ, and scales with luminosity. The evolution of the integrated luminosity throughout Run 2, along with the corresponding pile-up profile, is shown in Figure 5.3.

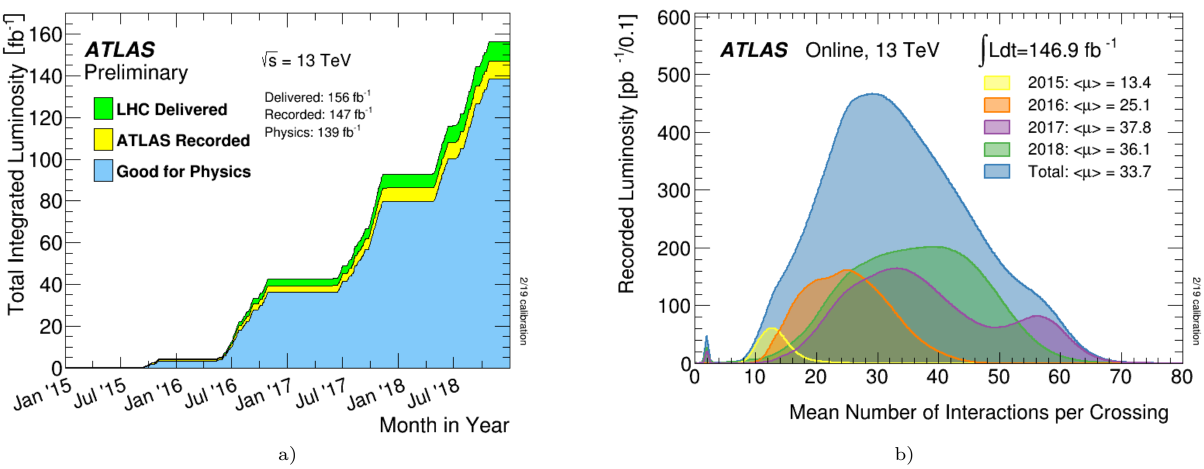

Figure 5.3: Delivered luminosity from the LHC and recorded luminosity by ATLAS during Run 2 (left), and the corresponding pile-up profile each year of data taking (right) [134].

5.2 The ATLAS detector

The ATLAS detector [126] is, together with CMS, one of two general-purpose particle detectors located along the LHC accelerator ring. It was designed to capture data from a broad range of physics processes, with a physics programme ranging from precision measurements of the SM to searches for more exotic, theorised BSM processes. The basic design has for the most part stayed the same since its construction. Protons collide in the beam pipe at the centre of the ATLAS geometry, which provides an almost 4π coverage around the Interaction Point (IP). Extending outwards from the IP are layers of sub-detector systems, each with a specific purpose and functionality. The Inner Detector is the innermost sub-system, responsible for tracking the trajectories of charged particles and measuring their momenta and decay vertices. A superconducting central solenoid magnet, located around the ID, generates a 2 T magnetic field, enabling momentum reconstruction from the curvature of charged particles. The calorimeter system is placed outside the ID and is composed by the electromagnetic calorimeter, dedicated to the identification and measurements of electromagnetic showers, and the hadronic calorimeter, designed to identify and measure the energy of hadronic showers. The Muon Spectrometer is the outermost sub-system, designed for the detection and momentum measurement of muons. It employs a system of superconducting toroidal magnets, which generate a field between 0.1 and 3.5 T, enabling measurements of muons and their momenta.

A schematic of the full layout of the ATLAS detector is shown in Figure 5.4. The main performance goals of each sub-system are listed in Table 5.1.

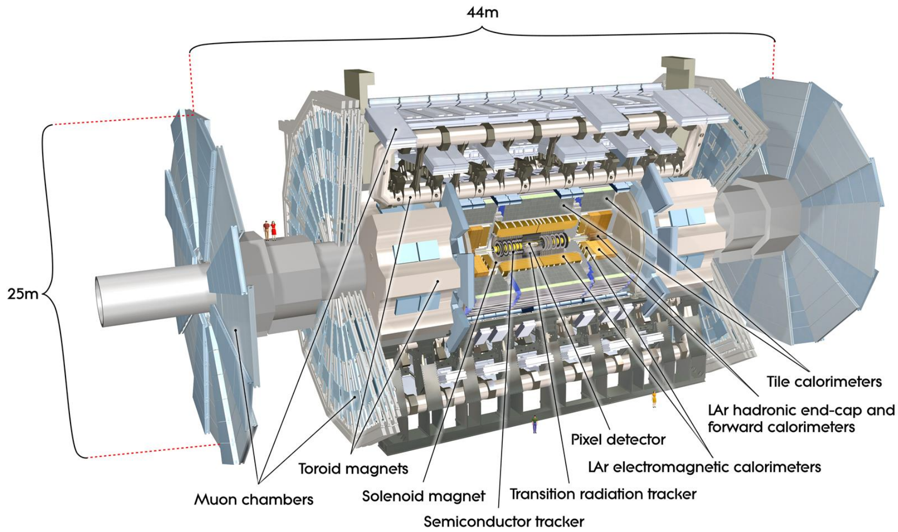

Figure 5.4: A schematic of the ATLAS detector highlighting the labelled sub-systems designed for various physics applications, including tracking, energy measurement, and muon detection. The detector operates within magnetic fields generated by both solenoid and toroidal magnets [135].

Detector component	**Required resolution**	**η coverage**	
		Measurement	**Trigger**
Tracking	$\sigma_{p_T}/p_T = 0.05\%\, p_T \oplus 1\%$	± 2.5	± 2.5
EM calorimetry	$\sigma_E/E = 10\%/\sqrt{E} \oplus 0.7\%$	± 3.2	± 2.5
Hadronic calorimetry (jets)			
Barrel and end-cap	$\sigma_E/E = 50\%/\sqrt{E} \oplus 3\%$	± 3.2	± 3.2
Forward	$\sigma_E/E = 100\%/\sqrt{E} \oplus 10\%$	$3.1 < \lvert\eta\rvert < 4.9$	$3.1 < \lvert\eta\rvert < 4.9$
Muon spectrometer	$\sigma_{p_T}/p_T = 10\%$ at $p_T = 1\,\mathrm{TeV}$	± 2.7	± 2.4

Table 5.1: General performance goals of the ATLAS detector showing the resolution and η coverage for different detector components [126].

5.2.1 Coordinate system

The geometry of the ATLAS detector is defined in terms of both a right-handed Cartesian and a cylindrical coordinate system, centred at the IP. In the Cartesian system, the z-axis is defined by the anticlockwise beam direction, the x-axis points from the IP towards the centre of the LHC ring, and the y-axis points vertically upward [126]. In cylindrical coordinates, the polar angle θ is measured from the beam axis, while the azimuthal angle ϕ is measured from the y-axis around the beam axis.

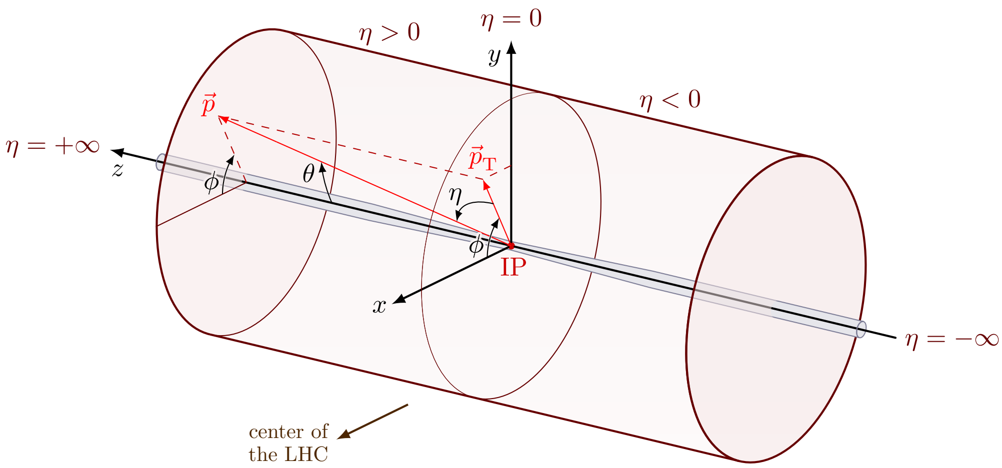

Figure 5.5: ATLAS coordinate system showing both the right-handed Cartesian and cylindrical coordinate systems. Figure generated with tikz based on Ref. [136].

The $x - y$ plane, transverse to the beam direction, is used to define quantities like the transverse momentum and energy of physics objects:

$$p_{\mathrm{T}} = \sqrt{p_x^2 + p_y^2} = |\boldsymbol{p}| \sin\theta, \quad E_{\mathrm{T}} = E \sin\theta. \tag{5.3}$$

The rapidity of a particle is defined as:

$$y = \frac{1}{2} \ln \left(\frac{E + p_z}{E - p_z} \right), \tag{5.4}$$

where E is the particle's energy and p_z is its momentum along the z-axis. For particles with small p_z with respect to E, the logarithmic term approaches one, and the rapidity approaches zero. This corresponds to particles moving predominantly in the transverse plane. In the opposite scenario, where the particle is directed close to the beamline, the rapidity approaches infinity. A related quantity, which is more convenient to measure for highly energetic particles, is the pseudorapidity, denoted as η. It is defined as:

$$\eta = -\ln \tan \left(\frac{\theta}{2} \right). \tag{5.5}$$

For massless particles, η is equivalent to y. Differences between two rapidities, or pseudorapidities, remain invariant under Lorentz boosts along the z-axis. Using this property, a distance parameter can be defined:

$$\Delta R = \sqrt{(\Delta\eta)^2 + (\Delta\phi)^2}, \tag{5.6}$$

which can be used to describe the relative positions of physics objects.

5.2.2 Inner Detector

The ATLAS Inner Detector (ID) [137, 138] refers to the collection of sub-detectors located closest to the beam pipe, designed to track charged particles by measuring their charge and momentum. Figure 5.6 presents a labelled schematic of the ID and its components. A central solenoid surrounding the ID generates a 2 T magnetic field, immersing the entire ID. When a charged particle enters this magnetic field, its trajectory is deflected, resulting in an arced path. The direction of curvature indicates the particle's charge, while the radius of curvature determines its momentum.

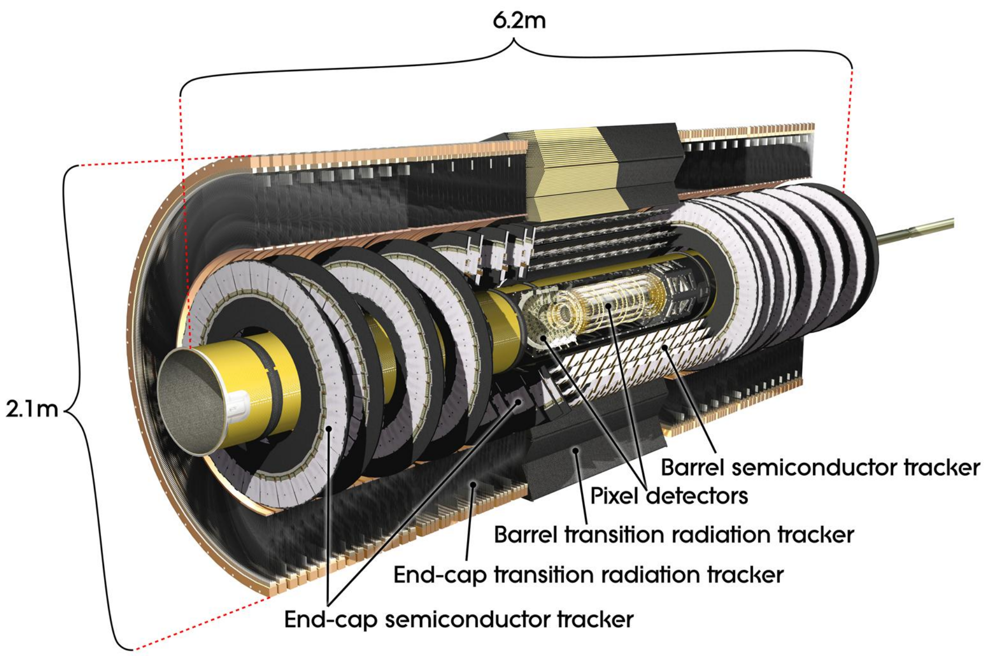

Figure 5.6: Schematic of the ATLAS ID with the different sub-systems highlighted [139].

The ID's proximity to the IP imposes several stringent requirements. Proton bunches collide every 25 ns within the ATLAS detector. This requires that the ID electronics have sufficiently fast readout speeds to handle the collision frequency. Furthermore, the electronics must be radiation-hard to endure the continuous particle flux generated by interactions.

To achieve the precise momentum reconstruction needed for physics analyses, the ID is segmented into three main subcomponents: the pixel detector, the Semi-Conductor Tracker (SCT), and the Transition Radiation Tracker (TRT). These sub-detectors work together to provide full coverage of the central detector region ($|\eta| < 2.5$) with complete azimuthal coverage ($0 < \phi < 2\pi$). The design resolution for transverse momentum in the ID is $\sigma_{p_{\mathrm{T}}}/p_{\mathrm{T}} = 0.05\% \oplus 1\%$ [126], where $\oplus$ denotes sum in quadrature.

Pixel detector

The innermost sub-detectors of the ATLAS ID are the pixel detector systems, which cover a radial distance from 45.5 mm to 242 mm, and provide high-granularity tracking [140]. Initially, the pixel detector consisted of three barrel layers and two end-cap layers. Before Run 2, an additional fourth barrel layer, known as the insertable b-layer (IBL) [141], was installed to improve track resolution very close to the IP, enhancing the identification of secondary vertices and the detection of jets from b-quark hadronization.

The pixel detector is composed of modules made from silicon pixels. Each pixel in the IBL measures $50\times250\ \mu\mathrm{m}^2$, while in the other layers, it measures $50 \times 400\ \mu\mathrm{m}^2$. A single module contains 46 080 individual pixel readout channels, resulting in a total of 80×10^6 readout channels across the entire pixel detector.

The silicon sensors operate by applying a reverse-biased voltage to a PN junction, creating a depletion region. When charged particles pass through this the depletion region, they generate electron-hole pairs in the material. These pairs drift to opposite sides of the sensor under the influence of the electric field, thereby generating a current. The amount of charge collected and the pixel's position correspond to the amount of energy lost by the particle and the particle's position, respectively. The spatial resolution of the pixel detector is therefore largely determined by the dimensions of the individual pixels.

Semi-Conductor Tracker

The Semi-Conductor Tracker (SCT) is the second layer of the ATLAS ID, positioned just beyond the pixel detector, covering a radial range from 255 mm to 549 mm [142]. Like the pixel detector, the SCT utilizes silicon as the active detector material but in the form of silicon-strip sensors instead of rectangular pixels. The SCT is composed of 4088 silicon-strip detectors arranged into four concentric layers in the barrel and two end-cap layers, providing tracking coverage up to $|\eta| < 2.5$.

Each silicon-strip module consists of two planes of silicon sensors glued to a baseboard, which serves as the structural backbone, providing mechanical stability and thermal management. The strip modules are further organized into pairs, offset by an angle to enable measurements along the strip length. This arrangement allows for precise tracking while being simpler and more cost-effective to manufacture compared to pixel sensors, although with reduced granularity.

The SCT contains a total of 6.3×10^6 readout channels, with an overall spatial resolution of 17 μm in the r-ϕ direction and 580 μm in the z direction. This configuration provides effective coverage for charged particle tracking, complementing the pixel detector and offering an intermediate layer of precision tracking in the ID.

Transition Radiation Tracker

The Transition Radiation Tracker (TRT) [143, 144] is the final and largest component of the ATLAS ID, covering a radial distance from 554 mm to 1082 mm. It consists of approximately 370 000 straw tubes, each with a diameter of 4 mm, aligned parallel to the beamline in the barrel and arranged perpendicularly in two disks in the end-caps. The straws, also known as polyimide drift tubes, are filled with a gas mixture, and each contains a 31 μm tungsten anode wire running through its center. During Run 1, the gas mixture consisted of Xe (70%), CO_2 (27%), and O_2 (3%). However, due to significant leaks and the high cost of xenon, some unrepaired regions were switched to a primarily argon-based mixture.

The TRT operates as a cylindrical drift chamber. Charged particles passing through the straws ionize the gas, releasing electrons that drift towards the positively charged central wire, resulting in a measurable electronic current from both ends of the straw. The accelerating electrons produce secondary ionizations within the gas, which further contributes to the overall signal.

A special feature of the TRT is its ability to identify electrons via the detection of transition radiation. This radiation is produced when charged particles pass between materials with different dielectric constants. Polypropylene fibres in the barrel and foils in the end-cap are placed between the straws to increase the amount of transition radiation. These photons interact with the gas, releasing additional electrons and produce a signal in the straws. Since this effect is largest for electrons due to their low mass compared to heavier particles like pions, the TRT effectively differentiates electrons from other charged particles.

5.2.3 Calorimeter system

Calorimeters are detectors designed to measure the energy of passing particles by collecting and quantifying the energy deposited by secondary particle showers initiated during the interaction of the incident particle with the calorimeter material. The ATLAS calorimeter systems are primarily designed to measure the energy of particles, but also provide additional aid in the determination of their position in conjunction with the ID.

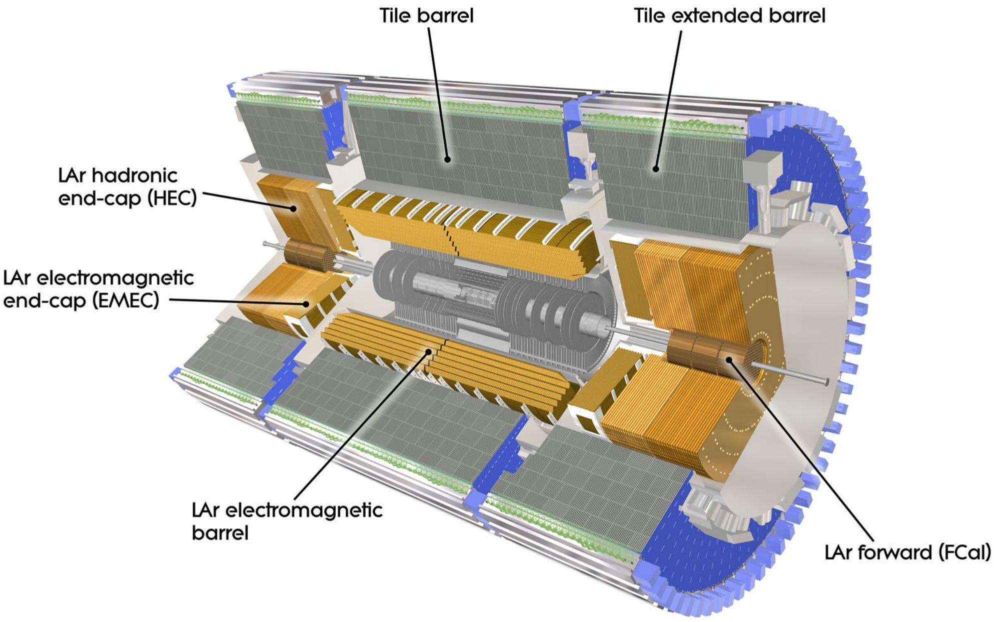

Figure 5.7: Schematic of the ATLAS Calorimeters with the different sub-systems highlighted [145].

The ATLAS calorimeter system [146, 147] illustrated in Figure 5.7, employs a sampling design for both its electromagnetic (ECal) and hadronic (HCal) calorimeters. High-energy particles interact with the absorber layers, producing cascades of secondary particles. The characteristics of these showers depend on the nature of the particle. Electromagnetic showers are induced by particles such as electrons and photons, while hadronic showers result from the interactions of hadrons via the strong force. The total calorimeter system provides a pseudorapidity coverage up to 4.9 in $|\eta|$ and full coverage in ϕ.

The calorimeter system is divided into two sub-systems with different designs and granularities. The ECal is designed with fine granularity to precisely measure EM showers, and the HCal calorimeter is designed with coarser granularity to capture the broader distribution of hadronic showers. Both sub-systems are designed with sufficient depth to fully contain the particle showers.

Electromagnetic calorimeter

The ECal uses liquid argon (LAr) as the active material and lead plates as absorber material. Incident particles interact with the absorber layers, producing showers of charged secondary particles. The charged particles travel into the LAr layer, producing electron currents that is read out via electrodes. The accordion shape of the electrodes allows for full ϕ coverage. The ECal consists of a barrel section, with $|\eta|$ coverage up to 1.475, and two end-cap sections (EMEC) covering $1.375 < |\eta| < 3.2$. In the barrel section two cylindrical half barrels are centred around $z = 0$. Each barrel contains 1024 absorbers. The end-cap sections are divided into two wheels. The outer wheels contain 758 absorbers, while the inner wheels contain 256 absorbers. The depth of the barrel section is over 22 radiation lengths X_0. This is a measure of how far a particle can travel through the material before reducing its energy (or intensity for photons) by factor of $1/e$. The end-cap sections have depths of over 24 X_0. The positional resolution is $\Delta\eta \times \Delta\phi = 0.025 \times 0.1$ in the barrel and 0.025×0.025 in the end-caps. The energy resolution of the ECal for electrons and photons is $\sigma_E/E = 10\%/\sqrt{E} \oplus 0.7\%$ [126].

Hadronic calorimeter

The HCal is built around the ECal. It consists of the tile calorimeter enveloping the the ECal barrel calorimeter, the LAr end-cap calorimeter (HEC) and LAr forward calorimeter (FCal). The tile calorimeter uses steel as absorber material and scintillating tiles as the active material. It is divided into a barrel part with 64 modules and three layers. The granularity of the first two layers is $\Delta\eta \times \Delta\phi = 0.1 \times 0.1$, and the granularity of the last layer is $\Delta\eta \times \Delta\phi = 0.2 \times 0.1$. The coarser granularity compared to ECal is sufficient to measure hadronic showers, since these are wider than EM showers. Instead of radiation length, interaction length λ is used as a measure for depth, which is defined as the mean free path of a hadronic particle between two inelastic interactions. The three barrel layers covers $|\eta| < 1.7$ and has a combined depth of 7.4 λ at $\eta = 0$ (9.7 λ when including the ECal system). The HEC consists of two wheels per end-cap and is located behind the EMEC. Each wheel is segmented into two layers, resulting in four layers per end-cap, each with 32 wedge-shaped modules. The HEC uses copper plates as the absorbing material and LAr as the active material. It covers the range $1.5 < |\eta| < 3.2$ and has a granularity of $\Delta\eta \times \Delta\phi = 0.1 \times 0.1$ for $|\eta| < 2.5$ and $\Delta\eta \times \Delta\phi = 0.2 \times 0.2$ for larger values. The depth of HEC is about 12 λ. The combined tile and HEC energy resolution is $\sigma_E/E = 50\%/\sqrt{E} \oplus 3\%$ [126].

The FCal is located closely to the beam pipe to cover forward-scattered particles within $3.1 < |\eta| < 4.9$. It consists of three different absorber layers. The first one is made of copper and is intended for measuring EM showers. The two others are made of tungsten and are intended for measuring hadronic showers. The active material is LAr. The FCal has a total interaction length of 10 λ and an energy resolution of $\sigma_E/E = 100\%/\sqrt{E} \oplus 10\%$ [126].

5.2.4 Muon Spectrometer

The muon spectrometer (MS) [148] is the outermost detector system in ATLAS. Although muons leave tracks in the ID they travel through the calorimeter system while retaining most of their incident energy. To identify muon tracks, the MS is built around the calorimeter.

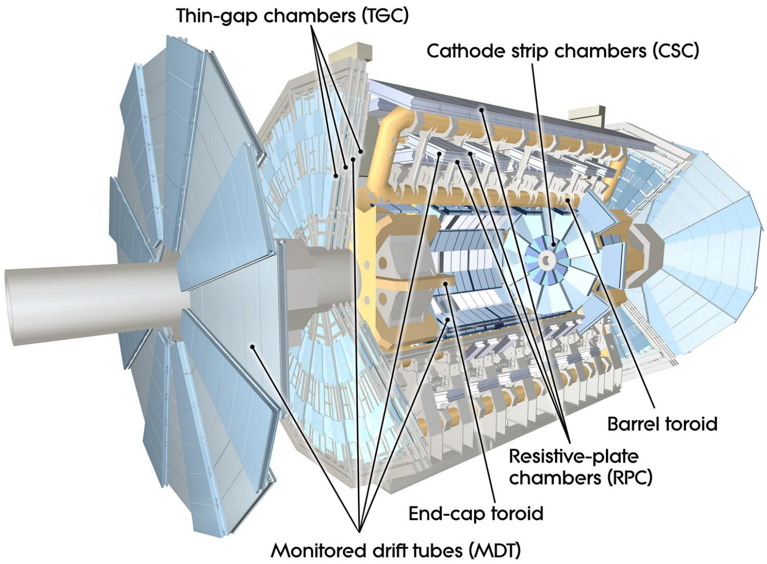

Figure 5.8: Schematic of the ATLAS MS with the different sub-systems highlighted [149].

It consists two types of precision tracking chambers: Monitored Drift Tubes (MDT) and Cathode Strip Chambers (CSC), as well as two types of trigger chambers: Resistive Plate Chambers (RPC) and Thin Gap Chambers (TGC). The precision tracking chambers has $|\eta|$ coverage up to 2.7, while the triggering is possible at $|\eta| < 2.4$. The toroidal field integral is between 2.0 and 6.0 T$\cdot m$ throughout most of the detector. The barrel toroid bends the muons in the region $|\eta| < 1.4$, while the end-cap toroids are responsible for the bending in the region $1.6 < |\eta| < 2.6$. In the transition regions between the two a combination of the toroidal fields are used. A schematic of the layout of the MS during Run 2 with its sub-detectors and toroidal magnet system is shown in Figure 5.8. The MS has a design resolution of $\sigma_{p_T}/p_T = 10\%$ at $p_{\mathrm{T}} = 1\,\mathrm{TeV}$ [126].

Precision Tracking chambers

For high-precision spatial resolution, MDT chambers are used in the region $|\eta| < 2.7$. These chambers operate in a similar way to the TRT section of the ID, using a gas mixture of argon and carbon dioxide that is ionised by traversing muons. The maximum drift time is 700 ns, and each chamber delivers a spatial resolution of $35\,\mu$m. In the innermost MS layer, MDTs cover only $|\eta| < 2.0$. Cathode Strip Chambers are used instead for

$2.0 < |\eta| < 2.7$. These offer better time resolution and rate capability, but their spatial resolution is slightly reduced, with each chamber having a spatial resolution of $40\,\mu$m.

Fast Trigger chambers

One of the design criteria for the MS was the ability to trigger on muon tracks. For this, track information must be available within a few tens of nanoseconds after a muon has passed. This is achieved by complementing the tracking chambers with RPCs and TGCs that are designed to process muon signals as quickly as possible. The fast trigger chambers can provide tracking in timescales between 15 and 25 ns, similar to the time interval of the LHC bunch spacing. The RPCs are located in the barrel region and cover $|\eta| < 1.05$. Each RPC consist two parallel resistive plates separated by a a gas volume filled with a mixture of predominantly $C_2H_2F_4$, and has a spatial resolution of 10 mm. TGCs cover the end-cap region of $1.05 < |\eta| < 2.4$. They are multiwire proportional chambers similar to the CSCs. They have a finer granularity than the RPCs and offer a spatial resolution between 2 and 6 mm.

5.2.5 Trigger and data acquisition system

The LHC operates at a nominal collision rate of 40 MHz, making it technically impossible to store all collision events for physics analysis. The role of the ATLAS Trigger and Data Acquisition (TDAQ) system [150] is to identify events containing interesting physics and record these in a way that meets the requirements of the readout rate, available processing power and storage capacity. In Run 2, this system was split into the hardware-based Level-1 (L1) trigger and software-based High-Level-Trigger (HLT). Any events that is not selected by both trigger systems is discarded. The L1 trigger reduces the the accepted event rate from 40 MHz to 100 kHz, while the HLT further reduces the rate down to approximately 1 kHz.

Level-1 Trigger

To process events as quickly as possible, the L1 trigger does not use information from the ID, as track reconstruction is too computationally intensive. Instead, events are selected based on information from the calorimeters, RPCs, and TGCs to perform a coarse analysis within $2.5\,\mu$s. The L1 trigger is divided into the calorimeter trigger (L1Calo), the muon trigger (L1Muon), and the event decision system implemented in the Central Trigger Processor (CTP). Event-level quantities, such as the total deposited energy in the calorimeter, muon p_{T} in the MS, and topological requirements like invariant masses and angular distances, are used to define Regions of Interest (RoIs) in the $\eta - \phi$ space of the detector. These RoIs are passed to the HLT for further processing, significantly reducing the amount of data needed to calculate the trigger decision. In some cases, however, the full event is also stored.

High-Level Trigger

The RoIs are provided to the HLT system, which executes reconstruction- and identification algorithms by using the full granularity of the detector in the RoIs or by using the full detector system. A two-step approach is used. In the first step, a fast reconstruction which rejects the majority of events is applied. In the second step, slower but more precise reconstruction- and identification algorithms are used. These algorithms are designed to have a minimum difference to the algorithms used in the offline reconstruction and identification. A menu of different trigger algorithms is designed to detect the presence of specific object(s) like electrons, muons, photons jets, hadronic τ-lepton decays, $E_{\mathrm{T}}^{\mathrm{miss}}$ candidates. For example, a single lepton trigger will select events with at least one lepton (electron or muon) with p_{T} above a predetermined threshold. The trigger chains can also be combined in order to select events with multiple objects and thresholds like ditau+$E_{\mathrm{T}}^{\mathrm{miss}}$ triggers. Events need to pass at least one of the triggers in the menu in order to be selected for permanent storage. The total processing time of the HLT system is about 200 ms.

5.3 Simulation of proton-proton collisions

In order to compare theoretical predictions with data recorded by the ATLAS detector and perform analyses, precise simulations of proton–proton collisions at the LHC are required. These simulations must model both the hard-scattering processes and the interactions of particles with the ATLAS detector material. This section introduces concepts involved in simulating such collisions, beginning with parton distribution functions as theoretical descriptions of the partonic structure relevant to hadron collisions, and continuing through the various stages of the event simulation chain, from the hard-scattering process to the detector response.

5.3.1 Modelling of proton-proton collisions

Since the proton is a composite particle, interactions in proton–proton collisions occur between its constituents, known as partons. The proton consists of three valence quarks: two u quarks and one d quark. However, due to the strong interactions between the valence quarks, additional partons, including heavier quark states and gluons, are momentarily produced. Determining the cross-section for producing a final state with n particles in proton–proton collisions, $\sigma(pp \to n)$, requires parametrising both the structure of the colliding protons and the partons involved in the hard scatter interaction, each associated with different scales of momentum transfer, Q. These contribution can however be treated separately due to the factorisation theorem [151]. The hard scattering between the partons typically have large momentum transfer and can be computed using perturbative QCD. Softer processes associated with momentum transfers on the order of the proton mass have to be described non-perturbatively by models fitted to experimental data. The probability to extract a parton of species a is quantified by parton distribution functions (PDFs), $f_a(x_a, Q)$. PDFs depend on the the momentum fraction x_a of the initial proton P, and is evaluated at some factorisation scale $Q = \mu_f$. This effectively defines the energy scale that separates the perturbative and non-perturbative parts of the calculation.

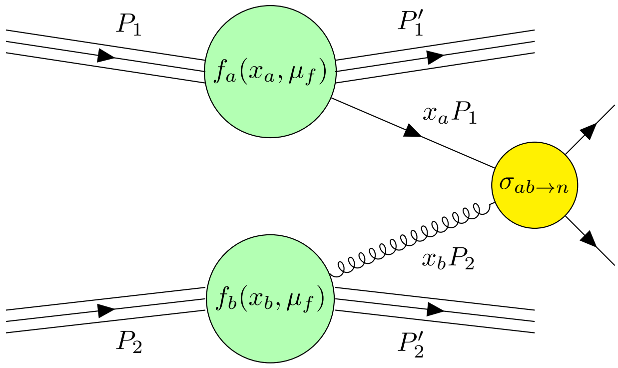

Figure 5.9: The two scales involved in a proton-proton collision. Two partons, a and b, carry momentum fractions $x_a P_1$ and $x_b P_2$ of the initial proton momenta P_1 and P_2. They are described by the PDFs $f_{a/b}(x_{1/2}, \mu_F)$ and scatter with a cross-section $\sigma_{ab \to n}$ to produce a final state with n particles.

Figure 5.9 illustrates the two-scale structure of a proton-proton collision, where the cross-section factorises into the PDFs for parton a and b, and the partonic cross-section $\sigma_{ab \to n}$ for producing a final state with n particles. The total cross-section, $\sigma(pp \to n)$ can be written as a sum over all possible parton configurations, weighted by the PDSs:

$$\sigma_{pp \to n} = \sum_{a,b} \int_0^1 \int_0^1 dx_a dx_b f_a\left(x_a, \mu_F\right) f_b\left(x_b, \mu_F\right) \sigma_{ab \to n}\left(x_a, x_b, \mu_R, \mu_F\right). \tag{5.7}$$

The partonic cross-section can be computed from the matrix elements $\mathcal{M}_{ab \to n}$ with perturbative QCD. This involves evaluating the corresponding Feynman diagrams at specific orders of the strong coupling constant, α_s. The cross-section can be expressed as a power series in α_s:

$$\sigma = \sum_{n=1}^{\infty} \alpha_s^n \sigma_n. \tag{5.8}$$

The lowest order of α_s that contributes to the cross-section is called the leading-order (LO), followed by next-to-leading order (NLO) and next-to-next-to-leading order (NNLO) etc. At higher orders, phase space integrations introduce ultraviolet divergences from loop diagrams. The ultraviolet divergences are absorbed into a redefinition of α_s through the process of renormalisation by introducing the renormalisation scale, μ_R [152].

Both the factorization and renormalization scale are arbitrary, unphysical parameters, typically set equal to the momentum transfer of the parton interaction, $\mu_R = \mu_F = Q$. The cross-section dependence on these scales arises because calculations are truncated at a fixed order in α_s. While higher order terms improve precision, their calculations also increase in complexity. As a result, cross-sections are usually evaluated at NLO or NNLO accuracy. In the limit $n \to \infty$, the dependence on μ_R and μ_F vanishes. At fixed orders however, theoretical uncertainties are included to account for scale choices and missing higher-order contributions.

5.3.2 Parton shower and hadronisation

At the energy scale of the hard scattering process, partons can radiate gluons or split into other partons, leading to additional emissions in both the initial and final states. These emissions are referred to as initial-state radiation (ISR) and final-state radiation (FSR), respectively. If the radiated partons carry sufficient momentum, they undergo further splittings via the processes $q \to qg$, $g \to q\bar{q}$, and $g \to gg$, leading to a parton shower. With each splitting, the average energy of the partons decreases until it reaches the scale $\Lambda_{\text{QCD}} \approx 1\,\text{GeV}$. Below this scale, partons begin to merge, forming colour-neutral bound states through a process known as hadronisation [153]. Since this cannot be calculated using perturbation theory, it is modelled through phenomenological programs tuned to data. Common models include the Lund string fragmentation model [154] used in the Pythia event generator and the parton-cluster fragmentation model [155] used in the Sherpa event generator.

5.3.3 Underlying event

The remaining parts of the protons that are not involved in the hard scattering process can undergo soft interactions leading to what is referred to as the underlying event (UE). This includes also interactions between the remaining partons within the protons, referred to as multiple-parton interactions (MPI). As with other soft interactions, UE modelling is described with models tuned to data. A schematic of the full simulation sequence up to this point can be seen in Figure 5.10.

5.3.4 Pile-up

Pile-up is another interaction that must be modelled in simulation. It is categorised into interactions occurring within the same bunch crossing (in-time pile-up) and those resulting from interactions occurring in preceding or subsequent bunches (out-of-time pile-up) [157]. Both effects are simulated inclusively following the simulation

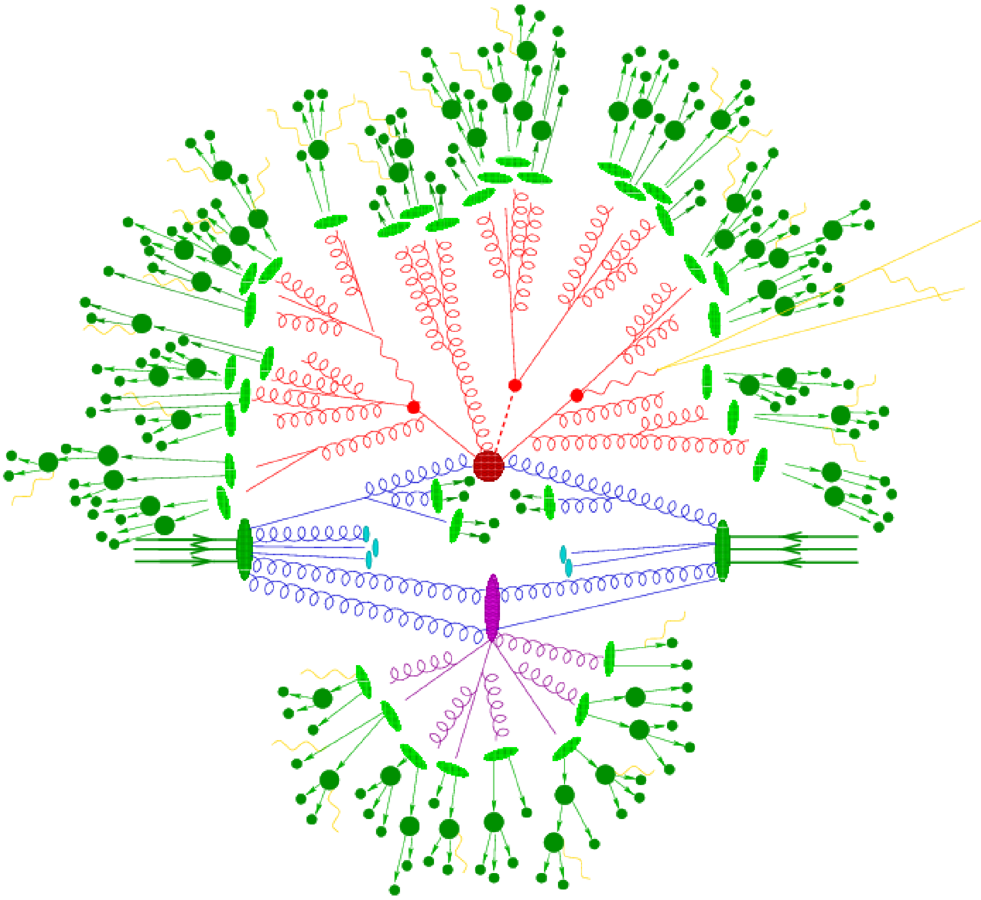

Figure 5.10: A pictorial representation of the different steps involved in MC simulations of proton-proton collisions. The red blob in the centre represents the hard scattering process. It is surrounded by a tree-like structure representing the partons showers. The hadronisation process and subsequent hadron decay is marked in light and dark green. The light blue blobs represents the beam remnants, and the underlying event activity is marked in purple [156].

chain described above and are then overlaid with the simulation of the hard scattering process. The number of interactions per bunch crossing (μ) depends on the beam conditions, so simulations are subsequently reweighted to match distributions observed in data.

5.3.5 Detector simulation

To enable a meaningful comparison with data recorded by the ATLAS detector, simulated events produced using the aforementioned simulation chain must be further processed through a detailed simulation of their interaction with the detector. The ATLAS detector simulation infrastructure [158] is built using the GEANT4 toolkit [159], which contains packages capable of simulating the detector response to particles interacting with the detector material. GEANT4 provides a detailed simulation of the entire ATLAS detector and its geometry, including magnetic field configurations, expected noise levels in readout electronics, and known detector defects.

The detector response to particles is digitised and converted into detector signals in the same manner as in data, ensuring an identical output format. This allows the same trigger-, identification- and reconstruction algorithms to be applied to both data and MC. Fully simulated events before detector simulation are referred to as "truth-level" events, whereas those after detector simulation are termed "reco-level" events.

The simulation of the complete ATLAS geometry using GEANT4 is referred to as full detector simulation. While this approach is the most precise and reliable, it is also highly computationally demanding, where each event can take several minutes to process. Since approximately 90% of CPU resources are spent on simulating the calorimeter response, more efficient alternatives are often employed for this step. The AtlFast-II method [160, 161] utilises faster simulation techniques for both the calorimeter and ID systems, while the remaining sub-detectors are still simulated using GEANT4. AtlFast-II significantly reduces CPU time while maintaining a satisfactory level of accuracy, making it particularly useful for simulating large signal grids, such as those required for the mono-Higgs analysis in Chapter 9.

Chapter **6**

Object reconstruction and particle identification

The particles produced from the proton–proton collisions in the ATLAS detector produce signals in the different sub-systems. These signals are combined and passed through the ATLAS software that performs reconstruction, calibration and identification of different physics objects that will be used for analysis. Objects include tracks, vertices, photons, electrons, muons, jets, hadronically decaying τ-leptons and missing transverse energy. This chapter aims to provide an overview of the algorithms used for different objects.

6.1 Tracks

The reconstruction of various objects, such as electrons, muons, and jets, relies on tracking the trajectories of charged particles in the ID. As these particles pass through the different layers of the ID, they leave hits, whose positions are used to determine their paths. Due to the solenoid magnetic field, these trajectories follow a helicoidal shape, with their curvature being inversely proportional to the transverse momentum of the particle. The tracks are described by five key parameters. These include the parameters p_{T}, θ, ϕ, as well as the transverse impact parameter relative to the nominal interaction point (d_0), and the longitudinal impact parameter relative to the nominal interaction point (z_0). These parameters are illustrated in Figure 6.1.

Track reconstruction follows a series of steps [163]. It begins by linking hits from different layers of the ID to establish track seeds. Hits in the pixel and SCT detectors that are above a certain energy threshold are combined to form clusters, which are then grouped into sets of three to create the initial seeds. A combinatorial Kalman filter subsequently incorporates additional clusters into these seeds, leading to the formation of track candidates [164].

The Kalman filter is a recursive technique that refines track candidates incrementally. Each new cluster provides updated information, allowing the algorithm to adjust parameters such as position and momentum while pre-

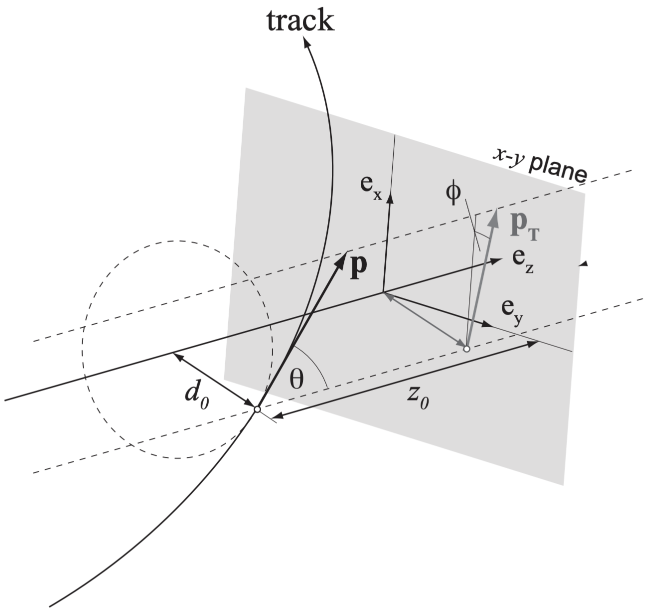

Figure 6.1: Parameters used for track reconstruction in ATLAS. The e_z direction is the unit vector in the z-direction which is parallel to the beam axis [162].

dicting the track's subsequent location in the next layer. Since multiple candidates may correspond to the same cluster, an ambiguity resolution method evaluates them and selects the most suitable one based on track quality.

To determine track quality, a scoring system is defined from the χ^2 value of the track fit, p_{T} of the track, the number of associated clusters and number of holes. A hole occurs when a hit is expected in a layer but is absent. Lower scores are assigned to tracks with holes and low p_{T}, as these are more likely to be incorrectly reconstructed. The candidate with the highest score is chosen as the final track.

Once the ambiguity is resolved, a set of selection criteria is applied to the track. It must contain at least seven clusters across the pixel and SCT detectors, with no more than two holes. Additionally, the p_{T} must exceed 500 MeV, and have $|\eta| < 2.5$. Further constraints require $|d_0| < 2$ mm and $|z_0 \sin\theta| < 3$ mm. Tracks that satisfy these conditions undergo a high-resolution fit that incorporates all hits in the ID.

6.2 Primary vertices

The tracks described in the previous section are used to reconstruct the primary vertices of events [165, 166]. A vertex-finding algorithm initially identifies the primary vertices, followed by a fitting procedure that refines their positions for improved precision. Tracks that are inconsistent with a given vertex are excluded from its reconstruction and may instead be used to identify other vertices. Among the reconstructed primary vertices, the one with the highest sum of squared transverse momentum of its associated tracks, $\sum p_{\mathrm{T}}^2$, is chosen as the hard-scatter vertex. The remaining vertices are classified as pile-up or secondary vertices.

6.3 Electrons

As electrons pass through the ATLAS detector, they produce tracks in the ID and deposit the majority of their energy in the ECal. Within the ECal, they primarily interact with the material through bremsstrahlung, generating photons that subsequently undergo e^+e^- pair production. This process results in the formation of an electromagnetic shower.

6.3.1 Reconstruction

The reconstruction of electrons [167, 168] starts with combining clusters of cells in the ECal with tracks from the ID. The first step involves the topological cell clustering algorithm [169]. Proto-clusters are first formed from seed cells with an energy exceeding four times the calorimeter noise level. Adjacent cells above twice the noise level are then added. Overlapping proto-clusters are merged, while clusters with two energy maxima above 500 MeV are split. The final clusters, known as topo-clusters [167], serve as electron or photon candidates if their ECal energy exceeds 400 MeV and accounts for more than 50% of the total cluster energy. If no compatible tracks are found in the ID, a pattern recognition algorithm corrects for bremsstrahlung energy losses to identify possible tracks. Tracks associated with topo-clusters are refined using a Gaussian Sum Filter [170]. To form electron seeds, topo-clusters are ranked by E_{T} and must exceed 1 GeV with an associated track containing at least four hits in the pixel or SCT detectors. Nearby topo-clusters, known as satellites, are incorporated if their angular separation from the seed cluster is within the window of $\Delta\eta \times \Delta\phi < 0.0075 \times 0.125$, extended to 0.125×0.3 if two clusters share a track. The combination of electron seeds and satellites forms a super-cluster.

Once tracks are matched to super-clusters, an initial energy calibration is applied. Clusters without a well-matched track are identified as photons, while those with a well-matched track are reconstructed as electrons. In ambiguous cases, both electron and photon objects are created for further analysis. Electron p_{T} is derived from the calorimeter energy measurement, while its η and ϕ are obtained from the associated track.

6.3.2 Identification

The reconstruction algorithm can misidentify other objects as electrons. A likelihood based identification algorithm was used in Run 2 to reject these cases [171]. This algorithm employs a multivariate analysis technique that combines several discriminating variables. These variables characterise the properties of the electron track in the ID, the matching between the track and the calorimeter cluster, as well as the longitudinal and lateral shapes of the electromagnetic shower in the calorimeters. The algorithm computes a discriminant that can separate signal electrons from background, using probability density functions (PDFs) derived from histograms in different $|\eta|$ and E_{T} bins. These PDFs are constructed from $Z \to ee$ events for signal and predominantly dijet events for background.

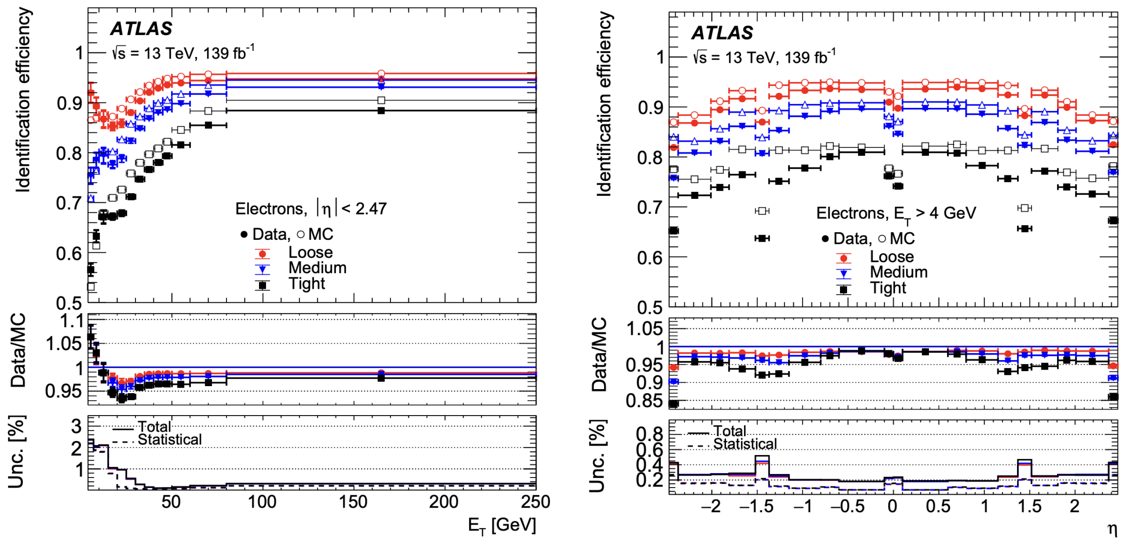

a) E_{T} b) η

Figure 6.2: Identification efficiencies of electrons from $Z \to ee$ decays as a function of the electron E_{T} (left) and η (right) for the different identification working points with the ATLAS Run 2 dataset [168].

The algorithm provides three working points (WPs): `Loose`, `Medium`, and `Tight`, each offering a trade-off between efficiency and background rejection. While all WPs use the same discriminant, their thresholds are different. The `Loose` WP achieves an efficiency of approximately 85% at $E_{\mathrm{T}} = 20$ GeV, increasing to 96% at $E_{\mathrm{T}} = 100$ GeV. The `Tight` WP ranges from 55% efficiency at $E_{\mathrm{T}} = 4.5$ GeV to 90% at $E_{\mathrm{T}} = 100$ GeV, prioritising background suppression. The performance of the `Medium` working point is designed to be between the `Loose` and `Tight` ones. The identification efficiencies are obtained from $Z \to ee$ events in both data and MC, and is defined as the fraction of reconstructed electrons that pass a certain WP threshold. Figure 6.2 shows the identification efficiencies as a function of E_{T} and η for different WPs in both data and MC. The efficiency drop in $1.37 < |\eta| < 1.52$ comes from the relative large amount of inactive material in the transition region between the barrel and end-caps. Dedicated scale factors are derived for the electron isolation WPs to correct for observed differences in data and MC.

6.3.3 Isolation

In addition to electron identification WPs, isolation requirements are applied to further suppress contribution from misidentified electrons. Like the identification WPs, the isolation WPs are chosen to balance efficiency and background rejection. The electron isolation is based on both calorimeter and track isolation variables, $E_{\mathrm{T}}^{\mathrm{coneXX}}$ and $p_{\mathrm{T}}^{\mathrm{coneXX}}$ respectively [172]. The calorimeter isolation variable represents the amount of energy deposited in calorimeter cells within the cone $\Delta R_{\mathrm{max}}^{\mathrm{XX}} < \mathrm{XX}/100$. The track isolation variable is defined as the p_{T} sum of tracks that are within the same cone size XX around the electron track. The XX value is usually set to 20 or 30. In events where electrons are produced in the decay of boosted particles, other particles can be produced very close to the direction of the electron. In these cases a track-based variable with varying cone size is defined, $p_{\mathrm{T}}^{\mathrm{varconeXX}}$, which shrinks for higher electron p_{T}. The variable cone size is defined as:

$$\Delta R = \min\left(\frac{10}{E_{\mathrm{T}}[\mathrm{GeV}]}, \Delta R_{\mathrm{max}}^{\mathrm{XX}}\right), \tag{6.1}$$

where $\Delta R_{\mathrm{max}}^{\mathrm{XX}}$ is usually either 0.2 or 0.3 following XX value. Table 6.1 shows the different isolation WPs and corresponding thresholds.

Selection criteria	Calorimeter isolation	Track isolation
`HighPtCaloOnly`	$E_{\mathrm{T}}^{\mathrm{cone20}} < \max(0.015 \times p_{\mathrm{T}}, 3.5)$ GeV	-
`TightTrackOnly_VarRad`	-	$p_{\mathrm{T}}^{\mathrm{varcone20}}/p_{\mathrm{T}} < 0.06$
`TightTrackOnly_FixedRad`	-	$p_{\mathrm{T}}^{\mathrm{varcone20}}/p_{\mathrm{T}} < 0.06$ for $E_{\mathrm{T}} < 50$GeV $p_{\mathrm{T}}^{\mathrm{cone20}}/p_{\mathrm{T}} < 0.06$ for $E_{\mathrm{T}} > 50$GeV
`Tight_VarRad`	$E_{\mathrm{T}}^{\mathrm{cone20}}/p_{\mathrm{T}} < 0.06$	$p_{\mathrm{T}}^{\mathrm{varcone20}}/p_{\mathrm{T}} < 0.06$
`Loose_VarRad`	$E_{\mathrm{T}}^{\mathrm{cone20}}/p_{\mathrm{T}} < 0.20$	$p_{\mathrm{T}}^{\mathrm{varcone20}}/p_{\mathrm{T}} < 0.15$

Table 6.1: Calorimeter and track isolation criteria for different isolation working points. For all working points XX is set to 20 and $\Delta R_{\mathrm{max}} = 0.2$.

Figure 6.3 shows the different electron isolation WPs as a function of E_{T} and η, obtained from $Z \to ee$ events in data. Dedicated scale factors are derived for the isolation WPs to correct for observed differences in data and MC.

6.4 Muons

Muons produced in proton–proton collisions in the ATLAS detector are typically minimum-ionising particles, depositing little energy in the sub-detectors. They create hits in the ID, leave small energy deposits in the calorimeters, and hits in MS. Muon reconstruction is therefore primarily based on information from the ID and MS tracking detectors, with calorimeter information playing a role mainly in the region $|\eta| < 0.1$ where readout cables in the ID leads to a gap in the MS and limited coverage.

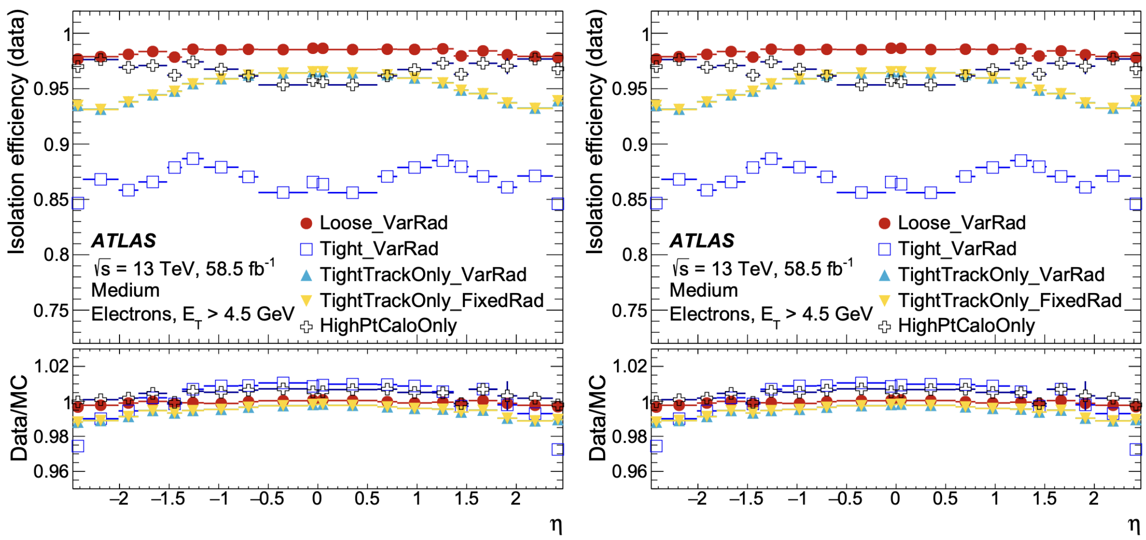

a) E_{T} b) η

Figure 6.3: Isolation efficiencies of electrons from $Z \to ee$ decays as a function of the electron E_{T} (left) and η (right) for the different isolation working points with the ATLAS 2018 dataset [168].

6.4.1 Reconstruction

Muon reconstruction [173, 174] combines measurements from the ID, MS, and to a lesser extent, the calorimeters. The reconstruction begins in the MS with a pattern recognition algorithm that forms local track segments within individual muon chambers. These segments, originating from different detector layers, are combined to create preliminary track candidates, which are required to point approximately toward the IP and exhibit the expected curvature due to the magnetic field. A χ^2 fit refines the track by incorporating additional hits along the predicted path while excluding outliers. This iterative process continues until an optimal trajectory is determined. If a track segment is associated with multiple candidates, an overlap removal algorithm assigns it to the best-fitting track or limits the number of associated tracks to at most two. The final track is re-fitted with a loose IP constraint before being extrapolated to the beamline. Global muon reconstruction combines the refined MS tracks with ID and calorimeter measurements. Depending on the region and what information is available from the ATLAS sub-detectors five different types of muons are defined:

Combined (CB) muons are defined based on tracks in the MS and ID. Muon tracks reconstructed in the MS are propagated inwards and matched to corresponding ID tracks. A global refit is then performed, incorporating hits from both detectors while accounting for energy loss in the calorimeters. Alternatively, ID tracks can be extended outward to the MS as an independent approach.

Inside-Out (IO) muons are defined using an inside-out algorithm that extrapolates ID tracks to the

MS, searching for at least three loosely-aligned MS hits. A combined track fit is then performed using the ID track, energy loss in the calorimeters, and MS hits. This method does not rely on independently reconstructed MS tracks, enhancing efficiency in regions with limited MS coverage.

Segmented (ST) muons are defined by ensuring that an ID track, when extrapolated to the MS, matches at least one reconstructed MS segment. If the ID track successfully matches, it is classified as a muon candidate, and the muon parameters are derived directly from the ID track fit.

Muon-Spectrometer Extrapolated (ME) muons are defined based on the extrapolation of MS track parameters to the beamline when no matching ID track is found. This definition allows the extension of acceptance beyond the ID coverage, fully utilising the MS coverage up to $|\eta| = 2.7$.

Calorimeter Tagged (CT) muons are identified by extrapolating ID tracks through the calorimeters to search for energy deposits consistent with a minimum-ionising particle. These deposits are used to tag the ID track as a muon, with the muon parameters determined directly from the ID track fit.

6.4.2 Identification

Muon identification in ATLAS applies additional selection criteria to reconstructed muons to enhance the purity and quality of the candidates. The main WPs are `Loose`, `Medium`, and `Tight`, while additional WPs such as low-p_T and high-p_T are defined for muons with very low or high p_{T}, respectively. `Loose` muons considers all muon types, with CT and ST muons restricted to $|\eta| < 0.1$. This WP was designed for final states with large muon multiplicity, such as $H \to 4\mu$ decays, which benefits from the higher efficiency at the cost of lower purity. The `Medium` WP is a subset of the `Loose` WP, accepting only CB and IO muons, and is the nominal muon requirement used by most ATLAS analyses. The `Tight` is the most restrictive, including the same muon types as the `Medium` WP while imposing additional selection criteria on the track parameters. It is optimised for especially low p_{T} muons where the misidentification rate is higher. The efficiency loss from `Loose` to `Medium` is around 20% for 3GeV $< p_{\mathrm{T}} <$ 5GeV and 1-2% for higher p_{T}. In the range of 6 GeV $< p_{\mathrm{T}} <$ 20 GeV, the `Tight` WP provides a background reduction of over 50% relative to `Medium`, resulting in an efficiency loss of about 6%. The muon identification efficiency for the different WPs is measured both in data and MC using $Z \to \mu\mu$ and $J/\psi \to \mu\mu$ events and can be seen in Figure 6.4. Dedicated scale factors are derived for the identification WPs to correct for observed differences.

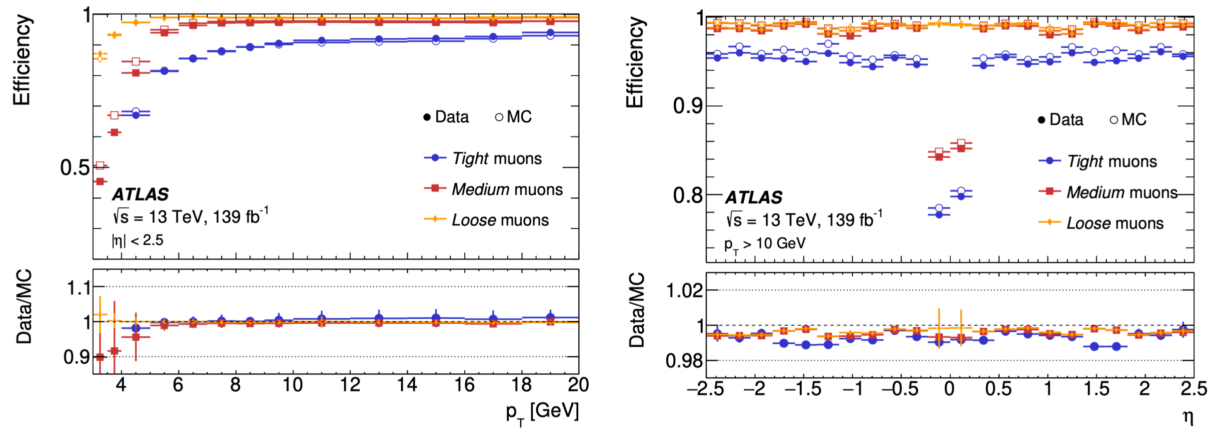

a) p_{T} b) η

Figure 6.4: Identification efficiencies of muons from $J/\psi \rightarrow \mu\mu$ decays as a function of the electron p_{T} (left) and from $Z \rightarrow \mu\mu$ as a function of η (right) with $p_{\mathrm{T}} > 10$ GeV for the different identification working points for both data and MC [174].

6.4.3 Isolation

Muon isolation is determined from calorimeter and track-based isolation variables, $E_{\mathrm{T}}^{\mathrm{topoconeXX}}$ and $p_{\mathrm{T}}^{\mathrm{coneXX}}$ respectively. These are measured in a similar way as the electron isolation variables explained in the previous section. Additionally, to account for variable cone length $p_{\mathrm{T}}^{\mathrm{varconeXX}}$ is defined according to Eq. 6.1. Figure 6.5 shows the distribution of different isolation variables divided by muon p_{T} in simulated $t\bar{t}$ events. The difference in shape for prompt and misidentified muon candidates is illustrated. Different WPs are defined from applying selections to these distributions. A summary of some of the isolation WPs used in ATLAS can be found in Table 6.2.

Selection criteria	Calorimeter isolation	Track isolation
`Loose_VarRad`	$E_{\mathrm{T}}^{\mathrm{topocone20}}/p_{\mathrm{T}} < 0.3$	$p_{\mathrm{T}}^{\mathrm{varcone30}}/p_{\mathrm{T}} < 0.15$
`Tight_VarRad`	$E_{\mathrm{T}}^{\mathrm{topocone20}}/p_{\mathrm{T}} < 0.15$	$p_{\mathrm{T}}^{\mathrm{varcone30}}/p_{\mathrm{T}} < 0.04$
`HighPtTrackOnly_VarRad`	-	$p_{\mathrm{T}}^{\mathrm{varcone20}} < 1.25$ GeV
`TightTrackOnly_VarRad`	-	$p_{\mathrm{T}}^{\mathrm{varcone30}}/p_{\mathrm{T}} < 0.06$

Table 6.2: Calorimeter and track isolation criteria for different isolation working points. For the varcone variables $XX = 20$ corresponds to $\Delta R_{\mathrm{max}} = 0.2$ and $XX = 30$ corresponds to $\Delta R_{\mathrm{max}} = 0.3$. All isolation working points require muon p_{T} above 1 GeV.

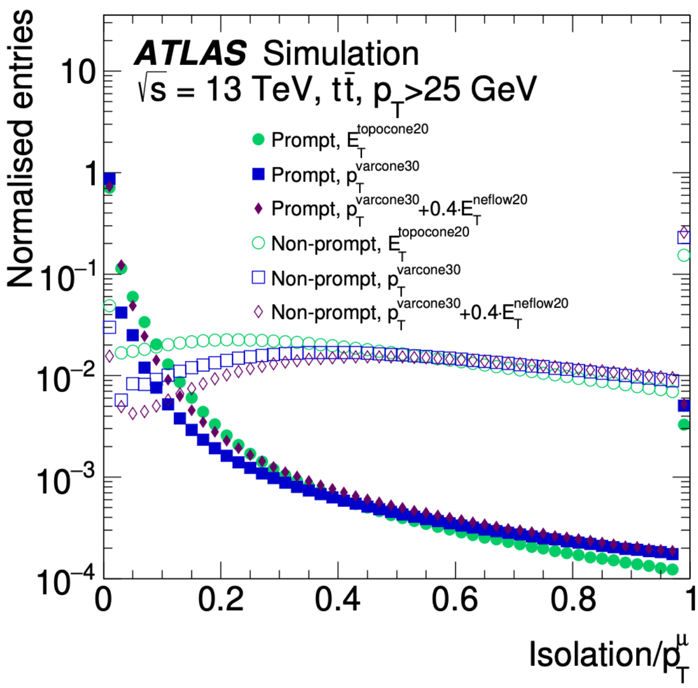

Figure 6.5: Distributions of isolation variables divided by muon p_{T} from simulated $t\bar{t}$ events. Prompt muons corresponds to muons candidates coming $t\bar{t}$ muon decay, while non-prompt muons corresponds to misidentified muon candidates [174].

6.5 Jets

Jets are collimated sprays of hadrons that arise when high-energy quarks or gluons fragment and hadronise as a consequence of colour confinement. Jets are measured and identified based on information from reconstructed tracks in the ID and energy deposits in both the ECal and HCal.

6.5.1 Reconstruction and calibration

Jet reconstruction relies on jet-clustering algorithms that sequentially combines close objects to define a single jet object. The most commonly employed jet clustering algorithm is the anti-k_t algorithm [175]. This algorithm introduces the distance d_{ij} between particles i and j and distance d_{iB} between particle i and the beam (B):

$$\begin{aligned} d_{ij} &= \min\left(p_{\mathrm{T},i}^{-2} p_{\mathrm{T},j}^{-2}\right) \frac{\Delta R_{ij}^2}{R^2}, \\ d_{iB} &= p_{\mathrm{T},i}^{-2}, \end{aligned} \tag{6.2}$$

where $p_{\mathrm{T},i}$ and $p_{\mathrm{T},j}$ represent the transverse momenta of the particles, and ΔR_{ij} denotes their angular separation. The jet size is determined by the radius parameter R, typically set to 0.4 for small-radius jets and 1.0 for large-radius jets [176]. The algorithm iteratively computes both distance measures for each particle, identifying the minimum value in each step. If d_{iB} is the smallest, particle i is classified as a jet candidate, removed from the input, and excluded from further iterations. Alternatively, if d_{ij} is the smallest, particles i and j are merged into a single entity, which is then included as an input particle in the next iteration. The procedure is repeated until no input particles are left.

Jet reconstruction is followed by a multi-step calibration process to correct for detector effects [177]. Pile-up corrections account for additional interactions using jet area and event energy density. The jet energy scale (JES) calibration [178] aligns reconstructed jet energy with truth-level jets using p_T- and η-dependent scale factors obtained from simulation. This is done to ensure that the reconstructed jet energy matches the energy of the initial parton at truth-level. The jet energy resolution (JER) is evaluated after the energy calibration to measure fluctuations in the reconstructed jet energy [177]. It is parametrised as a function of p_{T} and η and smeared to match resolution in data. Finally the Jet Vertex Tagger (JVT) algorithm [179] is employed to select jets originating from the hard scatter interaction and suppress pile-up jets. The JVT relies on track-based variables, such as the fraction of jet-associated tracks from the primary vertex, with corrections for number of vertices and pile-up-subtracted jet p_T. It is evaluated in the acceptance region of the ID, corresponding to $|\eta| < 2.5$. In the forward region the forward JVT (fJVT) algorithm [180] is used with an extended coverage up to $|\eta| < 0.45$.

6.5.2 b-jet tagging

Jet tagging is the process of identifying jets originating from specific quark flavours. In particular, b-tagging algorithms distinguish jets from B hadron decays (b-jets) from those produced by lighter quarks (light-jets). Characteristic features of B hadrons include their relatively long lifetimes leading to displaced secondary vertices with respect to the primary vertex.

Track-based taggers like IP2D and IP3D use the significance of impact parameters to identify tracks from displaced vertices [181, 182]. Secondary vertex reconstruction algorithms search for displaced vertices formed by B hadron decays, using variables like invariant mass, vertex flight distance, and track multiplicity. The track-based and secondary vertex taggers are then combined and used for b-tagging algorithms such as the DL1 and DL1r algorithms. These algorithms are built from deep neural network (DNN) architectures, which take the outputs of the track-based and secondary vertex taggers as inputs. The DL1r algorithm exploits a recurrent neural network (RNN) to learn track impact-parameter correlations, while DL1 is a less sophisticated feed-forward neural network. Both are multiclass classifiers with three outputs trained to classify b-jets, c-jets, and light-flavoured jets. The performance of b-tagging algorithms is usually evaluated based on light-flavour jet

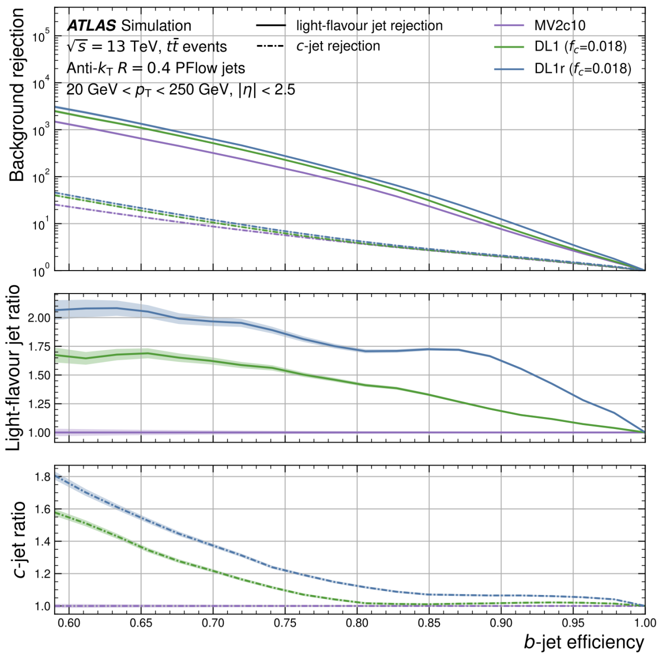

Figure 6.6: Different b-tagging algorithms as a function of light-flavour jet and c-jet rejection factors as a function of b-jet efficiency. The lower two panels show the ratios of light-flavour jet rejection and c-jet rejection rates of the algorithms compared to the MV2c10 algorithm [181].

and c-jet rejection factors as a function of b-jet efficiency. This can be seen in Figure 6.6 for the DL1, DL1r, and MV2c10 b-tagging algorithms using simulated $t\bar{t}$ events. The latter is based on boosted decision trees (BDTs) and was extensively used in early Run 2 analyses. DL1r provides the best performance and is the algorithm used in both analyses in this thesis.

Different working points are defined based on the b-tagging efficiency, typically chosen at 60%, 70%, 77% or 85% efficiency. Each point provides a trade-off between b-jet selection and background rejection. Additionally, dedicated scale factors are derived in $t\bar{t}$ regions, where flavour composition of jets are well understood, to correct the simulated b-jet tagging efficiency to match what is seen in data.

6.6 Hadronically decaying Taus

The τ-lepton can decay both leptonically and hadronically due to its relatively large mass of roughly 1.777 GeV. The dominant decay modes are listed in Table 6.3. Leptonic decays into electrons and muons, which account for approximately 35% of τ-lepton decays, are indistinguishable from prompt light lepton production and are reconstructed using the same identification algorithms described earlier for electrons and muons. However, a key difference is that the relatively long lifetime of τ-leptons leads to displaced vertices and distinct impact parameter distributions. The remaining 65% of τ-lepton decays occur hadronically, with about 77% involving a single charged hadron and roughly 23% producing three charged hadrons. These hadrons are primarily pions (π), with kaons (K) contributing to a lesser extent. Since neutrinos escape detection in ATLAS, they contribute to $E_{\mathrm{T}}^{\mathrm{miss}}$ and are not used in hadronic τ-lepton reconstruction. Hence, in this section, the τ-lepton objects will refer only to the visible part of the hadronic decay, commonly denoted as $\tau_{\mathrm{had_{vis}}}$.

Decay mode	BR [%]
Leptonic	35.21 ± 0.06
$e^-\bar{\nu}_e\nu_\tau$	17.82 ± 0.04
$\mu^-\bar{\nu}_\mu\nu_\tau$	17.39 ± 0.04
Hadronic	64.79 ± 0.17
$h^-\nu_\tau$	11.51 ± 0.05
$h^-\pi^0\nu_\tau$	25.93 ± 0.09
$h^-\pi^0\pi^0\nu_\tau$	9.48 ± 0.10
$h^-h^+h^-\nu_\tau$	9.80 ± 0.05
$h^-h^+h^-\pi^0\nu_\tau$	4.76 ± 0.05
other hadr.	3.31 ± 0.05

Table 6.3: Branching ratios for the decay modes of a negatively charged τ-leptom. h^- refers to either π^- or K^-.

6.6.1 Reconstruction

The reconstruction of hadronically decaying τ-leptons [183, 184] starts with jets that are reconstructed with the anti-k_t algorithm with a radius parameter of $\Delta R = 0.4$. The jets are required to have p_{T} above 10 GeV and $|\eta| < 2.5$, excluding jets in the transition region ($1.37 < |\eta| < 1.52$). Unlike the previously described jet objects the so-called "local hadronic calibration" (LC) [185] is applied to τ_{had} seed jets. The vertex associated with the τ-lepton candidate is selected by summing the p_{T} of tracks within $\Delta R < 0.2$ around the hadronic τ jet. The vertex with the largest momentum is chosen. Tracks associated with the τ-lepton candidate are required to have p_{T} above 1 GeV, at least two hits in the pixel detector, and at least seven hits in the SCT and TRT. Additionally, requirements on the impact parameters, $|d_0| < 1.0$ mm and $|z_0 \sin\theta| < 1.5$ mm, are imposed. The number of tracks associated with the τ-lepton decay is categorised into either 1-prong or 3-prong decays. The former corresponds to a single track, representing a single charged hadron in the decay, while the latter consists of three tracks from three charged hadrons. The reconstruction efficiency depends on the number of prongs, as seen in Figure 6.7. At low p_{T}, 3-prong decays are suppressed due to the minimum p_{T} requirement on charged decay products, while at high p_{T}, increased collimation increases the probability of missing tracks due to overlapping trajectories. Additionally, very high-p_{T} τ-leptons may decay beyond the first pixel layer, leading to incorrect prong assignments.

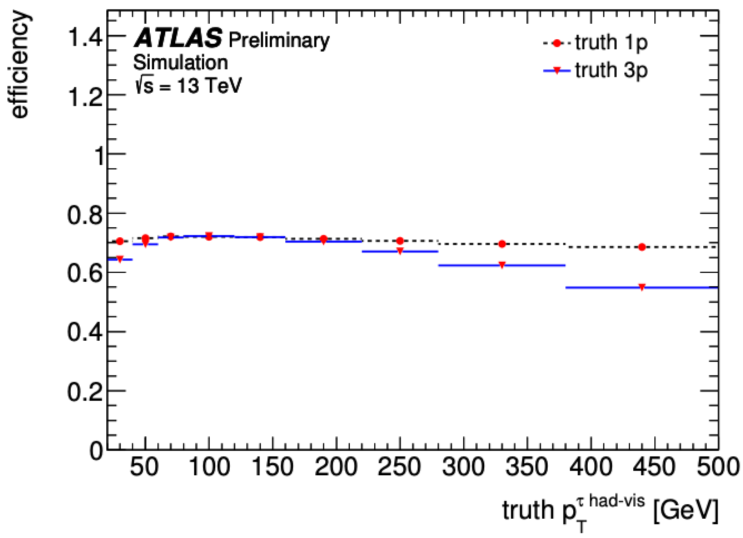

Figure 6.7: Simulated reconstruction efficiency for hadronic τ-lepton objects, separated into 1-prong and 3-prong candidates, as a function of the truth-level p_{T} [183].

6.6.2 Identification

The reconstructed hadronic τ-leptons provide minimal rejection against jet background. To distinguish these objects a RNN [186] is applied. Separate networks are trained for 1-prong and 3-prong decays, using a mixture of low-level features like track and cluster information, and high-level features derived from these. The output of the RNN defines four identification working points for both 1-prong and 3-prong. The WPs for 1-prong τ-leptons are categorised into `VeryLoose`, `Loose`, `Medium` and `Tight`, corresponding to 95%, 85%, 75% at 60% efficiency respectively. Similarly, four WPs are used for 3-prong τ-lepton objects, but at 95%, 75%, 60%, and 45% efficiency. The rejections rates of misidentified τ-leptons as a function of efficiency can be seen in Figure 6.8. The performance is also shown for the BDT algorithm, which was used in early Run 2. A separate classifier is also trained to reject backgrounds coming from electrons misidentified as 1-prong hadronic τ-lepton. This is called the electron-veto BDT (eBDT) and is built from calorimeter and track-based variables.

Dedicated scale factors for the τ-lepton identification and eBDT WPs are derived to correct for differences in simulation and data. These are mainly measured in $Z \to \tau\tau$ events, with higher p_{T} scale factors derived in $t\bar{t} \to b\mu\nu_{\mu}b\tau\nu_{\tau}$ events. The author also conducted studies on the potential to derive τ-lepton identification scale factors in the high p_{T} regime using $W \to \tau\nu +$jets events. In this topology, the W boson acquires a boost from its recoil against the jets, resulting in a higher p_{T} of the hadronic τ-lepton than what is typically observed in $Z \to \tau\tau$ events. However, due to the strong correlations between final-state objects, controlling background contributions from misidentified hadronic τ-leptons is particularly challenging. A novel background estimation strategy based on the data-driven ABCD method [187] was developed and is currently being refined for Run 3. A technical report detailing this work is available in Ref. [188], although it remains internal to the ATLAS Collaboration.

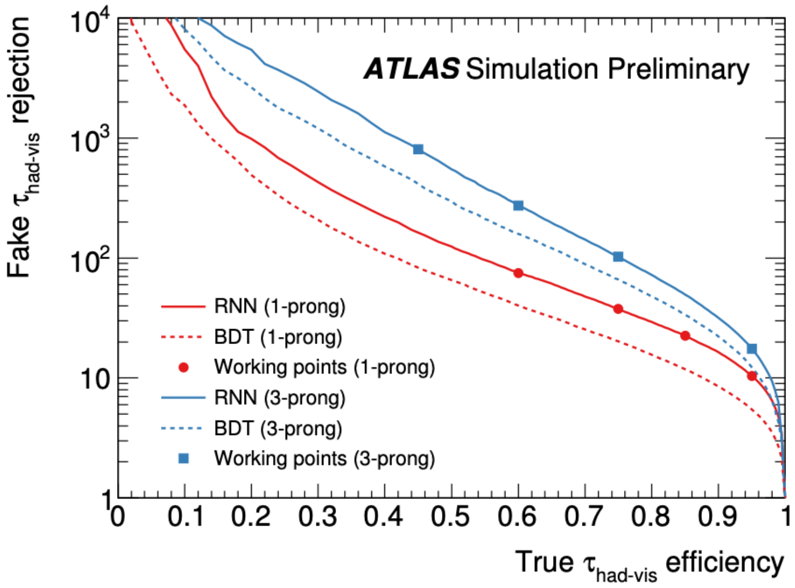

Figure 6.8: The rejection of quark and gluon jets misidentified as hadronic τ-leptons is shown as a function of the true hadronic τ-lepton efficiency for 1-prong (red) and 3-prong (blue) hadronic τ-lepton candidates, using the RNN (solid line) and BDT (dashed line) identification algorithms. The markers indicate the four defined WPs [186].

6.7 Missing transverse energy

The missing transverse momentum ($\vec{E}_{\mathrm{T}}^{\mathrm{miss}}$) is a vector quantity in the transverse plane of the detector that accounts for momentum carried by undetected particles, such as neutrinos (or a BSM particle). Since momentum is conserved, the total visible transverse momentum should sum to zero, with any imbalance suggesting the presence of invisible particles. The magnitude of $\boldsymbol{E}_{\mathrm{T}}^{\mathrm{miss}}$ is referred to as the missing transverse energy, $E_{\mathrm{T}}^{\mathrm{miss}}$. The reconstruction of $E_{\mathrm{T}}^{\mathrm{miss}}$ [189, 190] is calculated from the negative vectorial sum of all reconstructed and calibrated physics objects, i.e electrons, muons, jets and τ_{had}. Additionally, ID tracks not associated with any reconstructed physics object is taken into account. The negative vectorial sum of accepted physics objects is referred to as the hard term, while the unused ID tracks is referred to as the soft term:

$$\boldsymbol{E}_{\mathrm{T}}^{\mathrm{miss}} = -\Bigg(\underbrace{\sum_{\substack{\text{accepted}\\ \text{electrons}}} \boldsymbol{p}_{\mathrm{T}}^{e} + \sum_{\substack{\text{accepted}\\ \text{photons}}} \boldsymbol{p}_{\mathrm{T}}^{\gamma} + \sum_{\substack{\text{accepted}\\ \tau-\text{leptons}}} \boldsymbol{p}_{\mathrm{T}}^{\tau} + \sum_{\substack{\text{accepted}\\ \text{muons}}} \boldsymbol{p}_{\mathrm{T}}^{\mu} + \sum_{\substack{\text{accepted}\\ \text{jets}}} \boldsymbol{p}_{\mathrm{T}}^{\text{jet}}}_{\text{hard term}} + \underbrace{\sum_{\substack{\text{unused}\\ \text{tracks}}} \boldsymbol{p}_{\mathrm{T}}^{\text{track}}}_{\text{soft term}} \Bigg). \tag{6.3}$$

The performance of $E_{\mathrm{T}}^{\mathrm{miss}}$ reconstruction is typically evaluated by comparing simulated $Z \to \mu\mu$ events to data. For these events the true $E_{\mathrm{T}}^{\mathrm{miss}}$ is expected to be small, and discrepancies may arise due to detector limitations, jet mismeasurements, or pile-up effects, allowing the evaluation of the $E_{\mathrm{T}}^{\mathrm{miss}}$ response and resolution in the ATLAS detector.

The resolution of $E_{\mathrm{T}}^{\mathrm{miss}}$, quantified using the RMS of its x- and y-components relative to their expected values, is typically examined as a function of the transverse energy scalar sum ($\sum E_T$) of reconstructed objects. At low $\sum E_T$, it is primarily influenced by muon momentum resolution, whereas at high $\sum E_T$, it is dominated by the jet energy resolution.

6.8 Overlap Removal

Reconstructed physics objects are not necessarily exclusive, meaning energy clusters or tracks might be shared between multiple objects. Overlap removal refers the procedure used to resolve such ambiguities and prevent double-counting. The exact procedure might depend on specific analysis, but the same procedure is applied in both analyses in this thesis, with some differences to the baseline input objects. The procedure is summarised in Table 6.4 with each criteria being applied sequentially.

Reject	Against	Criteria
Electron	Electron	Shared track, $p_{\mathrm{T},1} < p_{\mathrm{T},2}$
Tau	Electron	$\Delta R < 0.2$
Tau	Muon	$\Delta R < 0.2$
Muon	Electron	is Calo-Muon and shared ID track
Electron	Muon	shared ID track
Jet	Electron	$\Delta R < 0.2$
Electron	Jet	$\Delta R < 0.4$
Jet	Muon	`NumTrack` < 3 and (ghost-associated or $\Delta R < 0.2$)
Muon	Jet	$\Delta R < 0.4$
Jet	Tau	$\Delta R < 0.2$

Table 6.4: Overview over the criteria used for the overlap removal in both analyses in this thesis.

Chapter **7**

Statistical Methods

The general framework for collecting and simulating data coming from the ATLAS detector have been detailed in previous chapters. At its core, this involves comparing data recorded by the ATLAS detector with MC simulations that approximate the underlying physics processes and model detector effects. To assess the compatibility between data and theoretical predictions, and to extract measurements of model parameters, a rigorous statistical treatment is required. This chapter provides an overview of the statistical methods used in both analyses presented in this thesis. A more detailed discussion of the specific fit models and uncertainty treatments can be found in Section 8.7 for the VBF CP analysis and Section 9.6 for the mono-Higgs search. This chapter is primarily based on Ref. [191] and the HistFactory documentation [192] and aims to summarise the relevant statistical concepts.

7.1 Likelihood function

Physics analyses rely on statistical inference to determine the most probable values of physical parameters ϕ given a set of observed events $\{x_i\}$. Since the true probability density $p(x|\phi)$ is often inaccessible in practice, MC simulations are used to approximate the probability distribution $p(x|\phi')$ for some assumed parameters ϕ', from which pseudo-experiments can be drawn. Given a sufficiently large number of simulated events $\{\tilde{x}_i\}$, an empirical probability density $p(\tilde{x}|\phi')$ can be constructed. This simulated probability density then forms the basis for likelihood-based inference.

In an ATLAS analysis, this approach is used to build a statistical model that describes the expected data in terms of contributions from signal and background processes, as well as their associated uncertainties. The model is parametrised by a set of parameters, which includes the parameter of interest (POI), often a signal strength factor μ scaling the signal yield, and nuisance parameters $\boldsymbol{\theta}$, representing systematic uncertainties.

The likelihood function $L(\mu, \boldsymbol{\theta})$ expresses the probability of observing n^{obs} events in data as a function of these parameters.

For binned data, as is typical in ATLAS analyses employing HistFactory, the likelihood is constructed as a product of Poisson probabilities across all bins:

$$L(\mu, \boldsymbol{\theta} \mid n^{\mathrm{obs}}) = \prod_{i}^{N} \frac{(\mu s_i(\boldsymbol{\theta}) + b_i(\boldsymbol{\theta}))^{n_i^{\mathrm{obs}}}}{n_i^{\mathrm{obs}}!} e^{-(\mu s_i(\boldsymbol{\theta}) + b_i(\boldsymbol{\theta}))}, \tag{7.1}$$

where n_i^{obs} denotes the observed number of events in bin i, $\mu s_i(\boldsymbol{\theta})$ and $b_i(\boldsymbol{\theta})$ are the expected signal with signal strength μ and background yields in bin i, respectively, and N is the total number of bins. The dependence on the nuisance parameters allows systematic uncertainties to be incorporated into the fit model. For example, a normalisation uncertainty might scale s_i or b_i by a factor, while a shape uncertainty might alter the distribution of events among bins. For both analyses in this thesis, as well as for most analyses in ATLAS, the likelihood function is constructed using HistFactory [192] and RooStats [193] and minimisation and uncertainty estimation is done with RooFit [194] using Minuit [195].

The likelihood can be extended to include multiple analysis channels and regions. In this case, an additional multiplicative factor is introduced for each channel and region, such that the full likelihood factorises over the number of channels, regions, and bins. The same POI is typically shared across channels, while some nuisance parameters are correlated between channels and others are channel-specific. Maximising the likelihood with respect to all parameters yields the best fit values $\hat{\mu}$ and $\hat{\boldsymbol{\theta}}$. In practice, however, the interest is usually in the POI, while the nuisance parameters are treated as a means of incorporating systematic uncertainties. This is handled by the profile likelihood.

7.2 Parameter estimation and uncertainties

In the presence of nuisance parameters, the dependence of the likelihood on μ is studied using the profile likelihood. The profile likelihood function is defined as:

$$L_p(\mu) = L\big(\mu, \hat{\boldsymbol{\theta}}(\mu)\big), \tag{7.2}$$

where $\hat{\boldsymbol{\theta}}(\mu)$ are the conditional maximum likelihood estimates of the nuisance parameters for each fixed value of μ.

The best fit value $\hat{\mu}$ corresponds to the value of μ that maximises the profile likelihood. In practice, it is more convenient to work with the negative logarithm of the likelihood, such that the estimation problem becomes a minimisation problem. The minimum of $-\ln L_p(\mu)$ corresponds to the maximum of $L_p(\mu)$.

The uncertainty on $\hat{\mu}$ is extracted by examining the shape of the profile likelihood around its minimum. Under the assumption that the likelihood behaves approximately Gaussian near the best fit value, the confidence intervals can be constructed using Wilks' theorem. This states that, for large samples, the test statistic $q(\mu)$:

$$q(\mu) = -2 \ln \frac{L_p(\mu)}{L_p(\hat{\mu})}, \tag{7.3}$$

asymptotically follows a χ^2 distribution with one degree of freedom [196].

In particular, the 68% confidence interval is defined by the values of μ where:

$$-2\Delta \ln L_p(\mu) = 1. \tag{7.4}$$

Similarly, the 95% confidence interval is defined by where μ gives:

$$-2\Delta \ln L_p(\mu) = 3.84. \tag{7.5}$$

These thresholds follow from the properties of the χ^2 distribution. A value of $q(\mu) = 1$ corresponds to the 68% quantile, and $q(\mu) = 3.84$ corresponds to the 95% quantile for one degree of freedom. In practical terms, the profile likelihood is scanned as a function of μ, and the 68% confidence level interval corresponding to an uncertainty at 1σ is determined by identifying the points where $-\Delta \ln L_p(\mu) = 1/2$ relative to the best fit $\hat{\mu}$. Similarly, the 95% confidence interval is obtained by identifying the points where $-\Delta \ln L_p(\mu) = 1.92$. Systematic uncertainties, encoded via the profiled nuisance parameters $\hat{\boldsymbol{\theta}}(\mu)$ for each μ, broaden the profile likelihood curve. In this way, the uncertainties on the nuisance parameters are propagated to the POI and are reflected in the total uncertainty with $\hat{\mu} \pm \sigma_\mu$.

An example of the application of the profile likelihood method can be found in the combined Higgs boson mass measurement performed by ATLAS and CMS during Run 1, using the $H \to \gamma\gamma$ and $H \to 4\ell$ channels. The corresponding scan of the test statistic is shown in Figure 7.1, with the POI identified as the Higgs boson mass $\mu = m_H$. The curve is defined in terms of the profile likelihood ratio test statistic $q(\mu) = -2 \ln \Lambda(m_H) = -2 \ln (L(m_H)/L(\hat{m}_H))$, where $L(m_H)$ is the profile likelihood evaluated at a given mass hypothesis. The minimum of the curve occurs at $\hat{m}_H = 125.09$ GeV. The uncertainty on the measurement is obtained by identifying the values of m_H where the curve intersects fixed thresholds corresponding to confidence levels. Specifically, the 68% confidence interval is approximated at $q(\mu) = 1$, and the 95% confidence interval* is approximated at $q(\mu) = 4$. From these intersections, the uncertainty on the Higgs boson mass is determined to be 125.09 ± 0.24 GeV at 95% confidence level. The figure also illustrates two important effects. The inclusion

*Strictly speaking, $q(\mu) = 4$ corresponds to the 95.45% confidence interval, i.e. 2σ. The exact 95% confidence interval corresponds to 1.96σ, or $q(\mu) \approx 3.84$.

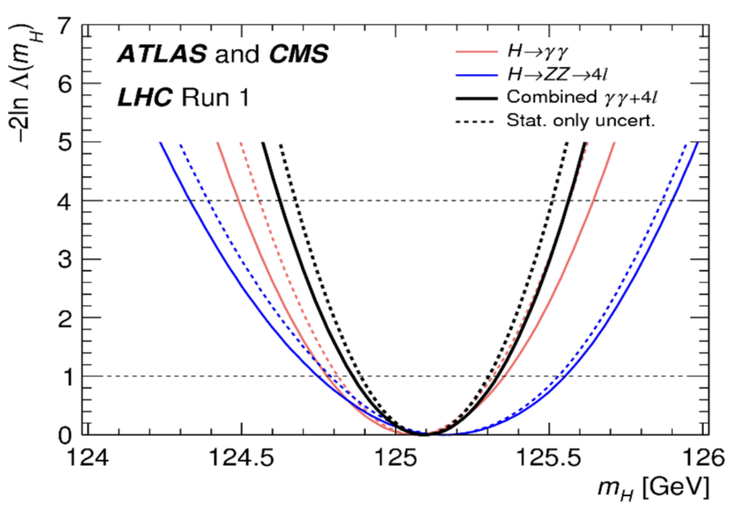

Figure 7.1: Measurement of the Higgs boson mass by the ATLAS and CMS experiments in $H \to \gamma\gamma$ and $H \to 4\ell$ during Run 1 using the formalism described above. The POI is set as the Higgs mass $\mu = m_H$ and the test statistic $q(\mu) = -2\ln\Lambda(m_H) = -2\ln(L(m_H)/L(\hat{m}_H))$. The solid lines shows the measurements with systematic uncertainties (black is combined), and the dashed lines shows the measurement without systematic uncertainties. Approximate 68% and 95% confidence intervals are drawn where there curve intersects with 1 and 4 respectively [197].

of multiple analysis channels improves the sensitivity, leading to a narrower ΔNLL curve, while the inclusion of systematic uncertainties broadens the curve, resulting in a larger overall uncertainty on the POI.

A similar statistical procedure will also be applied for the measurement of the EFT parameters $\tilde{d}$ and $c_{H\tilde{W}}$ in the VBF CP analysis detailed in Chapter 8. It should be noted that some modifications are necessary to adapt the approach from a normalisation measurement of signal strength μ to a shape-dependent fit. These adaptations will be discussed in Section 8.7 when introducing the fit model.

7.3 Hypothesis testing

In the previous section, the profile likelihood function was introduced and used for parameter estimation of model parameters. Hypothesis testing concerns the statistical evaluation of specific signal hypotheses, applying the profile likelihood ratio to either test the presence of a signal or constrain it by setting exclusion limits. In particle physics analyses, this is typically formulated by defining a null hypothesis H_0 and an alternative hypothesis H_1, and constructing a test statistic based on $L_p(\mu)$ to distinguish between them. Two important scenarios are considered: testing the background-only hypothesis against the presence of a new physics signal (discovery), and testing a specific signal-plus-background hypothesis to set upper limits on the signal strength (exclusion).

For a discovery search, the null hypothesis H_0 corresponds to the background-only model (no signal), typically associated with $\mu = 0$ if μ represents the signal strength parameter, while the alternative hypothesis H_1 corresponds to the signal-plus-background model with $\mu > 0$. The objective is to assess whether the observed data is incompatible with H_0 in favour of H_1, with the signature of discovery being an excess of events above the background expectation.

The compatibility of the data and the background-only hypothesis is quantified using the test statistic q_0, defined as:

$$q_0 = -2 \ln \frac{L_p(\mu = 0)}{L_p(\hat{\mu})}, \tag{7.6}$$

where $L_p(0)$ is the profile likelihood evaluated at $\mu = 0$, and $L_p(\hat{\mu})$ is the maximum profile likelihood at the best fit signal strength $\hat{\mu}$. By construction, $q_0 \geq 0$, and larger values of q_0 indicate greater incompatibility with the background-only hypothesis. In the context of discovery, only positive values of μ are considered, since the presence of a signal is expected to lead to an excess. If the best fit $\hat{\mu}$ is negative, it is set to zero, resulting in $q_0 = 0$. Therefore, q_0 acts as a one-sided profile likelihood ratio statistic for testing $H_0 : \mu = 0$ against $H_1 : \mu > 0$.

Given an observed value q_0^{obs}, the p-value for the background-only hypothesis is defined as:

$$p_0 = P(q_0 \geq q_0^{\text{obs}}), \tag{7.7}$$

representing the probability that background-only would produce a test statistic at least as large as that observed. A small p_0 indicates that the background-only hypothesis is incompatible with data. It is customary to convert the p-value into a significance Z, expressed in units of standard deviations, using:

$$Z = \Phi^{-1}(1 - p_0), \tag{7.8}$$

where Φ^{-1} is the inverse cumulative distribution function of the standard normal distribution. For example, a $p_0 = 2.87 \times 10^{-7}$ corresponds to a significance of $Z = 5$, the conventional threshold for claiming discovery in particle physics.

For exclusion tests, the roles of the hypotheses are reversed. The null hypothesis H_0 is taken to be the signal-plus-background model with a some signal strength μ, while the alternative hypothesis H_1 corresponds to the background-only model. The aim is to assess whether the data is more compatible with background-only hypothesis, leading to the exclusion of the considered μ. The test statistic for exclusion is defined as:

$$q_\mu = -2 \ln \frac{L_p(\mu)}{L_p(\hat{\mu})}, \tag{7.9}$$

where $L_p(\mu)$ is the profile likelihood evaluated at the fixed signal strength μ, and $L_p(\hat{\mu})$ is the maximum profile likelihood at the best fit value $\hat{\mu}$. When setting limits, only deficits in the fitted signal strength relative to the tested value should be used as evidence against the hypothesis. If the best fit signal strength $\hat{\mu}$ is greater than the tested value μ, the data indicate a preference for an even larger signal and cannot be interpreted as evidence to exclude μ. In this case, the test statistic is set to zero by definition. This procedure ensures that only downward fluctuations reduce the compatibility between the data and the tested hypothesis, leading to the definition of the modified one-sided test statistic:

$$\tilde{q}_\mu = \begin{cases} -2\ln\frac{L_p(\mu)}{L_p(\hat{\mu})}, & \text{if } \hat{\mu} \leq \mu, \\ 0, & \text{if } \hat{\mu} > \mu. \end{cases} \tag{7.10}$$

By construction, $\tilde{q}_\mu \geq 0$, and larger values indicate greater incompatibility between the data and the signal-plus-background hypothesis at the tested signal strength. For a given μ, the corresponding p-value is defined as:

$$p_{s+b}(\mu) = P(q_\mu \geq q_\mu^{\text{obs}}), \tag{7.11}$$

where the probability is computed under the assumption that the signal is present with strength μ. This p-value quantifies the probability of observing a test statistic at least as incompatible with the signal hypothesis as the value obtained from the data. In general statistical terms a hypothesis is excluded at 95% confidence level if $p_{s+b} < 0.05$.

However, exclusion based solely on p_{s+b} can be misleading if the analysis has limited sensitivity to a signal. In particular, downward fluctuations of the background can artificially produce small p_{s+b} values even when the data is fully consistent with the background-only hypothesis. In such cases, a signal hypothesis could be excluded even if the analysis does not have sensitivity to it. To address this issue, the modified frequentist CL_s method was developed [198]. The CL_s value is defined as:

$$\text{CL}_\text{s} = \frac{p_{s+b}}{1 - p_b}, \tag{7.12}$$

where p_b is the p-value for the background-only hypothesis. If the analysis has little sensitivity, $1 - p_b$ becomes small, inflating CL_s and preventing false exclusions. CL_s therefore ensures that a signal hypothesis is only excluded if the data provide genuine sensitivity to distinguish it from the background. A signal hypothesis is excluded at 95% confidence level if $\text{CL}_\text{s} < 0.05$. The 95% CL upper limit on μ is the largest signal strength for which this condition holds.

In the case of multiple signal hypotheses, the CL_s value can be computed for each signal point to form an exclusion contour. This prescription is applied in the mono-Higgs analysis in Chapter 9 when setting limits on the 2HDM+a model.

7.4 The Asimov dataset and expected sensitivity

To evaluate the expected sensitivity of an analysis without relying on real data, the Asimov dataset provides a powerful tool [191]. The Asimov dataset is a constructed pseudo-dataset in which the observed event counts in each bin are set exactly equal to their expected values under a given hypothesis. This ensures that the best fit parameters match the true parameters used to generate the dataset:

$$\hat{\mu} = \mu, \quad \hat{\boldsymbol{\theta}} = \boldsymbol{\theta}. \tag{7.13}$$

The same profile likelihood procedure can then be applied to the Asimov dataset, enabling the evaluation of the fit model and the expected sensitivity of the analysis. Typically when producing the Asimov dataset, μ is set to 0, and the fit is run assuming that the data behaves according to the background-only hypothesis. Or if μ represents the signal strength for a SM process it is typically set to 1.

Under the Asimov construction, the expected sensitivity of an analysis can also be evaluated analytically using asymptotic approximations based on Wilks' theorem [196]. In particular, the median expected significance for rejecting the background-only hypothesis ($\mu = 0$) in favour of the signal-plus-background hypothesis with $\mu = 1$ is obtained from the Asimov value of q_0. For a simple counting experiment, where s and b denote the expected number of signal and background events respectively, the median expected discovery significance is given by:

$$\text{median } Z_0 = \sqrt{2\left((s+b)\ln\left(1+\frac{s}{b}\right) - s\right)}. \tag{7.14}$$

This formula assumes that the background expectation b is perfectly known. In the presence of background uncertainties, characterized by a variance θ_b^2, the expected significance generalises to the so-called Asimov significance:

$$Z_{\mathrm{A}} = \sqrt{2\left((s+b)\ln\left[\frac{(s+b)(b+\theta_b^2)}{b^2+(s+b)\theta_b^2}\right] - \frac{b^2}{\theta_b^2}\ln\left[1+\frac{s\theta_b^2}{b^2+b\theta_b^2}\right]\right)}. \tag{7.15}$$

7.5 Systematic and Statistical Uncertainties

In order to constrain the nuisance parameters within physically reasonable ranges, additional constraint terms are introduced into the likelihood. These constraints act as prior probability density functions for the nuisance parameters, reflecting independent estimates of the size of each systematic uncertainty. Typically, each θ_k is assumed to follow a standard normal distribution centred at zero with unit width, so that $\theta_k = \pm 1$ corresponds to a 1σ variation. The likelihood function is then extended to include the product of all such constraint terms.

The full likelihood can then be written as

$$L(\mu, \boldsymbol{\theta}) = \prod_{i=1}^{N_{\text{bins}}} \text{Pois}\Big(n_i^{\text{obs}} \,\Big|\, n_i^{\text{exp}}(\mu, \boldsymbol{\theta})\Big) \;\times\; \prod_k G(\theta_k)\,, \tag{7.16}$$

where $G(\theta_k)$ denotes the unit Gaussian function used as the constraint for θ_k:

$$G(\theta_k) = \frac{1}{\sqrt{2\pi}} e^{-\theta_k^2/2}. \tag{7.17}$$

Moving θ_k away from its nominal value $\theta_k^0 = 0$ penalises the likelihood, with larger shifts being increasingly suppressed. In this way, the nuisance parameter in the fit will typically stay within the uncertainty range unless the data provide a strong global indication that the overall event rate is inconsistent with the nominal value. Two types of systematic effects are typically handled by the nuisance parameters. These are pure normalisation uncertainties, which affect the overall rate of a process uniformly across all bins, and shape uncertainties, which alter the relative yields in different bins, thereby changing the shape.

In addition to systematic uncertainties, statistical uncertainties from the finite size of MC samples are incorporated into the likelihood model. Limited simulated statistics in individual bins introduce uncertainties in the predicted yields, especially in regions with low event counts. To model this, a set of auxiliary nuisance parameters $\{\gamma_i\}$ is introduced, where each γ_i represents the statistical precision of the MC estimate in bin i. The expected yield in that bin is scaled by γ_i, and a constraint term is applied to keep it near unity, consistent with the statistical uncertainty.

Unlike systematic effects, these uncertainties are not modelled with Gaussian constraints. Instead, a Poisson distribution is used, based on the effective number of simulated events in bin i, defined as $m_i = (n_i/\delta_i)^2$, where n_i is the predicted yield and δ_i its statistical uncertainty [192]. The corresponding constraint term takes the form:

$$P(m_i \,|\, \gamma_i m_i) = \frac{(\gamma_i m_i)^{m_i}}{m_i!} e^{-\gamma_i m_i} \;, \tag{7.18}$$

with γ_i having a nominal value of 1. Since statistical fluctuations are uncorrelated, a separate γ_i is assigned to each bin.

In addition to nuisance parameters associated with systematic and statistical uncertainties, normalisation factors (NFs) are included in the fit. NFs are introduced for selected background processes to control their normalisation and calibrate them to data. This is typically done in dedicated regions that are rich in the targeted background process.

7.6 ATLAS fitting strategy

ATLAS analyses typically follow a combined fitting strategy that uses multiple regions of data to constrain backgrounds and search for signals. These regions are generally classified as signal regions (SRs), control regions (CRs), and validation regions (VRs). The statistical model in HistFactory is built to include SRs and CRs in a simultaneous likelihood fit, while VRs are generally used for cross-checks.

Signal Regions (SRs): An important part of the analysis strategy is to know where to look. The typical approach is therefore to define a region of phase space where the effect of the considered signal is expected to be noticeable. These regions are referred to as signal regions, and are typically defined by setting requirements on kinematic variables and/or the output score of a multivariate algorithm. The requirements are chosen to maximise the expected signal-to-background ratio or some related metric. Following ATLAS policies, the data in the signal regions is "blinded" when doing the optimisation. That means that the analysis should demonstrate that the background modelling and effects from systematic uncertainties is well understood before looking at data. Only when the analysis strategy is completed and validated, the SRs becomes "unblinded". This is done to avoid bias from potential statistical fluctuations in data that might influence the SR definitions.

Control regions (CRs): Since the aim of the SR requirements is to maximise sensitivity, they are often characterised by reduced background yields. Dedicated CRs are therefore typically defined for specific background processes to both check and correct any potential background mismodelling. These regions are constructed to have high purity of the targeted background process and minimal signal contamination. The background modelling can then be calibrated to data in the CRs, and any observed discrepancies can be corrected and propagated to the SRs through the fit via NFs.

Validation regions (VRs): To ensure that the extrapolation of NFs from the CRs to the SRs is reliable, dedicated validation regions are typically defined. These regions are designed to be kinematically closer to the SRs while still maintaining a low expected signal contribution. The VRs do not contribute to the fit directly. However, the effects of the fit, including the constraints and NFs derived from the CRs, are propagated to them. A good agreement between the post-fit prediction and the observed data in the VRs provides confidence in the background modelling and extrapolation strategy.

Part III

Analyses

Chapter 8

Searching for anomalous CP-odd couplings in VBF Higgs production

This chapter describes a test of CP invariance in Higgs boson production via vector-boson fusion performed in the $H \to \tau\tau$ channel. A direct measurement of EFT parameters is performed with interpretation in both the HISZ and Warsaw basis using the Optimal Observable method discussed in Chapter 3. This is an enhancement of the partial Run 2 36.1 fb^{-1} ATLAS analysis [51] published in 2020 with additional interpretations in the Warsaw basis.

Decays of two τ-leptons are classified into three final states: the $\tau_\ell\tau_\ell$ Different Flavour (DF), $\tau_\ell\tau_h$ and $\tau_h\tau_h$ channel, where the subscript specifies if the τ decayed leptonically or hadronically. The $\tau_\ell\tau_\ell$ Same Flavour (SF) channel was discarded as it provided minimal sensitivity due to the difficulty of separating these events from $Z \to \ell\ell$ events. Hence, the $\tau_\ell\tau_\ell$ DF channel corresponding to $\tau_e\tau_\mu$ and $\tau_\mu\tau_e$ will be written as $\tau_\ell\tau_\ell$ in the following unless stated otherwise. The branching factions of the different decay channels is shown in Figure 8.1.

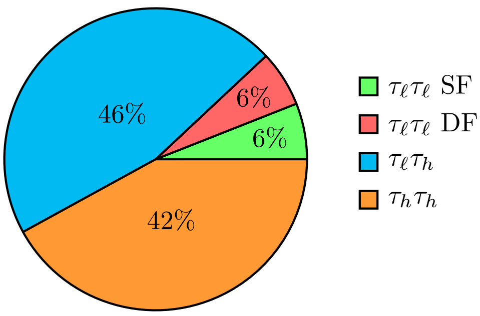

Figure 8.1: Branching fractions of the di-τ decay into different channels. The $\tau_\ell\tau_\ell$ DF is not considered in the analysis.

While the signal process is independent of the decay channels, the background composition varies greatly and depends on the channel. Therefore, they are treated separately and then combined. The following sections will detail the general analysis strategy with particular focus on the $\tau_\ell\tau_\ell$ channel and also describe the statistical combination of the three channels. In the end a comparison with other ATLAS results will be discussed. The signal considered in this analysis is the VBF $H \to \tau\tau$ process, as well as the VBF $H \to WW \to \ell\nu\ell\nu$ process. The latter only has significant contribution in the $\tau_\ell\tau_\ell$ channel due to the leptons in the final state.

8.1 Data and simulated samples

8.1.1 Data

This analysis uses the full Run 2 dataset collected by the ATLAS detector the LHC, produced from proton-proton collisions at a centre-of-mass energy of $\sqrt{s} = 13\,\text{TeV}$. Events are selected only if they were recorded under stable beam conditions where all relevant detector subsystems were in good operating condition [199], and pass data-quality requirements. This corresponds to a total integrated luminosity of 140.1 ± 1.2 fb^{-1} [200].

8.1.2 Simulated samples

Common MC samples are produced centrally within the HIGP leptons subgroup in ATLAS and have been used in several recent $H \to \tau\tau$ analyses [201, 202].

The Z+jets and W+jets processes are simulated with Sherpa 2.2.1 [203] using NNLO-accurate matrix elements matched to the Sherpa parton shower [204], with the NNPDF3.0nnlo [205] PDF set and a dedicated tune. Electroweak V+jets production is modelled using Sherpa 2.2.11 with LO matrix elements and the NNPDF3.0nnlo PDF set.

$t\bar{t}$ and single-top processes are generated with Powheg Box v2 [206] interfaced to Pythia 8.230 [207] for parton showering and hadronisation, using the A14 tune. The matrix elements use the NNPDF3.0nlo set, while parton showering uses the NNPDF2.3lo PDF set. Diboson processes are simulated with Sherpa 2.2.2 at NLO accuracy using the NNPDF3.0nnlo PDF set and the standard Sherpa tune.

Pile-up effects are modelled by overlaying the simulated hard-scattering events with minimum-bias proton–proton collisions generated with Pythia 8.186 using the A3 tune and the NNPDF2.3lo PDF set [208].

Higgs boson production via ggF and VBF is simulated with Powheg Box v2 interfaced to Pythia 8 for parton showering and hadronisation, using the AZNLO tune and the PDF4LHC15nnlo [209] PDF set. ggF production is simulated at NNLO accuracy, and VBF production at NLO accuracy. VH production is simulated using Powheg Box v2 interfaced with Pythia 8 with the AZNLO tune, and normalised to NNLO cross-sections. The $t\bar{t}H$ process is modelled with Powheg Box v2 interfaced to Pythia 8.230, using the A14 tune. Matrix elements are generated with the NNPDF3.0nlo PDF set, and the parton shower uses NNPDF2.3lo. tHq production is simulated with MadGraph5_aMC@NLO 2.6.0 interfaced to Pythia 8.230, using the A14 tune and the same PDF configuration as for $t\bar{t}H$.

The normalisation of all Higgs boson samples includes higher-order QCD and electroweak corrections where available, and branching ratios are taken from HDECAY[47, 210] and Prophecy4f [45, 46]. A summary of the MC generators used for all simulated processes is provided in Table 8.1.

Process	Generator		PDF set		Tune	Order
	ME	PS	ME	PS		
Backgrounds						
V+jets	Sherpa 2.2.1		NNPDF3.0nnlo		Sherpa	NNLO
EWK V+jets	Sherpa 2.2.11		NNPDF3.0nnlo		Sherpa	LO
$t\bar{t}$	Powheg	Pythia 8	NNPDF3.0nlo	NNPDF2.3lo	A14	NLO
Single top	Powheg	Pythia 8	NNPDF3.0nlo	NNPDF2.3lo	A14	NLO
Diboson	Sherpa 2.2.2		NNPDF3.0nnlo		Sherpa	NLO
Higgs						
VBF	Powheg	Pythia 8	PDF4LHC15nnlo	CTEQ6L1	AZNLO	NNLO
ggF	Powheg	Pythia 8	PDF4LHC15nnlo	CTEQ6L1	AZNLO	NNLO
VH	Powheg	Pythia 8	PDF4LHC15nnlo	CTEQ6L1	AZNLO	NNLO
$t\bar{t}H$	Powheg	Pythia 8	NNPDF3.0nlo	NNPDF2.3lo	A14	NLO
tHq	MadGraph5_aMC@NLO 2.6.0	Pythia 8.230	NNPDF3.0nlo	NNPDF2.3lo	A14	NLO

Table 8.1: Summary of nominal samples used in the analysis. The VBF Higgs samples are considered signal in the analysis.

8.1.3 Signal reweighing procedure

The nominal VBF $H \to \tau\tau$ samples are simulated under the SM hypothesis and do not include explicit information about CP-odd couplings. The goal of this analysis is to determine which values of the CP-violating EFT parameters best describe the data. Various scenarios need to be tested across a wide range of parameter values. While these can be generated, doing so would be computationally expensive as it requires simulation of events over small intervals of these parameters. Therefore, a reweighting procedure using the nominal Powheg +Pythia 8 SM VBF samples is employed. This approach not only saves time and reduces cost but also provides more flexibility, allowing for arbitrary values of the EFT parameters to be obtained.

HISZ basis reweighting

The reweighting procedure for different values of $\tilde{d}$ is derived from the matrix elements in Eq. 3.18, defined as the ratio of the matrix element with $\tilde{d} \neq 0$ to the SM matrix element with $\tilde{d} = 0$:

$$w(\tilde{d}) = \frac{|\mathcal{M}|^2}{|\mathcal{M}_{\rm SM}|^2} = 1 + \tilde{d} \cdot \underbrace{\frac{2RE\left(\mathcal{M}^*_{\rm SM}\mathcal{M}_{\rm CP-\ odd}\right)}{|\mathcal{M}_{\rm SM}|^2}}_{\rm w_{lin}} + \tilde{d}^2 \cdot \underbrace{\frac{|\mathcal{M}_{\rm CP-\ odd}|^2}{|\mathcal{M}_{\rm SM}|^2}}_{\rm w_{quad}}. \tag{8.1}$$

Here, $w_{\rm lin}$ represents the linear weight, proportional to the interference term, while $w_{\rm quad}$ corresponds to the quadratic weight, proportional to the CP-odd squared term. As with the Optimal Observable described in Section 3.3.1, the matrix elements are computed using the HAWK framework [82–84]. For reweighting, HAWK takes inputs from each event's truth record, specifically the flavour of incoming and outgoing partons, the four-vector of the outgoing Higgs boson, and the Bjorken x values of the initial partons. This computation is performed once per event and can then later be scaled by the desired $\tilde{d}$ value to obtain a target CP-odd scenario.

To validate the reweighting procedure samples are also generated with MadGraph5_aMC@NLO using the Higgs Characterisation (HC) model [211]. This model uses a slightly different parametrisation than the HISZ basis which is implemented in HAWK. The effective Lagrangian is expressed as follows:

$$\begin{aligned}
\mathcal{L}^M_{eff} = \Bigg\{ & c_\alpha \kappa_{\rm SM} \left[\frac{1}{2} g_{HZZ} Z_\mu Z^\mu + g_{HWW} W^+_\mu W^{-\mu}\right] \\
& - \frac{1}{4}\left[c_\alpha \kappa_{H\gamma\gamma} g_{H\gamma\gamma} A_{\mu\nu} A^{\mu\nu} + s_\alpha \kappa_{A\gamma\gamma} g_{A\gamma\gamma} A_{\mu\nu} \tilde{A}^{\mu\nu}\right] \\
& - \frac{1}{2}\left[c_\alpha \kappa_{HZ\gamma} g_{HZ\gamma} Z_{\mu\nu} A^{\mu\nu} + s_\alpha \kappa_{AZ\gamma} g_{AZ\gamma} Z_{\mu\nu} \tilde{A}^{\mu\nu}\right] \\
& - \frac{1}{4}\left[c_\alpha \kappa_{Hgg} g_{Hgg} G^a_{\mu\nu} G^{a,\mu\nu} + s_\alpha \kappa_{Agg} g_{Agg} {}^{a}_{\mu\nu} \tilde{A}^{a,\mu\nu}\right] \\
& - \frac{1}{4\Lambda}\left[c_\alpha \kappa_{HZZ} Z_{\mu\nu} Z^{\mu\nu} + s_\alpha \kappa_{AZZ} Z_{\mu\nu} \tilde{Z}^{\mu\nu}\right] \\
& - \frac{1}{2\Lambda}\left[c_\alpha \kappa_{HW} W^+_{\mu\nu} W^{-\mu\nu} + s_\alpha \kappa_{AWW} W^+_{\mu\nu} \tilde{W}^{-\mu\nu}\right] \\
& - \frac{1}{\Lambda} c_\alpha \left[\kappa_{H\partial\gamma} Z_\nu \partial_\mu A^{\mu\nu} + \kappa_{H\partial Z} Z_\nu \partial_\mu Z^{\mu\nu} + \left(\kappa_{H\partial W} W^+_\nu \partial_\mu W^{-\mu\nu} + \text{ h.c. }\right)\right] \Bigg\} H,
\end{aligned} \tag{8.2}$$

where the mixing angle α between CP-even and CP-odd Higgs states is represented by $c_\alpha = \cos\alpha$ and $s_\alpha = \sin\alpha$. The parameters g and κ determines the strength of the HVV couplings, with the subscript A or H corresponding to the CP-odd and CP-even couplings to vector bosons, respectively. The κ parameters are dimensionless, and is set by the user as model inputs in MadGraph5_aMC@NLO . The model should be able to reproduce the the SM couplings while also allowing for additional CP-odd couplings. This can be achieved by setting $c_\alpha = 0.6$ and $\kappa_{SM} = 5/3$, implying $s_\alpha = 0.8$. Note that in the pure SM case $c_\alpha = 1.0$ and $k_{SM} = 1.0$. In the HISZ basis the $HZ\gamma$ coupling vanishes when enforcing the constraint $\tilde{d} = \tilde{d}_B$. Hence, κ_{AZZ}, κ_{AWW} and $\kappa_{A\gamma\gamma}$ are the only parameters in the HC model that are affected by variations in $\tilde{d}$. To translate between the two parametrisations the following relations are used:

$$\begin{aligned}\kappa_{AZZ} = \kappa_{AWW} &= -\frac{2g\Lambda}{m_W s_\alpha}\tilde{d},\\ \kappa_{A\gamma\gamma} &= -\frac{3\pi v g}{2m_W s_\alpha \alpha_{\mathrm{EM}}}\tilde{d}.\end{aligned} \tag{8.3}$$

Three CP-odd scenarios are generated this way, for $\tilde{d} = 0.1$, $\tilde{d} = -0.2$ and $\tilde{d} = 0.6$, which are then used to validate the reweighing model by comparing their distributions in the Optimal Observable. Table 8.2 shows the model parameter used for generating events with $\tilde{d} = 0.1$.

Parameter	Value
Cut off scale	$\Lambda = 1000$ GeV
Cosine of mixing angle	$\cos\alpha = 0.6$
SM coupling parameter	$\kappa_{\mathrm{SM}} = 5/3$
Coupling parameter for AWW vertex	$\kappa_{AWW} = -1.98$
Coupling parameter for AZZ vertex	$\kappa_{AZZ} = -1.98$
Coupling parameter for $A\gamma\gamma$ vertex	$\kappa_{A\gamma\gamma} = -151.5$
Coupling parameter for $AZ\gamma$ vertex	$\kappa_{AZ\gamma} = 0$

Table 8.2: Parameters used in the HC model to generate events for $\tilde{d} = 0.1$. All other anomalous couplings are set to 0.

Figure 8.2 shows the corresponding distributions in the Optimal Observable for both generated and reweighted events. The close agreement observed across the the three distributions confirms the validity of the reweighting procedure, demonstrating that the reweighted events accurately reproduce the expected shape and behaviour of the CP-odd couplings in the Optimal Observable.

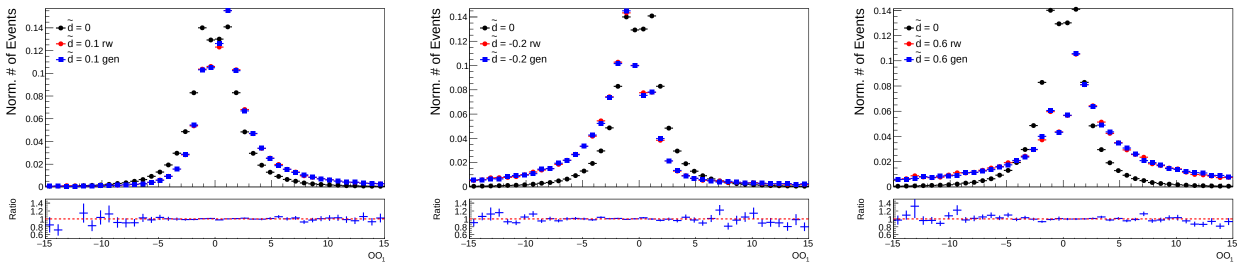

a) $\tilde{d} = 0.1$ b) $\tilde{d} = -0.2$ c) $\tilde{d} = 0.6$

Figure 8.2: Optimal Observable distribution showing SM (black), SM reweighted to BSM (red) and generated BSM (blue) events for different values of $\tilde{d}$.

Warsaw basis reweighting

Since HAWK is designed for the HISZ basis, it is not technically possible to apply the same reweighting procedure in the Warsaw basis. As discussed in Section 3.2.2, a conversion between the two bases is possible under specific conditions, namely setting $c_{H\tilde{W}} = c_{H\tilde{B}}$ and $c_{HB\tilde{W}} = 0$. However, in this analysis the Warsaw basis coefficients are treated as three distinct and separate EFT parameters, so the assumptions from the HISZ basis do not apply.

Instead of using Eq. 8.1, reweighting is performed using samples generated with the SMEFTsim package in MadGraph [212], which allows direct specification of Warsaw basis parameter values. A similar reweighting method to what is explained here was done in the VBF CP $H \to \gamma\gamma$ analysis [53]. Samples are generated for all three CP-odd Wilson coefficients ($c_{H\tilde{W}}$, $c_{H\tilde{B}}$, and $c_{HB\tilde{W}}$), varying one parameter at a time while keeping the others at zero. It is worth noting again that there is little to no sensitivity to $c_{H\tilde{B}}$ and $c_{HB\tilde{W}}$, as VBF production is dominated by the HWW vertex. Therefore, the following discussion focuses on the $c_{H\tilde{W}}$, although the same procedure applies to the other two parameters. The reweighting is carried out using correction factors (k) obtained from the ratio of BSM ($c_{H\tilde{W}} \neq 0$) to SM ($c_{H\tilde{W}} = 0$) generated events with SMEFTsim, as a function of the Optimal Observable:

$$k = \frac{d\sigma/dOO\,(c_{H\tilde{W}} \neq 0)}{d\sigma/dOO\,(c_{H\tilde{W}} = 0)}. \tag{8.4}$$

28 signal points are generated for $c_{H\tilde{W}}$ between -7 and 7, with smaller intervals closer to 0. The correction factor is then computed for different bins (bin width 1) of the Optimal Observable and then fitted with a parabolic function in each bin. This parabolic function has the form:

$$w(c_{H\tilde{W}}) = p_0 + c_{H\tilde{W}} \cdot \underbrace{p_1(OO)}_{w_{\text{lin}}} + c^2_{H\tilde{W}} \cdot \underbrace{p_2(OO)}_{w_{\text{quad}}}, \tag{8.5}$$

where p_0 is a constant term, p_1 is a linear term and p_2 is a quadratic term. The form of the reweighting is similar to Eq. 8.1 in the HISZ basis.

This way any value of $c_{H\tilde{W}}$ can be obtained from the best fit values for the parameters as a function of the Optimal Observable. Figure 8.3 shows the k-factor computed for the 28 generated $c_{H\tilde{W}}$ points, which is fitted to the parabolic function in Eq. 8.5. This gives one value for each of the three terms per bin of the Optimal Observable.

The final linear and quadratic terms in Eq. 8.5 are defined by the best fit values of p_i as a function of OO. The fitted curves for the three terms in the Optimal Observable are shown in Figure 8.4.

The reweighting is validated by comparing generated and reweighted samples of $c_{H\tilde{W}}$ in the Optimal Observable. This is shown for CP-odd scenarios with $c_{H\tilde{W}} = 0.4$, $c_{H\tilde{W}} = 2.0$ and $c_{H\tilde{W}} = -1.0$ in Figure 8.5. Also in the Warsaw basis good closure is observed between generated and reweighted distributions for multiple values of $c_{H\tilde{W}}$.

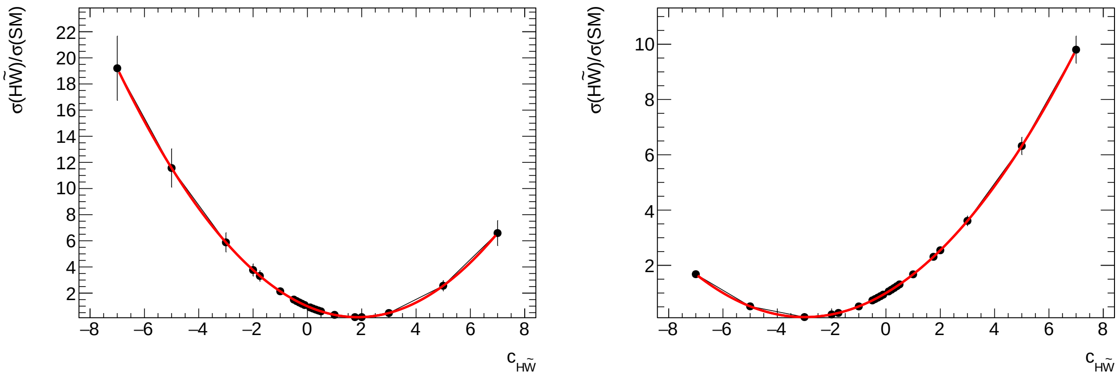

a) $OO_1 \in [-6, -5]$ b) $OO_1 \in [3, 4]$

Figure 8.3: Ratio of the cross-section for SM ($c_{H\tilde{W}} = 0$) and CP-odd scenarios ($c_{H\tilde{W}} \neq 0$) with different values of $c_{H\tilde{W}}$ ranging from -7 to 7 in different bins of the Optimal Observable. Results are obtained with $-6 < OO_1 < -5$ (left) and $3 < OO_1 < 4$ (right). The red curve is a parabolic function fitted to the correction factor computed for each generated signal point of $c_{H\tilde{W}}$.

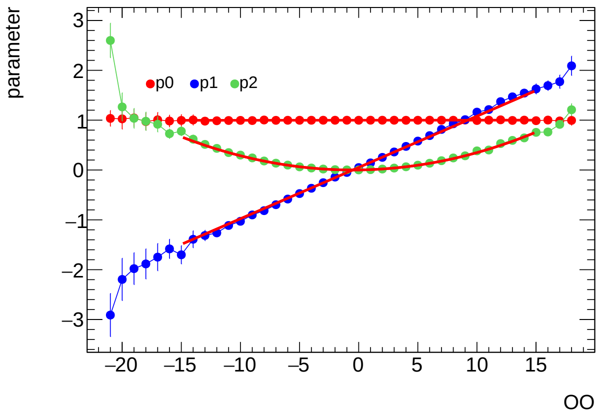

Figure 8.4: The three terms used for the reweighting as a function of the Optimal Observable. The constant term p_0 (red), the linear term p_1 (blue) and the quadratic term p_2 (green), are all fitted with respective functions. The best fit values are used for the final reweighting.

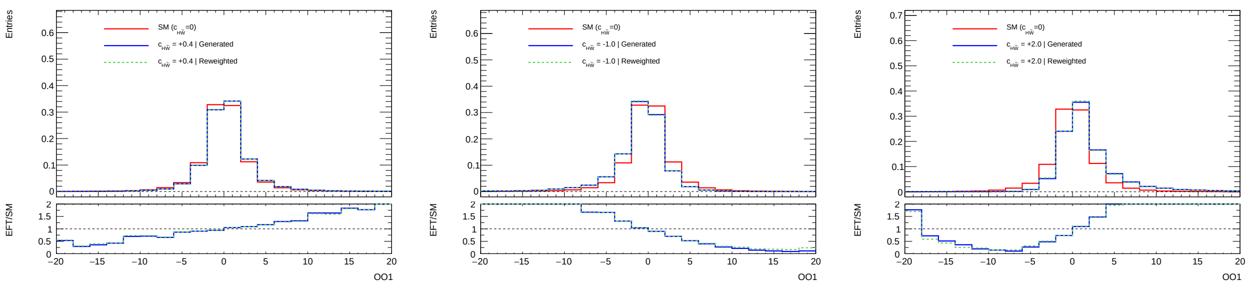

a) $c_{H\tilde{W}} = 0.4$ b) $c_{H\tilde{W}} = 2.0$ c) $c_{H\tilde{W}} = -1.0$

Figure 8.5: Optimal Observable distribution showing SM (red), SM reweighted to BSM (green) and generated BSM (blue) events for different values of $c_{H\tilde{W}}$. The lower panel shows the ratio of both the generated and simulated BSM to SM.

8.2 Object definitions

The physics objects used in this analysis are reconstructed and calibrated according to the procedures described in Chapter 6. The definitions used in this analysis generally follow what is described in Ref. [201]. Most objects have a baseline definition, along with a more strict signal definition. The signal definition corresponds to the objects that are used in the final analysis, while the baseline objects are used for the overlap removal procedure. Any baseline object that is accepted after overlap removal is required to pass the signal requirements. Similar signal definitions are applied across the three analysis channels. A summary of the signal object requirements for each channel can be seen in Table 8.3.

Electrons must satisfy $p_T > 15$ GeV, $|\eta| < 2.47$, and avoid the calorimeter transition region ($1.37 < |\eta| < 1.52$). Baseline electrons must pass the `LooseBlayerLHH` ID WP and the `BadClusterElectron` flag. After overlap removal, they must pass the `Medium` ID WP and the `Loose_VarRad` isolation WP. Muons must satisfy $p_T > 10$ GeV and $|\eta| < 2.47$. Baseline muons pass the `Loose` ID WP. After overlap removal, they must pass the `TightTrackOnly_VarRad` isolation WP. Baseline hadronic τ-leptons are required to have 1 or 3 tracks and satisfy $p_T > 20$ GeV, $|\eta| < 2.47$, avoiding $1.37 < |\eta| < 1.52$. Baseline τ-leptons are required to have a RNN score grater than 0.01, while signal τ-leptons are required to pass the `Medium` ID WP and `Loose` eBDT WP after overlap removal.

Jets are reconstructed using anti-k_t ($R = 0.4$) with PFlow inputs and must satisfy $p_T > 30$ GeV, $|\eta| < 4.4$. Pile-up suppression is applied using the JVT `Tight` WP for jets with $p_T < 60$ GeV and $|\eta| < 2.5$, and fJVT `Loose` WP for $|\eta| > 2.5$. The b-jets are identified using DL1r, using the 85% WP in the $\tau_\ell\tau_\ell$ and $\tau_\ell\tau_h$ channel and 70% WP in the $\tau_h\tau_h$ channel.

Electrons	Signal requirement
Kinematics	$p_{\mathrm{T}} > 15$ GeV
	$\|\eta\| < 2.47$, (excl. $1.37 < \|\eta\| < 1.52$)
Identification	`Medium`
Isolation	`Loose_VarRad`
Muons	**Signal requirement**
Kinematics	$p_{\mathrm{T}} > 10$ GeV and $\|\eta\| < 2.5$
Identification	`Medium`
Isolation	`TightTrackOnly_VarRad`
Impact parameter	$\|d_0/\sigma(d_0)\| < 3$, $\|z_0 \sin\theta\| < 0.5$
Hadronic taus	**Signal requirement**
Kinematics	$p_{\mathrm{T}} > 20$ GeV & $\|\eta\| < 2.47$ (excl. $1.37 < \|\eta\| < 1.52$)
N_{Tracks}	1 or 3 with $p_{\mathrm{T}} > 20$ GeV & $\|\eta\| < 2.47$
Identification	RNN `Medium`
	EBDT `Loose`
Jets	**Signal requirement**
Algorithm	anti-k_t ($R = 0.4$, PFlow)
Kinematics	$p_{\mathrm{T}} > 30$ GeV and $\|\eta\| < 4.4$
Pileup Mitigation	JVT Tight for $p_{\mathrm{T}} < 60$ GeV & $\|\eta\| < 2.5$
	fJVT `Loose` for $p_{\mathrm{T}} < 60$ GeV & $\|\eta\| > 2.5$
b-tagging	DL1r 85% WP (70% $\tau_h\tau_h$)
	$p_{\mathrm{T}} > 20$ GeV and $\|\eta\| < 2.5$

Table 8.3: Summary of the signal definitions for different objects used in the analysis.

8.3 Event selection

The event selection is done in four stages. Events passing the object selection requirements are first assigned to one of the channels: $\tau_\ell\tau_\ell$, $\tau_\ell\tau_h$ and $\tau_h\tau_h$. Dedicated triggers for each channel are employed and a preselection is applied to select events that pass the trigger offline thresholds in a relevant subset of phase space and to ensure orthogonality to other analyses. Events are further selected according to the VBF topology with cuts on the τ-leptons and VBF jets. Finally, to optimise signal sensitivity a neural network classifier is trained separately in each channel to define the SRs that goes into the fit model.

8.3.1 Triggers

The trigger selection is identical to what has been used in other $H \to \tau\tau$ analyses, i.e Ref. [202, 213]. In the $\tau_\ell\tau_\ell$ channel a combination of the single- and di-lepton triggers are used. Trigger matching is required for the for the corresponding leptons selected for the analysis. The lowest unprescaled triggers used in the analysis and corresponding online and offline p_{T} thresholds are summarised in Table 8.4.

Trigger	Running period	HLT trigger name	HLT threshold	Offline threshold

Single-electron	2015
	2016-2018
		`e24_lhmedium_L1EM20VH`, `e60_lhmedium` or `e120_lhloose`
		`e26_lhtight_nod0_ivarloose`, `e60_lhmedium_nod0`
		or `e140_lhloose_nod0`
			$p_{\mathrm{T}}(e) > 24$ GeV
			$p_{\mathrm{T}}(e) > 26$ GeV
				$p_{\mathrm{T}}(e) > 25$ GeV
				$p_{\mathrm{T}}(e) > 27$ GeV

Single-muon	2015 2016-2018	`mu20_iloose_L1MU15` or `mu50` `mu26_ivarmedium` or `mu50`	$p_{\mathrm{T}}(\mu) > 20$ GeV $p_{\mathrm{T}}(\mu) > 26$ GeV	$p_{\mathrm{T}}(\mu) > 21$ GeV $p_{\mathrm{T}}(\mu) > 27.3$ GeV
Electron-muon	2015 2016-2018	`e17_loose_mu14` `e17_lhloose_nod0_mu14`	$p_{\mathrm{T}}(e/\mu) > 17/14$ GeV $p_{\mathrm{T}}(e/\mu) > 17/14$ GeV	$p_{\mathrm{T}}(e/\mu) > 18/14.7$ GeV $p_{\mathrm{T}}(e/\mu) > 18/14.7$ GeV

Table 8.4: Trigger items used in this analysis for the $\tau_\ell\tau_\ell$ channel. The employed trigger logic is a combination of the single-lepton and lepton-triggers. The online and offline p_{T} thresholds are also shown for the different triggers.

The final trigger selection is based on an logical `OR` between the single-electron, single muon and electron-muon triggers, applied together with their corresponding offline p_{T} cuts:

```
trigger = (electron_trigger && pT(e) > threshold_e) ||
(muon_trigger && pT(mu) > threshold_mu) ||
(e-mu_trigger && pT(mu) > threshold_mu_2 && pT(e) > threshold_e_2).
```

This logic along with scale factors used to correct for data/MC discrepancies is handled by the TrigGlobalEfficiencyCorrectionTool maintained by the ATLAS EGAM working group.

8.3.2 Mass estimators

Since the analysis targets the Higgs boson decay, viable mass reconstruction is important for the analysis. The simplest mass estimator is the visible mass of the $\tau-$leptons, defined as:

$$m_{\tau\tau}^{\mathrm{vis}} = \sqrt{(E_\mu + E_e)^2 - (\vec{p}_\mu + \vec{p}_e)^2}, \tag{8.6}$$

where $E_{\mu/e}$ and $\vec{p}_{\mu/e}$ are the energy and momentum of the visible part of the τ-lepton decays. Since the $E_{\mathrm{T}}^{\mathrm{miss}}$ from the neutrinos in the decays are completely neglected the mass distribution is shifted to lower values. One way to include the missing energy is with the collinear approximation [214]. This assumes that the visible part of the decay is collinear with the $E_{\mathrm{T}}^{\mathrm{miss}}$ coming from the neutrinos and that neutrinos are the only source of $E_{\mathrm{T}}^{\mathrm{miss}}$. The collinear approximation x_i is defined as:

$$x_i = \frac{p_{\mathrm{T}_i}^{vis}}{p_{\mathrm{T}_i}^{vis} + p_{\mathrm{T}}^{\mathrm{miss}}}, \tag{8.7}$$

where i corresponds to to lepton i (e/μ) in the $\tau_\ell\tau_\ell$ decay and $p_{\mathrm{T}}^{\mathrm{miss}}$ is the p_{T} of the corresponding neutrino in the decay. The mass of the ditau system can then be calculated as:

$$m_{\tau\tau}^{\mathrm{coll}} = \frac{m_{\tau\tau}^{\mathrm{vis}}}{\sqrt{x_\mu x_e}}. \tag{8.8}$$

A technique that does not depend on the boost of the τ-lepton system is the so-called Missing Mass Calculator (MMC) [85]. This still assumes that neutrinos are the only source of $E_{\mathrm{T}}^{\mathrm{miss}}$, but does not assume collinearity of the decay products. For each event a scan over the possible configurations of the visible and invisible part of the τ-decay is performed in a Markov chain. For each kinematic configuration, the final weight is defined as a log-likelihood of its total probability. The solution with the highest likelihood and largest weight is set as a final estimator for $m_{\tau\tau}^{\mathrm{MMC}}$. Compared to $m_{\tau\tau}^{\mathrm{coll}}$, the MMC provides a mass estimator with reduced high-mass tails, leading to better separation between $H/Z \to \tau\tau$ processes. It is used to reconstruct the Higgs four-momentum necessary for computing the Optimal Observable described in Section 3.3.1. A comparison between the three mass estimators is shown in Figure 8.6.

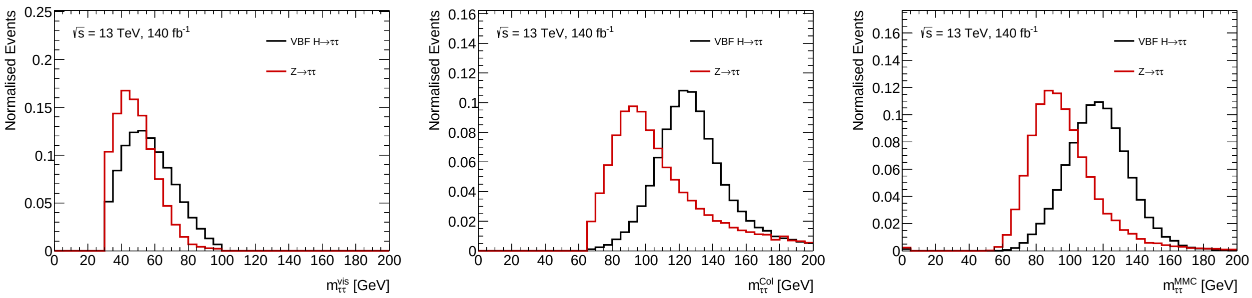

a) $m_{\tau\tau}^{\mathrm{vis}}$ b) $m_{\tau\tau}^{\mathrm{col}}$ c) $m_{\tau\tau}^{\mathrm{MMC}}$

Figure 8.6: Simulated distributions for $m_{\tau\tau}^{\mathrm{vis}}$ (left), $m_{\tau\tau}^{\mathrm{col}}$ (middle) and $m_{\tau\tau}^{\mathrm{MMC}}$ (right). Distributions for VBF $H \to \tau\tau$ is shown in black while distributions for $Z \to \tau\tau$ are shown in red.

8.3.3 Signal selection

For each channel a series of selection criteria are applied to enhance the sensitivity to the VBF SM Higgs signal ($H \to \tau\tau$ and $H \to WW$) and to ensure orthogonality to other analyses. In the $\tau_\ell\tau_\ell$ channel, events are required to have a single reconstructed electron and a single reconstructed muon following the signal object definitions in Table 8.3. The reconstructed leptons used in the analysis are required to be matched with those passing the trigger chain with p_{T} above the offline thresholds listed Table 8.4. The preselection is summarised in the upper part in Table 8.5. For completeness the preselection in the $\tau_\ell\tau_h$ and $\tau_h\tau_h$ channels are also shown.

In order to select lepton coming from the $H \to \tau_\ell\tau_\ell$ decay and suppress events coming from W+jets and top processes, the charge product is required to be negative. The collinear mass is required to be larger than $m_Z - 25$ GeV and the visible mass is limited to be between 30 and 100 GeV to suppress $Z \to \tau\tau$ events and to ensure orthogonality to analyses probing $H \to WW$, like in Ref. [215]. To further suppress contribution of $Z \to \tau\tau$ processes, which are typically produced with low p_{T} and large angular separation at the LHC, upper

	$\tau_\ell\tau_\ell$	$\tau_\ell\tau_h$ ($e\tau_h$)	$\tau_\ell\tau_h$ ($\mu\tau_h$)	$\tau_h\tau_h$
Preselection				
Object counting	# of $e = 1$, # of $\mu = 1$, # of $\tau_h = 0$	# of $e/\mu = 1$, # of $\tau_h = 1$		# of $e/\mu = 0$, # of $\tau_h = 2$
p_{T} cut	e/μ : p_{T} cut 10 GeV to 27.3 GeV	e/μ : p_{T} cut 21 GeV to 27.3 GeV, τ_h: $p_{\mathrm{T}} > 30$ GeV		τ_h: $p_{\mathrm{T}} > 40$,30 GeV
ID, Isolation, and eveto	e/μ: Medium e: FCLoose, μ: FCTightTrackOnlyVarRad	e/μ: Medium, τ_h: RNN Medium e: FCLoose, μ: FCTightTrackOnlyVarRad 1-prong τ_h: eleBDT e-veto		τ_h: RNN Medium
Charge product	Opposite charge	Opposite charge		Opposite charge
Kinematics	$m_{\tau\tau}^{\mathrm{coll}} > m_Z - 25$ GeV $30 < m_{e\mu} < 100$ GeV	$m_{\mathrm{T}} < 70$ GeV		
Angular	$\Delta R_{e\mu} < 2.5$, $\lvert\Delta\eta_{e\mu}\rvert < 1.5$	$\Delta R_{\ell\tau_h} < 2.5$, $\lvert\Delta\eta_{\ell\tau_h}\rvert < 1.5$		$0.6 < \Delta R_{\tau_h\tau_h} < 2.5$ $\lvert\Delta\eta_{\tau_h\tau_h}\rvert < 1.5$
b-veto	# of b-jets = 0 wp: DL1r_FixedCutBEff_85	# of b-jets = 0 wp: DL1r_FixedCutBEff_85		# of b-jets = 0 wp: DL1r_FixedCutBEff_70
$E_{\mathrm{T}}^{\mathrm{miss}}$	$E_{\mathrm{T}}^{\mathrm{miss}} > 20$ GeV	$E_{\mathrm{T}}^{\mathrm{miss}} > 20$ GeV		$E_{\mathrm{T}}^{\mathrm{miss}} > 20$ GeV
Coll. app. x_1/x_2	$0.1 < x_1 < 1.0$, $0.1 < x_2 < 1.0$	$0.1 < x_1 < 1.4$, $0.1 < x_2 < 1.2$		$0.1 < x_1 < 1.4$, $0.1 < x_2 < 1.4$
Leading jet	$p_{\mathrm{T}} > 40$ GeV	$p_{\mathrm{T}} > 40$ GeV		$p_{\mathrm{T}} > 70$ GeV, $\lvert\eta\rvert < 3.2$
VBF inclusive	sub-leading jet $p_{\mathrm{T}} > 30$ GeV $m_{jj} > 350$ GeV, $\lvert\Delta\eta_{jj}\rvert > 3$ $\eta(j_0) \times \eta(j_1) < 0$ lepton centrality: visible decay products of the τ leptons between VBF jets			

Table 8.5: Summary of the preselection and VBF selection for the $\tau_\ell\tau_\ell$ (left), $\tau_\ell\tau_h$ (middle) and $\tau_h\tau_h$ (right) channel.

thresholds on $\Delta R_{e\mu} < 2.5$ and $|\Delta\eta_{e\mu}| < 1.5$ are applied. To reduce contributions from top processes an explicit requirement is placed to veto events with b-tagged jets. The requirement on $E_{\mathrm{T}}^{\mathrm{miss}}$, as well as requirements on the momentum fraction carried by the visible part of decay products (x_0, x_1), are applied to improve the mass estimation. Finally, a 40 GeV p_{T} requirement is applied for general background suppression and enhancing the VBF contribution.

A set of additional cuts are applied to target the VBF production topology of the Higgs boson. For these cuts it is assumed that the two leading jets in the events are the two "tagging" VBF jets. Although this assumption is not necessarily true for all events, studies in other VBF $H \to \tau\tau$ analyses have shown that this is a good approximation [201, 202].

This introduces the following additional selection criteria: the sub-leading jet must have a transverse momentum $p_T^{j_1} > 30$ GeV, the invariant mass of the two leading jets must satisfy $m_{jj} > 350$ GeV, the two leading jets must have pseudo-rapidity separation, $|\Delta\eta_{jj}| > 3$. The jets must be located in opposite hemispheres of the detector, requiring $\eta(j_0) \times \eta(j_1) < 0$. Finally, the visible decay products of the τ-leptons must lie between the two VBF jets, ensuring lepton centrality. The same VBF cuts are applied to all three channels in the analysis and defines what will be referred to as the VBF inclusive region in the following. The expected yields for background and signal in this region is shown in Table 8.6.

Process	Expected yield after VBF selection
VBF $H \to \tau\tau$	41.03 ± 0.64
VBF $H \to WW$	17.32 ± 0.27
Other Higgs	14.98 ± 0.24
$Z \to \tau\tau$	901.03 ± 14.48
$Z \to \ell\ell$	8.99 ± 0.16
Top	175.90 ± 2.78
Diboson	64.70 ± 1.04
Fakes (Misidentified leptons)	155.95 ± 2.64
Total	1380.40 ± 21.94
s/b	0.044

Table 8.6: Expected number of events per process after the VBF selection. The uncertainties are statistical only. The considered signal in the $\tau_\ell\tau_\ell$ channel includes both VBF $H \to \tau\tau$ and $H \to WW$ processes. Other Higgs includes ggH, ttH and VH processes.

Distributions comparing the MC prediction with data in the VBF inclusive region for some final state variables can be seen in Figure 8.7-8.10. Although the distributions generally indicate good agreement, slight mismodelling coming from the $Z \to \tau\tau$ normalisation can be observed. However, no correction from the object level embedding procedure has been applied at this point. The description and application of this procedure is detailed in Section 8.6.3.

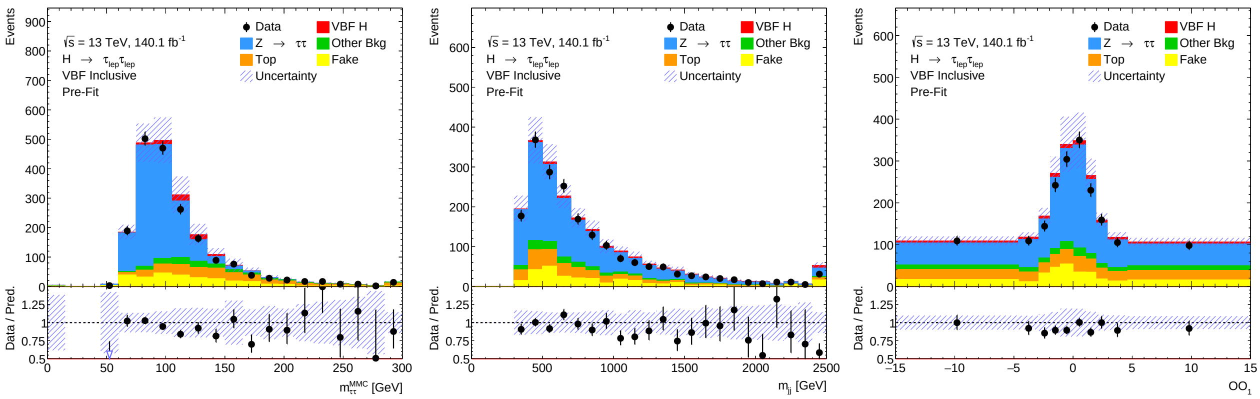

a) $m_{\tau\tau}^{\mathrm{MMC}}$ b) m_{jj} c) Optimal Observable

Figure 8.7: Distributions showing both data and MC in the VBF Inclusive region for $m_{\tau\tau}^{\mathrm{MMC}}$ (left), m_{jj} (middle) and the Optimal Observable (right). The uncertainty band includes both statistical and systematic uncertainties.

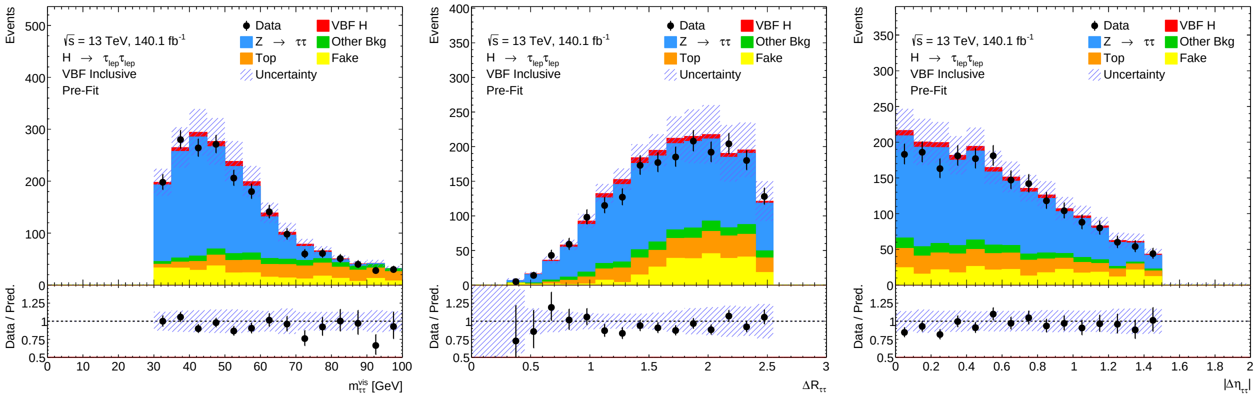

a) $m_{\tau\tau}^{\text{vis}}$ b) $\Delta R_{\tau\tau}$ c) $\Delta\eta_{\tau\tau}$

Figure 8.8: Distributions showing both data and MC in the VBF Inclusive region for $m_{\tau\tau}^{\text{vis}}$ (left), $\Delta R_{\tau\tau}$ (middle) and $\Delta\eta_{\tau\tau}$ (right). The uncertainty band includes both statistical and systematic uncertainties.

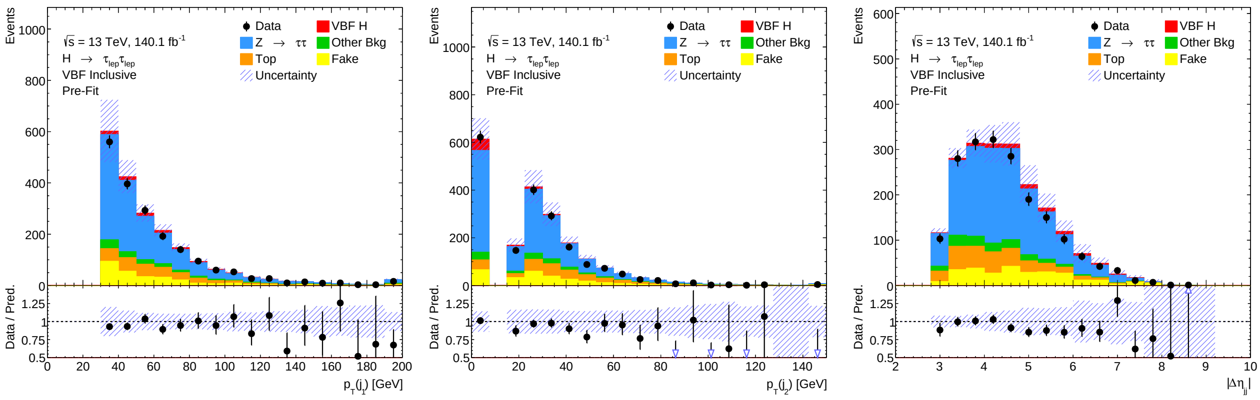

a) $p_T(j_0)$ b) $p_T(j_2)$ c) $\Delta\eta_{jj}$

Figure 8.9: Distributions showing both data and MC in the VBF Inclusive region for $p_T(j_1)$ (left), $p_T(j_2)$ (middle) and $\Delta\eta_{jj}$ (right). The uncertainty band includes both statistical and systematic uncertainties.

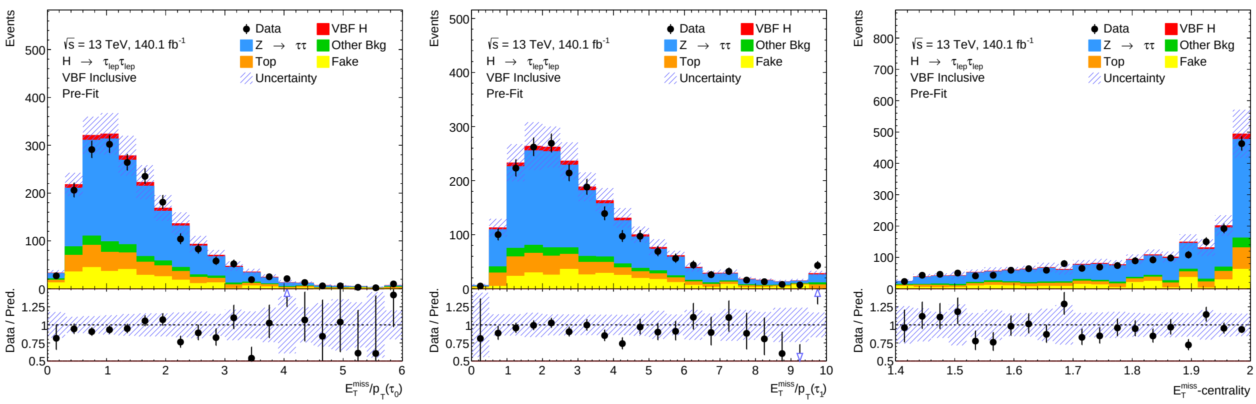

a) $m_T(\tau_1, E_{\text{T}}^{\text{miss}})$ b) $m_T(\tau_2, E_{\text{T}}^{\text{miss}})$ c) $E_{\text{T}}^{\text{miss}}$-centrality

Figure 8.10: Distributions showing both data and MC in the VBF Inclusive region for $m_T(\tau_1, E_{\text{T}}^{\text{miss}})$ (left), $m_T(\tau_2, E_{\text{T}}^{\text{miss}})$ (middle) and $E_{\text{T}}^{\text{miss}}$-centrality (right). The uncertainty band includes both statistical and systematic uncertainties.

8.4 Multivariate signal extraction

To achieve sufficient sensitivity to the shape effects on the Optimal Observable arising from anomalous HVV couplings in this analysis, it is essential to select signal pure regions enriched with VBF Higgs events. Although the preselection and VBF cuts described in the previous section target the VBF topology, the resulting signal-to-background ratio remains too low for precise measurements. To address this, an additional event selection step is introduced, where SRs are defined using the output score of a neural network. A similar strategy was employed in the partial Run 2 analysis with BDTs [51]. This section begins with a brief overview of neural networks, followed by a detailed explanation of their training and implementation within the context of this analysis.

8.4.1 Neural Networks

Machine Learning (ML) focuses on developing models from data, primarily through two approaches: supervised and unsupervised learning. Supervised learning uses labelled data, pairing inputs with outputs to train models that map inputs to outputs accurately. In contrast, unsupervised learning uses unlabelled data to uncover underlying patterns. While both approaches are common in ATLAS, this analysis uses supervised learning to classify events into signal and background processes.

Supervised artificial neural networks, a subset of ML techniques, consist of interconnected units called nodes in a set of layers. Each node receives one or more inputs from a previous layer, applies a non-linear transformation via an activation function, and produces a single output that is passed to the next layer. A bias term can be added to the activation function's argument to provide additional flexibility. The output of node i in layer j is computed as:

$$y_i^{(j)} = f\left(\sum_{k=1}^{n_{j-1}} w_{ik}^{(j)}\, y_k^{(j-1)} + b_i^{(j)}\right), \tag{8.9}$$

where $f(\cdot)$ is the activation function, $w_{ik}^{(j)}$ is the weight associated with the connection between node k in layer $j-1$ and node i in layer j, $b_i^{(j)}$ is the bias term for node i in layer j, and n_{j-1} is the number of nodes in the previous layer. In this analysis, two activation functions are considered. The rectified linear unit (ReLU) is used for the hidden layers (layers between input and output) and is defined as:

$$f(y) = \max(0, y). \tag{8.10}$$

The softmax activation function is used for output layers, and is defined as:

$$\text{softmax}(y_i) = \frac{e^{y_i}}{\sum_k e^{y_k}}, \tag{8.11}$$

where k runs over the the number of nodes in the last layer. The softmax function normalises the raw output values y_i by exponentiating each output and dividing by the sum of the exponentiated outputs. This ensures that the outputs are non-negative and that the sum of all outputs equals 1.

This analysis employs a feed-forward neural network (NN), characterised by a layered structure with no cyclic connections. The network is composed of three types of layers: the input layer, which receives the input variables, one or more hidden layers, which capture complex patterns in the data, and the output layer, which computes the final prediction. Each node in a given layer is connected to every node in the next layer, allowing information to flow sequentially from the input to the output.

The objective of training a NN is to identify the optimal set of weights and biases that minimise the discrepancy between the network's predictions and the actual class values. For example if an event belongs to the signal class the network should reward signal class scores closer to 1 and penalise larger discrepancies. The discrepancy is quantified by the loss function L. In classification tasks, particularly those involving multiple classes, the categorical cross-entropy loss function is commonly employed. The categorical cross-entropy loss for a single event is defined as:

$$L = -\sum_i y_i \log(\hat{y}_i), \tag{8.12}$$

where y_i denotes the true label for class i, and $\hat{y}_i$ represents the predicted output score for class i. To minimise this loss, the Stochastic Gradient Descent (SGD) algorithm is utilised. The weights and biases, collectively represented by $\boldsymbol{\omega}$, are randomly initialized. The first step, known as forward propagation, passes the input data through the network to compute the loss $L(\boldsymbol{\omega})$. In the second step, called backpropagation, the gradient of the loss $\nabla_{\boldsymbol{\omega}} L(\boldsymbol{\omega})$ is computed using a randomly selected subset of the data. The weights and biases are then updated by moving them in the direction opposite to the gradient, scaled by the learning rate η. Each weight/bias in each layer is updated according to:

$$\boldsymbol{\omega}^{(t)} = \boldsymbol{\omega}^{(t-1)} - \eta \nabla_{\boldsymbol{\omega}} L(\boldsymbol{\omega}^{(t-1)}), \tag{8.13}$$

where t denotes the weight update iteration index. For each update of the network parameters, a subset of the training data is used. This is referred to as a batch. The gradient is computed by averaging the loss over all events in the batch. A complete training iteration of the dataset is referred to an epoch.

In this analysis a modified version of SGD is used, namely the Adaptive Moment Estimation (Adam) optimizer [216]. The Adam optimizer extends SGD by incorporating adaptive learning rates for each parameter, as well as momentum to accelerate convergence. Specifically, Adam computes individual learning rates for different parameters from estimates of the first and second moments of the gradients. This is achieved by maintaining two moving averages: the first moment m_t (the mean of the gradients) and the second moment v_t (the uncentered variance of the gradients). These moments are updated at each iteration t as follows:

$$m_t = \beta_1 m_{t-1} + (1 - \beta_1)\nabla_{\boldsymbol{\omega}} L(\boldsymbol{\omega}^{(t-1)}), \tag{8.14}$$

$$v_t = \beta_2 v_{t-1} + (1 - \beta_2)\left(\nabla_{\boldsymbol{\omega}} L(\boldsymbol{\omega}^{(t-1)})\right)^2, \tag{8.15}$$

where β_1 and β_2 are decay rates. To correct for initialization bias, bias-corrected estimates $\hat{m}_t$ and $\hat{v}_t$ are computed as:

$$\hat{m}_t = \frac{m_t}{1 - \beta_1^t}, \quad \hat{v}_t = \frac{v_t}{1 - \beta_2^t}. \tag{8.16}$$

The weights and biases are then updated using these corrected moments according to:

$$\boldsymbol{\omega}^{(t)} = \boldsymbol{\omega}^{(t-1)} - \eta \frac{\hat{m}_t}{\sqrt{\hat{v}_t} + \epsilon}, \tag{8.17}$$

where η is the learning rate and ϵ is a small constant introduced to prevent division by zero. The initial moments, m_0 and v_0 are set to 0, and the parameters β_1, β_2 and ϵ are set to 0.99, 0.999 and 10^{-9} respectively [216]. The adaptive nature of Adam allows for more efficient training by adjusting the learning rate based on the magnitude of past gradients, leading to faster convergence compared to standard SGD, particularly in the presence of large datasets.

Training a NN requires specifying a set of hyperparameters, including the learning rate, batch size, number of epochs and number of layers. After each epoch, the performance of the model is evaluated on an independent validation dataset to assess its ability to generalise. Although the network may perform well on the training data, it can fail to generalise to unseen validation data, a phenomenon known as overtraining. Techniques are therefore often introduced to obtain more generalised training.

One method is so-called L2 Regularization, also referred to as ridge regression. This technique adds a penalty term to the loss function, proportional to the sum of the squared values of the weights:

$$L_{\text{reg}} = L + \lambda \sum_i \omega_i^2, \tag{8.18}$$

where L is the original loss, the index i represents the individual weights in the network and λ is a the regularisation parameter. This way large weights are penalised, encouraging the model to prefer simpler solutions. Another technique is dropout, which randomly deactivates a subset of neurons during each training iteration to prevent reliance on specific nodes. Learning rate decay is also used, where the learning rate decreases over time by a factor λ_d:

$$\eta_{i+1} = \eta_i \frac{1}{1 + \lambda_d \cdot i}. \tag{8.19}$$

This allows the model to make larger updates initially and finer adjustments as it converges. In this analysis λ_d is set constant at 0.001.

To further increase the robustness of the model, k-fold cross validation is used. In this method, the dataset is partitioned into k equal subsets, known as folds. The model is trained k times, each time using a different configuration of $k-2$ subsets of data, and validated on a different validation subset. An additional subset is set aside in each fold and used when applying the model for further physics analysis. This is known as the test set. In this analysis $k = 5$. The 5-fold cross-validation approach not only improves generalisation but also enables the entire dataset to be utilised for training. Table 8.7 illustrates how different parts of the dataset is utilised for training, validation and testing in each fold.

	Partition 1	Partition 2	Partition 3	Partition 4	Partition 5
Fold 1	Train	Train	Train	Test	Val
Fold 2	Train	Train	Test	Val	Train
Fold 3	Train	Test	Val	Train	Train
Fold 4	Test	Val	Train	Train	Train
Fold 5	Val	Train	Train	Train	Test

Table 8.7: The full dataset is partitioned into 5 folds for this analysis. For each fold, the train set is used for training the model, the val set for validation, and the test set for testing. The test set from each fold is evaluated using the corresponding trained model and subsequently used for the physics analysis.

8.4.2 NN training and signal region selection

In this analysis the NN classifier is implemented with the FreeForestML package [217]. It based on KERAS [218] with a TensorFlow [219] back-end. The baseline network configuration is the same across the three channels, but each network is trained and tuned separately. Table 8.8 summarises the common configuration and the tunable parameters of the model. The signal considered during the training stage is the SM VBF Higgs processes, with reweighting applied only in the fitting stage detailed in Section 8.7.

Set network configuration		
Loss function	Binary cross-entropy	Eq. 8.12
Optimizer	ADAM (Adaptive Moment Estimation)	Eq. 8.17
Hidden layer activation function	ReLU (Rectified Linear Unit)	Eq. 8.10
Output layer activation function	Softmax	Eq. 8.11
Tunable Hyperparameters		
Number of hidden layers	Tuned to optimise model complexity and performance	
Number of nodes per layer	Adjusted to balance model capacity and overfitting risk	
Batch size	Number of samples processed before model parameter updates	
L2 regularisation parameter	Controls the strength of the L2 penalty to prevent overfitting	Eq. 8.18
Learning rate and decay	Determines optimisation step size and its reduction over time	Eq. 8.19

Table 8.8: Neural network configuration and tunable hyperparameters.

The considered input variables are those representing the final state, i.e variables built from $E_{\mathrm{T}}^{\mathrm{miss}}$, τ-leptons and jets. Similar variables were used for the BDT employed by the partial Run 2 analysis [51] and for the VBF tagger employed by the full Run 2 couplings analysis [213]. The list of input variables is summarised in Table 8.9. In the table, $E_{\mathrm{T}}^{\mathrm{miss}}$-centrality refers to the the sum of the x- and y-components of the $E_{\mathrm{T}}^{\mathrm{miss}}$ unit vector in the transverse plane transformed such that the direction of the τ-lepton decays is orthogonal. It is defined as:

$$\frac{E_{\mathrm{T}}^{\mathrm{miss}}\text{-centrality}}{\sqrt{2}} = \frac{r+s}{\sqrt{r^2+s^2}}, \quad r = \frac{\sin(\phi(E_{\mathrm{T}}^{\mathrm{miss}}) - \phi(\tau_0))}{\sin(\phi(\tau_1) - \phi(\tau_0))}, \quad s = \frac{\sin(\phi(\tau_1) - \phi(E_{\mathrm{T}}^{\mathrm{miss}}))}{\sin(\phi(\tau_1) - \phi(\tau_0))}. \tag{8.20}$$

The centrality of the τ-leptons with respect to the dijet system is defined as:

$$C_{j_0,j_1}(\tau_i) = \exp\left[\frac{-4}{(\eta_{j_0} - \eta_{j_1})^2}\left(\eta_{\tau_i} - \frac{\eta_{j_0}+\eta_{j_1}}{2}\right)^2\right], \tag{8.21}$$

where i refers to the leading or sub-leading $\tau-$lepton. This variable has a value of unity when the τ-lepton is halfway in η between the two jets, 1/e when the τ-lepton is aligned with one of the jets, and $< 1/\mathrm{e}$ when the τ-lepton is not between the jets in η.

A larger number of events in the training phase improves NN network performance by reducing the impact of statistical fluctuations and noisy data. Therefore, parts of the selection in Table 8.5 is removed to increase the training statistics.

Variable	Description	
$\eta^{j_1} \times \eta^{j_2}$	Product of η of the leading and sub-leading jets	
$p_{\mathrm{T}}(j_0, j_1)$	p_{T} of the di-jet system	
$p_{\mathrm{T}}(j_1)$	p_{T} of the sub-leading jet	
$m_{\tau\tau}^{\mathrm{vis}}$	Visible mass from two τ-candidates	Eq. 8.6
$m(\tau, \tau, j_0)$	Visible mass from two τ-candidates and the leading jet	
$m_{\tau\tau}^{\mathrm{MMC}}$	Invariant Higgs mass reconstructed using the MMC	Ref.[85]
$m_{\mathrm{T}}(\tau_0, E_{\mathrm{T}}^{\mathrm{miss}})$	Transverse mass from the leading τ-candidate and $E_{\mathrm{T}}^{\mathrm{miss}}$	Eq. 9.2
$m_{\mathrm{T}}(\tau_1, E_{\mathrm{T}}^{\mathrm{miss}})$	Transverse mass from the sub-leading τ-candidate and $E_{\mathrm{T}}^{\mathrm{miss}}$	Eq. 9.2
$\Delta R_{\tau\tau}$	Angular distance between the two τ-candidates	
$\Delta\eta_{\tau\tau}$	Angular distance in η-direction between the two τ-candidates	
$\Delta\phi_{\tau\tau}$	Angular distance in ϕ-direction between the two τ-candidates	
$p_{\mathrm{T}}(\tau_0) + p_{\mathrm{T}}(\tau_1)$	Scalar sum of the two τ-candidate transverse momenta	
$p_{\mathrm{T}}(\tau\tau)$	p_{T} of the two τ-candidates system	
$p_{\mathrm{T}}(\tau\tau, E_{\mathrm{T}}^{\mathrm{miss}})$	p_{T} of the Higgs candidate	
$p_{\mathrm{T}}(\tau\tau, j_0, E_{\mathrm{T}}^{\mathrm{miss}})$	p_{T} of the system of two τ-candidates, the leading jet and $E_{\mathrm{T}}^{\mathrm{miss}}$	
$p_{\mathrm{T}}(\tau_0)/p_{\mathrm{T}}(\tau_1)$	Ratio of transverse momenta of the two τ-candidates	
$\Delta p_{\mathrm{T}}(\tau\tau)/\Sigma p_{\mathrm{T}}(\tau)$	Ratio of p_{T} difference and scalar sum of the two τ-candidates	
$E_{\mathrm{T}}^{\mathrm{miss}}$-centrality	Centrality based on ϕ-angle transformation of transverse plane	Eq. 8.20
$E_{\mathrm{T}}^{\mathrm{miss}}/p_{\mathrm{T}}(\tau_0)$	Ratio of $E_{\mathrm{T}}^{\mathrm{miss}}$ and p_{T} of leading τ-candidate	
$E_{\mathrm{T}}^{\mathrm{miss}}/p_{\mathrm{T}}(\tau_1)$	Ratio of $E_{\mathrm{T}}^{\mathrm{miss}}$ and p_{T} of sub-leading τ-candidate	
$E_{\mathrm{T,HPTO}}^{\mathrm{miss}}$	$E_{\mathrm{T}}^{\mathrm{miss}}$ calculated from identified leptons and jets	
$\Delta\eta_{jj}$	Angular distance in η-direction between the two leading jets	
m_{jj}	Invariant mass of the two leading jets	
$p_{\mathrm{T}}(\tau\tau, j_0, j_1, E_{\mathrm{T}}^{\mathrm{miss}})$	p_{T} of the two τ-candidates, the two leading jets and $E_{\mathrm{T}}^{\mathrm{miss}}$	
$p_{\mathrm{T}}(j_2)$	p_{T} of the third jet	
$C_{jj}(\tau_0)$	Centrality of the leading τ-candidate w.r.t. the two leading jets	Eq. 8.21
$C_{jj}(\tau_1)$	Centrality of the sub-leading τ-candidate w.r.t. the two leading jets	Eq. 8.21
$\Delta\phi(H, j_1)$	Angular distance in ϕ-direction between the Higgs candidate and sub-leading jet	

Table 8.9: List of input variables used for training.

The following cuts are dropped in the training stage:

$\Delta R_{e\mu} < 2.5$

$m_{jj} > 350\,\mathrm{GeV}$ (Still applied for any pair of jets)

$|\Delta\eta_{jj}| > 3$

$\eta(j_0) \times \eta(j_1) < 0$

Lepton centrality requirement

The composition of raw and weighted events used for training with the VBF and loosened selection is detailed in Table 8.10. Loosening the selection increases signal statistics by a factor of 2 and background statistics by a factor ranging from 6 to 12 depending on the background process.

Process	VBF Selection		Loosened Selection		Factor of
	Raw	Weighted	Raw	Weighted	Increase
VBF $H \to \tau\tau$	70523	41.03	150097	86.86	2.13
VBF $H \to WW$	20651	17.32	35811	34.09	1.73
Other Higgs	9536	14.98	52168	85.42	5.47
$Z \to \tau\tau$	52537	901.02	321436	16287.63	6.12
$Z \to \ell\ell$	147	8.99	1447	62.79	9.84
Top	4403	175.95	44829	1790.61	10.18
Diboson	8287	64.70	100007	759.46	12.07
Fakes	2395	155.95	21304	1808.42	8.90
Total	168479	1380.40	727099	10915.30	4.32

Table 8.10: Composition of raw and weighted number of events per process after the VBF selection and with the loosened selection, including the factor of increase in raw statistics. The processes classified as signal for NN training in the $\tau_\ell\tau_\ell$ channel are VBF $H \to \tau\tau$ and VBF $H \to WW$ processes. Other Higgs includes ggH, ttH, WH, and ZH processes.

Pre-Optimisation

Table 8.10 shows that there is class imbalance among the background processes. The $Z \to \tau\tau$ process is dominant, exceeding other backgrounds by a factor of 9. As a result, a binary classifier will primarily learn to distinguishing between $Z \to \tau\tau$ and signal processes. A multiclass classifier can however simultaneously learn to separate between multiple background components, offering greater flexibility to the training process. A baseline setup with the parameters listed in Table 8.11 is trained as a starting point prior to optimisation. This enables studies on how the NN architecture affects expected sensitivity. Figure 8.11 presents the results

Parameter	Value
Number of hidden layers	2
Number of nodes per layer	512
L2 tuning parameter	1.6×10^{-6}
Learning rate	0.001
Batch size	256
Number of epochs	50

Table 8.11: Baseline parameter values used for the NN training.

of a study on the expected sensitivity obtained with the baseline setup using two output nodes (signal and background), compared to the same setup with four output nodes. The results show a steeper ΔNLL curve and hence a sensitivity gain when additional output nodes are introduced for the background processes. The following classes are therefore selected as outputs, reflecting the dominant sources of background in the VBF phase space:

Output node 1: Signal (VBF $H \to \tau\tau$ and VBF $H \to WW$)

Output node 2: $Z \to \tau\tau$

Output node 3: Top (singletop and $t\bar{t}$)

Output node 4: Other backgrounds (Primarily Fakes and Diboson)

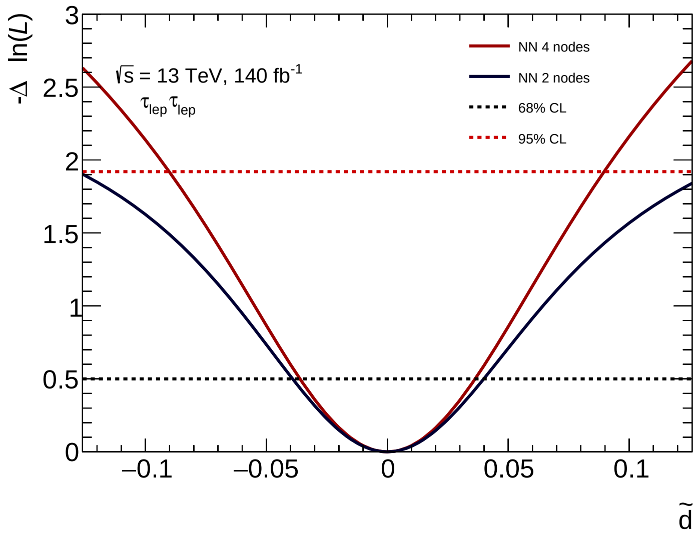

Figure 8.11: Comparison of the expected ΔNLL curves from the fit result, based on a signal region defined by the signal NN output score for $\tau_\ell\tau_\ell$, using a baseline setup with either two (black) or four (red) output nodes.

To asses the importance of the different input variables in training and potentially identify poorly performing ones a permutation scan is performed. The network is initially trained with all variables in Table 8.9, and the signal output score is scanned to find the cut that maximises the statistical significance metric, $s/\sqrt{s+b}$. Each variable is then independently shuffled randomly among events and the significance is recalculated. The permutation importance is calculated as the the nominal significance ($\mathrm{Sig}^{\mathrm{nom}}$) divided by the permuted significance ($\mathrm{Sig}^{\mathrm{perm}}$) for each variable:

$$I = \frac{\mathrm{Sig}^{\mathrm{nom}}}{\mathrm{Sig}^{\mathrm{perm}}}. \tag{8.22}$$

Each variable is permuted five times, and the average significance is calculated. The ranking plot for the variables based on permutation importance is shown in Figure 8.12. In general, all variables contribute to the NN performance, with the largest performance gain coming from m_{jj} and variables derived from τ-leptons and jets. While some angular τ-lepton variables have a minimal impact, no variables degrade the network's performance. Therefore, all variables are kept.

The correlation matrix of the input variables, as well as their correlation to the four output scores can be seen in Figure 8.13. Large correlations are expected since many of the variables are built from the same $E_{\mathrm{T}}^{\mathrm{miss}}$, τ-lepton and jet objects. The correlations are consistent with the variable importance, with m_{jj} having the largest correlation to the signal output score $\mathrm{NN}_{\mathrm{sig}}^{\mathrm{out}}$.

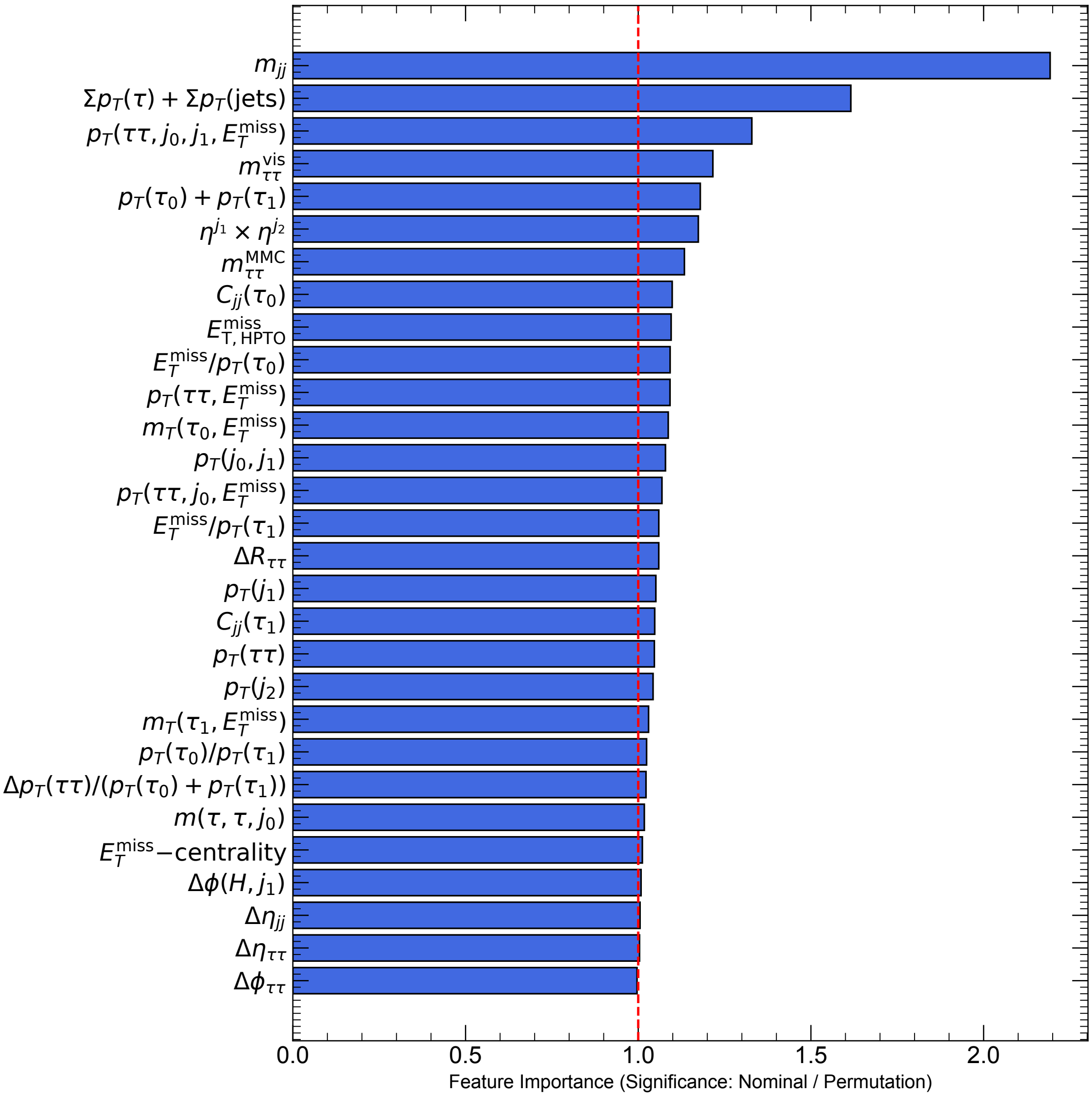

Figure 8.12: Permutation importance ranking of the input variables used for training in the $\tau_\ell\tau_\ell$ channel. Importance score larger than 1 indicate that the network performs better with the variable, and conversely scores less than 1 indicates that the network performs worse with the variable. This boundary is illustrated by the red line.

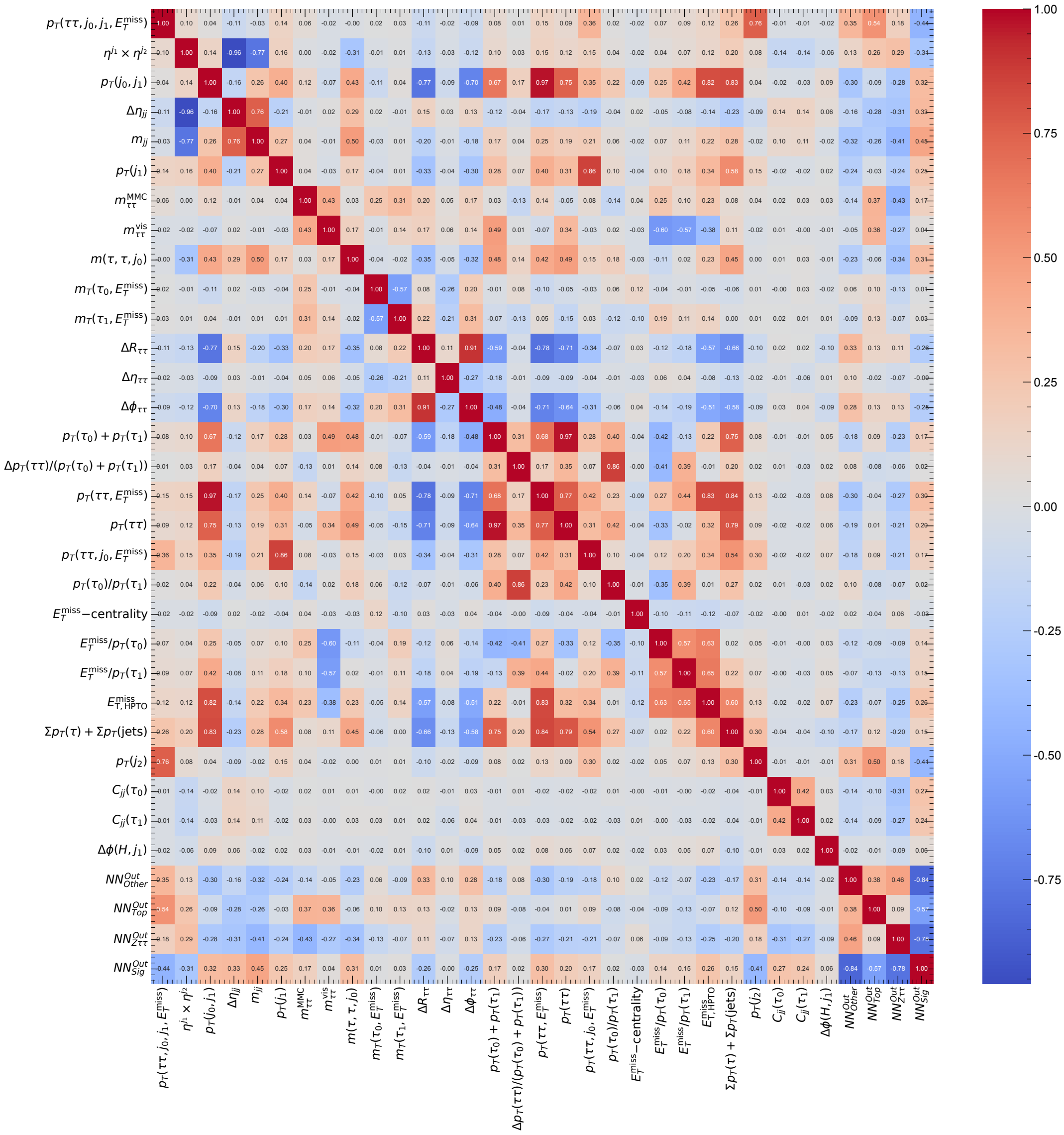

Figure 8.13: Correlation matrix of the input variables, including also the four output scores. The matrix visualises the pairwise correlations between the variables, with positive correlations shown in red and negative correlations in blue.

Optimisation of hyperparameters

To identify the hyperparameter values that gives the best performing model, a hyperparameter scan is performed using the OPTUNA framework [220]. In Optuna, the objective function, $f(\mathbf{x})$ is defined as the performance metric to be optimised on a hyperparameter set $\mathbf{x}$. In the case of this analysis, the objective function is given by the statistical significance metric, $s/\sqrt{s+b}$, obtained by scanning the signal output score for each trial. The optimisation process involves evaluating this objective function over a search space $\mathcal{X}$ of hyperparameters, where Optuna employs the Tree-structured Parzen Estimators (TPE) [221] algorithm to iteratively sample new hyperparameters based on the performance of previous trials. Each trial represents a trained network using a specific set of hyperparameters sampled from $\mathcal{X}$. This allows for a more efficient search process than iteratively varying each parameter separately like in a grid search. The goal is to maximise the objective function, thereby improving the model's ability to distinguish the signal from the background.

In total 200 trials were tested with the ranges of parameter values listed in Table 8.12. The trial with the configuration of hyperparameters yielding the best performing network is chosen as the final model.

Parameter	Scanned range or values	Chosen value
Number of hidden layers	[2-10]	3
Number of nodes per layer	[128,256,512]	256
Batch size	[128, 256, 512, 1024, 2048]	512
Learning rate	$[10^{-6} - 10^{-2}]$	0.001
L2 Regularisation	$[10^{-6} - 10^{-3}]$	2.36×10^{-6}

Table 8.12: OPTUNA scanning parameters in the $\tau_\ell\tau_\ell$ channel. The chosen values represent the configuration that yields the best performance.

The results of the scan can be seen in Figure 8.14. The significance for each trial is shown in blue, and the red line tracks the best performing ones. A sharp improvement is observed during the early trials, followed by a plateau where further gains become increasingly rare. After reaching this plateau, larger fluctuations are expected due to the optimiser exploring more diverse regions of the hyperparameter space in search of potentially better configurations. Notably, a small number of trials yield significance values close to 1.5, which indicates poor signal–background separation. These trials likely correspond to suboptimal hyperparameter combinations that significantly limit the network's discriminating power, such as the use of overly shallow architectures, inappropriate learning rates, or excessive regularisation.

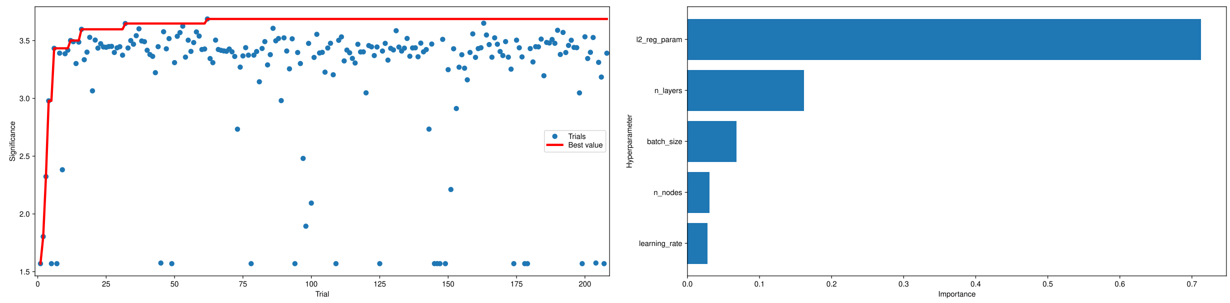

a) Sigficance per trial

b) Importance ranking of the hyperparameters

Figure 8.14: Results from the hyperparameter scan showing the significance ($s/\sqrt{s+b}$) per trial (left) and the ranking of the importance of the hyperparameters (right).

Final network and signal regions

The final network is chosen as the configuration with the best performing hyperparameters in Table 8.12. Figure 8.15 shows the training and validation loss as a function of the number of epochs, along with the confusion matrix summarising the predictions for the four output classes. The test and training losses follow each other closely without significant divergence, suggesting stable training. The confusion matrix reveals that the network is most efficient at identifying signatures coming from the signal and $Z \to \tau\tau$ background. This is expected since these two classes are the most statistical dominant.

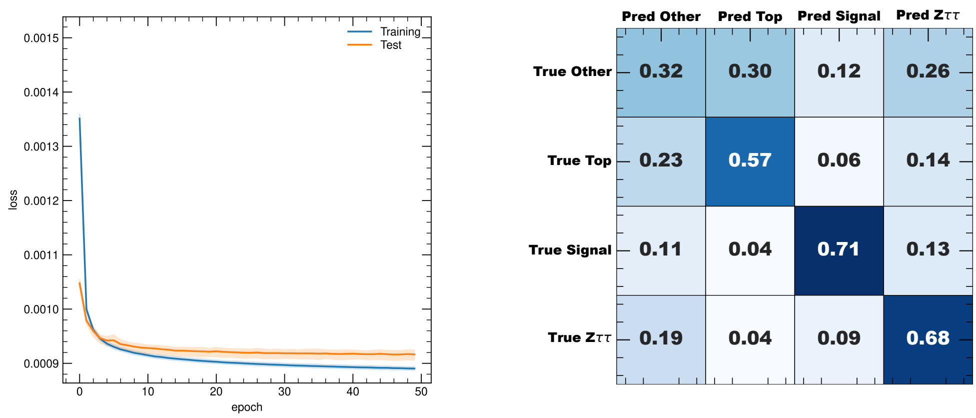

a) Loss

b) Confusion matrix

Figure 8.15: The training and validation loss as a function of number of epochs (left) and the confusion matrix for the 4 output classes (right). In the matrix, each row represents the true class instances, while each column represents the predicted class instances. The predicted class is assigned by selecting the argmax of the four outputs for each event.

To maintain consistency with the VBF phase space, the previously dropped cuts from training are reapplied before defining SR cuts on the signal output score. The output score for the signal can be seen in Figure 8.16

in the VBF inclusive region. The output scores for the three background classes can be seen in Figure 8.17. Good agreement can be seen within uncertainty in the high NN signal score, with slight mismodelling (within uncertainties) from the $Z \to \tau\tau$ normalisation seen in the low NN signal score. Distributions are however pre-fit, with no correction factors applied. The low NN signal score (<0.6) where $s/b < 1\%$ is defined as a VR to validate the propagation of the background normalisation factors on the prediction.

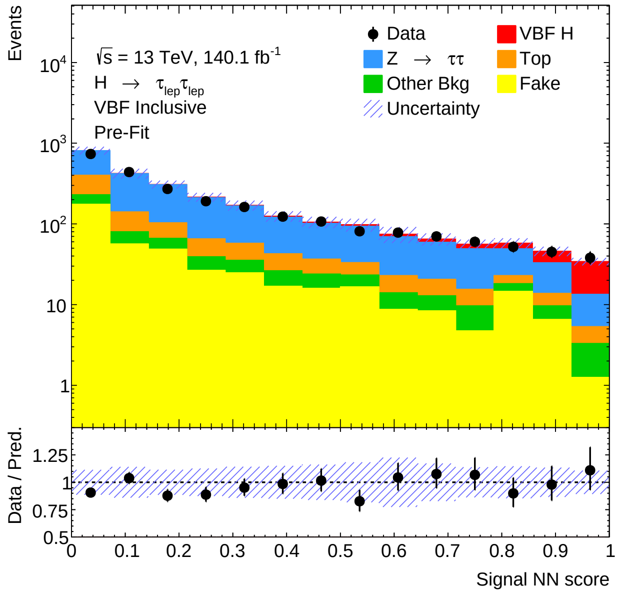

Figure 8.16: Signal NN output score with the VBF selection applied. The uncertainty band includes both statistical and systematic uncertainties. The low NN SR is defined from 0.67 to 0.91 and the high NN SR is defined from 0.91 to 1.0. The low NN VR is defined from 0 to 0.6

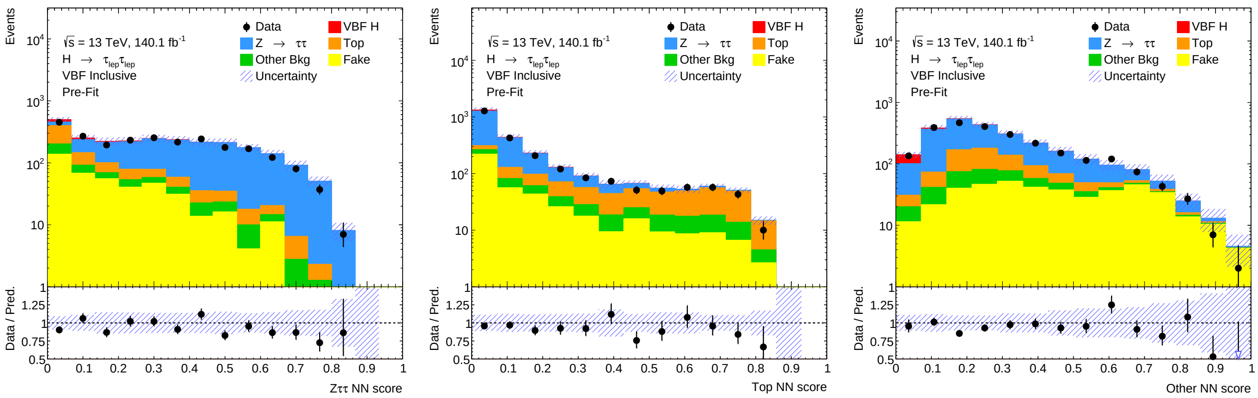

a) $Z\tau\tau$ NN score

b) Top NN score

c) Other bkg NN score

Figure 8.17: The NN output scores of the three background classes with the VBF selection applied. The uncertainty band includes both statistical and systematic uncertainties.

While the statistical significance is a useful metric for assessing the overall performance of the network, it does not necessarily determine the optimal cuts, as the analysis is also sensitive to the choice of binning. To define the final SR, a simplified fit setup, designed to replicate the full fit procedure described in Section 8.7, is performed using the PYHF fitting framework [222].

The signal output score is scanned from 0.7 to 1.0 in increments of 0.01. For each score value, three fits are carried out using MC statistical uncertainties only, corresponding to configurations of 8, 10, and 12 bins. The binning is chosen such that the signal is equally distributed across the bins, as this approach was shown to yield the most sensitive results in the VBF $H \to ZZ$ CP analysis [52]. The cut and binning that together yields the smallest 68% confidence interval is chosen as the final high NN SR. This corresponds to 10 bins with a signal NN score cut at 0.91, yielding a confidence interval length of 0.072.

There is however still signal present in-between the high NN SR and the low NN VR. Although this intermediate region have a lower signal-to-background ratio, including it leads to a 6% improvement in the expected limits and ensures that no data are discarded. The same procedure is therefore repeated, scanning the NN score from 0.65 to 0.91, resulting in a confidence interval of 0.5 corresponding to 10 bins and a signal NN score cut at 0.67 with an upper bound at 0.91. This defines the low NN SR. The event composition in the two SRs is summarised in Table 8.13.

Process	SR High NN > 0.91	SR Low NN $\in [0.67, 0.91]$
VBF $H \to \tau\tau$	18.42 ± 0.49	18.38 ± 0.39
VBF $H \to WW$	5.45 ± 0.14	7.23 ± 0.14
$Z \to \tau\tau$	10.98 ± 0.27	90.18 ± 1.92
$Z \to \ell\ell$	0.19 ± 0.01	0.95 ± 0.04
Top	3.03 ± 0.09	17.25 ± 0.34
ggH	1.26 ± 0.03	4.39 ± 0.10
VV	1.32 ± 0.04	7.11 ± 0.14
Fake	1.19 ± 0.03	20.67 ± 0.42
Total	41.87 ± 1.08	166.22 ± 3.46
S/B	1.34	0.18

Table 8.13: Background composition in the $\tau_\ell\tau_\ell$ channel after applying the optimal NN signal score cut for the high (left) and low (right) NN SRs. The uncertainties are statistical only.

As a final check, a test is conducted to verify that the NN signal score is not biased to CP-odd effects and does not depend on $\tilde{d}$. The NN is evaluated with the SM hypothesis ($\tilde{d}$=0) and two BSM CP-mixing scenarios ($\tilde{d} = \pm 0.15$), corresponding to the the maximum variations used in the final fit. This is shown in Figure 8.18. Other than some small variations in individual bins, no dependence on $\tilde{d}$ is visible.

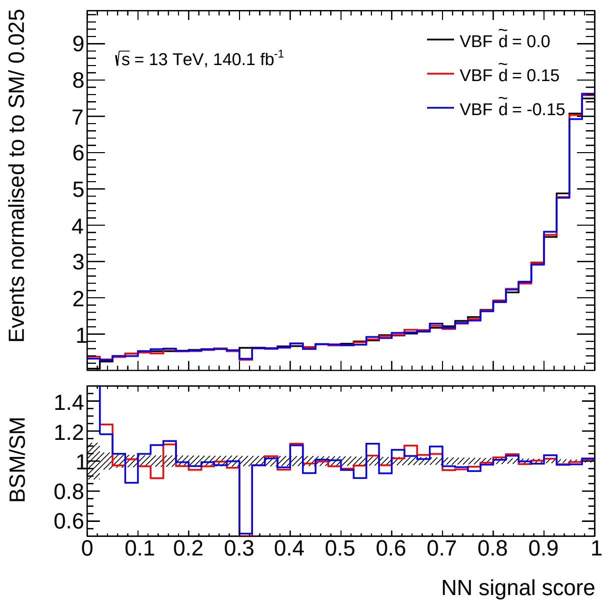

Figure 8.18: The NN signal score evaluated for the the signal sample with $\tilde{d}$= -0.15, 0, 0.15. The lower panel shows the ratio of the $\tilde{d}$= ±0.15 prediction over the SM. No dependence on $\tilde{d}$ is visible.

8.5 Background estimation

The main background source in this analysis is coming from $Z \to \tau\tau$ + jets events. These events share the same signature as the Higgs signal and are kinematically very similar. They constitute approximately 65% of the background in both SRs. Events are estimated with MC, but is corrected with a data-driven procedure called object-level-embedding.

The second most dominant background component originates from either misidentified leptons or top quark processes, depending on the region. Misidentified leptons, commonly referred to as fakes, occur when jets or photons are incorrectly identified as electrons or muons. Their contribution is estimated from data, as MC predictions for such processes are generally unreliable. Overall, they account for around 8% of the background in the high NN SR and 15% in the low NN SR.

The top background correspond to $t\bar{t}$, tW, and single-top processes. Although these processes are significantly suppressed by the requirement of a b-veto in the signal selection, some events still enter the SRs. They constitute roughly 17% of the background in the high NN SR and 12% in the low NN SR. Their estimation relies on MC, but a top CR is defined to control the normalisation.

All remaining backgrounds are modelled directly using MC, since their contributions are small.

8.5.1 Z+jets background

Since $Z \to \tau\tau+$ jets is the main background, good modelling is important for the analysis. However, due to the kinematic similarity to $H \to \tau\tau$ events, it is challenging to define a pure signal-free CR to control the $Z \to \tau\tau$ normalisation. Instead, a data-driven method called object level embedding was developed during Run 1 to improve the modelling of these processes [223]. However, due to mandatory changes to the reconstruction software some changes were implemented for Run 2. The Run 2 method is based on the fact that $Z \to \ell\ell$ and $Z \to \tau\tau$ are kinematically identical processes at truth-level. This means that it is possible to obtain a template for $Z \to \tau\tau$ events by substituting leptons (e/μ) with τ-leptons in $Z \to \ell\ell$ events. This template can then be used to constrain the $Z \to \tau\tau$ MC in a CR without having issues with signal contamination. The method starts with defining two regions:

Source region: Used to select $Z \to \ell\ell$ events in data.

Target region: Used to select events after the embedding procedure.

The source region is looser and completely covers the phase space of the target region. The selection of the source region is summarised in Table 8.14. The target region is obtained with the same selection as the SRs, since this is where the procedure will be applied in the end.

Requirement	Value
N_ℓ	2 OS Same Flavour ($e^+e^-/\mu^+\mu^-$)
p_{T}^{ℓ} [GeV]	e: 15 / 27 (if trigger matched)
	μ: 10/27.3 (if trigger matched)
ID	`Medium`
Isolation	e: `Loose_VarRad`
	μ: `TightTrackOnly_VarRad`
$m_{\ell\ell}^{vis}$	> 80 GeV
$\Delta R_{\ell\ell}$	< 2.5
$\|\Delta\eta_{\ell\ell}\|$	< 1.5

Table 8.14: Selection criteria for the $Z \to \ell\ell$ Embedding Source Region.

The events in the source region are corrected through an unfolding procedure to remove detector effect. Unfolding means that an inverse transformation of efficiency maps related to the object reconstruction are applied, allowing for a truth-level approximation of the reco-level objects. This is needed since the kinematic equivalence of $Z \to \ell\ell$ and $Z \to \tau\tau$ events is only valid at truth-level. Efficiency maps are computed using $Z \to \ell\ell$ MC with correction factors that account for trigger, reconstruction, ID/isolation and charge flip efficiency. All the maps are parametrised in p_T and η. Figure 8.19 shows the trigger efficiency maps for electrons and muons. After the

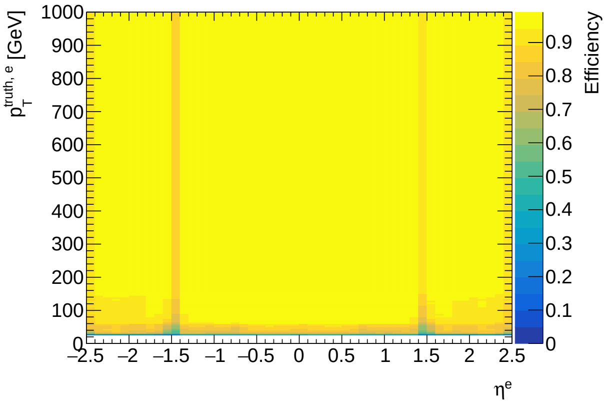

a) Electron

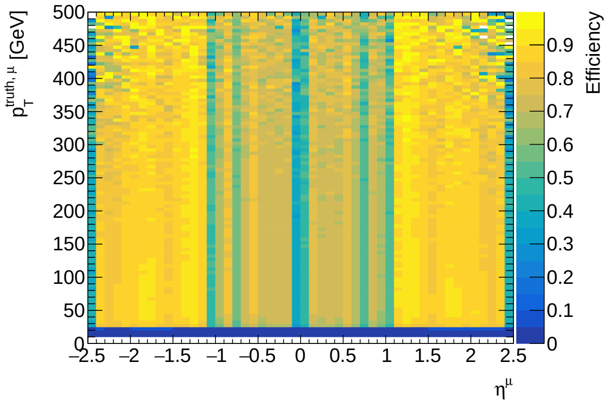

b) Muon

Figure 8.19: Trigger efficiency maps for electrons (left) and muons (right) parametrised in p_T and η.

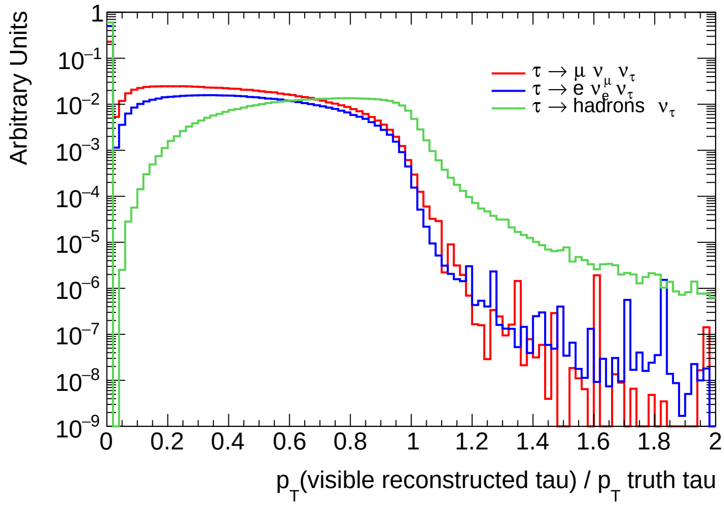

Figure 8.20: Probability distribution of the ratio of visible reconstructed τ-lepton p_{T} to truth τ-lepton p_{T}, for the three τ-lepton decay channels.

unfolding procedure the leptons are substituted with $\tau-$leptons. The decay mode of each substituted τ-lepton is chosen at random, such that τ_e, τ_μ and τ_{had} decays are equally probable.

The p_{T} of the substituted τ-lepton is corrected to account for the invisible part of the decay. This correction is implemented using scale factors derived from the ratio of the visible reconstructed p_{T} of the τ-lepton to its truth-level p_{T}. These ratios form a probability distribution for each decay mode of the τ-lepton, as shown in Figure 8.20. For each event, a correction factor is randomly sampled from the corresponding distribution and applied to the substituted $\tau-$lepton. The spike at zero in the distribution originates from τ-leptons that are not reconstructed. To ensure that both substituted τ-leptons are reconstructed with p_{T} above the threshold required by the analysis selection, each event is repeatedly sampled until a valid configuration is found. A maximum of 10 iterations is imposed to limit the computation time. The correction factors are applied to the substituted τ-lepton p_{T}, and $E_{\mathrm{T}}^{\mathrm{miss}}$ is subsequently recomputed. Specifically, the pre-embedding four-vectors are added to $E_{\mathrm{T}}^{\mathrm{miss}}$, while the post-embedding four-vectors are subtracted. All other variables that depend on $E_{\mathrm{T}}^{\mathrm{miss}}$ and τ-lepton p_{T} are then updated accordingly. Finally, the efficiency maps are reapplied in the reverse procedure, referred to as folding. The reconstruction, identification, isolation, and charge-flip efficiencies are applied again, based on the decay channel of the new τ-lepton, using the updated p_{T} and η. These events can now be used to construct a $Z \to \tau\tau$ template in both data and MC and subsequently be applied in the analysis phase space by implementing the appropriate selection.

The method is validated in simulation by applying the embedding procedure to $Z \to \ell\ell$ MC and comparing the result with the nominal $Z \to \tau\tau$ MC in the VBF-inclusive region. This comparison, shown in Figure 8.21, demonstrates good agreement across most bins. In the final fit model, two CRs, each corresponding to the selection of the two SRs, are defined to constrain the $Z \to \tau\tau$ normalisation. These CRs utilise embedded MC calibrated to embedded data, and a common normalisation factor is propagated to the SRs. Any discrepancies between the nominal and embedded $Z \to \tau\tau$ templates is treated as a systematic uncertainty.

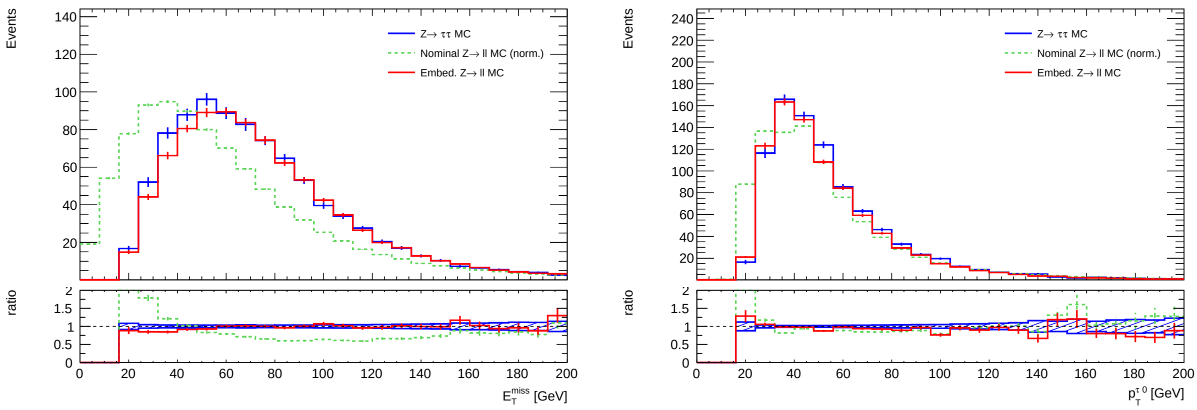

a) $E_{\mathrm{T}}^{\mathrm{miss}}$

b) p_{T} (τ_0)

Figure 8.21: Validation distributions in the VBF inclusive region for the embedding procedure in $E_{\mathrm{T}}^{\mathrm{miss}}$ (left) and p_{T} (τ_0) (right) using events from the $\tau_\ell\tau_\ell$ channel. The nominal $Z \to \tau\tau$ MC is shown in blue, the nominal $Z \to \ell\ell$ MC in green and the embedded $Z \to \ell\ell$ events in red.

To validate the application of the embedding procedure in data a fit is performed in the low NN VR. This region inverts the requirement on the NN score used to obtain the SRs, and does not have significant signal contamination. This way the assessment of the modelling after the fit can be isolated by fitting the background processes only, with $Z \to \tau\tau$ being the dominant component. Figure 8.22 shows the distribution of the Optimal Observable in the low NN VR before and after the fit. The corresponding embedded $Z \to \ell\ell$ MC and data in the embedded CR can be seen in Figure 8.23. The fit corrects the $Z \to \ell\ell$ embedded MC to data in a CR following the same kinematic selection as the VR, and propagates this normalisation factor to the VR. The normalisation factor is estimated to be $NF_{Z\tau\tau}^{\mathrm{EmbVR}} = 0.91 \pm 0.09$. Applying this normalisation factor to the $Z \to \tau\tau$ background in the low NN VR corrects the normalisation and leads to better background modelling in all bins of the Optimal Observable.

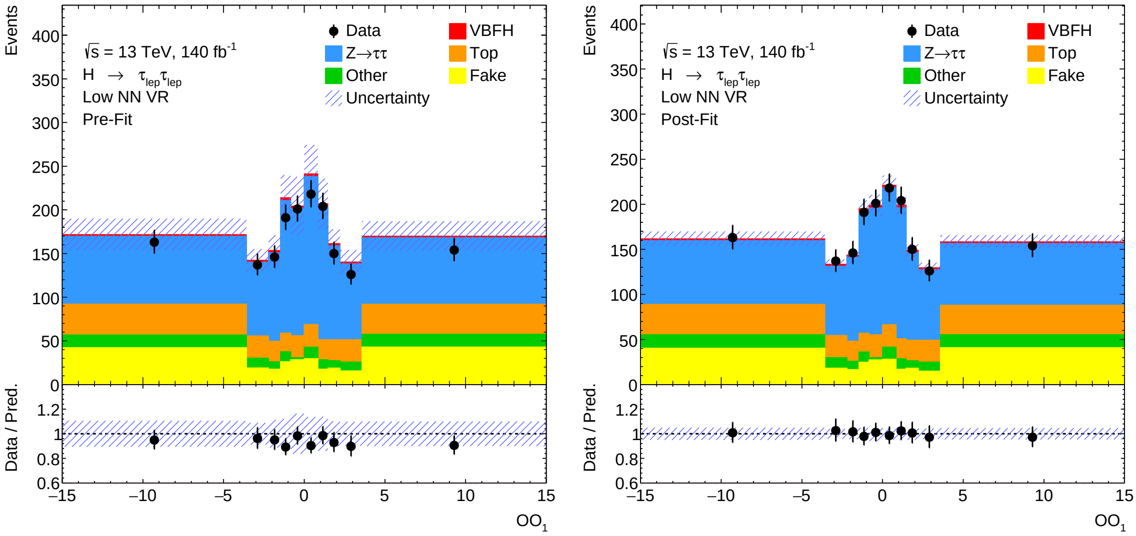

a) Before fit b) After fit

Figure 8.22: Distribution of the Optimal Observable in the low NN VR before (left) and after (right) the fit. The $Z \to \tau\tau$ correction factor is obtained from normalising the $Z \to \ell\ell$ embedding MC to data in a CR following the same.

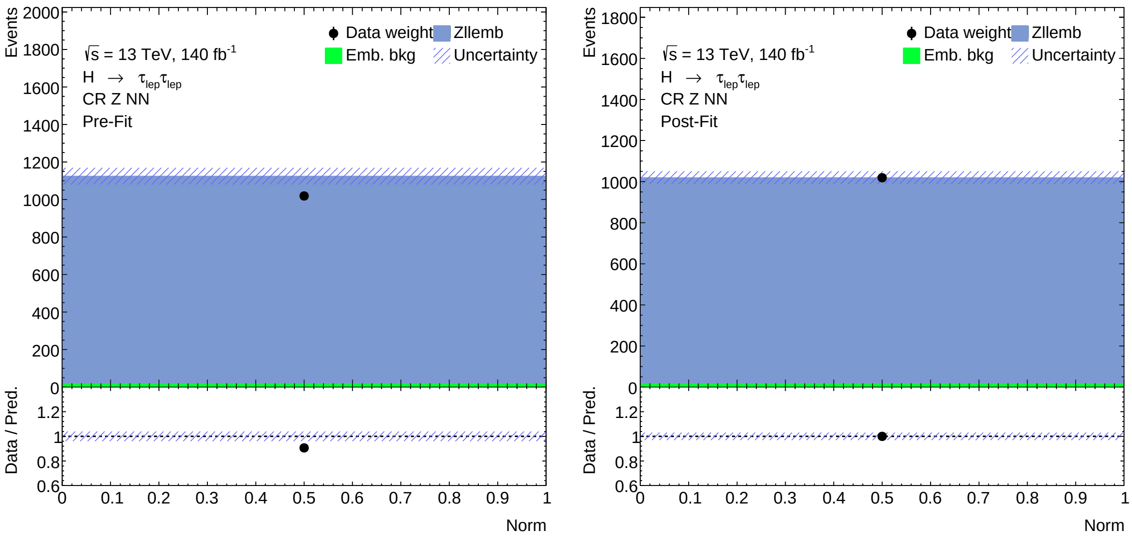

a) Before fit b) After fit

Figure 8.23: Embedded $Z \to \ell\ell$ MC and data in the embedded $Z \to \ell\ell$ CR before (left) and after (right) the fit. Weighted data means that the embedding procedure is applied. Embedded background corresponds processes other than $Z \to \ell\ell$ that are present in the source region.

8.5.2 Fake background

The two leptons considered in this analysis are based on the identification criteria detailed in Section 8.3 and mainly originate from the di-τ decay of the Z or Higgs boson. These are genuine leptons and will be referred to prompt or real leptons in the following. There are however also non-prompt and non-leptonic particles that may satisfy these same selection criteria, giving rise to what is referred to fake leptons. In the case of electrons, these include contributions from semi-leptonic decays of b- and c-quarks, photon conversions and jets with large electromagnetic energy. Non-prompt or fake muons can originate from semi-leptonic decays of b- and c-quarks, from charged hadron decays in the tracking volume or in hadronic showers, or from punch-through particles emerging from high-energy hadronic showers [224]. In events with two leptons the fake background is dominated by W+jets and semi-leptonic $t\bar{t}$ events, with a fake lepton in addition to the real one, and more rarely events with two fake leptons.

MC simulation for these processes is usually not well modelled, so in this analysis estimation is taken from data using the Matrix Method [224]. The method requires two sets of selection criteria, namely Loose and Tight. Tight corresponds to the same isolation and ID criteria as the signal leptons while Loose is less restrictive. The two sets of requirements for electrons and muons are summarised in Table 8.15.

Requirement	Electron	Muon
Tight	`Loose_VarRad` isolation and `Medium` ID	`TightTrackOnly_VarRad` isolation and `Medium` ID
Loose	No isolation and `Loose` ID	No isolation and `Medium` ID

Table 8.15: Selection criteria for loose and tight electrons and muons used for the fake estimation.

These two working points can the be used to define two probabilities. The probability for a real lepton to pass the Tight selection criteria is evaluated using truth-matched MC and is referred to as the real efficiency, ϵ_r:

$$\epsilon_r = \frac{N_{Tight}^{MC_{Truth}}}{N_{Loose}^{MC_{Truth}}}. \tag{8.23}$$

The probability for a fake lepton to pass the Tight selection criteria is evaluated using truth-matched MC subtracted from the data and is referred to as the fake efficiency, ϵ_f:

$$\epsilon_f = \frac{N_{Tight}^{Data} - N_{Tight}^{MC_{Truth}}}{N_{Loose}^{Data} - N_{Loose}^{MC_{Truth}}}. \tag{8.24}$$

The truth-matching is done with the TruthClassification package provided by the ATLAS isolation fake forum, where leptons are assigned to different background categorises depending on their truth record. A lepton is considered truth-matched if its truth category corresponds class 2 (prompt electrons), class 3 (charge-flip electrons), class 4 (prompt muons), class 6 (electrons from muons) or class 11 (charge-flip muons). Using the real and fake efficiencies, relations can be obtained from the observed event counts as functions of the number of events containing fake-fake (N_{ff}), fake-real (N_{fr}), real-fake (N_{rf}) and real-real (N_{rr}) lepton pairs. This can be expressed as a matrix:

$$\begin{bmatrix} N_{TT} \\ N_{TL} \\ N_{LT} \\ N_{LL} \end{bmatrix} = \begin{bmatrix} \epsilon_r\epsilon_r & \epsilon_r\epsilon_f & \epsilon_f\epsilon_r & \epsilon_f\epsilon_f \\ \epsilon_r\bar{\epsilon}_r & \epsilon_r\bar{\epsilon}_f & \bar{\epsilon}_f\epsilon_r & \epsilon_f\bar{\epsilon}_f \\ \bar{\epsilon}_r\epsilon_r & \bar{\epsilon}_r\epsilon_f & \bar{\epsilon}_f\epsilon_r & \bar{\epsilon}_f\epsilon_f \\ \bar{\epsilon}_r\bar{\epsilon}_r & \bar{\epsilon}_r\bar{\epsilon}_f & \bar{\epsilon}_f\bar{\epsilon}_r & \bar{\epsilon}_f\bar{\epsilon}_f \end{bmatrix} \begin{bmatrix} N_{rr} \\ N_{rf} \\ N_{fr} \\ N_{ff} \end{bmatrix}, \tag{8.25}$$

where $\bar{\epsilon} = 1 - \epsilon$. The number of fake signal leptons can be determined by projecting the first row of the matrix onto the vector, only considering events containing at least one fake lepton:

$$N_{TT}^{fake} = \epsilon_r\epsilon_f N_{rf} + \epsilon_f\epsilon_r N_{fr} + \epsilon_f\epsilon_f N_{ff}. \tag{8.26}$$

Direct measurements of real and fake leptons cannot be obtained from data. These can however be computed from the real and fake efficiencies by inverting the matrix:

$$M^{-1} = \frac{1}{(\epsilon_{r,1} - \epsilon_{f,1})(\epsilon_{r,2} - \epsilon_{f,2})} \begin{bmatrix} \bar{\epsilon}_{f,1}\bar{\epsilon}_{f,2} & \bar{\epsilon}_{f,1}\epsilon_{f,2} & -\epsilon_{f,1}\bar{\epsilon}_{f,2} & \epsilon_{f,1}\epsilon_{f,2} \\ -\bar{\epsilon}_{f,1}\bar{\epsilon}_{r,2} & \bar{\epsilon}_{f,1}\epsilon_{r,2} & -\epsilon_{f,1}\bar{\epsilon}_{r,2} & -\epsilon_{f,1}\epsilon_{r,2} \\ -\bar{\epsilon}_{r,1}\bar{\epsilon}_{f,2} & \bar{\epsilon}_{r,1}\epsilon_{f,2} & -\bar{\epsilon}_{r,1}\bar{\epsilon}_{f,2} & -\epsilon_{r,1}\epsilon_{f,2} \\ \bar{\epsilon}_{r,1}\bar{\epsilon}_{r,2} & -\bar{\epsilon}_{r,1}\epsilon_{r,2} & -\epsilon_{r,1}\bar{\epsilon}_{r,2} & \epsilon_{r,1}\epsilon_{r,2} \end{bmatrix}, \tag{8.27}$$

where the numbering scheme corresponds to if the efficiency is applied to the first or second lepton. This inverted matrix can then be applied to the Loose and Tight leptons in data to obtain an estimate for the fake events passing the tight requirement:

$$\begin{aligned} N_{TT}^{fake} &= \epsilon_{r,1}\epsilon_{f,2}N_{rf} + \epsilon_{f,1}\epsilon_{r,2}N_{fr} + \epsilon_{f,1}\epsilon_{f,2}N_{ff} \\ &= \underbrace{\alpha\left[\epsilon_{r,1}\epsilon_{f,2}(\epsilon_{f,1}-1)(1-\epsilon_{r,2}) + \epsilon_{f,1}\epsilon_{r,2}(\epsilon_{r,1}-1)(1-\epsilon_{f,2}) + \epsilon_{f,1}\epsilon_{f,2}(1-\epsilon_{r,1})(1-\epsilon_{r,2})\right]}_{w_{TT}} N_{TT} \\ &+ \underbrace{\alpha\epsilon_{f,2}\epsilon_{r,2}\left[\epsilon_{r,1}(1-\epsilon_{f,1}) + \epsilon_{f,1}(1-\epsilon_{r,1}) + \epsilon_{f,1}(\epsilon_{r,1}-1)\right]}_{w_{TL}} N_{TL} \\ &+ \underbrace{\alpha\epsilon_{f,1}\epsilon_{r,1}\left[\epsilon_{f,2}(1-\epsilon_{r,2}) + \epsilon_{r,2}(1-\epsilon_{f,2}) + \epsilon_{f,2}(\epsilon_{r,2}-1)\right]}_{w_{LT}} N_{LT} \\ &- \underbrace{\alpha\epsilon_{f,1}\epsilon_{f,2}\epsilon_{r,1}}_{w_{LL}}\epsilon_{r,2}N_{LL}, \end{aligned} \tag{8.28}$$

where w_{TT}, w_{TL}, w_{LT} and w_{LL} are the weights applied to data depending on the Loose/Tight configuration of the lepton pair.

The real and fake efficiencies are computed separately for muons and electrons, using two regions designed to be enriched in real and fake leptons, respectively. Both regions are defined with a loosened selection criteria. The Real region requires two opposite-sign leptons, while the Fake region require same-sign leptons. In each region only the targeted lepton is truth-matched, but in the Fake region an additional lower bound is required for the p_{T} of the second lepton to suppress contribution from fake processes such as W+jets. An electron p_T threshold at 25 GeV is required in the muon Fake region and a muon p_T threshold at 30 GeV is required in the electron Fake region. The selection used for defining the the two regions is summarised in Table 8.16.

Real region	Fake region
1 e & 1 μ (OS)	1 e & 1 μ (SS)
$E_{\mathrm{T}}^{\mathrm{miss}} > 20$ GeV	$E_{\mathrm{T}}^{\mathrm{miss}} > 20$ GeV
At least 2 jets with $m_{jj} > 200$ GeV	At least 2 jets with $m_{jj} > 200$ GeV
At least 1 jet with $p_T > 30$ GeV	At least 1 jet with $p_T > 30$ GeV
b-veto	b-veto
—	p_{T} $(e) > 25$ GeV or p_{T} $(\mu) > 30$ GeV

Table 8.16: Real and fake regions used to compute efficiencies.

The efficiencies depend on the lepton kinematics and are therefore binned in p_{T} and η. However, the muon fake efficiency is only binned in p_{T} to reduce statistical uncertainties as minimal dependence on η was observed. For electrons the η from the electron cluster is used to properly reject the calorimeter crack in the transition region ($|\eta| \in [1.37, 1.52]$). The real efficiency plots can be seen in Figure 8.24 and the fake efficiency plots can be seen in Figure 8.25.

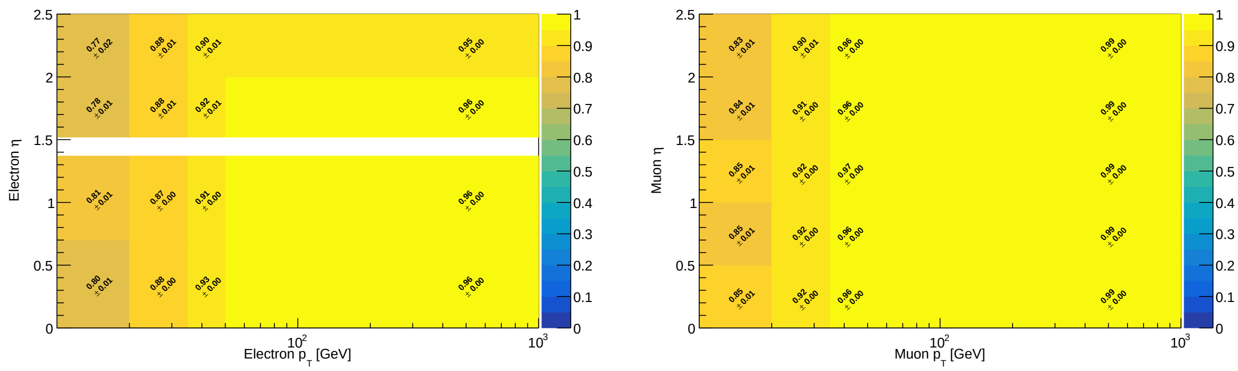

a) Electrons

b) Muons

Figure 8.24: Real efficiency histograms for electrons (left) and muons (right) binned in p_{T} and η.

The fake estimation from the Matrix Method is validated in a same-sign VR. This region follows the same selection criteria as the VBF inclusive region, except that the opposite-sign requirement on the lepton charges is replaced with a same-sign condition. Figure 8.26 shows the MMC mass and the Optimal Observable. Addi-

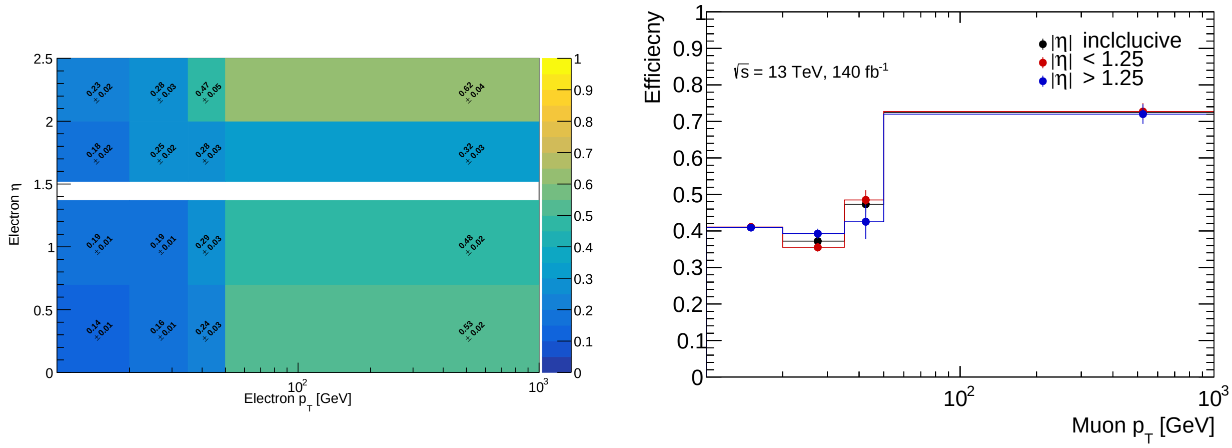

a) Electrons

b) Muons

Figure 8.25: Fake efficiency histograms for electrons (left) and muons (right). The electron efficiency histogram is binned in p_{T} and η and the muon efficiency is binned in p_{T} only.

tionally, Figure 8.27 shows p_{T} distributions for the electron, muon and dijet system. Overall, good agreement is observed across the final state and in the CP-odd observable. Any non-closure is incorporated as a shape-dependent systematic uncertainty based on the closure in the Optimal Observable.

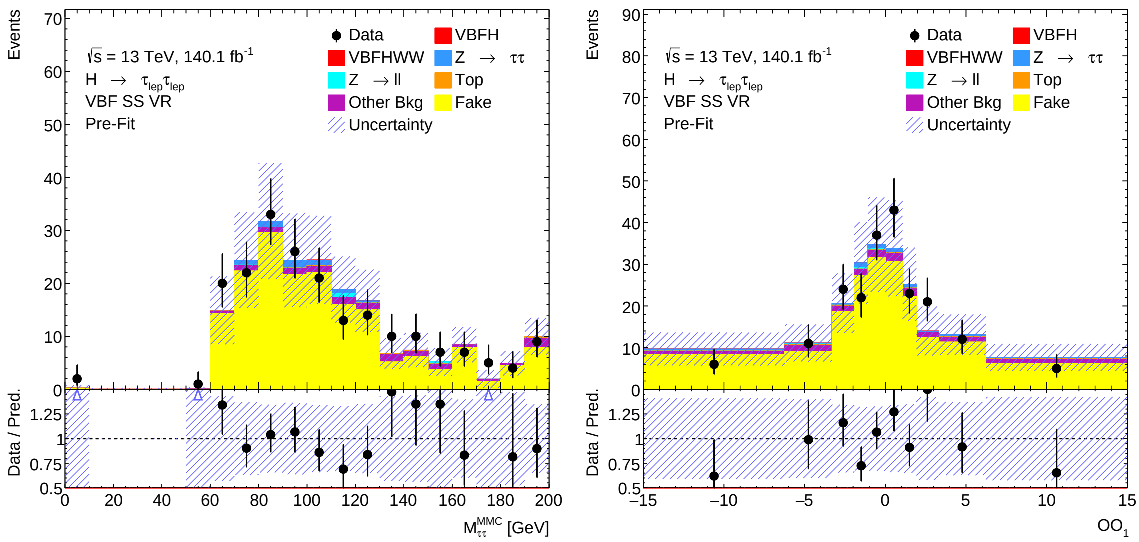

a) $m_{\tau\tau}^{\mathrm{MMC}}$

b) Optimal Observable

Figure 8.26: Distributions for $m_{\tau\tau}^{\mathrm{MMC}}$ (left) and the Optimal Observable (right) in the VBF SS VR. The uncertainty band includes both statistical and fake related systematic uncertainties

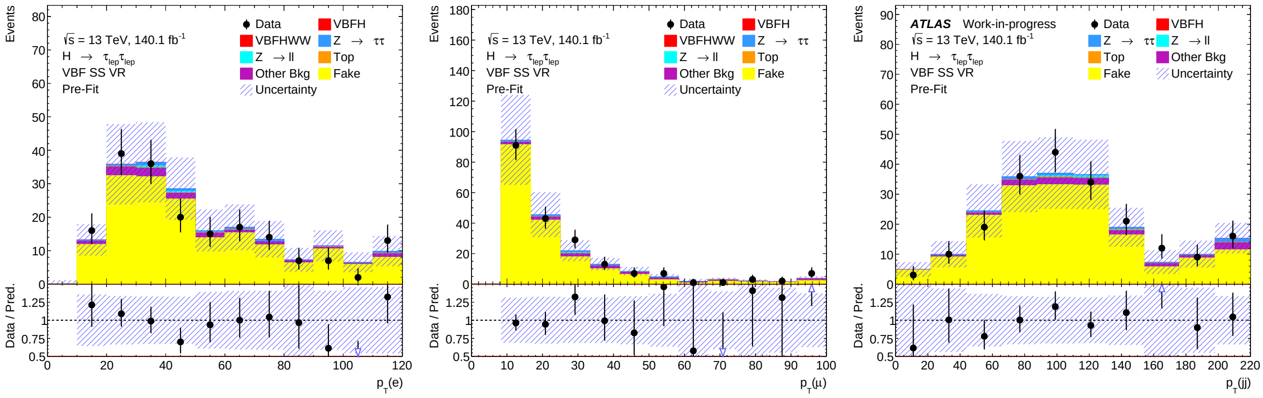

a) Electron p_{T} b) Muon p_{T} c) $p_{\mathrm{T}}(jj)$

Figure 8.27: Distributions for the electron p_{T} (left), muon p_{T} (middle) and the p_{T} of the dijet system (right) in the VBF SS VR. The uncertainty band includes both statistical and fake related systematic uncertainties

8.5.3 Top background

The normalisation of the top background in the $\tau_\ell\tau_\ell$ channel is constrained by a normalisation factor derived from a dedicated top CR. In the $\tau_\ell\tau_\ell$ channel, the top CR is defined relative to the VBF inclusive region by inverting the b-veto. In both the SRs and the top CR, $t\bar{t}$ has a dominant contribution of at least $\geq 85\%$.

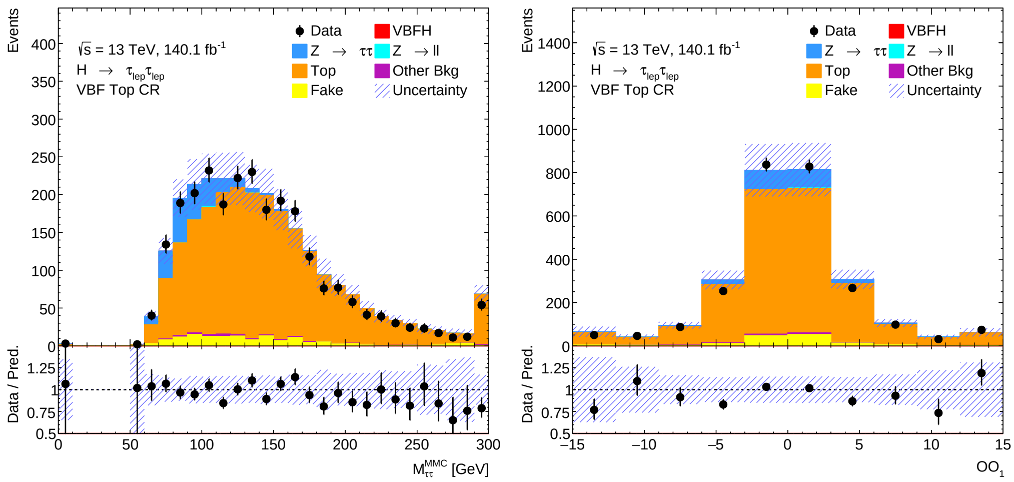

a) $m_{\tau\tau}^{\mathrm{MMC}}$ b) Optimal Observable

Figure 8.28: Distributions of $m_{\tau\tau}^{\mathrm{MMC}}$ (left) and the Optimal Observable (right) in the $\tau_\ell\tau_\ell$ top CR. The uncertainty band include statistical and systematic uncertainties.

Since the nominal fake estimate relies on a b-veto for the calculation of real and fake efficiencies, the fake leptons must be re-estimated. This selection is inverted for the Real and Fake regions, and the efficiencies are recomputed and reapplied to data in the top CR. The fraction of top events relative to the total expected yield is approximately 81%, with a negligible signal contribution. The modelling in the top CR is shown in Figure 8.28 for $m_{\tau\tau}^{\mathrm{MMC}}$ and the Optimal Observable. However, for the final fit configuration, only a single-bin region is considered.

8.6 Systematic uncertainties

Systematic uncertainties from various sources influence the VBF $H \to \tau\tau$ CP measurement. These sources affect both the signal and background prediction and are classified into three categories based on their origin:

1 **Theoretical uncertainties** are uncertainties related to the choice of MC generator and the specific theoretical parameters set in the simulation.

2 **Experimental uncertainties** are uncertainties related to the detector performance and the reconstruction and calibration of the physics objects used in the analysis.

3 **Data-driven uncertainties** are uncertainties related to the modelling of the data-driven techniques used in the analysis for estimating the fake and embedded $Z \to \ell\ell$ background.

Systematic uncertainties are evaluated from variations and comparing the resulting distributions to the nominal prediction. A general overview of how systematic uncertainties are incorporated into the likelihood model is provided in Chapter 7. Technically, they can be classified into two categories based on their implementation. The first category consists of variations applied as alternative event weights, modifying the nominal weight expression to account for systematic shifts. These variations affect both the overall normalisation and the shape of certain distributions. The second category includes uncertainties that impact the kinematic properties of reconstructed physics objects. These effects are typically implemented in dedicated samples, requiring a full event reprocessing to recompute variables such as $m_{\tau\tau}^{\mathrm{MMC}}$ and the Optimal Observable. The resulting kinematic shifts can lead to event migrations and changes in acceptance relative to the nominal prediction. For both categories, the shifted distributions are compared to the nominal expectation, and the corresponding variations are taken as the systematic uncertainty.

Furthermore, systematic uncertainties can either be provided as one or two variations. When two variations are provided, they correspond to $\pm 1\sigma$ shifts and are often referred to as up/down variations relative to the nominal prediction. In some cases, particularly in regions with limited statistics, both variations may shift in the same direction (either up or down). To address this, a two-sided symmetrisation procedure is often applied, where the difference between the up and down variations is computed bin-by-bin, divided by two, and mirrored to ensure that both variations are symmetrically distributed around the nominal prediction. In cases where only a single variation is available, such as systematic uncertainties derived from alternative generators, a second variation can be introduced as a mirrored version of the original.

8.6.1 Theoretical uncertainties

VBF signal and other Higgs processes

Theoretical uncertainties for the VBF $H \to \tau\tau$ signal and other Higgs processes used this analysis are evaluated following the guidelines of the LHC Higgs Cross-Section Working Group [44, 225]. These recommendations ensure consistency across different Higgs boson analyses and provide a unified framework for combining results. The uncertainties account for various sources, including PDFs, the strong coupling constant (α_s), QCD scale variations from missing higher order terms, parton shower modelling, and uncertainties associated with the matrix element generator.

The PDF uncertainties are evaluated according to the most recent recommendations of the PDF4LHC15NLO collaboration [209]. The PDF set comes with 30 eigenvector variations that are incorporated by modifying the MC weights in a reweighting scheme applied within the Powheg Box event generator. Each resulting variation is treated as an independent nuisance parameter (NP). The uncertainty from the strong coupling constant is evaluated by varying the value of α_s around its central value and combined with the PDF variations as independent nuisance parameters in the fit model.

The QCD scale uncertainties, arising from missing higher-order terms in perturbation theory, are estimated by varying the renormalization scale (μ_R) and factorization scale (μ_F) by factors of 2 and 0.5 relative to their nominal values. These variations are applied through internal reweighting in the Powheg Box event generator. All seven possible combinations of μ_R and μ_F variations are considered simultaneously. The final scale uncertainty is treated as a single nuisance parameter, determined by taking the envelope of these variations, i.e., the maximum deviation from the nominal prediction.

Uncertainties associated with the modelling of the parton shower and underlying event are assessed by varying the parton shower model while keeping the matrix element generator fixed. The nominal samples, generated using the Pythia 8 parton shower generator, are compared to alternative samples produced with Herwig 7. The resulting difference between the two samples is evaluated as the parton shower uncertainty. Uncertainties related to the matrix element calculation are evaluated by varying the matrix element generator while keeping the parton shower model unchanged. The nominal samples, generated with Powheg Box, are compared to alternative samples produced using the MadGraph5_aMC@NLO matrix element generator. The resulting difference between the two samples is evaluated as the matrix element uncertainty.

$Z \to \tau\tau$ background

Several sources of uncertainty are considered for the $Z \to \tau\tau$ background, including sources from PDFs, scale variations, the CKKW matching scheme and QCD scale factors (QSF). Uncertainties from the scale variations are handled in the same way as the Higgs processes. $Z \to \tau\tau$ samples are generated using the Sherpa event generator, which simultaneously handles the matrix element calculation and parton shower modelling. This makes it challenging to disentangle the effects of these components and perform a reliable comparison with alternative samples. A study done by the analysis in Ref. [201] investigated a comparison between Sherpa-generated samples and those produced with MadGraph5_aMC@NLO , but this approach lead to very noisy variations and significantly overestimated the associated uncertainties. Consequently, uncertainties related to parton shower and matrix element modelling in $Z \to \tau\tau$ have been omitted in this analysis.

The uncertainties from the PDF is estimated using 100 weight variations provided by the NNPDF3.0nnlo PDF set in the Sherpa simulation [205]. The difference of each variation N_i and nominal prediction N_0 is calculated and the standard deviation is evaluated as the the uncertainty. The uncertainties on the strong coupling constant are obtained by varying α_s around its central value.

The uncertainty associated with the choice of PDF is evaluated by comparing the nominal prediction from NNPDF3.0nnlo with two alternative PDF sets: MMHT2014nnlo [226] and CT14nnlo [227]. An envelope is constructed from these alternative predictions, and the uncertainty is taken as the maximum deviation from the nominal prediction within this envelope.

Uncertainties related to jet-parton merging (CKKW) and the resummation scale (QSF) used in the Sherpa generation are evaluated by using a truth-level parametrisation as a function of jet multiplicity and $p_{\mathrm{T}}(Z)$.

Top background

Several sources of uncertainty are considered for the $t\bar{t}$ and single-top backgrounds, including contributions from PDFs, initial-state radiation (ISR), final-state radiation (FSR), parton shower modelling, and matrix element calculations. The uncertainty from PDFs is evaluated similarly to previous cases, based on the 30 eigenvariations in the chosen PDF set. Uncertainties related to parton shower modelling and matrix element calculations are assessed by comparing the same two generators used for the Higgs processes.

Effects from ISR and FSR can lead to higher jet multiplicity and jet energies than the hard process. The uncertainties are evaluated by varying different parameters in the simulation, like μ_R, μ_F and h_{damp} [206]. This leads for an increase or decrease of the amount of QCD radiation with respect to the nominal prediction. The effect from FSR is parametrised as event weights in the nominal $t\bar{t}$ and single-top samples, while the effect from ISR is parametrised in alternative samples. The resulting difference with respect to the nominal prediction is taken as the uncertainty.

8.6.2 Experimental uncertainties

Experimental systematic uncertainties quantifies the limitations in the precision and accuracy of detector simulation. The different reconstruction and calibration techniques leads to several sources of systematic uncertainty for each physics object.

Electrons

The electron uncertainties are estimated using the techniques described in Ref. [168]. These uncertainties arise from several sources, including energy resolution and scale factors associated with trigger efficiency, reconstruction, identification, and isolation. The uncertainties in the electron energy scale and resolution are incorporated into the analysis through two nuisance parameters, which account for variations across different η regions and energy ranges. Table 8.17 summarise the different sources of electron systematic uncertainty considered in this analysis.

Nuisance Parameter	Description
`EG_RESOLUTION_ALL`	Energy resolution uncertainty
`EG_SCALE_ALL`	Energy scale uncertainty
`EL_EFF_ID_TOTAL_1NPCOR_PLUS_UNCOR`	Identification efficiency uncertainty
`EL_EFF_Iso_TOTAL_1NPCOR_PLUS_UNCOR`	Isolation efficiency uncertainty
`EL_EFF_Reco_TOTAL_1NPCOR_PLUS_UNCOR`	Reconstruction efficiency uncertainty
`EL-CHARGEID-STAT, EL-CHARGEID-SYS`	Charge identification uncertainty
`EL_EFF_Trigger_TOTAL_1NPCOR_PLUS_UNCOR`	Trigger efficiency uncertainty
`EL_EFF_TriggerEff_TOTAL_1NPCOR_PLUS_UNCOR`	Trigger scale-factor uncertainty

Table 8.17: Summary of electron-related systematic uncertainties in the analysis.

Muons

The muon uncertainties are estimated using the techniques described in Ref. [173]. These arise from various factors, including momentum scale and resolution, as well as scale factors related to trigger efficiency, reconstruction, and isolation. These uncertainties account for effects such as track resolution, overall momentum calibration, and charge-dependent momentum scale corrections. Additionally, statistical and systematic uncertainties influence the scale factors applied to trigger, reconstruction, and isolation efficiencies. Table 8.18 summarise the different sources of muon systematic uncertainty considered in this analysis.

Nuisance parameters	Description
MUON_ID	Inner detector resolution uncertainty
MUON_MS	Muon spectrometer resolution uncertainty
MUON_SAGITTA_RESBIAS	Track resolution uncertainty
MUON_SAGITTA_RHO	
MUON_SCALE	Momentum scale uncertainty
MUON_EFF_RECO_STAT	Reconstruction efficiency uncertainty
MUON_EFF_RECO_STAT_LOWPT	
MUON_EFF_RECO_SYS	
MUON_EFF_RECO_SYS_LOWPT	
MUON_EFF_ISO_STAT	Isolation efficiency uncertainty
MUON_EFF_ISO_SYS	
MUON_EFF_TrigStatUncertainty	Trigger efficiency uncertainty
MUON_EFF_TrigSystUncertainty	

Table 8.18: Summary of the muon-related nuisance parameters considered in the analysis.

Tau leptons

The hadronic τ-lepton uncertainties are estimated using the techniques described in Ref. [184]. These arise from various sources, including energy scale, reconstruction efficiency, and identification efficiency. Additionally, identification efficiency uncertainties are based on comparisons of τ-lepton identification in data and MC samples, and trigger efficiency uncertainties are derived from comparing data and simulation for different years. Table 8.19 summarises the different sources of hadronic τ-lepton systematic uncertainty considered in this analysis.

Jets

The jet uncertainties are estimated using the techniques described in Ref. [177]. These arise from various sources, including JES and JER uncertainties. The JES uncertainties are divided into several categories, including statistical, mixed, modelling, and detector uncertainties. JER uncertainties account for differences between data and MC in various regions of phase space. Additional uncertainties arise from factors such as inter-calibration, punch-through effects, pile-up subtraction, and single particle responses. Flavour-related uncertainties are included to account for variations in jet flavour composition and response. Furthermore, uncertainties in JVT and b-tagging are considered, with separate contributions for b, c, and light flavour jets. Table 8.20 summarises the different sources of jet systematic uncertainty considered in this analysis.

Nuisance Parameter	Description
TAUS_TRUEHADTAU_SME_TES_INSITUEXP	Energy scale uncertainty
TAUS_TRUEHADTAU_SME_TES_INSITUFIT	
TAUS_TRUEHADTAU_SME_TES_DETECTOR	
TAUS_TRUEHADTAU_SME_TES_MODEL_CLOSURE	
TAUS_TRUEHADTAU_SME_TES_PHYSICSLIST	
TAUS_TRUEHADTAU_EFF_RECO_TOTAL	Reconstruction efficiency uncertainty
TAUS_TRUEHADTAU_EFF_RNNID_1PRONGSTATSYSTPT2025	Identification efficiency uncertainty
TAUS_TRUEHADTAU_EFF_RNNID_1PRONGSTATSYSTPT2530	
TAUS_TRUEHADTAU_EFF_RNNID_1PRONGSTATSYSTPT3040	
TAUS_TRUEHADTAU_EFF_RNNID_1PRONGSTATSYSTPTGE40	
TAUS_TRUEHADTAU_EFF_RNNID_SYST	
TAUS_TRUEHADTAU_EFF_RNNID_HIGHPT	
TAUS_TRUEHADTAU_EFF_TRIGGER_STATDATA161718	Trigger efficiency uncertainty
TAUS_TRUEHADTAU_EFF_TRIGGER_STATMC161718	
TAUS_TRUEHADTAU_EFF_TRIGGER_SYST161718	
TAUS_TRUEHADTAU_EFF_TRIGGER_SYSTMU161718	
TAUS_TRUEHADTAU_EFF_TRIGGER_STATDATA2018	
TAUS_TRUEHADTAU_EFF_TRIGGER_STATMC2018	
TAUS_TRUEHADTAU_EFF_TRIGGER_SYST2018	
TAUS_TRUEHADTAU_EFF_TRIGGER_SYSTMU2018	
TAUS_TRUEELECTRON_EFF_ELEBDT_STAT	Electron veto uncertainty
TAUS_TRUEELECTRON_EFF_ELEBDT_SYST	

Table 8.19: Summary of the nuisance parameters related to hadronically decaying τ-leptons considered in the analysis.

Missing transverse energy

The uncertainties on $E_{\mathrm{T}}^{\mathrm{miss}}$ arise from the soft term calibration and are estimated using the techniques described in Ref. [189]. These include uncertainties related to the resolution of the soft term in both the parallel and perpendicular components relative to the beam axis, as well as uncertainties related to the energy scale of the soft term. The different sources $E_{\mathrm{T}}^{\mathrm{miss}}$ systematic uncertainty considered in this analysis is summarised in Table 8.21.

Nuisance Parameter	Description
JET-EffectiveNP-Statistical[1-6]	Energy scale uncertainty
JET-BJES-Response	
JET-EtaIntercalibration-Modelling	
JET-EtaIntercalibration-Modelling-2018data	
JET-EtaIntercalibration-TotalStat	
JET-EtaIntercalibration-NonClosure-highE	
JET-EtaIntercalibration-NonClosure-negEta	
JET-EtaIntercalibration-NonClosure-posEta	
JET-SingleParticle-HighPt	
JET-EffectiveNP-Mixed[1-3]	
JET-Pileup-OffsetMu	Pile-up subtraction uncertainty
JET-Pileup-OffsetNPV	
JET-Pileup-PtTerm	
JET-Pileup-RhoTopology	
JET-EffectiveNP-Modelling[1-4]	Calibration uncertainty
JET-EffectiveNP-Detector[1-2]	
JET-JER-EffectiveNP-[1-12]	Energy resolution uncertainty
JET-JER-DataVsMC	
JET-PunchThrough-MC16	Punch-through uncertainty
JET-Flavor-Composition	Flavour composition uncertainty
JET-Flavor-Response	Flavour response uncertainty
JET-JvtEfficiency	Jet vertex tagger efficiency uncertainty
JET-fJvtEfficiency	Forward jet vertex tagger efficiency uncertainty
FT-EFF-Eigen-B-[0-2]	b-tagging uncertainty
FT-EFF-extrapolation	
FT-EFF-Eigen-C-[0-2]	c-tagging uncertainty
FT-EFF-extrapolation-from-charm	
FT-EFF-Eigen-Light-[0-3]	Light flavour tagging uncertainty
FT-EFF-Eigen-Light-4	

Table 8.20: Summary of the different sources of jet systematic uncertainty. The systematic sources containing brackets are parametrised as multiple nuisance parameters.

Nuisance Parameter	Description
MET-SoftTrk-ResoPara	Resolution uncertainty (parallel component)
MET-SoftTrk-ResoPerp	Resolution uncertainty (perpendicular component)
MET-SoftTrk-Scale	Soft track energy scale uncertainty

Table 8.21: Summary of the different sources of MET systematic uncertainty.

8.6.3 Uncertainties for data-driven background estimation

Modelling uncertainties arise from both the object-level embedding procedure and the fake estimation using the matrix method. Both methods are detailed in Section 8.5.

Object level embedding uncertainties

In the embedding procedure, several sources of systematic uncertainty are considered. All experimental systematic uncertainties described previously are propagated to the embedded sample. Additionally, the impact of experimental systematics on the efficiency and unfolding/folding maps used in the embedding procedure is evaluated. A separate map is computed for each systematic variation, and the embedding procedure is repeated accordingly. These uncertainties account for lepton/τ-lepton trigger efficiency, electron and muon energy scale and resolution, electron isolation efficiency, muon reconstruction efficiency, and τ-lepton reconstruction efficiency.

Finally, a closure systematic is evaluated by comparing the embedded $Z \to \ell\ell$ MC to the nominal $Z \to \tau\tau$ MC in the CRs. This is the main source of uncertainty from the embedding procedure, and can be seen in Figure 8.29.

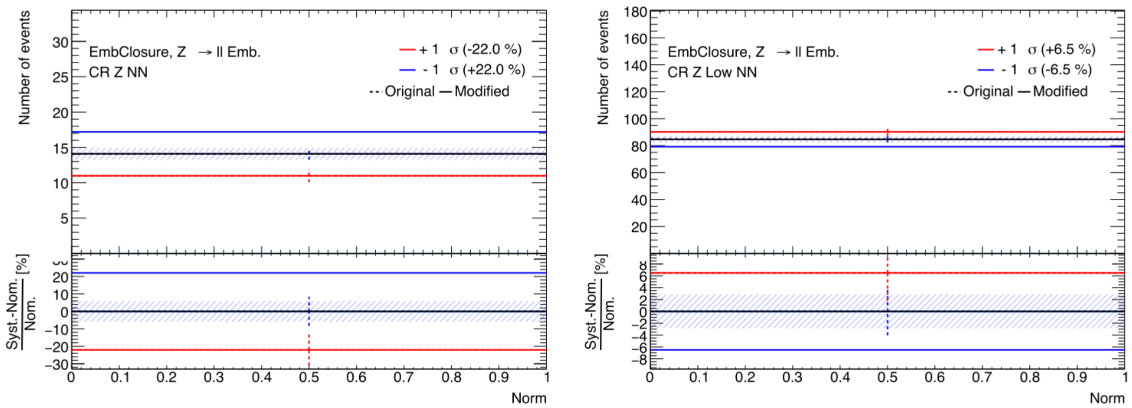

a) CR high NN

b) CR low NN

Figure 8.29: Closure systematic uncertainty in the high and low NN embedding CRs. These regions follow the same selection as the SRs, but with embedded MC and data. The embedded $Z \to \ell\ell$ prediction is indicated in black, and the nominal $Z \to \tau\tau$ MC prediction is indicated in red, with a one-sided symmetrisation procedure being applied to obtain the mirrored symmetrisation indicated in blue.

Fake uncertainties

Uncertainties related to the fake estimation arise from statistical uncertainties, flavour composition and prompt lepton contribution for the simulated events used to compute the real and fake efficiencies. Additionally, the statistical uncertainties on the efficiencies themselves are propagated to the estimated fake sample.

Uncertainties related to the statistical precision of the efficiencies are evaluated by varying the real electron, real muon, fake electron, and fake muon efficiencies up and down within their statistical uncertainties, and recomputing the fake estimate. This procedure results in four separate uncertainty components.

In the fake estimation procedure prompt leptons are subtracted in order to isolate the fake contribution in data. To evaluate the uncertainty on the prompt component, the normalisation of truth-matched MC is varied up/down by 30% in the electron and muon Fake region. The efficiencies are re-computed separately for electrons and muons and the resulting variations in the estimated fake samples with respect to nominal is taken as the uncertainty. This results in two uncertainties on the final estimation.

The flavour composition in the Fake region used to derive efficiencies differs from the SRs where they are applied. To account for this uncertainty, fake efficiencies are recalculated using a selection that requires a b-jet instead of a b-veto. This modification increases the heavy flavour content, leading to significantly different efficiencies. The procedure is performed separately for muons and electrons, introducing two uncertainties on the final estimate. While this approach may not fully capture the flavour transition between SS and OS regions, it provides a conservative uncertainty that covers and slightly overestimates these effects.

Real efficiencies are derived in regions with a looser selection than the VBF inclusive region, using $Z \to \ell\ell$, top, and diboson events. To assign an uncertainty, efficiencies are recalculated using the inclusive VBF SR selection. This procedure is performed separately for muons and electrons, resulting in two uncertainties in the final estimate.

The closure in the VBF SS VR is evaluated by comparing the fake estimate with data. The deviations per bin in the Optimal Observable (Figure 8.26 b) is propagated to the SRs and evaluated as a systematic uncertainty.

8.7 Fit model

To obtain the best estimates and uncertainties for the EFT parameters ($\tilde{d}$, $c_{H\tilde{W}}$, $c_{H\tilde{B}}$ and $c_{H\tilde{W}B}$) maximum likelihood fits are performed. Each parameter is fitted separately where the POI in the fit model is set accordingly. The general fit setup follows the procedure described in Section 7.2 where the negative log likelihood is computed in the ranges summarised in Table 8.22. The ranges differ based on the measured EFT parameter, reflecting the sensitivity of the analysis to the parameter. The signal points used to construct samples for BSM scenarios in these ranges are obtained with the reweighting procedures described in Section 8.1.3. The difference in the computed likelihood between each point and the minimum is calculated, and interpolated to construct a ΔNLL curve. The minimum of the curve corresponds to the best fitted and central value of the measured POI. The 68% and 95% confidence intervals are extracted from where the curve intersects the values 0.5 and 1.92 respectively. This approximately corresponds to the 1σ and 2σ uncertainty bands on the measurement. Measurements of the EFT parameters therefore implies finding the best fit value of the POI ($\hat{\mu}$) and its 68% and 95% confidence interval:

$$[\hat{\mu} - \sigma_{\hat{\mu}}, \hat{\mu} + \sigma_{\hat{\mu}}], \tag{8.29}$$

The fits are implemented in the TrexFitter [228] (internal) framework developed by ATLAS, which is built from the HistFactory [192] and RooStats [193] packages.

POI (EFT parameter)	Number of scan points	Range [min, max]
$\tilde{d}$	121	[-0.15, 0.15]
$c_{H\tilde{W}}$	121	[-5.0, 5.0]
$c_{H\tilde{B}}$	121	[-20.0, 20.0]
$c_{H\tilde{W}B}$	121	[-20.0, 20.0]

Table 8.22: Ranges used to compute the maximum likelihood for each measured EFT parameter.

Figure 8.30 shows the predicted SM distribution alongside the two endpoints of the range ($\tilde{d} = \pm 0.15$) used in the ΔNLL scan, illustrating how the shape evolves with $\tilde{d}$ in the high NN SR. The shape effects from the Warsaw basis parameters follow a similar pattern. To ensure that the analysis remains sensitive only to changes in the shape from the interference term in Eq. 3.18, and not to the overall normalisation, the CP-odd VBF Higgs distributions are normalised to the SM.

Profile likelihood fits are generally used to extract the normalisation of a given distribution. However, in this analysis, multiple distributions are fitted simultaneously, each corresponding to different reweighting scenarios where the POI affects the shape of the signal prediction. To reformulate this as a normalisation problem, template morphing is employed. This method interpolates between templates, assigning each bin i a normalisation weight w_i that depends on the POI:

$$S_i = \sum_t w_i^t(\mathrm{POI}) \cdot T_i. \tag{8.30}$$

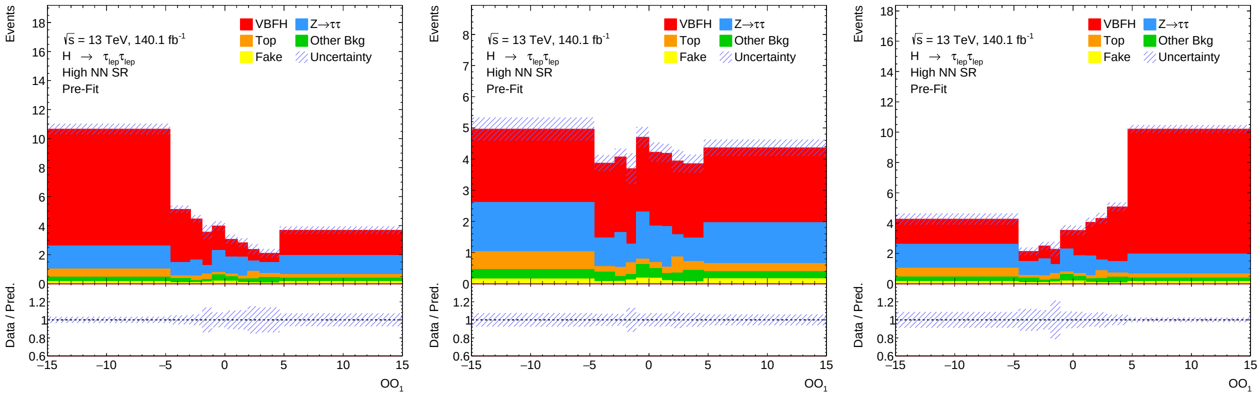

a) $\tilde{d} = -0.15$ b) $\tilde{d} = 0$ c) $\tilde{d} = 0.15$

Figure 8.30: Optimal Observable distributions in the high NN SR for $\tilde{d} = -0.15$ (left), $\tilde{d} = 0$ (middle), and $\tilde{d} = 0.15$ (right). These signal points define the maximum range used in the ΔNLL scan, where $\tilde{d} = 0$ corresponds to the SM prediction without reweighting.

Here, T_i represents the SM VBF prediction, w_i^t is the reweighting factor, and S_i is the resulting signal prediction. The likelihood for each template is then computed to evaluate the compatibility between different signal hypotheses and data. The interpolation is achieved using bin-by-bin polynomial fits to the signal templates.

Since the templates are normalised to the SM, the quadratic dependence expected from the reweighting expressions does not fully capture the evolution of the EFT parameters. To allow for more flexibility in the tempalte morphing fit, an octic parametrization is used instead. Figure 8.31 illustrates the procedure, showing how a quadratic polynomial fit describes the template points in the first bin of the Optimal Observable as a function of $\tilde{d}$. Without the SM normalisation, the quadratic fit captures the dependence well. However, once normalisation is applied, the quadratic function lacks the flexibility needed to fit the curve to the signal points. Switching to an octic parametrisation resolves this issue, accurately capturing the dependence on $\tilde{d}$. When computing the likelihoods, signal predictions are extracted from the fitted octic curve in each bin of the Optimal Observable.

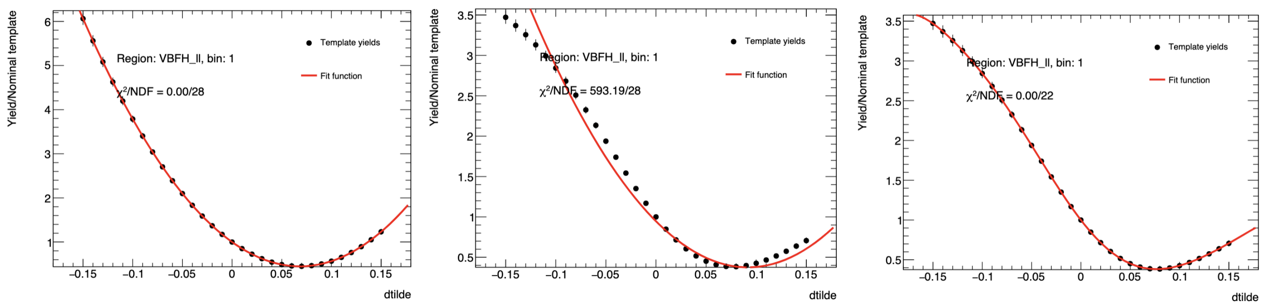

a) Quadratic b) Quadratic SM norm c) Octic SM norm

Figure 8.31: Fitted templates for $\tilde{d}$ in the first bin of the Optimal Observable in the high NN SR. The plots compare a quadratic polynomial fit without SM normalisation (left), a quadratic fit with SM normalisation (middle), and an octic polynomial fit with SM normalisation (right).

The general fitting procedure for each POI is divided into two steps. First single channel fits for $\tau_\ell\tau_\ell$, $\tau_\ell\tau_h$ and $\tau_h\tau_h$ are done separately to evaluate the sensitivity in each channel. Secondly, a combined fit is performed where all experimental and theoretical systematic uncertainties are considered 100% correlated across channels. In the $\tau_\ell\tau_\ell$ channel 5 regions are fitted simultaneously to data:

VBF Higgs SRs: Two signal regions are defined in the low and high NN score regions, based on the kinematic and NN selection described in Section 8.3. Both regions are binned in the Optimal Observable using 10 bins with variable width, chosen such that the VBF Higgs signal is equally populated in each bin.

$Z\tau\tau$ CRs: Two corresponding CRs are defined utilising the embedding procedure described in Section 8.6.3. These regions follow the exact same kinematic and NN selection as the the two SRs. A common normalisation factor $NF^{\ell\ell}_{Z\tau\tau}$ is assigned to the embedded $Z \to \ell\ell$ MC in the CRs and propagated to control the normalisation of $Z \to \tau\tau$ in SRs. In the fit, the $Z \to \ell\ell$ MC is normalised to the embedded data in the CRs, while in the SRs, $Z \to \tau\tau$ MC is normalised to data. The same procedure is followed in all three channels.

Top CR: A dedicated top CR is defined by inverting the b-veto in the VBF inclusive selection as described in Section 8.5.3. A single normalisation factor $NF^{\ell\ell}_{Top}$ is assigned to the top MC in the CR and propagated to control the normalisation in the SRs. This NF is only applied in the $\tau_\ell\tau_\ell$ channel.

In addition to the two background normalisation factors, the normalisation of the VBF signal is controlled by a free-floating normalisation factor, $NF^{\ell\ell}_{VBF}$. This is included to avoid probing effects coming from overall changes in the cross-section that may arise from additional CP-even terms, ensuring that only differences in the shape of the Optimal Observable due to the interference term are considered when measuring each POI. In the individual channels, the signal normalisation factor is treated as uncorrelated, whereas in the combined fit, a common signal normalisation factor is used across all three channels. The $Z \to \tau\tau$ normalisation factor, obtained from the embedded CRs, is treated separately in each channel both in the individual and combined fits, as there is some channel-dependence on the embedding procedure. The regions and normalisation factors are summarised in Table 8.23.

8.7.1 Results in the $\tau_\ell\tau_\ell$ channel

The predicted and observed distributions in the Optimal Observable in the low and high NN SRs are shown in Figure 8.32 before and after the fit. All previously mentioned systematic uncertainty sources are incorporated

NF	MC Sample	Region
$NF^{hh}_{Z\tau\tau}$	$Z \to \ell\ell$ (Embedding) / $Z \to \tau\tau$	$Z\tau\tau$CR^{hh} + SR^{hh} (high/low NN)
$NF^{\ell h}_{Z\tau\tau}$	$Z \to \ell\ell$ (Embedding) / $Z \to \tau\tau$	$Z\tau\tau$CR$^{\ell h}$ + SR$^{\ell h}$(high/low NN)
$NF^{\ell\ell}_{Z\tau\tau}$	$Z \to \ell\ell$ (Embedding) / $Z \to \tau\tau$	$Z\tau\tau$CR$^{\ell\ell}$ + SR$^{\ell\ell}$ (high/low NN)
$NF^{\ell\ell}_{Top}$	$t\bar{t}$/ single top	TopCR$^{\ell\ell}$ + SR$^{\ell\ell}$(high/low NN)
NF^{hh}_{VBF}	VBF Higgs ($H \to \tau\tau/H \to WW$)	SR^{hh} (high/low NN)
$NF^{\ell h}_{VBF}$	VBF Higgs ($H \to \tau\tau/H \to WW$)	SR$^{\ell h}$ (high/low NN)
$NF^{\ell\ell}_{VBF}$	VBF Higgs ($H \to \tau\tau/H \to WW$)	SR$^{\ell\ell}$ (high/low NN)
NF_{VBF}	VBF Higgs ($H \to \tau\tau/H \to WW$)	SR$^{\ell\ell}$+SR$^{\ell h}$+ SR^{hh} (high/low NN)

Table 8.23: List of normalisation Factors used in the fit, the MC they are used for, and the region where the NFs are estimated.

as nuisance parameters in the fit. They are set to their best fit values and constrained from fitting the prediction to data in all the regions.

The data is symmetric in the Optimal Observable and consistent with the SM prediction within uncertainties. No sign of CP violation is observed in data. The mean value of the data in the Optimal Observable for both SRs is summarised in Table 8.24 and is consistent with zero in both cases.

High NN SR	$\langle OO \rangle = -0.12 \pm 0.57$
Low NN SR	$\langle OO \rangle = -0.09 \pm 0.31$

Table 8.24: The observed mean value of the Optimal Observable and associated uncertainty in the low and high NN SR.

A summary plot of the all regions that enter the fit can be found in Figure 8.33, showing the pre-fit and post-fit normalisation in each SR and CR with systematic and statistical uncertainties. The estimated normalisation factors from the fit are summarised in Table 8.25, all consistent with one within uncertainties. The post-fit yields for each process in all regions are shown in Table 8.26.

Normalisation factor	Value
$NF^{\ell\ell}_{VBF}$	$1.13^{+0.28}_{-0.32}$
$NF^{\ell\ell}_{Z\tau\tau}$	$1.01^{+0.10}_{-0.10}$
$NF^{\ell\ell}_{Top}$	$0.95^{+0.08}_{-0.07}$

Table 8.25: Normalisation factors estimated by the simultaneous fit in the CRs and SRs in the $\tau_\ell\tau_\ell$ channel.

In order to set limits on the EFT parameters, separate fits are performed where for each fit the POI is set to the targeted EFT scenario. The ΔNLL curves for the considered EFT parameters are shown in Figure 8.34. For each POI, three fits are conducted: two to extract the expected ΔNLL curves using the MC prediction with and without systematic uncertainties, and one to obtain the observed result using data including systematic uncertainties. The expected curves are derived using Asimov pseudodata in the SRs, but using observed data

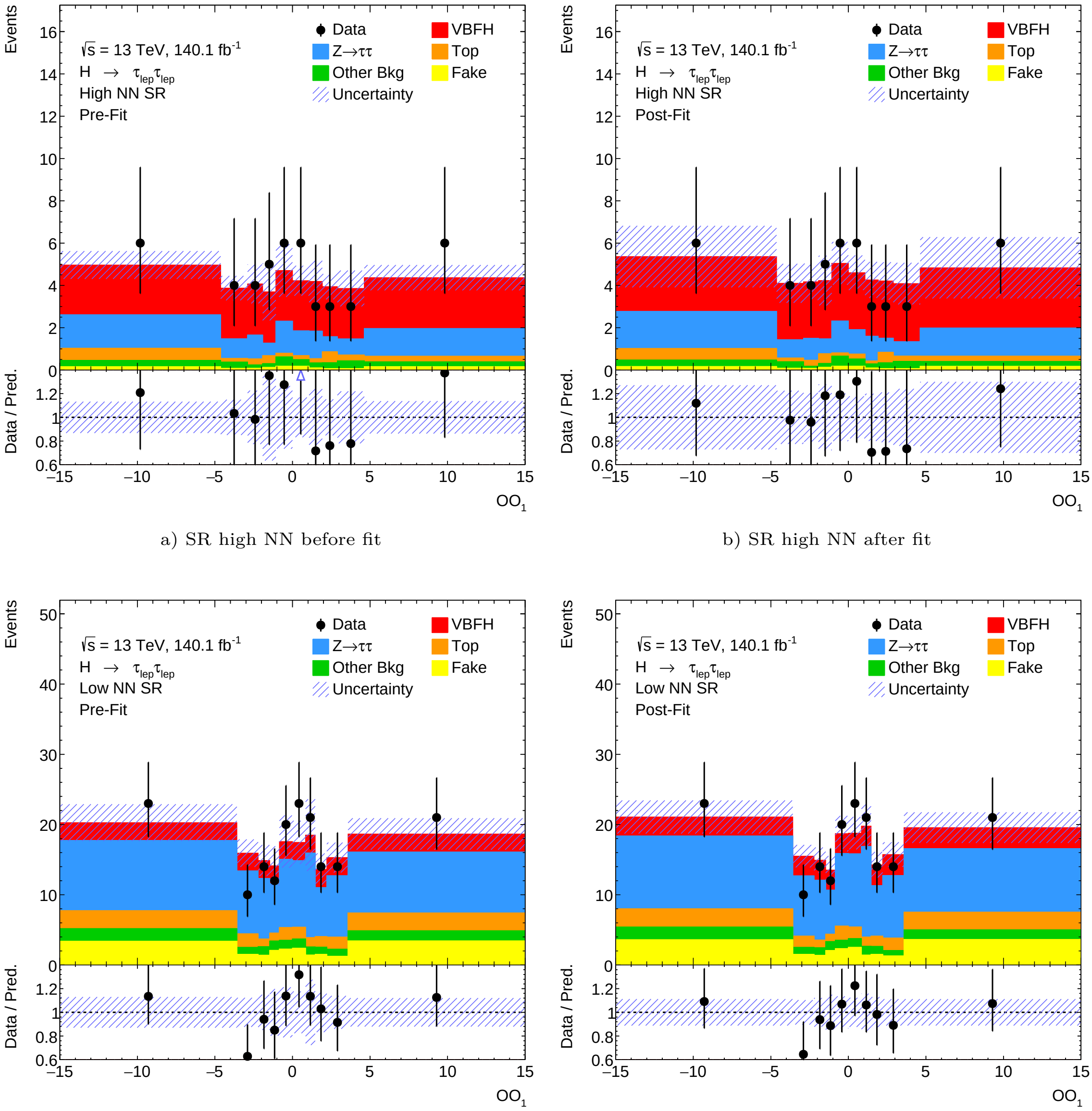

a) SR high NN before fit

b) SR high NN after fit

c) SR low NN before fit

d) SR low NN after fit

Figure 8.32: Predicted and observed distributions in the high (top) and low (bottom) NN Optimal Observable SRs before the fit (left) and after the fit (right).

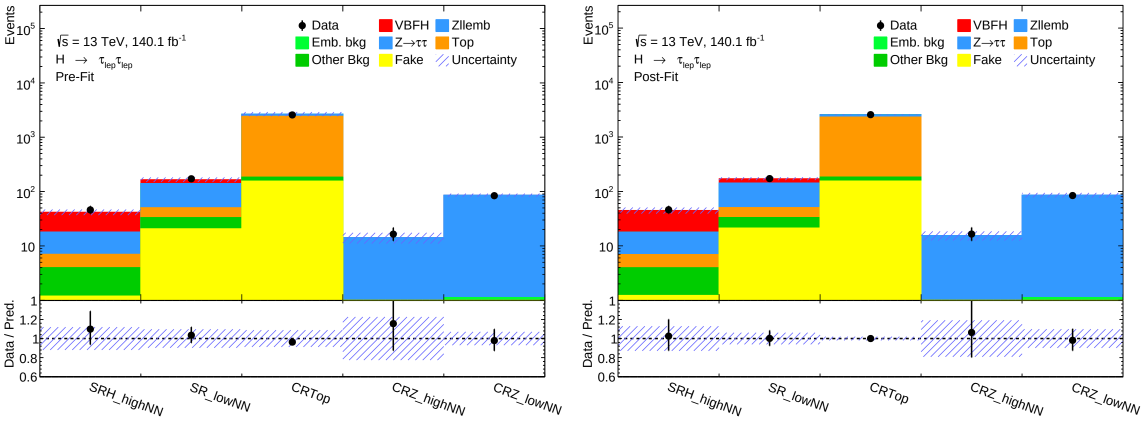

a) Normalisation before fit

b) Normalisation after fit

Figure 8.33: Summary of all regions that enter the fit before and after the fit.

	High NN SR	Low NN SR	High NN $Z \to \tau\tau$ CR	Low NN $Z \to \tau\tau$ CR	Top CR
VBFH	27 ± 7	29 ± 7			7.7 ± 0.6
$Z \to \ell\ell$ Emb.			15.3 ± 3.0	84 ± 8	
Emb. bkg			0.16 ± 0.01	1.12 ± 0.03	
$Z \to \tau\tau$	10.9 ± 3.4	93 ± 12			239 ± 35
Top	3.0 ± 1.2	17 ± 4			2140 ± 60
Other Higgs	1.3 ± 0.4	4.4 ± 1.7			3.0±0.6
Other backgrounds	1.4 ± 0.4	7.6 ± 1.4			22.9 ± 2.5
Fake	1.2 ± 0.4	21 ± 6			155.6 ± 1.0
Total	45 ± 6	172 ± 10	15.5 ± 3.0	86 ± 8	2570 ± 50
Data	46	172	16	84	2571

Table 8.26: Post-fit yields in each region of the analysis. The uncertainty includes both statistical and systematic uncertainties which are constrained by the fit. The normalisation of the signal, top and $Z \to \tau\tau$ have been corrected with corresponding normalisation factors. Other Higgs corresponds to ggF and VH production, while other backgrounds correspond to $Z \to \ell\ell$ and diboson processes.

in the CRs. This ensures that the same background normalisation factors are propagated to the SRs for both the expected and observed results. The observed curve is obtained with data in all regions. The minimum value of each curve gives the best fit value for the corresponding POI, and the 1σ and 2σ uncertainty bands are obtained from the 68% and 95% confidence intervals, extracted from where the curves intersect the values 0.5 and 1.92 respectively. The expected and observed best fit values as well as associated 68% and 95% confidence intervals for each measured EFT parameter are summarised in Table 8.27. All measurements are consistent with the SM and no sign of CP violation is observed. Both the expected and observed $\tau_\ell\tau_\ell$ results in the HISZ basis are more sensitive than the results from the combined partial Run $H \to \tau\tau$ analysis [51], which measured $\tilde{d} \in [-0.035, 0.033]$ (expected) and $\tilde{d} \in [-0.090, 0.035]$ (observed) at 68% confidence level.

It should be noted again that the analysis is mainly sensitive to $\tilde{d}$ and $c_{H\tilde{W}}$, as the VBF topology is dominated

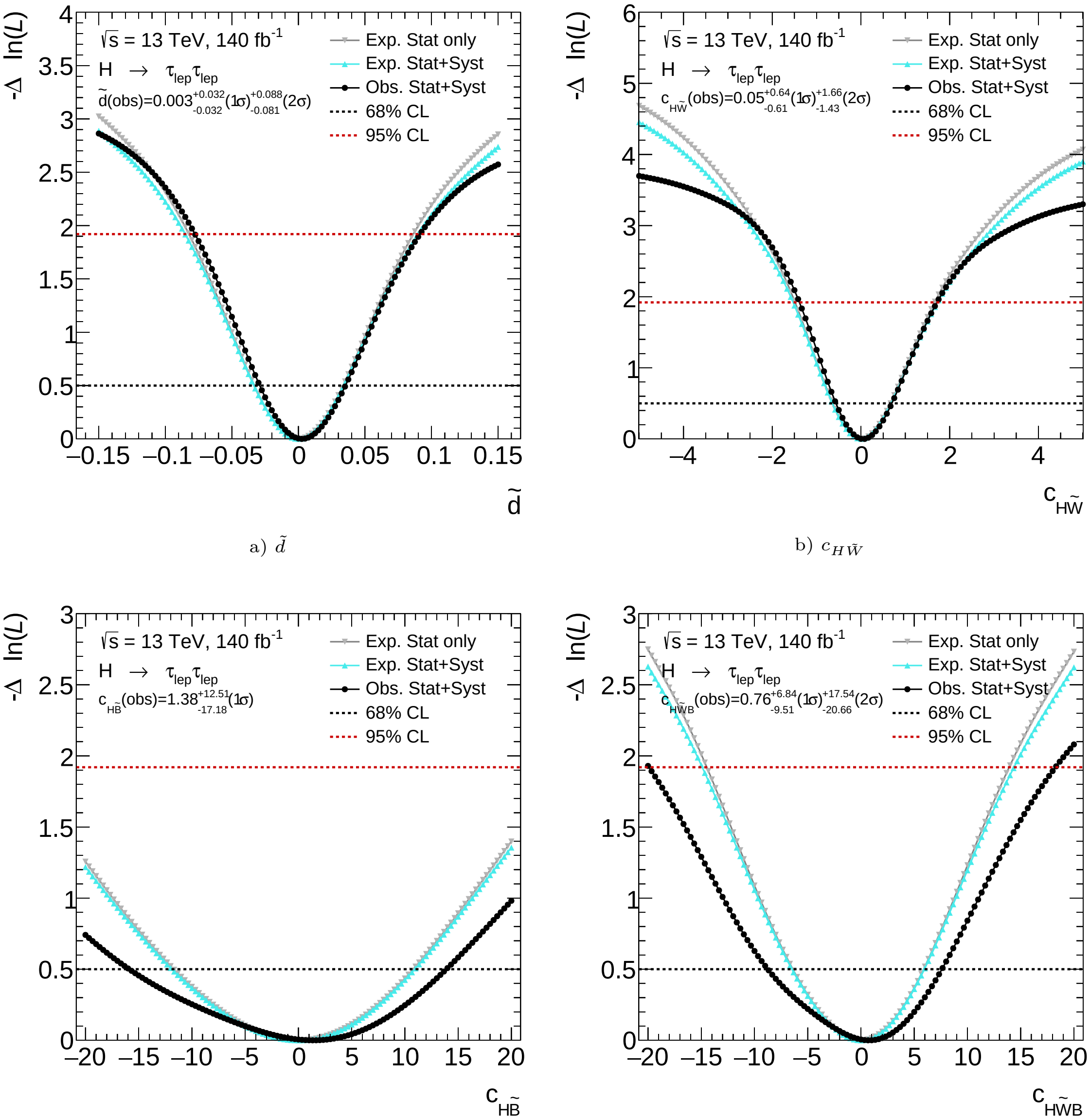

a) $\tilde{d}$

b) $c_{H\tilde{W}}$

c) $c_{H\tilde{B}}$

d) $c_{H\tilde{W}B}$

Figure 8.34: ΔNLL curves for all considered EFT parameters in the $\tau_\ell\tau_\ell$ channel are shown, with measurements presented in the HISZ basis via $\tilde{d}$ (top left), and in the Warsaw basis via $c_{H\tilde{W}}$ (top right), $c_{H\tilde{B}}$ (bottom left), and $c_{H\tilde{W}B}$ (bottom right). The expected curves, obtained with and without systematic uncertainties, are shown in grey and cyan respectively, while the observed curve is shown in black. The measurement of each EFT parameter is also shown, corresponding to the best observed fit value, along with its 1σ and 2σ uncertainties, corresponding to the 68% (black dashed line) and 95% (red dashed line) confidence intervals, respectively.

by interactions in the HWW vertex. Consequently, setting limits on $c_{H\tilde{B}}$ and $c_{H\tilde{W}B}$ requires evaluating the likelihood scans over extended intervals that may lie outside the validated range of the reweighting procedure and the Optimal Observable. For this reason these EFT parameters were dropped from the measurement in the $H \to \gamma\gamma$ analysis [53]. They are however kept in this thesis for consistency. To evaluate how much of the sensitivity comes the linear interference term in Eq. 3.18, additional fits are performed where only the linear term is used for reweighting. Since the analysis aims to probe the interference term it is expected that this should be the dominant source of sensitivity. This is indeed what is observed, with the linear-only and linear+quadratic fit results agreeing within roughly 10-15%.

Parameter	Observed Best Value	68 % CI (Exp.)	95 % CI (Exp.)	68 % CI (Obs.)	95 % CI (Obs.)
$\tilde{d}$	0.003	$[-0.034, 0.034]$	$[-0.085, 0.089]$	$[-0.029, 0.035]$	$[-0.078, 0.091]$
$\tilde{d}$ (lin. only)	0.003	$[-0.030, 0.031]$	$[-0.072, 0.077]$	$[-0.025, 0.032]$	$[-0.061, 0.078]$
$c_{H\tilde{W}}$	0.05	$[-0.65, 0.68]$	$[-1.53, 1.72]$	$[-0.56, 0.69]$	$[-1.38, 1.71]$
$c_{H\tilde{W}}$ (lin. only)	0.06	$[-0.57, 0.63]$	$[-1.30, 1.68]$	$[-0.51, 0.61]$	$[-1.11, 1.43]$
$c_{H\tilde{W}B}$	0.76	$[-6.49, 5.96]$	$[-14.91, 14.36]$	$[-8.75, 7.60]$	$[-19.9, 18.3]$
$c_{H\tilde{B}}$	1.38	$[-11.88, 10.93]$	$-$	$[-15.8, 13.89]$	-

Table 8.27: Expected and observed 68 % and 95 % confidence intervals for the $\tau_\ell\tau_\ell$ fit results in the Optimal Observable with interpretations both in the HISZ and Warsaw basis. The observed best fit value is also shown. All parameters are measured with linear and quadratic reweighting, with additional linear-only fits performed for $\tilde{d}$ and $c_{H\tilde{W}}$. Neither the observed nor excepted 95% confidence interval are reached for the $c_{H\tilde{B}}$ curves.

The grouped impact of different sources of systematic uncertainty is shown in Table 8.28, alongside the total statistical uncertainty. The analysis is dominated by statistical uncertainties, but among the systematics, the jet energy resolution and calibration, as well as uncertainties related to the $E_{\mathrm{T}}^{\mathrm{miss}}$ soft term, have the largest impact.

The 30 individual NPs with the largest impact on the measurement of $\tilde{d}$ are shown and ranked in Figure 8.35, along with their respective pull values. The pull measures how much a NP deviates from its nominal value after being fit to data. It is defined as:

$$\mathrm{pull} = \frac{\hat{\theta} - \theta_0}{\Delta\theta}, \tag{8.31}$$

where $\hat{\theta}$ is the best-fit value of the NP, θ_0 is the nominal value, and $\Delta\theta$ is the pre-fit uncertainty. A pull close to zero means the fit has not significantly changed the NP, while a pull far from zero could indicate tension between prediction and data. In addition to the JER and $E_{\mathrm{T}}^{\mathrm{miss}}$-related systematics, notable contributions arise from MC statistical uncertainties in the first and last bins of the Optimal Observable distribution in the high NN SR, as well as from the normalisation factor for the VBF signal. This is expected, as the edge bins are particularly sensitive to any signal asymmetry, and the signal normalisation directly affects the signal yield in these regions, thereby influencing the overall sensitivity of the measurement. Importantly, the ranking and impact of the systematics show good agreement between the expected and observed results, indicating the fit

Source	**Relative impact on the $\tilde{d}$ 68% CL interval**
Higgs theory	± 2.78%
Top theory	± 3.80%
$Z \to \tau\tau$ theory	± 3.14%
Flavour tagging	± 0.49%
Luminosity	± 0.19%
Lepton reconstruction	± 3.14%
Jet and $E_{\mathrm{T}}^{\mathrm{miss}}$ reconstruction	± 19.1%
Embedding	± 0.38%
Fake	± 2.91%
Normalisation factors	± 5.21%
MC sample size	± 15.4%
Total Systematic	± 26.7%
Total Statistical	± 96.2%

Table 8.28: Grouped impact of different systematic uncertainty sources and the total statistical uncertainty on the 68% confidence level fit result for $\tilde{d}$ in the $\tau_\ell\tau_\ell$ channel. Experimental systematics on the reconstruction of the objects include the reconstruction efficiency, energy scale and resolution, and trigger efficiencies. Sample size includes the per-bin statistical uncertainties in the simulated MC samples, and on the data-driven backgrounds of misidentified taus. The individual sources of systematic uncertainty can be correlated and do not necessarily add in quadrature to equal the total uncertainty.

is stable and that there is good agreement between the simulated prediction and data. Furthermore, all NPs remain within 1σ of their nominal values, with no of large pulls observed.

The uncertainties on the NPs after the fit are derived from the covariance matrix V_{ij}, which captures how parameters vary together. It is computed as the inverse of the second derivative (Hessian) of the log-likelihood:

$$V_{i,j} = \mathrm{cov}(\theta_i, \theta_j) = -\left[\frac{\partial^2 \ln L(\boldsymbol{\theta})}{\partial\theta_i \partial\theta_j}\right]^{-1}. \tag{8.32}$$

The related correlation matrix for the observed fit result on $\tilde{d}$ is shown in Figure 8.36, with correlation threshold set to 0.1. The observed correlations look reasonable, with top theory systematics correlated with the top NF, embedding closure correlated with the $Z \to \tau\tau$ NF and highest ranked NPs correlated with $\tilde{d}$. To evaluate how much each NP affects the measurement of $\tilde{d}$, its value is shifted up and down by one standard deviation ($\pm 1\sigma$) and the fit is repeated. The resulting variation in the fitted value of $\tilde{d}$ is then evaluated to obtain the impact of each NP.

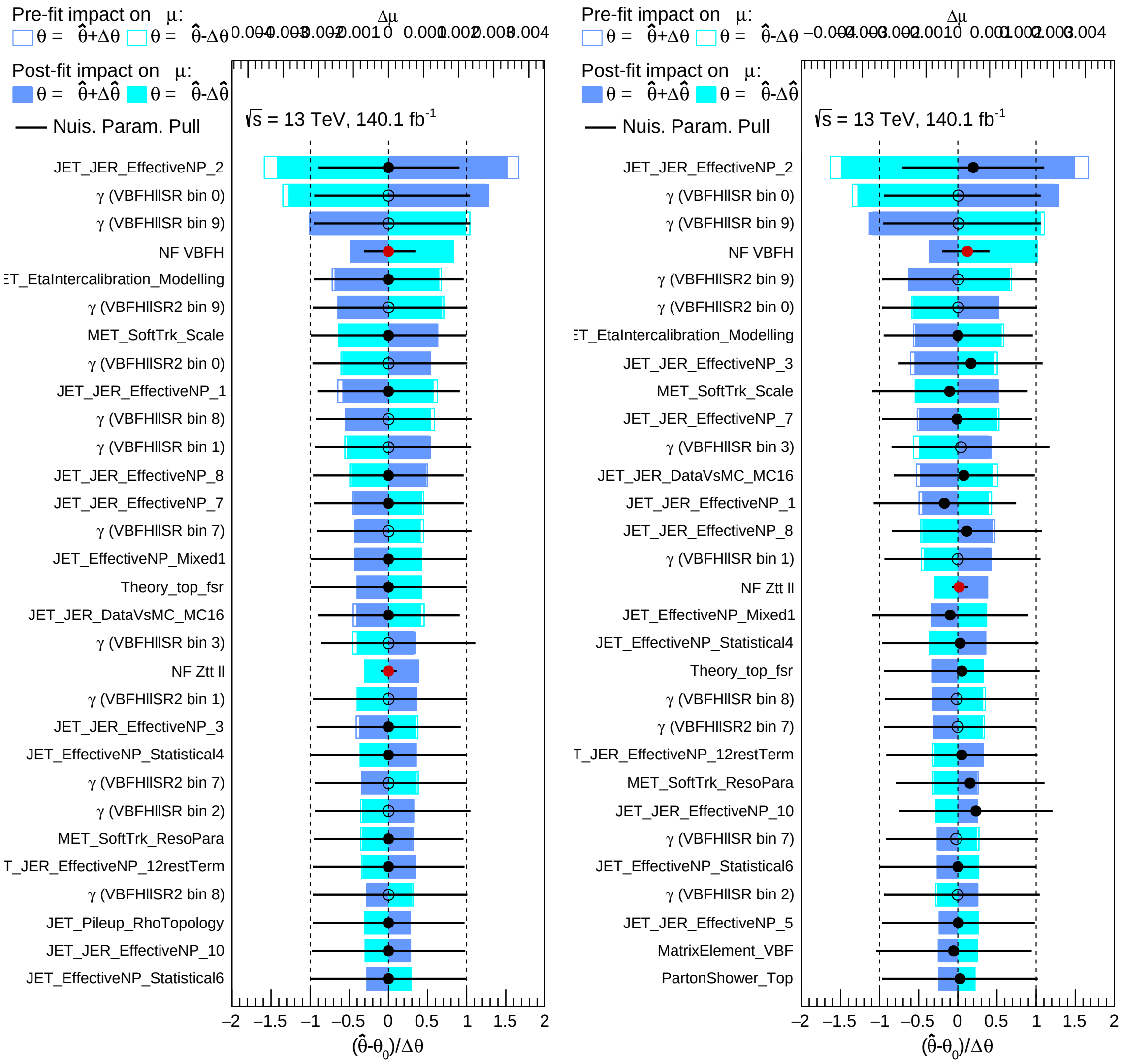

a) Expected NP ranking

b) Observed NP ranking

Figure 8.35: Top 30 ranked nuisance parameters in the expected (left) and observed (right) fit $\tilde{d}$ fit results. The NPs are ordered by their post-fit impact on the parameter on $\tilde{d}$. The blue and cyan bars represent the post-fit and pre-fit impacts, respectively, while the black dots and error bars indicate the fitted NP values (pulls) and their associated uncertainties.

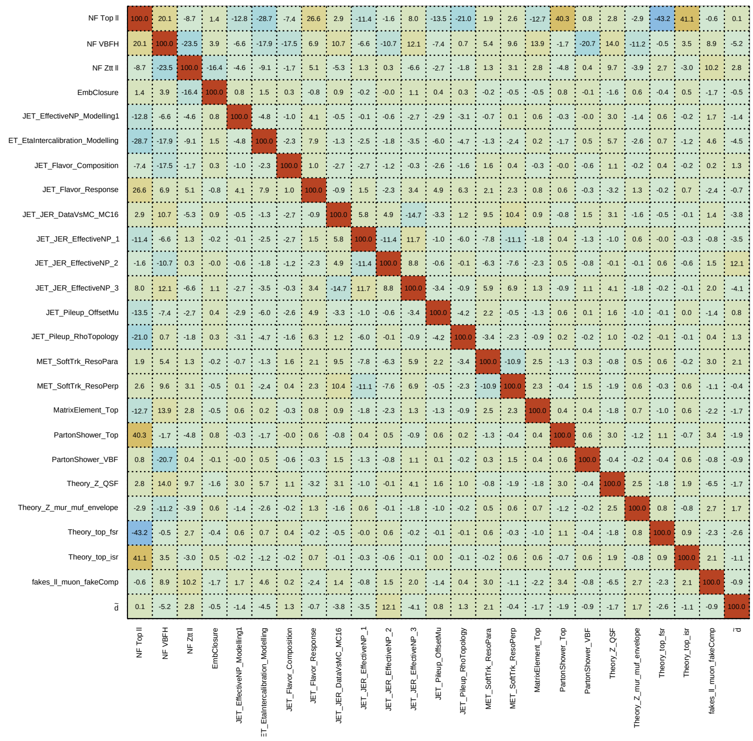

Figure 8.36: Correlation matrix showing pairwise correlations between the NPs among themselves and $\tilde{d}$. Only parameters with absolute correlation above 0.1 are shown.

8.7.2 Combined results with the $\tau_\ell\tau_h$ and $\tau_h\tau_h$ channel

A combined fit is performed with a similar setup as detailed in the previous section, but including also the $\tau_\ell\tau_\ell$ and $\tau_\ell\tau_h$ channel. These two channels each introduces two additional SRs defined from corresponding NN scores and two embedded $Z \to \ell\ell$ CRs following the same kinematic and NN selection. No top CR is defined for either of these channels since contribution from top processes are negligible. One notable difference between the combined fit and stand-alone $\tau_\ell\tau_\ell$ fit is that the signal normalisation factor is now obtained from data in all three channels, NF_{VBF}. This treatment reflects the common VBF production mode, where differences should only arise from the changes in the signal acceptance. The $Z \to \tau\tau$ normalisation factors are treated as uncorrelated since the embedding procedure is implemented separately in each channel. All experimental and theoretical systematic uncertainties are treated as 100% correlated between channels, while channel-specific data-driven uncertainties are treated as uncorrelated.

The post-fit distributions for each channel in the corresponding low and high NN SRs are shown in Figure 8.37. The signal normalisation in each distribution is obtained with the common VBF normalisation factor. The pre-fit distributions for the VBF signal is indicated by the dashed magenta line. Generally data agrees with

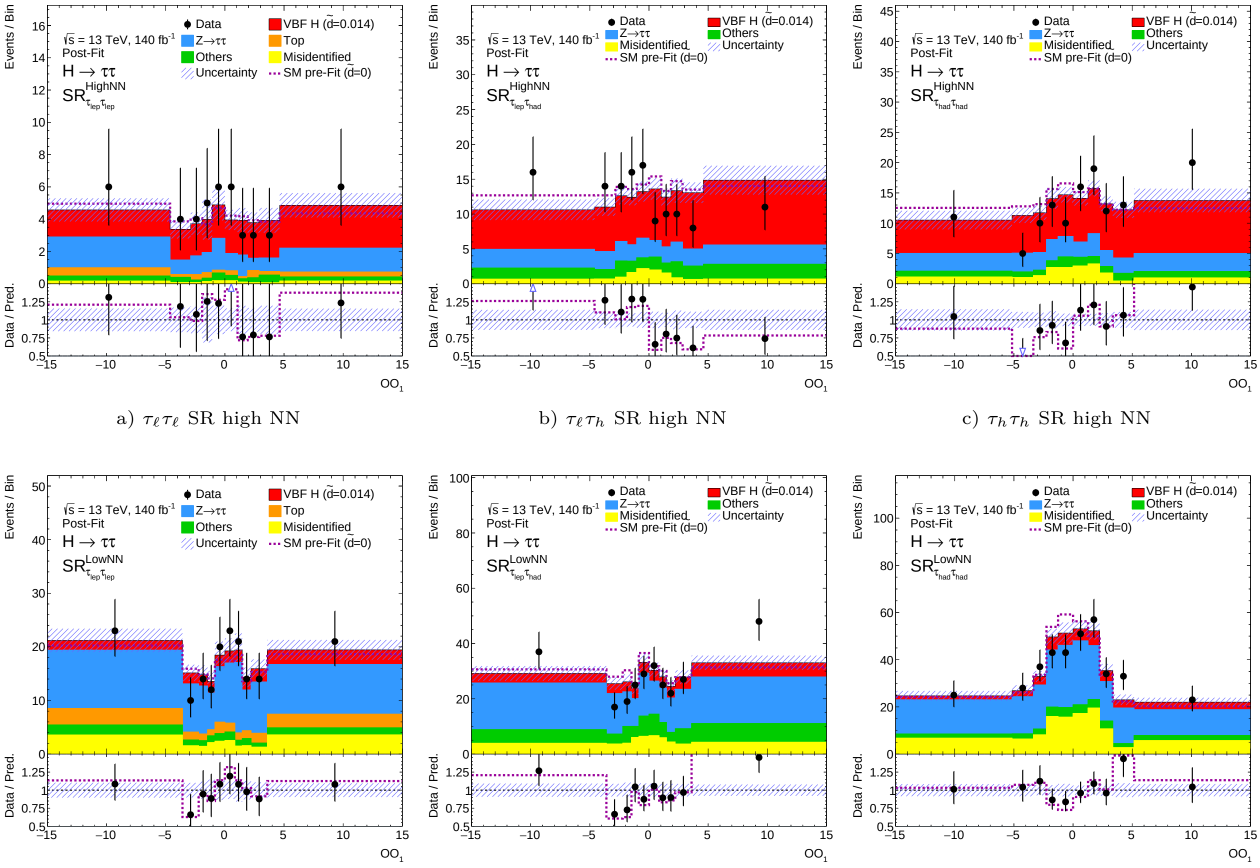

a) $\tau_\ell\tau_\ell$ SR high NN b) $\tau_\ell\tau_h$ SR high NN c) $\tau_h\tau_h$ SR high NN

d) $\tau_\ell\tau_\ell$ SR low NN e) $\tau_\ell\tau_h$ SR low NN f) $\tau_h\tau_h$ SR low NN

Figure 8.37: Post-fit distributions for the high (top) and low (bottom) NN SRs in the $\tau_\ell\tau_\ell$ (left), $\tau_\ell\tau_h$ (middle) and $\tau_h\tau_h$ (right) channel in the Optimal Observable. The pre-fit VBF signal distribution is indicated by the dashed magenta line and $\tilde{d} = 0.014$ corresponds to the best combined fit value in the HISZ basis. In the $\tau_\ell\tau_h$ and $\tau_h\tau_h$ channels Others also include the top background.

prediction within uncertainties in all three channels, with some excess observed in the last bin of the Optimal Observable in the $\tau_\ell\tau_h$ and $\tau_h\tau_h$ high NN SR. Additionally there is a slight under-prediction in the first bin in the $\tau_\ell\tau_h$ high NN SR, and slight excess in the last bin of the $\tau_\ell\tau_h$ low NN SR. Both these channels therefore exhibit slight asymmetry, but in opposite parts of the Optimal Observable distribution. However, no statistical significant deviation with respect to the SM is observed. As also shown in the previous section, data agrees well with prediction in both regions in the $\tau_\ell\tau_\ell$ channel with no asymmetry observed.

The normalisation factors obtained from the fit are summarised in Table 8.29. The common signal normalisation factor is reduced by 22% with respect to the stand-alone $\tau_\ell\tau_\ell$ fit, which has a direct impact of the post-fit yields and sensitivity of the channel.

The expected and observed combined ΔNLL curves for all considered EFT parameters is shown in Figure 8.38. Additionally, curves showing the contribution from each channel are included for comparison. The combined

Normalisation factor	Value
NF_{VBF}	$0.87^{+0.14}_{-0.13}$
$NF^{\ell\ell}_{Z\tau\tau}$	$1.01^{+0.10}_{-0.10}$
$NF^{\ell h}_{Z\tau\tau}$	$0.95^{+0.18}_{-0.15}$
$NF^{hh}_{Z\tau\tau}$	$0.93^{+0.07}_{-0.07}$
$NF^{\ell\ell}_{Top}$	$0.95^{+0.08}_{-0.07}$

Table 8.29: Normalisation factors estimated by the simultaneous fit in all CRs and SRs in the $\tau_\ell\tau_\ell$, $\tau_\ell\tau_h$ and $\tau_h\tau_h$ channel. The same NF_{VBF} is applied in the three channels and is obtained from measurements of data in all 6 SRs.

measurements for each EFT parameter are summarised in Table 8.30. No evidence for CP violation is observed. The results are compatible with the SM prediction within 1σ for $\tilde{d}$ and $c_{H\tilde{W}}$, and within roughly 1.5σ for $c_{H\tilde{B}W}$ and $c_{H\tilde{B}}$. Although larger deviations are observed in the $\tau_\ell\tau_h$ and $\tau_h\tau_h$ channels, the effects largely cancel out in the combined result, as the associated asymmetries appear in opposite regions of the Optimal Observable. The compatibility between the combined and single-channel results are evaluated by comparing the ΔNLL from the respective fits, assuming a χ^2 distribution with two degrees of freedom. The compatibility is found to be at 2.3σ ($p = 0.92\%$), and although this indicates slight tensions between the channels, especially in the $\tau_h\tau_h$ channel, it is not statistically significant.

Parameter	Observed Best Value	68 % CI (Exp.)	95 % CI (Exp.)	68 % CI (Obs.)	95 % CI (Obs.)
$\tilde{d}$	0.014	$[-0.011, 0.011]$	$[-0.023, 0.023]$	$[0.002, 0.028]$	$[-0.011, 0.044]$
$\tilde{d}$ (lin. only)	0.012	$[-0.010, 0.010]$	$[-0.020, 0.020]$	$[0.001, 0.023]$	$[-0.010, 0.035]$
$c_{H\tilde{W}}$	0.27	$[-0.21, 0.21]$	$[-0.43, 0.44]$	$[0.01, 0.53]$	$[-0.24, 0.84]$
$c_{H\tilde{W}}$ (lin. only)	0.20	$[-0.19, 0.19]$	$[-0.38, 0.40]$	$[-0.01, 0.43]$	$[-0.21, 0.69]$
$c_{HB\tilde{W}}$	3.98	$[-2.09, 1.98]$	$[-4.44, 3.96]$	$[1.21, 6.89]$	$[-1.98, 10.36]$
$c_{H\tilde{B}}$	7.23	$[-3.82, 3.61]$	$[-8.10, 7.24]$	$[2.15, 12.59]$	$[-3.65, 18.95]$

Table 8.30: Expected and observed 68 % and 95 % confidence intervals for the combined fit results in the Optimal Observable with interpretations both in the HISZ and Warsaw basis. The central value is zero for the expected confidence intervals and the best fit value for the observed confidence intervals. All parameters are measured with linear and quadratic reweighting, with additional linear-only fits performed for $\tilde{d}$ and $c_{H\tilde{W}}$.

The uncertainty breakdown on the combined $\tilde{d}$ fit result is shown in Table 8.31. It is consistent with the stand-alone $\tau_\ell\tau_\ell$ result, with the major source of uncertainty being statistical, and the dominant systematic uncertainty components arising from jet and $E_{\mathrm{T}}^{\mathrm{miss}}$ reconstruction. The increase in relative uncertainty on the fake estimates mainly comes from the $\tau_h\tau_h$ channel, where the fake contribution is significant at high NN. Additionally, uncertainties from the hadronic τ-lepton reconstruction become relevant in both the $\tau_\ell\tau_h$ and $\tau_h\tau_h$ channels. This is also included in the $\tau_\ell\tau_\ell$ fit, but due to the fully leptonic final state, the effect is negligible.

The sensitivity of this analysis is evaluated against similar measurements in other ATLAS analyses using the full Run 2 dataset. A summary of the measured values for $\tilde{d}$ and $c_{H\tilde{W}}$, along with the corresponding 95% confidence intervals, is shown in Figure 8.39. The result in the HISZ basis is found to be more sensitive than the $H \to \gamma\gamma$

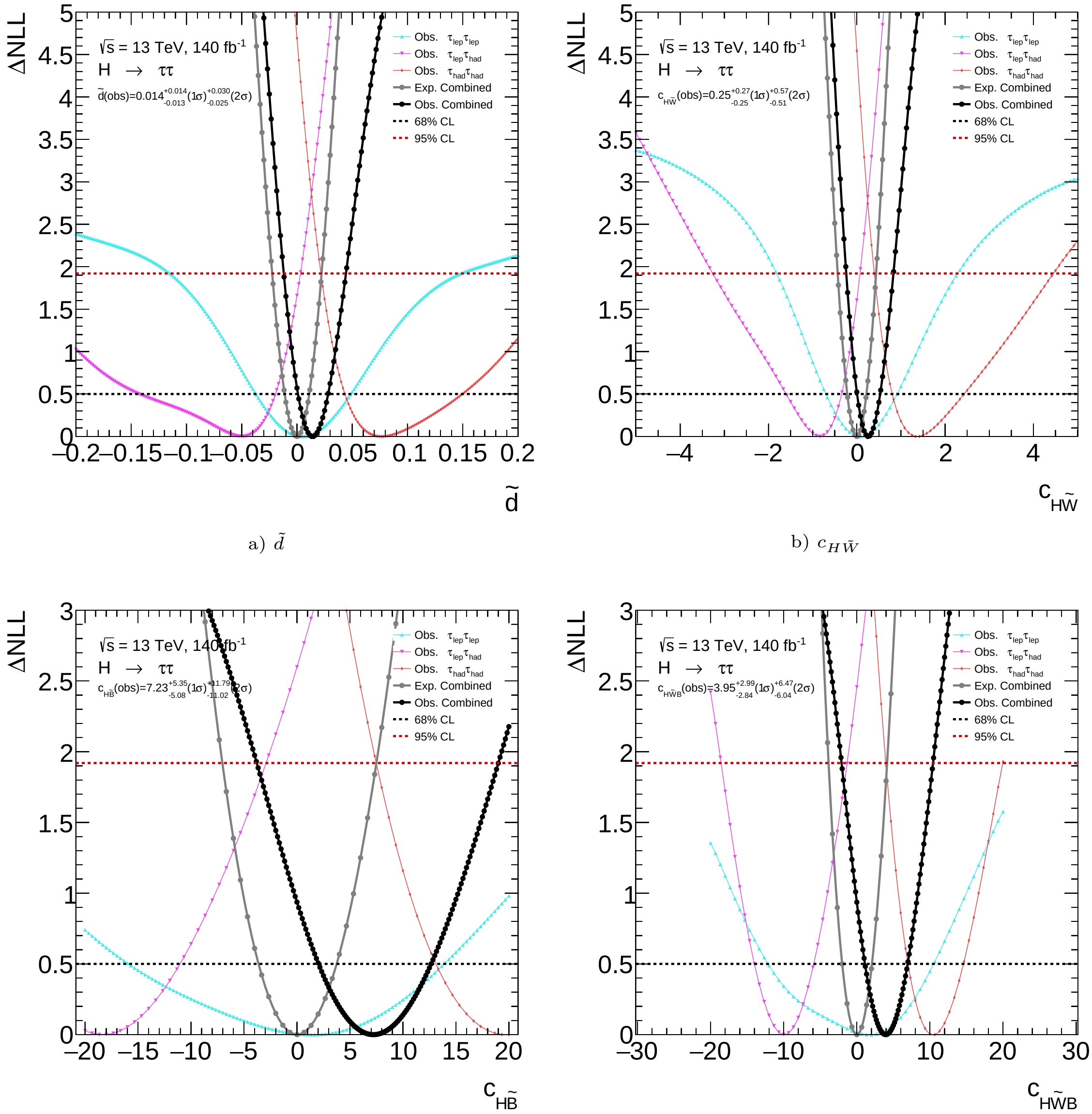

a) $\tilde{d}$

b) $c_{H\tilde{W}}$

c) $c_{H\tilde{B}}$

d) $c_{H\tilde{W}B}$

Figure 8.38: ΔNLL curves for all considered EFT parameters in the combined fit, with measurements presented in the HISZ basis via $\tilde{d}$ (top left), and in the Warsaw basis via $c_{H\tilde{W}}$ (top right), $c_{H\tilde{B}}$ (bottom left), and $c_{H\tilde{W}B}$ (bottom right). The expected curve is shown in grey, while the observed curve is shown in black. Results from simultaneous fit with 3 POIs for the the $\tau_\ell\tau_\ell$ (cyan), $\tau_\ell\tau_h$ (magenta) and $\tau_h\tau_h$ (red) channels are also shown. In the 3 POI fit the common signal normalisation factor is applied. The measurement of each EFT parameter is also shown, corresponding to the best observed fit value, along with its 1σ and 2σ uncertainties, corresponding to the 68% (black dashed line) and 95% (red dashed line) confidence intervals, respectively.

Source	Relative impact on the $\tilde{d}$ 68% CL interval
Higgs Theory	± 15%
Background Theory	± 11%
Flavour Tagging	± 0.3%
Luminosity	± 0.4%
Lepton reconstruction	± 2.4
Tau reconstruction	± 4.0
Jet/$E_{\mathrm{T}}^{\mathrm{miss}}$ reconstruction	± 20
Embedding	± 0.2
Fake	± 4.8
Normalisation Factors	$^{+6.0}_{-5.5}$
Sample size	± 3.0
Full Systematics	± 30
Total statistical uncertainty	± 95

Table 8.31: Summary of the different sources of systematic uncertainty and their impact on the final fit results, as a percentage of the 68% CL $\tilde{d}$ interval. Experimental systematics on the reconstruction of the objects include the reconstruction efficiency, energy scale and resolution, and trigger efficiencies. Sample size includes the per-bin statistical uncertainties in the simulated MC samples, and on the data-driven backgrounds of misidentified taus.

analysis [53], but slightly less sensitive than the $H \to ZZ \to 4\ell$ analysis [52]. The latter analysis benefits from the additional information provided by the HZZ decay vertex, allowing for more sensitive measurements of the $c_{H\tilde{B}}$ and $c_{H\tilde{W}B}$ operators, which results in improved sensitivity on $\tilde{d}$.

For measurements of $c_{H\tilde{W}}$, this analysis provides among the most stringent limits to date within ATLAS, comparable to the $H \to \tau\tau$ differential cross-section analysis [202]. The differential analysis employed a similar dataset, but used a different unfolding strategy based on the variable $\Delta\phi_{jj}^{\mathrm{signed}}$. A similar approach was also adopted in the $H \to WW$ differential analysis [229], although only the linear term was considered in the EFT interpretation.

In addition, this analysis measures the 68% confidence interval for $\tilde{d}$ with approximately a factor of three greater precision compared to the earlier partial Run 2 VBF CP analysis [51], which did not have sufficient sensitivity to achieve an observed 95% confidence interval.

A larger effort is planned in ATLAS to combine the Warsaw basis results from analyses that specifically targets CP violation with the Optimal Observable. This is currently being implemented with results expected later this year.

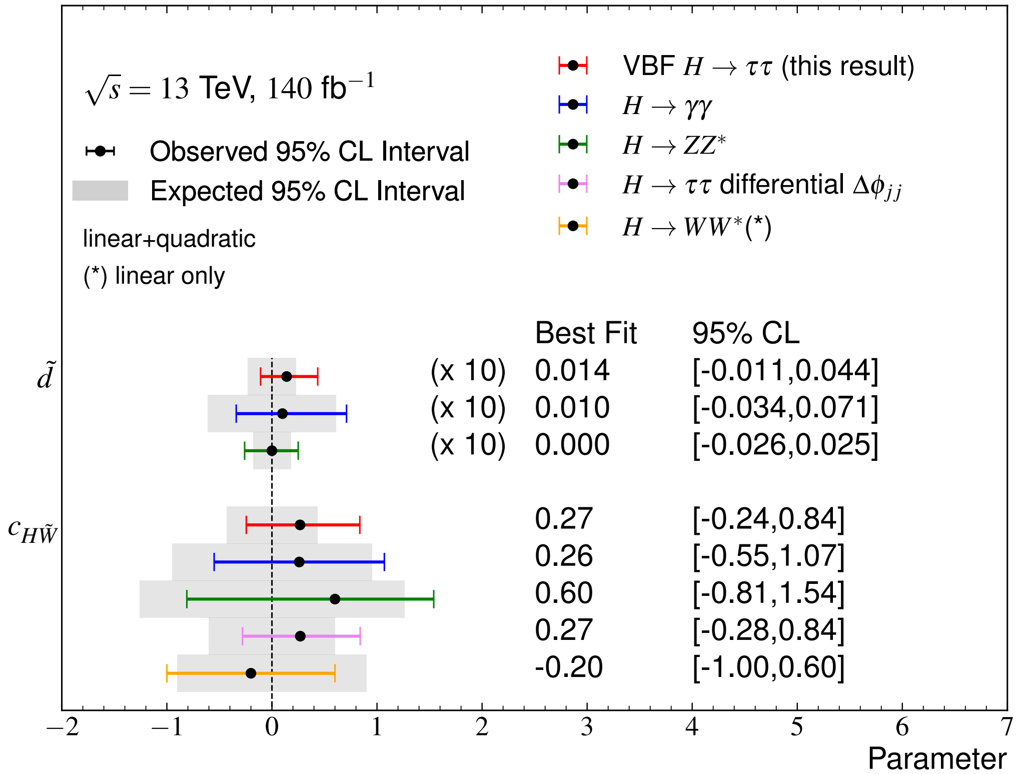

Figure 8.39: Comparison of results of the analysis presented with the ATLAS $H \to ZZ \to 4\ell$ analysis [52] and the ATLAS $H \to \gamma\gamma$ measurements [53] for $\tilde{d}$ and $\tilde{c}$. The results for $\tilde{d}$ are also compared to interpretations provided by the ATLAS $H \to \tau\tau$ and $H \to WW$ differential cross-section measurements [202, 229] based on $\Delta\phi_{jj}^{\text{signed}}$. The data points show the observed results, and the uncertainty bands correspond to the 95% confidence interval, including statistical and systematic uncertainties. The $\tilde{d}$ values are scaled by a factor of 10 in order to have the same dimension in the figure as the other operators. All results are obtained with linear+quadratic interpretation, except the $H \to WW$ result which is linear-only.

8.7.3 Sensitivity check with other observables

The expected sensitivity of the Optimal Observable is also evaluated against the angular observables to ensure that the most sensitive result is used in the analysis. The (blinded) distributions for the two additional angular observable in the $\tau_\ell\tau_\ell$ high NN SR after the fit can be seen in Figure 4.7. The corresponding ΔNLL curves, obtained from a combined fit of all three channels, is shown in Figure 8.41. It can be seen that $\Delta\phi_{jj}^{\text{signed}}$ has the worst performance, with the Optimal Observable performing slightly better than the $p_T(j_1)p_T(j_2)\sin\Delta\phi_{jj}^{\text{signed}}$ observable.

The result confirms the assumption of the Optimal Observable being the most sensitive CP-odd observable. The similar performance of $p_T(j_1)p_T(j_2)\sin\Delta\phi_{jj}^{\text{signed}}$ does however show that there is a well-performing analytical alternative that doesn't rely on matrix element information.

Additionally, an observable constructed from the output scores of a multiclass NN classifier trained to separate positive interference, negative interference, and SM events has been discussed in recent literature [230]. Early studies of this observable within the context of this analysis showed promise. However, the studies did not converge in time to be included in the final results.

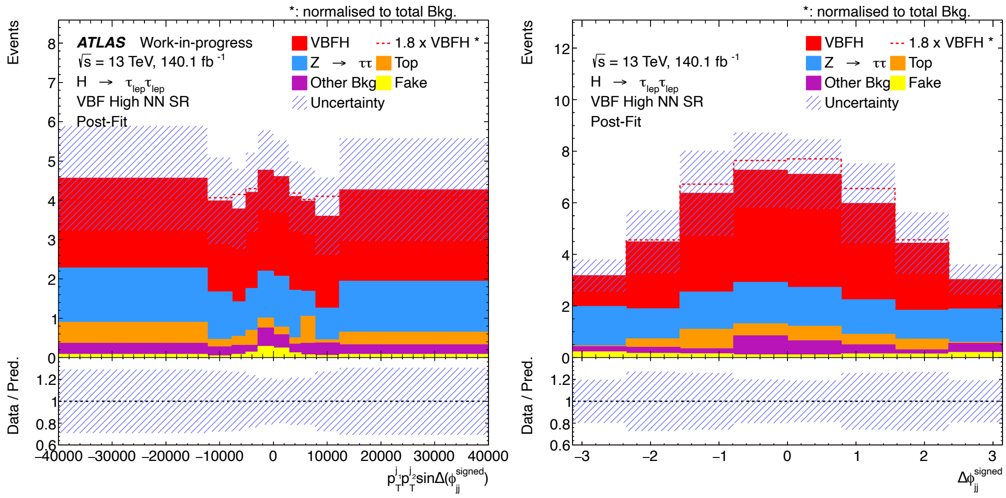

a) $p_T(j_1)p_T(j_2)\sin\Delta\phi_{jj}^{\text{signed}}$ b) $\Delta\phi_{jj}^{\text{signed}}$

Figure 8.40: Simulated (blinded) post-fit distributions for the $p_T(j_1)p_T(j_2)\sin\Delta\phi_{jj}^{\text{signed}}$ (left) and $\Delta\phi_{jj}^{\text{signed}}$ (right) observables in the High NN signal region after the fit to Asimov pseudodata.

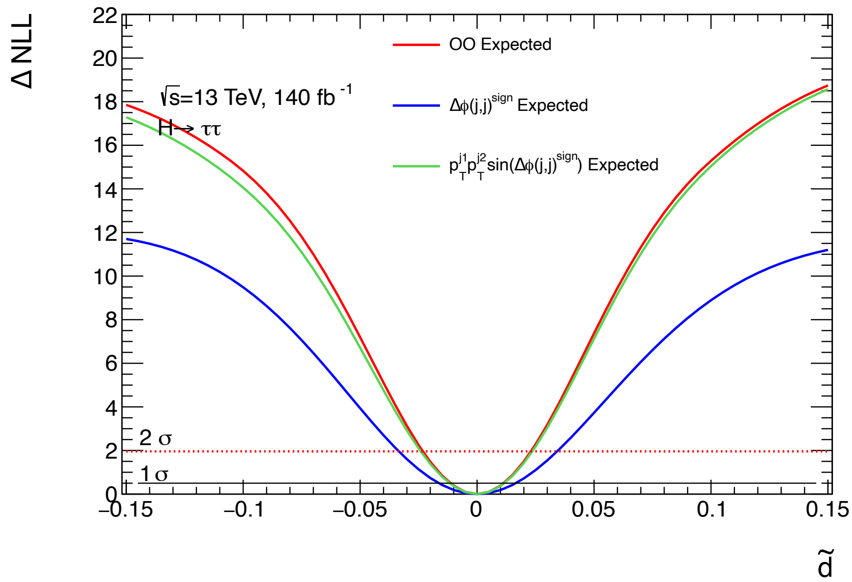

Figure 8.41: Expected ΔNLL curves for $\tilde{d}$ using different observables. The curves are obtained from a combined fit of the $\tau_\ell\tau_\ell$, $\tau_\ell\tau_h$ and $\tau_h\tau_h$ channel using Asimov pseudodata.

Chapter **9**

Search for associated DM production in the mono-Higgs topology using the 2HDM+a model

This analysis consider a SM Higgs boson decaying into two τ-leptons produced in association with $E_{\mathrm{T}}^{\mathrm{miss}}$ in search for a DM signal. The studied signal model is the 2HDM+a model detailed in section 4.5. The model has been recommended by the ATLAS/CMS DM Forum, which refers to it as "the simplest gauge-invariant and renormalizable extension of the simplified pseudoscalar model" [112]. The mono-Higgs topology can be produced either vi ggF or $b\bar{b}$ induced production. The Feynman diagrams for these processes are shown in Figure 9.1. Two scans are performed in the parameter space of the model using the benchmark parameters listed in Table 4.1. The $m_A - m_a$ scan varies the mass of the light (m_a) and heavy (m_A) pseudoscalar with the mixing angle set to $\sin\theta = 0.35$ and $\tan\beta = 1.0$. For this particular configuration contribution from $b\bar{b}$ production is negligible. It does however contribute in other parameter configuration with larger values of $\tan\beta$, and is therefore relevant, but still subdominant, in the $m_A - \tan\beta$ scan.

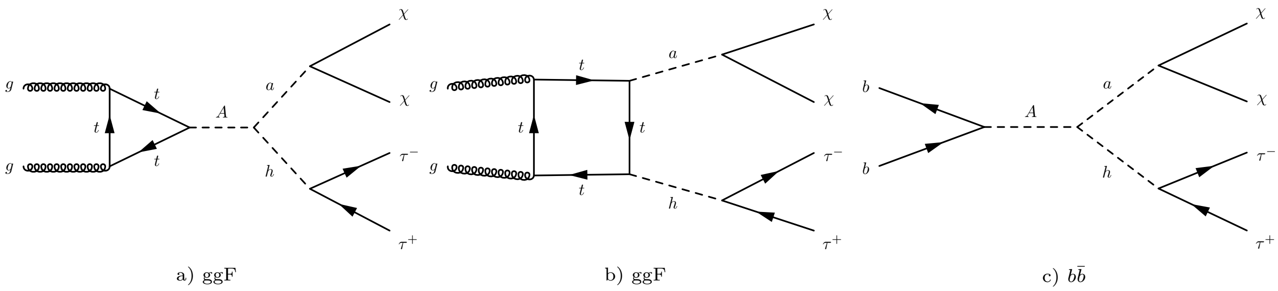

Figure 9.1: Feynman diagrams describing the 2HDM+a processes leading to the production of the mono-Higgs signatures via gluon-gluon fusion (left/middle), and $b\bar{b}$ annihilation (right).

This analysis only considers the the fully hadronic channel of the τ-lepton decay. Although the $\tau_\ell\tau_\ell$ and $\tau_\ell\tau_h$ channel in principle also could be included, they come with larger backgrounds and a completely different set of optimisations. Ideally all channels should be investigated to perform a proper combination, like in the VBF CP analysis. However, due to lack of manpower and lower expected background in the $\tau_h\tau_h$ channel, the other channels were disregarded in this analysis. The analysis was published in the Journal For High Energy Physics (JHEP) in 2023 [231].

9.1 Data and simulated samples

9.1.1 Data

The dataset used in this analysis was recorded by ATLAS during Run 2 of the LHC, spanning the data-taking period from 2015 to 2018. At the time of the analysis, the integrated luminosity was determined to be 139 ± 2.4 fb^{-1} [232]. A subsequent refinement by ATLAS updated this value to 140.1 ± 1.2 fb^{-1} [200]. However, for the results presented in this work, the first scenario assumed.

9.1.2 Simulation of background samples

MC simulations are used to model the signal and all major background processes in the analysis. A summary of the generators, parton showers, and theoretical accuracies is provided in Table 9.1.

The Z+jets and W+jets samples are generated with Sherpa 2.2.1 [203], using matrix elements calculated at NNLO accuracy, matched to the Sherpa parton shower. A dedicated parton-shower tune is applied, and the NNPDF3.0nnlo [205] PDF set is used both for matrix element generation and showering. Diboson processes are simulated with either Sherpa 2.2.1 or Sherpa 2.2.2, depending on the channel. Matrix elements are calculated at NLO and matched to the Sherpa parton shower using the MEPS@NLO prescription [233], with the NNPDF3.0nnlo PDF set.

$t\bar{t}$ and single-top processes are generated with Powheg Box v2 [206], interfaced to Pythia 8.230 [207] for parton showering, hadronisation, and the underlying event. The A14 tune is used, with the NNPDF3.0nlo PDF set for matrix elements and NNPDF2.3lo for parton showering. The $t\bar{t}H$ and $t\bar{t}V$ samples are simulated at NLO accuracy using Powheg Box v2 and MadGraph5_aMC@NLO 2.3.3 [234], respectively, both interfaced with Pythia 8 using the A14 tune and the same PDF configuration as for $t\bar{t}$.

VH production is simulated using Powheg Box v2 interfaced to Pythia 8.212, with the AZNLO tune and the PDF4LHC15nnlo PDF set [209]. All samples are normalised to the highest-order available cross-section predictions, including QCD and electroweak corrections where applicable.

All SHERPA-based samples use a dedicated parton-shower tune provided by the authors [204, 235].

Physics process	Generator	Parton Shower	Accuracy	Tune	PDF (ME)	PDF (PS)
$Z(\rightarrow \ell\ell)$+jets	SHERPA 2.2.1	SHERPA 2.2.1	NNLO	Dedicated	NNPDF3.0NNLO	NNPDF3.0NNLO
$W(\rightarrow \ell\nu)$+jets	SHERPA 2.2.1	SHERPA 2.2.1	NNLO	Dedicated	NNPDF3.0NNLO	NNPDF3.0NNLO
Diboson	SHERPA 2.2.1, 2.2.2	SHERPA 2.2.1, 2.2.2	NLO	Dedicated	NNPDF3.0NNLO	NNPDF3.0NNLO
$t\bar{t}$	POWHEG BOX v2	PYTHIA 8.230	NNLO+NNLL	A14	NNPDF3.0NLO	NNPDF2.3LO
Single-top:						
Wt	POWHEG BOX v2	PYTHIA 8.230	NLO+NNLL	A14	NNPDF3.0NLO	NNPDF2.3LO
s- and t-channels	POWHEG BOX v2	PYTHIA 8.230	NLO	A14	NNPDF3.0NLO	NNPDF2.3LO
$t\bar{t}+H$	POWHEG BOX v2	PYTHIA 8.230	NLO	A14	NNPDF3.0NLO	NNPDF2.3LO
$t\bar{t}+V$	MADGRAPH5_AMC@NLO 2.3.3	PYTHIA 8.210	NLO	A14	NNPDF3.0NLO	NNPDF2.3LO
$VH(\rightarrow \tau\tau)$	POWHEG BOX v2	PYTHIA 8.212	NNLO + NLO	AZNLO	NNPDF3.0NLO	PDF4LHC15NNLO

Table 9.1: Summary of the generators used to simulate the background processes considered in the analysis. The dedicated tune refers to the set of tuned parton-shower parameters developed by the SHERPA authors. The symbol V stands for a vector boson.

9.1.3 Simulation of signal samples

The 2HDM+a signal samples are simulated in grids of the signal parameters, chosen to ensure consistency with other ATLAS analyses and to enable model combinations. Two grids are considered: the $m_A - m_a$ grid with $\sin\theta = 0.35$ and $\tan\beta = 0.1$, and the m_A–$\tan\beta$ grid with $\sin\theta = 0.7$ and $m_a = 250$ GeV. All other model parameters follow the benchmark values given in Table 4.1. Tables 9.2 and 9.3 show the produced samples in the $m_A - m_a$ and $m_A - \tan\beta$ grid, respectively.

m_A [GeV] \ m_a [GeV]	100	150	200	250	300	350	400	500
300	x	x	-	-	-	-	-	-
400	x	x	x	-	-	-	-	-
500	-	-	x	x	x	-	-	-
600	x	x	x	x	x	x	-	-
700	-	-	-	x	x	x	x	-
800	x	x	x	x	x	x	x	x
1000	x	x	x	x	x	-	-	-
1200	x	x	-	-	-	-	-	-

Table 9.2: Grid of produced ggF signal samples in the $m_A - m_a$ grid. The produces signal points are indicated with green boxes. All samples in this grid were produced with $\sin\theta = 0.35$ and $\tan\beta$ =0.1.

The specific parameter choices are based on recommendations from the LHC Dark Matter Working Group [112] and early sensitivity studies. Gluon fusion and $b\bar{b}$-initiated production are generated as separate samples, scaled according to their respective cross-sections, and then combined. The $b\bar{b}$ induced production samples are all generated with $\tan\beta = 10$, and internal reweighting is used to obtain predictions for other $\tan\beta$ values within the grid. Gluon fusion induced production samples are generated for each considered signal point without reweighting.

$\tan\beta \setminus m_A$ [GeV]	500	600	700	800	900	1000	1100	1200	1300
20	x	x	x	x	x	x	x	x	x
10	x	x	x	x	x	x	x	x	x
5	x	x	x	x	x	x	x	x	x
3	x	x	x	x	x	x	x	x	x
2	x	x	x	x	x	x	x	x	x
1	x	x	x	x	x	x	x	x	x
0.5	x	x	x	x	x	x	x	x	x
0.3	x	x	x	x	x	x	x	x	x

Table 9.3: Grid of produced ggF signal samples in the m_A-$\tan\beta$ grid. The produces signal points are indicated with green boxes. All samples were produced with $\sin\theta = 0.7$ and $m_a = 250$ GeV. Signal points in the orange region is only available with $b\bar{b}$ initiated proudction.

The orange region indicated in Table 9.2, corresponding to points with $m_A > 1000$ GeV and are not generated for ggF production. These points were added at a later stage in the analysis, but due to the limited sensitivity for signal points with $\tan\beta \geq 3.0$, samples exceeding this threshold were not produced. For $b\bar{b}$-initiated production, however, predictions for these points can still be obtained through reweighting. Consequently, the orange region represents only $b\bar{b}$-induced production derived from reweighting.

All signal samples are generated with MadGraph5_aMC@NLO 2.6.5 [234] interfaced with Pythia 8.240 [207] for parton showering, hadronisation, and underlying event modelling. The resulting events are passed through the AtlFast-II detector simulation. To validate the fast simulation, a single mass point, $[m_A, m_a] = [750, 250]$ GeV in the $m_A - m_a$ grid, is additionally produced with the full detector simulation using Geant4 [159]. A comparison between the two simulations is shown for both $E_{\mathrm{T}}^{\mathrm{miss}}$ and leading τ-lepton p_{T} in Figure 9.2. The agreement is generally good, with small deviations observed near the $E_{\mathrm{T}}^{\mathrm{miss}}$ peak. The absolute difference between the two simulations is treated as an overall systematic uncertainty.

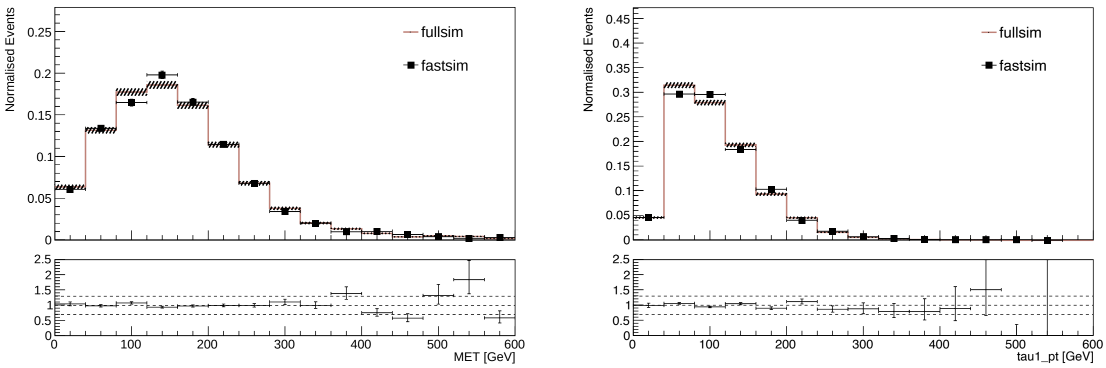

a) $E_{\mathrm{T}}^{\mathrm{miss}}$ b) $p_{\mathrm{T}}(\tau_1)$

Figure 9.2: Normalised $E_{\mathrm{T}}^{\mathrm{miss}}$ (left) and leading τ-lepton p_{T} (right) distributions for the ATLFAST II fast simulation (black) and the full detector simulation with GEANT4 (red). The only requirement is a simple preselection with $N_\tau = 2$.

9.2 Object definitions

The object selection in this analysis is similar to that used in the VBF CP analysis described in Section 8.2. The same general overlap removal procedure is applied (Section 6.8), but with some modifications to the baseline and signal definitions. The object definitions are summarised in Table 9.4.

Baseline electrons follow the same p_{T} and upper threshold on η, but electrons in the transition region are included. Additionally, they must satisfy requirements on the significance of the impact parameter with respect to the primary vertex, $|d_0/\sigma(d_0)| < 5.0$, and on the longitudinal impact parameter, $|z_0 \sin\theta| < 0.5$ mm. Signal electrons must have p_{T} above 25 GeV and satisfy the `Tight` identification criteria. They must also pass the `FCLoose` isolation WP, and for p_{T} above 200 GeV, the `FCHighPtCaloOnly` isolation WP. Baseline muons are required to pass the same p_{T} and η thresholds as descried in Section 8.2. Additionally, they must satisfy the `Medium` identification criterion, with $|d_0/\sigma(d_0)| < 3.0$ and $|z_0 \sin\theta| < 0.5$ mm. Signal muons must also have p_{T} above 25 GeV and pass the `FCLoose` isolation WP. Baseline hadronic τ-leptons follow the same p_{T} and η requirements as described in Section 8.2. They must also pass the `VeryLoose` RNN identification WP, while signal τ-leptons must satisfy the `Medium` WP. To discriminate between electrons and τ-leptons, signal τ-leptons must also pass the `Loose` eBDT isolation WP. Jets are defined in the same way described in Section 8.2, but with the b-tagging WP set at 77% efficiency.

Electrons	Signal requirement
Kinematics	$p_{\mathrm{T}} > 25$ GeV $\lvert\eta\rvert < 2.47$
Identification	`Tight`
Isolation	`FCLoose`, `FCHighPtCaloOnly` (for $p_{\mathrm{T}} > 200$ GeV)
Impact parameter	$\lvert d_0/\sigma(d_0)\rvert < 5.0$ and $\lvert z_0 \sin\theta\rvert < 0.5$ mm
Muons	**Signal requirement**
Kinematics	$p_{\mathrm{T}} > 25$ GeV and $\lvert\eta\rvert < 2.7$
Identification	`Medium`
Isolation	`FCLoose`
Impact parameter	$\lvert d_0/\sigma(d_0)\rvert < 3.0$ and $\lvert z_0 \sin\theta\rvert < 0.5$ mm
Hadronic taus	**Signal requirement**
Kinematics	$p_{\mathrm{T}} > 20$ GeV & $\lvert\eta\rvert < 2.47$ (excluding $1.37 < \lvert\eta\rvert < 1.52$)
N_{Tracks}	1 or 3 with $p_{\mathrm{T}} > 20$ GeV & $\lvert\eta\rvert < 2.47$
Identification	RNN `Medium`
eBDT	`Loose`
Jets	**Signal requirement**
Algorithm	anti-k_t ($R = 0.4$, PFlow)
Kinematics	$p_{\mathrm{T}} > 30$ GeV and $\lvert\eta\rvert < 4.4$
Pileup Mitigation	JVT `Tight` for $p_{\mathrm{T}} < 60$ GeV & $\lvert\eta\rvert < 2.5$ fJVT `Loose` for $p_{\mathrm{T}} < 60$ GeV & $\lvert\eta\rvert > 2.5$
DL1r b-tagging	77% WP

Table 9.4: Summary of the signal object definition used in this analysis.

9.3 Event selection

The expected signature of the model is two oppositely charged τ-leptons coming from the Higgs decay and $E_{\mathrm{T}}^{\mathrm{miss}}$ from the DM decay of the pseudoscalar a. The analysis was designed and optimised with respect to points in the $m_A - m_a$ grid, with the $m_A - \tan\beta$ interpretation added later as a supplementary measurement based on the same selection. Hence, the optimisation strategy discussed in the following will primarily focus on the $m_A - m_a$ benchmark scenario.

Events passing the object selection criteria must satisfy the offline trigger thresholds detailed in the next section. A general preselection is then applied to ensure consistency with the signal topology before performing a cut-based optimisation on the kinematics of the final state. This defines a region inclusive of the entire signal grid, referred to as the common SR preselection. Within this region, two SRs are defined, each optimised to target different parts of the signal grid.

The relevant kinematic variables used in the analysis are discussed in Section 9.3.2. Distributions of these variables are shown in Figures 9.3–9.5 for signal samples in the $m_A - m_a$ grid with fixed $m_a = 150$ GeV and

m_A varied between 400 and 1200 GeV. Similarly, Figures 9.6–9.8 show the corresponding distributions for fixed $m_A = 600$ GeV and m_a varied between 100 and 350 GeV. The only requirements applied to the signal samples in these plots are that events pass the overlap removal procedure and contain exactly two hadronically decaying τ-leptons, with events containing muons, electrons, or b-tagged jets being vetoed. A dependence on m_A is observed, where larger values of m_A result in extended tails in the $E_{\mathrm{T}}^{\mathrm{miss}}$ distribution, while smaller values of m_A produce peaks at lower $E_{\mathrm{T}}^{\mathrm{miss}}$ values. In contrast, the dependence on m_a is comparatively small, due to the smaller mass splitting between the heavy and light pseudoscalars in the considered samples. For the particular choice of parameters $\tan\beta = 1.0$ and $\sin\theta = 0.35$, the contribution from $b\bar{b}$-initiated production processes is negligible, with the associated cross-section becoming relevant only for $\tan\beta \geq 10$.

In the m_A–$\tan\beta$ grid, where the $\tan\beta$ is varied, contribution from $b\bar{b}$-initiated processes becomes non-negligible. Although the $b\bar{b}$ production cross-section scales with $\tan\beta$, it still contributes at lower values. In contrast, the ggF production cross-section is largest at small $\tan\beta$ and decreases as $\tan\beta$ increases. The kinematic dependence of the relevant analysis variables for both production mechanisms is illustrated in Figures 9.9–9.11 for ggF initiated production, and Figures 9.12–9.14 for $b\bar{b}$ initiated production. The same set of signal points are considered in both production modes, with the mass of the heavy pseudoscalar fixed at $m_A = 700$ GeV and $\tan\beta$ varied between 0.3 and 20. For ggF production, the peak of the $E_{\mathrm{T}}^{\mathrm{miss}}$ distribution shifts towards larger values as $\tan\beta$ increases, with signal points showing similar kinematic dependence from around $\tan\beta \sim 1.0$. A similar trend is observed for $b\bar{b}$ production, although the resulting $E_{\mathrm{T}}^{\mathrm{miss}}$ peaks are generally broader at larger values of $\tan\beta$.

Variations in m_A with $\sin\theta = 0.35$ and $\tan\beta = 1.0$

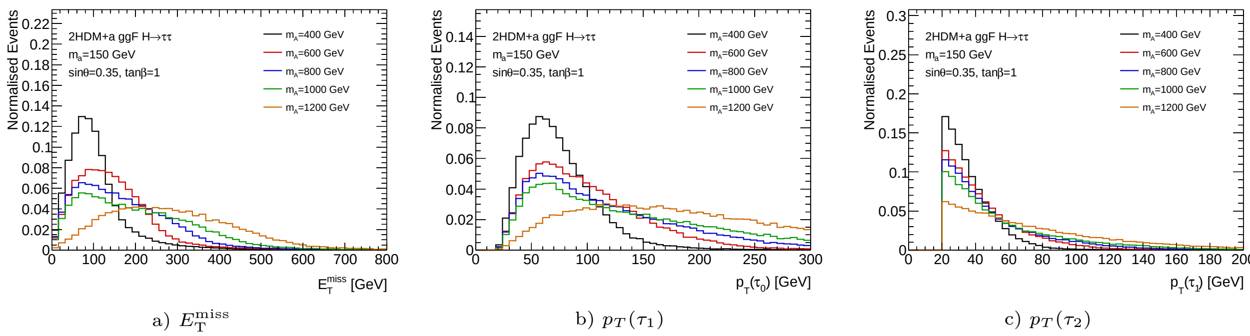

Figure 9.3: Kinematic distributions for various 2HDM+a signal points with $\sin\theta = 0.35$ and $\tan\beta = 1.0$ for $E_{\mathrm{T}}^{\mathrm{miss}}$ (left), leading (middle) and subleading (right) τ-lepton p_{T}. The pseudoscalar mass is fixed at $m_a = 150$ GeV, while the heavy pseudoscalar mass m_A is varied between 400 and 1200 GeV.

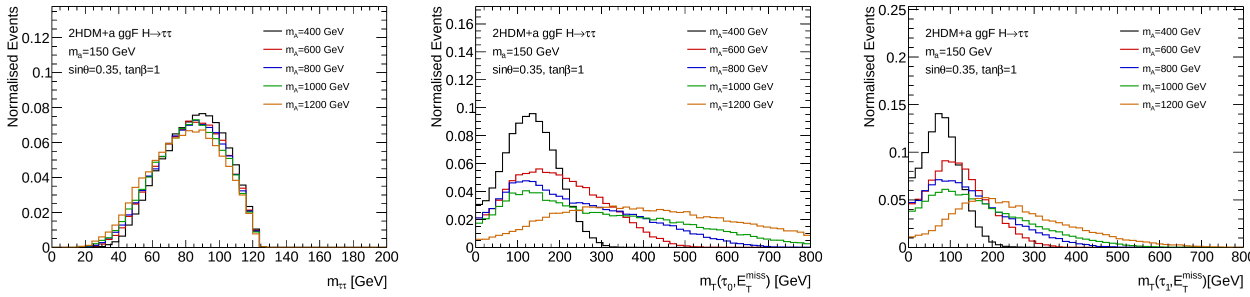

a) $m_{\tau\tau}^{\mathrm{vis}}$ b) $m_{\mathrm{T}}^{\tau 1}$ c) $m_{\mathrm{T}}^{\tau 2}$

Figure 9.4: Kinematic distributions for various 2HDM+a signal points with $\sin\theta = 0.35$ and $\tan\beta = 1.0$ for the visible mass of the τ-lepton pair (left) and the transverse mass of the leading (middle) and and subleading (right) τ-lepton. The pseudoscalar mass is fixed at $m_a = 150$ GeV, while the heavy pseudoscalar m_A is varied between 400 and 1200 GeV.

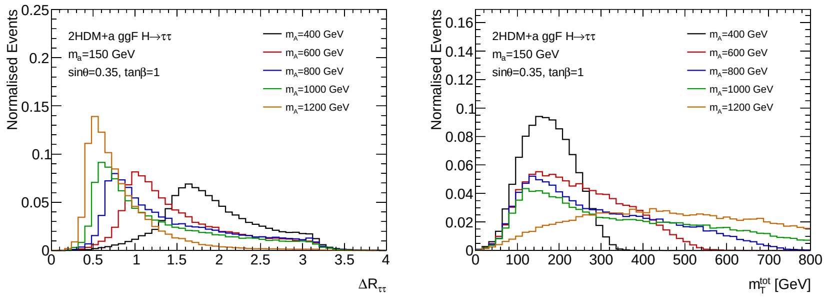

a) $\Delta R_{\tau\tau}$ b) m_T^{tot}

Figure 9.5: Kinematic distributions for various 2HDM+a signal points with $\sin\theta = 0.35$ and $\tan\beta = 1.0$ for $\Delta R_{\tau\tau}$ (left) and the total transverse mass (right). The pseudoscalar mass is fixed at $m_a = 150$ GeV, while the heavy pseudoscalar m_A is varied between 400 and 1200 GeV.

Variations in m_a with $\sin\theta = 0.35$ and $\tan\beta = 1.0$

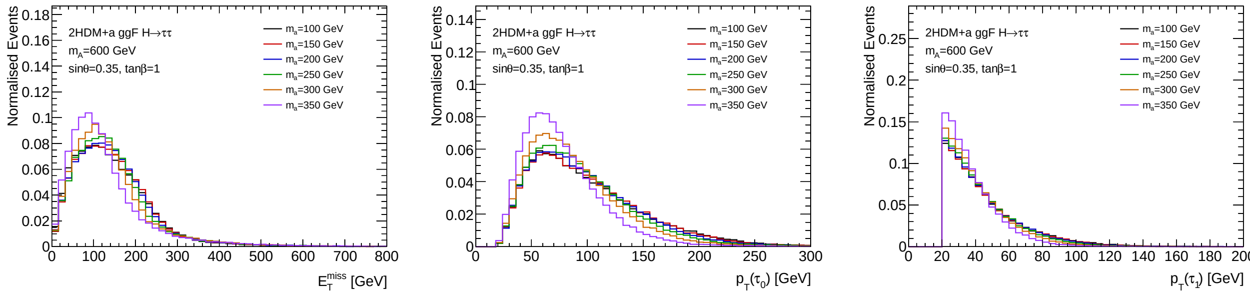

a) $E_{\mathrm{T}}^{\mathrm{miss}}$ b) $p_T(\tau_1)$ c) $p_T(\tau_2)$

Figure 9.6: Kinematic distributions for various 2HDM+a signal points produced via ggF with $\sin\theta = 0.35$ and $\tan\beta = 1.0$ for $E_{\mathrm{T}}^{\mathrm{miss}}$ (left), leading (middle) and subleading (right) τ-lepton p_{T}. The heavy pseudoscalar mass is fixed at $m_A = 600$ GeV, while the pseudoscalar mass m_a is varied between 100 and 350 GeV.

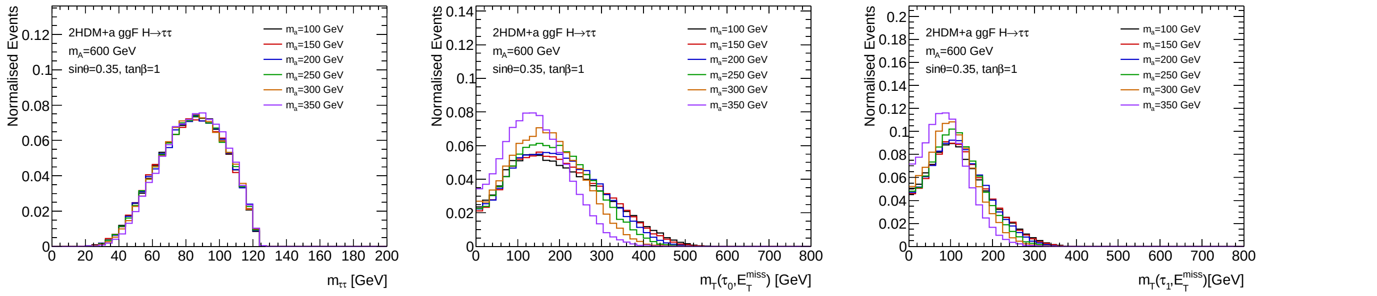

a) $m_{\tau\tau}^{\mathrm{vis}}$ b) $m_{\mathrm{T}}^{\tau 1}$ c) $m_{\mathrm{T}}^{\tau 2}$

Figure 9.7: Kinematic distributions for various 2HDM+a signal points produced via ggF with $\sin\theta = 0.35$ and $\tan\beta = 1.0$ for the visible mass of the τ-lepton pair (left) and the transverse mass of the leading (middle) and and subleading (right) τ-lepton. The heavy pseudoscalar is fixed at $m_A = 600$ GeV, while the pseudoscalar mass m_a is varied between 100 and 350 GeV.

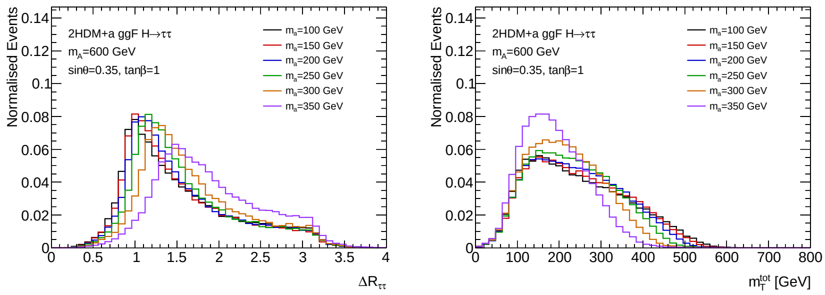

a) $\Delta R_{\tau\tau}$ b) m_{T}^{tot}

Figure 9.8: Kinematic distributions for various 2HDM+a signal points produced via ggF with $\sin\theta = 0.35$ and $\tan\beta = 1.0$ for $\Delta R_{\tau\tau}$ (left) and the total transverse mass (right). The heavy pseudoscalar is fixed at $m_A = 600$ GeV, while the pseudoscalar mass m_a is varied between 100 and 350 GeV.

Variations in $\tan\beta$ with $\sin\theta = 0.7$ ggF

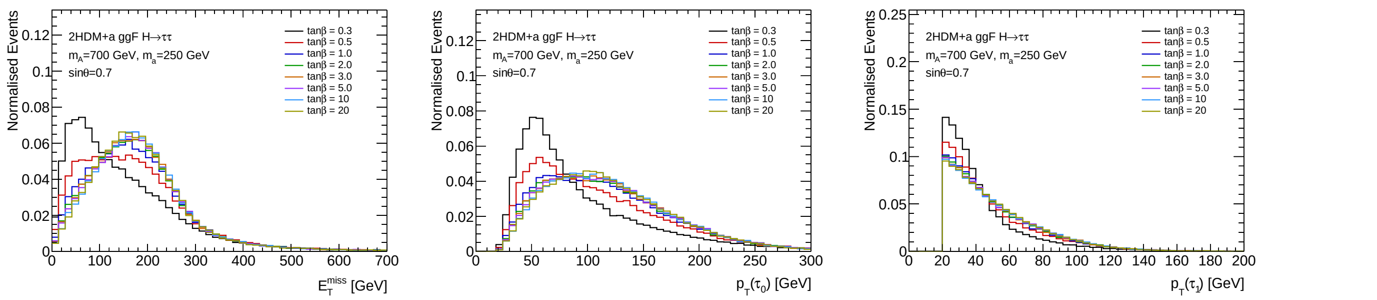

a) $E_{\mathrm{T}}^{\mathrm{miss}}$ b) $p_T(\tau_1)$ c) $p_T(\tau_2)$

Figure 9.9: Kinematic distributions for various 2HDM+a signal points produced via ggF with $\sin\theta = 0.7$ and $m_a = 250$ for $E_{\mathrm{T}}^{\mathrm{miss}}$ (left), leading (middle) and subleading (right) τ-lepton p_{T}. The heavy pseudoscalar mass is fixed at $m_A = 700$ GeV, while $\tan\beta$ is varied between 0.3 and 20.

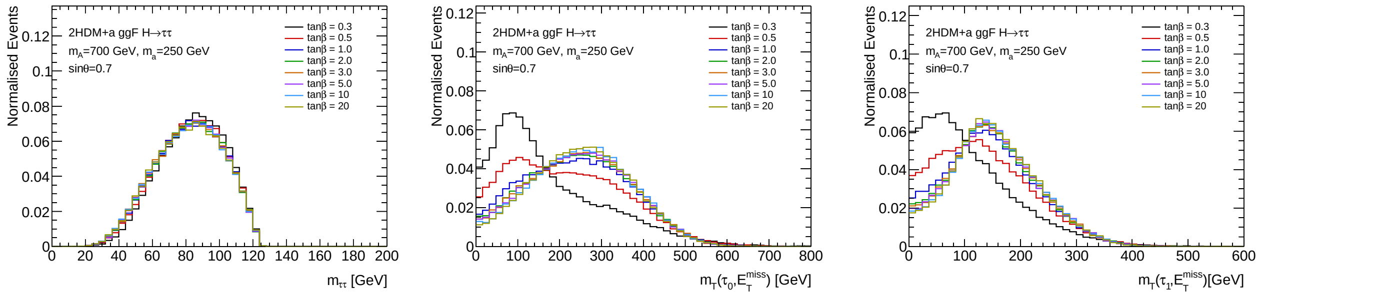

a) $m_{\tau\tau}^{\text{vis}}$ b) $m_{\mathrm{T}}^{\tau 1}$ c) $m_{\mathrm{T}}^{\tau 2}$

Figure 9.10: Kinematic distributions for various 2HDM+a signal points produced via ggF with $\sin\theta = 0.7$ and $m_a = 250$ for the visible mass of the τ-lepton pair (left) and the transverse mass of the leading (middle) and and subleading (right) τ-lepton. The heavy pseudoscalar mass is fixed at $m_A = 700$ GeV, while $\tan\beta$ is varied between 0.3 and 20.

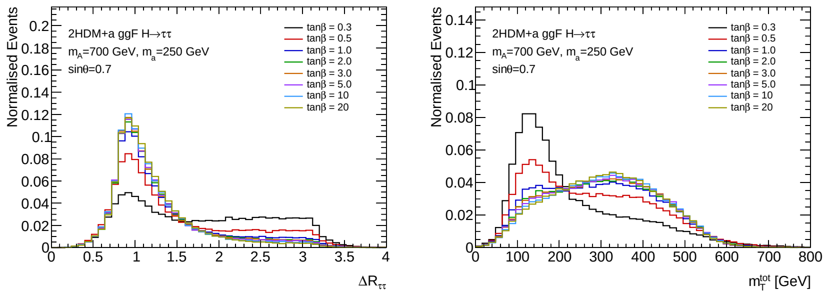

a) $\Delta R_{\tau\tau}$ b) m_T^{tot}

Figure 9.11: Kinematic distributions for various 2HDM+a signal points produced via ggF with $\sin\theta = 0.7$ and $m_a = 250$ for $\Delta R_{\tau\tau}$ (left) and the total transverse mass (right). The heavy pseudoscalar mass is fixed at $m_A = 700$ GeV, while $\tan\beta$ is varied between 0.3 and 20.

Variations in $\tan\beta$ with $\sin\theta = 0.7$ $b\bar{b}$

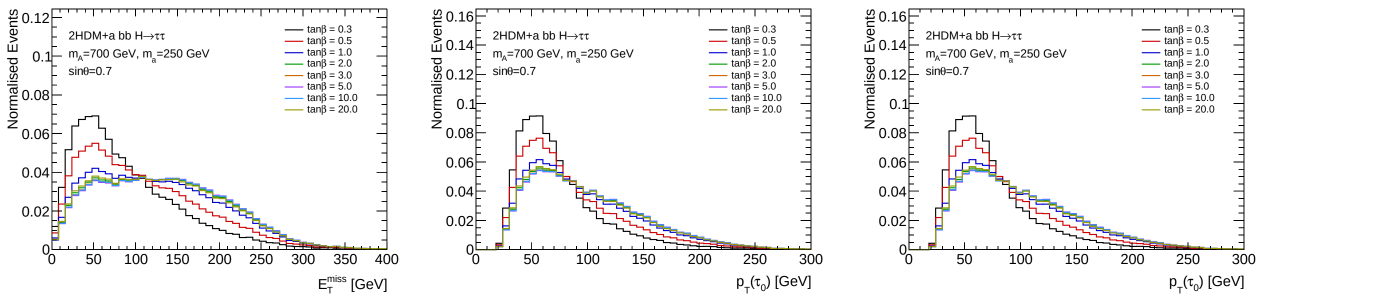

a) $E_{\mathrm{T}}^{\text{miss}}$ b) $p_T(\tau_1)$ c) $p_T(\tau_2)$

Figure 9.12: Kinematic distributions for various 2HDM+a signal points produced via $b\bar{b}$ with $\sin\theta = 0.7$ and $m_a = 250$ for $E_{\mathrm{T}}^{\text{miss}}$ (left), leading (middle) and subleading (right) τ-lepton p_{T}. The heavy pseudoscalar mass is fixed at $m_A = 700$ GeV, while $\tan\beta$ is varied between 0.3 and 20.

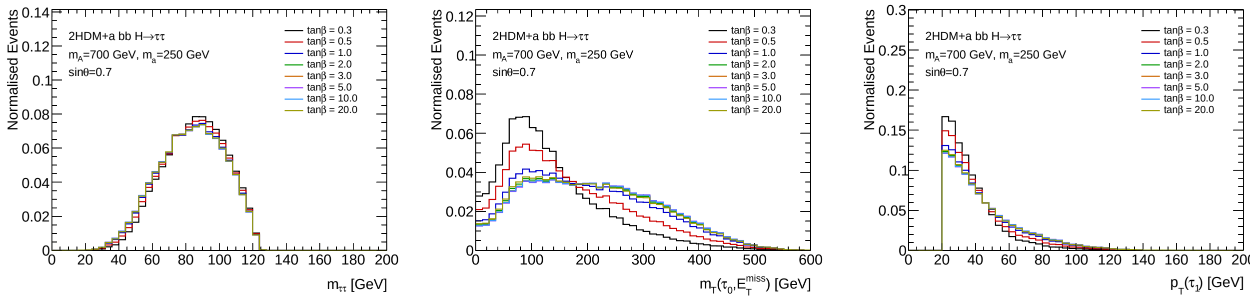

a) $m_{\tau\tau}^{\mathrm{vis}}$ b) $m_{\mathrm{T}}^{\tau 1}$ c) $m_{\mathrm{T}}^{\tau 2}$

Figure 9.13: Kinematic distributions for various 2HDM+a signal points produced via $b\bar{b}$ with $\sin\theta = 0.7$ and $m_a = 250$ for the visible mass of the τ-lepton pair (left) and the transverse mass of the leading (middle) and and subleading (right) τ-lepton. The heavy pseudoscalar mass is fixed at $m_A = 700$ GeV, while $\tan\beta$ is varied between 0.3 and 20.

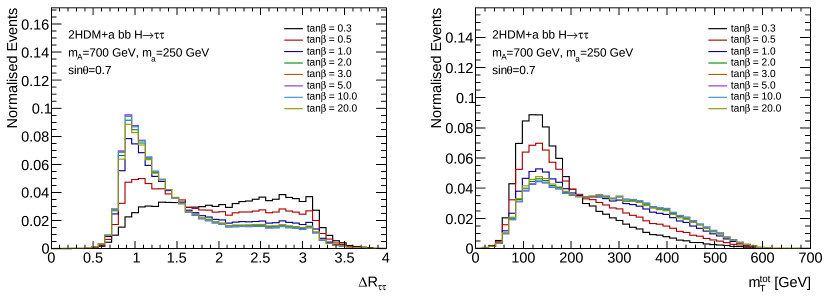

a) $\Delta R_{\tau\tau}$ b) m_T^{tot}

Figure 9.14: Kinematic distributions for various 2HDM+a signal points produced via $b\bar{b}$ with $\sin\theta = 0.7$ and $m_a = 250$ for $\Delta R_{\tau\tau}$ (left) and the total transverse mass (right). The heavy pseudoscalar mass is fixed at $m_A = 700$ GeV, while $\tan\beta$ is varied between 0.3 and 20.

9.3.1 Trigger

The expected signature of the model consists of two oppositely charged τ-leptons and $E_{\mathrm{T}}^{\mathrm{miss}}$, which constrains the available trigger choices to those based on these physics objects. Single-τ triggers are generally avoided due to high p_T requirements or significant pre-scaling. Ditau triggers, while more viable, impose strict p_T thresholds on the subleading τ-lepton, which can impact signal acceptance. Pure $E_{\mathrm{T}}^{\mathrm{miss}}$-based triggers require a high $E_{\mathrm{T}}^{\mathrm{miss}}$ threshold (>200 GeV) to reach efficiency plateaus, which is not optimal given the kinematics of the signal. The combined ditau+$E_{\mathrm{T}}^{\mathrm{miss}}$ trigger provides the best compromise, and is therefore also what is used in this analysis. This trigger chain evolved throughout Run 2 with varying τ-lepton p_{T} threshold and identification algorithms (BDT vs RNN). An overview of the triggers employed in the different running periods is given in Table 9.5.

The main difference between the triggers is the p_T threshold on the leading τ-lepton, efficiency improvements at high pileup, and enhancements in τ-lepton identification and energy calibration. These improvements include RNN-based identification, refined track reconstruction, and multivariate energy calibration for better

Running period	Trigger name	$E_{\mathrm{T}}^{\mathrm{miss}}$	$p_{\mathrm{T}}(\tau_1)$	$p_{\mathrm{T}}(\tau_2)$	Lumi
2015 – 2017	HLT_tau35_medium1_tracktwo_tau25_medium1_tracktwo_xe50	> 150 GeV	> 40 GeV	> 30 GeV	77.2 fb^{-1}
parts of 2017	HLT_tau60_medium1_tracktwo_tau25_medium1_tracktwo_xe50	> 150 GeV	> 65 GeV	> 30 GeV	3.3 fb^{-1}
2018 period B-K	HLT_tau60_medium1_tracktwoEF_tau25_medium1_tracktwoEF_xe50	> 150 GeV	> 65 GeV	> 30 GeV	18.3 fb^{-1}
2018 from period K on	HLT_tau60_medium1_tracktwoEF_tau25_medium1_tracktwoEF_xe50 OR HLT_tau60_mediumRNN_tracktwoMVA_tau25_mediumRNN_tracktwoMVA_xe50	> 150 GeV	> 65 GeV	> 30 GeV	40.2 fb^{-1}

Table 9.5: Triggers used in different years and running periods. The corresponding offline thresholds imposed on $p_T(\tau_1)$, $p_T(\tau_2)$ and $E_{\mathrm{T}}^{\mathrm{miss}}$ are also shown.

performance. Both τ-leptons are required to have a p_{T} greater than 5 GeV above the online trigger threshold. Specifically, the leading τ has offline p_{T} thresholds of 40 or 65 GeV, while the subleading τ has a offline p_{T} threshold of 30 GeV. Although the HLT $E_{\mathrm{T}}^{\mathrm{miss}}$ requirement remained fixed at 50 GeV throughout Run 2, events must satisfy $E_{\mathrm{T}}^{\mathrm{miss}} > 150$ GeV to ensure the trigger operates at maximum efficiency. Additionally, dedicated per-event scale factors are applied to account for discrepancies between data and MC in the $E_{\mathrm{T}}^{\mathrm{miss}}$ efficiency (turn-on) curve.

9.3.2 Signal selection

The analysis is designed to be sensitive to the considered 2HDM+a signal points in the $m_A - m_a$ grid. The cuts are optimised using the Asimov significance (Eq. 7.15) as a metric, and the selection is performed in two steps. First, a common SR preselection is applied. In addition to requiring two oppositely charged τ-leptons with p_{T} and $E_{\mathrm{T}}^{\mathrm{miss}}$ above the trigger thresholds, events containing electrons, muons, or b-jets are vetoed, as the analysis only considers the $\tau_h\tau_h$ component of the Higgs decay.

To ensure compatibility with Higgs boson decays, the visible mass of the $\tau-$leptons, $m_{\tau\tau}^{\mathrm{vis}}$, is constrained to be between 40 and 125 GeV. The angular separation $\Delta R_{\tau\tau}$ is required to be less than 2 to suppress $t\bar{t}$ and W+jets backgrounds. To reduce $Z \to \tau\tau$ contributions, the variable m_T^{tot} is used, defined as:

$$m_{\mathrm{T}}^{\mathrm{tot}} = \sqrt{\left(p_{\mathrm{T}}^{\tau_1} + p_{\mathrm{T}}^{\tau_2} + p_{\mathrm{T}}^{\mathrm{miss}}\right)^2 - \left(p_x^{\tau_1} + p_x^{\tau_2} + p_x^{\mathrm{miss}}\right)^2 - \left(p_y^{\tau_1} + p_y^{\tau_2} + p_y^{\mathrm{miss}}\right)^2}, \tag{9.1}$$

where p_x^{miss} and p_y^{miss} are the x and y components of the $E_{\mathrm{T}}^{\mathrm{miss}}$ vector. Events with $m_{\mathrm{T}}^{\mathrm{tot}} < 50$ GeV are used for trigger efficiency studies and to derive trigger scale factors. To maintain orthogonality, events passing the inclusive preselection must therefore satisfy $m_{\mathrm{T}}^{\mathrm{tot}} > 50$ GeV.

The transverse mass of each τ-lepton is defined as:

$$m_{\mathrm{T}}^{\tau_i} = \sqrt{2p_{\mathrm{T}}^{\tau_i} E_{\mathrm{T}}^{\mathrm{miss}} \left(1 - \cos\Delta\phi\left(\tau_i, p_{\mathrm{T}}^{\mathrm{miss}}\right)\right)}, \tag{9.2}$$

Variable	Common SR Preselection	
N_τ	2 OS	
$N_e, N_\mu, N_{b-\mathrm{jet}}$	0	
$p_\mathrm{T}(\tau_1)$	$> 40/60$ GeV	
$p_\mathrm{T}(\tau_2)$	> 30 GeV	
$E_\mathrm{T}^\mathrm{miss}$	> 150 GeV	
$\Delta R_{\tau\tau}$	< 2	
$m_\mathrm{T}^\mathrm{tot}$	> 50 GeV	
$m_{\tau\tau}^\mathrm{vis}$	$\in [40, 125]$ GeV	
$m_\mathrm{T}^{\tau_1} + m_\mathrm{T}^{\tau_2}$	> 100 GeV	
	Low_{m_A} SR	High_{m_A} SR
$\Delta R_{\tau\tau}$	$\in [0.6, 1.9]$	< 2
$m_\mathrm{T}^\mathrm{tot}$	-	> 400 GeV
$m_\mathrm{T}^{\tau_1}$	> 50 GeV	-
$m_\mathrm{T}^{\tau_2}$	> 25 GeV	-
$m_{\tau\tau}^\mathrm{vis}$	> 75 GeV	$\in [40, 125]$ GeV
$m_\mathrm{T}^{\tau_1} + m_\mathrm{T}^{\tau_2}$ binning	$[100, 250, 400, 550, \infty]$ GeV	$[400, 750, \infty]$ GeV

Table 9.6: Summary of the selection requirements used to define the SRs. The upper part of the table describes the common SR preselection while the lower part of the table describes specific selections to define the Low_{m_A} and High_{m_A} SRs.

which is typically large when τ_i and $E_\mathrm{T}^\mathrm{miss}$ are back-to-back, as expected from the signal signature. To further suppress $Z \to \tau\tau$ contributions, where the τ-leptons and $E_\mathrm{T}^\mathrm{miss}$ tend to be more collimated, the sum $m_\mathrm{T}^{\tau_1} + m_\mathrm{T}^{\tau_2}$ is required to be greater than 100 GeV. The common SR preselection is shown in the upper part of Table 9.6.

Kinematic distributions for the different benchmark scenarios after the common SR preselection are shown in Figure 9.15 for varying m_A with $\sin\theta = 0.35$ and $\tan\beta = 1.0$, and in Figure 9.16 for varying $\tan\beta$ with $\sin\theta = 0.7$ and $m_a = 250$ GeV.

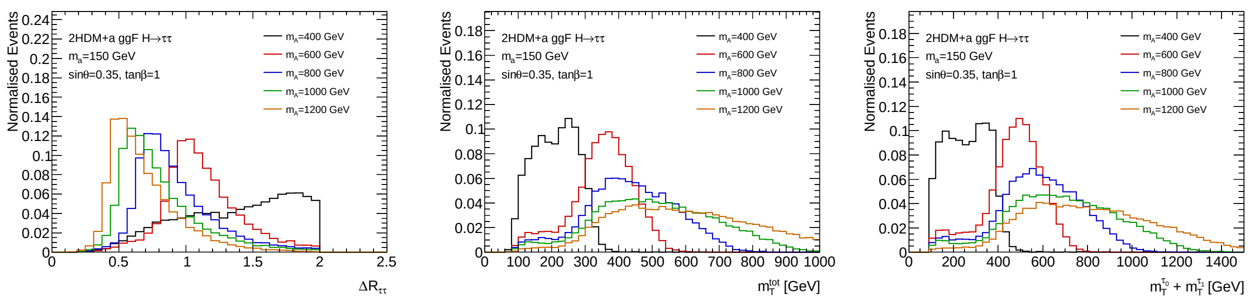

a) $\Delta R_{\tau\tau}$ b) $m_\mathrm{T}^\mathrm{tot}$ c) $m_\mathrm{T}^{\tau_1} + m_\mathrm{T}^{\tau_2}$

Figure 9.15: Kinematic distributions for various signal points produced via ggF with $\sin\theta = 0.35$ and $\tan\beta = 1.0$ after the common SR pre-selection for $\Delta R_{\tau\tau}$ (left), $m_\mathrm{T}^\mathrm{tot}$ (middle) and $m_\mathrm{T}^{\tau_1} + m_\mathrm{T}^{\tau_2}$ (right). The light pseudoscalar mass is fixed at $m_a = 150$ GeV, while m_A is varied between 400 and 1200 GeV.

In the $m_A - m_a$ parameter space, the kinematic distributions depend primarily on the mass of the heavy pseudoscalar. Small values of m_A result in softer $m_\mathrm{T}^\mathrm{tot}$ and $m_\mathrm{T}^{\tau_1} + m_\mathrm{T}^{\tau_2}$ distributions, while larger m_A values

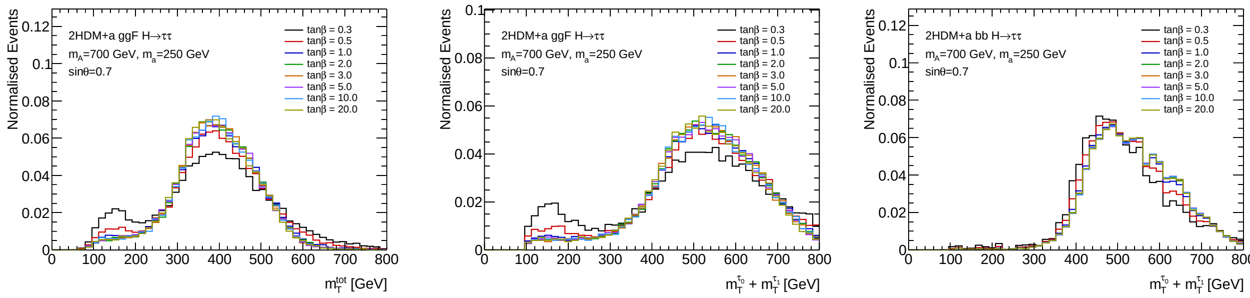

a) $m_{\mathrm{T}}^{\mathrm{tot}}$ b) $m_{\mathrm{T}}^{\tau_1} + m_{\mathrm{T}}^{\tau_2}$ ggF c) $m_{\mathrm{T}}^{\tau_1} + m_{\mathrm{T}}^{\tau_2}$ $b\bar{b}$

Figure 9.16: Kinematic distributions for various signal points with $\sin\theta = 0.7$ and $m_a = 250$ GeV after the common SR pre-selection produced via ggF: $\Delta R_{\tau\tau}$ (left) and $m_{\mathrm{T}}^{\tau_1} + m_{\mathrm{T}}^{\tau_2}$ (middle), and produced via $b\bar{b}$: $m_{\mathrm{T}}^{\tau_1} + m_{\mathrm{T}}^{\tau_2}$ (right). The heavy pseudoscalar mass is fixed at $m_A = 700$ GeV, while $\tan\beta$ is varied between 0.3 and 20.

shift the distributions towards higher masses with broader peaks. In contrast, the dependence on $\tan\beta$ is less pronounced, with most signal points exhibiting similar shapes. It should be noted that even if $b\bar{b}$-induced production contributes in the m_A–$\tan\beta$ benchmark scenario, its impact is significantly suppressed by the event selection. Hence, sensitivity mainly arises for smaller values of $\tan\beta$, where ggF production dominates.

Corresponding distributions of the background prediction after applying this selection for $\Delta R_{\tau\tau}$, $m_{\tau\tau}^{\mathrm{vis}}$, $m_{\mathrm{T}}^{\mathrm{tot}}$ and $m_{\mathrm{T}}^{\tau_1}$ can be seen in Figure 9.17. Representative signal points from both benchmark scenarios are also shown. The background predictions show good agreement with the data within uncertainties across all bins. After the common preselection, two non-orthogonal SRs are designed to target signal points in the $m_A - m_a$ parameter space with high and low masses of the heavy pseudoscalar, as these signal points have different kinematic properties.

The Low$_{m_A}$ SR is designed to target the part of the $m_A - m_a$ signal grid with $m_A \leq 800$ GeV and to be sensitive to points with as large m_a as possible. The angular distance $\Delta R_{\tau\tau}$ is further constrained to be between 0.6 and 1.9, and the visible mass of the τ-lepton pair is required to be greater than 75 GeV. The transverse mass of the τ-leptons is required to be greater than 50 GeV and 25 GeV for the leading and subleading τ-lepton, respectively. The Low$_{m_A}$ SR is divided into four bins in $m_{\mathrm{T}}^{\tau_1} + m_{\mathrm{T}}^{\tau_2}$.

The High$_{m_A}$ SR is designed to target signal points in the $m_A - m_a$ signal grid where $m_A > 800$ GeV. Both the total transverse mass, $m_{\mathrm{T}}^{\mathrm{tot}}$, and $m_{\mathrm{T}}^{\tau_1} + m_{\mathrm{T}}^{\tau_2}$ are further constrained to be above 400 GeV. The High$_{m_A}$ SR is divided into two bins, also in $m_{\mathrm{T}}^{\tau_1} + m_{\mathrm{T}}^{\tau_2}$. The selection criteria for the Low$_{m_A}$ SR and High$_{m_A}$ SR are summarised in the bottom section of Table 9.6.

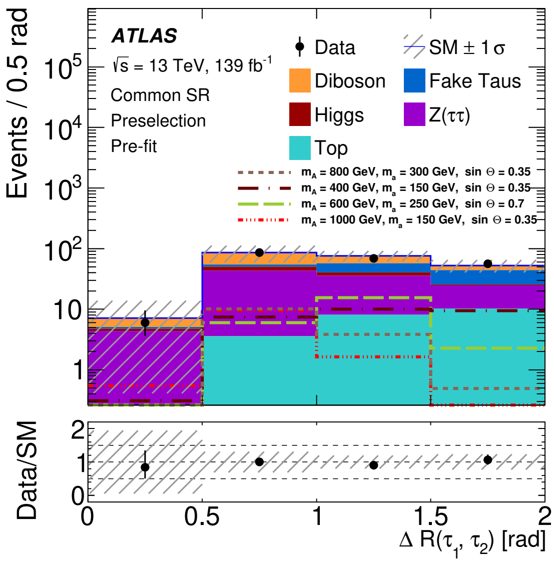

a) $\Delta R_{\tau\tau}$

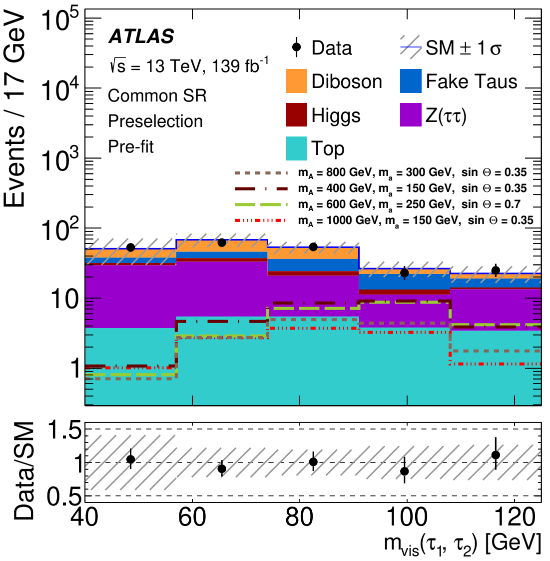

b) $m_{\tau\tau}^{\mathrm{vis}}$

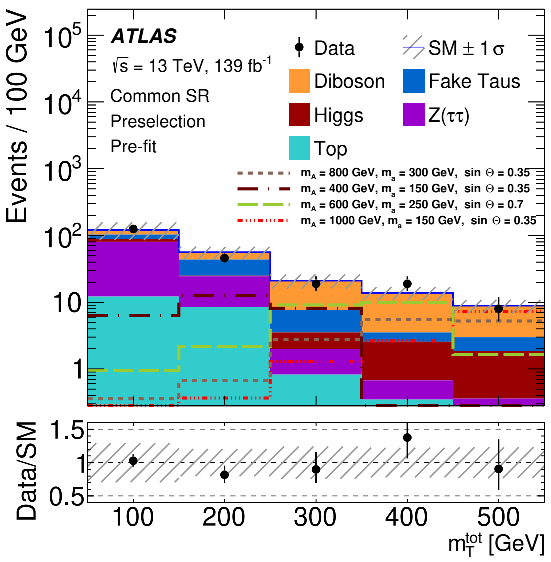

c) m_T^{tot}

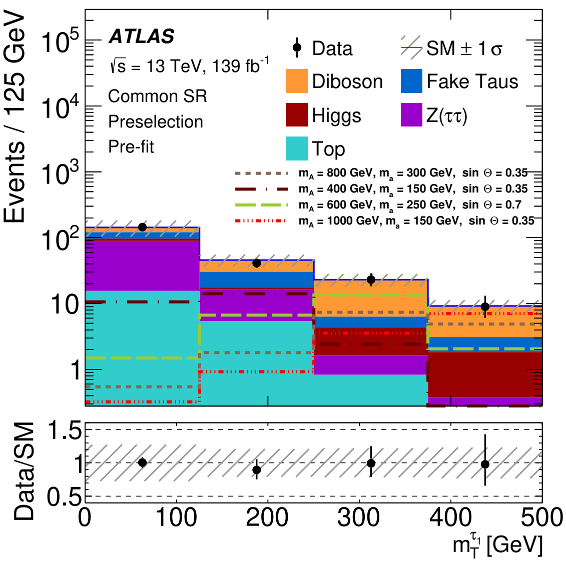

d) $m_{\mathrm{T}}^{\tau_1}$

Figure 9.17: Distributions for $\Delta R_{\tau\tau}$ (top left), $m_{\tau\tau}^{\mathrm{vis}}$ (top right), m_T^{tot} (bottom left) and $m_{\mathrm{T}}^{\tau_1}$ (bottom right) in the common SR. The uncertainty band include both statistical and systematic uncertainties. Four signal points are plotted on top of the expected SM backgrounds: $[m_A = 800,\ m_A = 300]$ GeV (beige), $[m_A = 400,\ m_A = 150]$ GeV (brown), $[m_A = 1000,\ m_A = 150]$ GeV (red) with $\sin\theta = 0.35$ and $\tan\beta = 1.0$ from the $m_A - m_a$ benchmark scenario, and $[m_A = 600,\ m_A = 250]$ GeV (green) with $\sin\theta = 0.7$ and $\tan\beta = 1.0$ from the $m_A - \tan\beta$ benchmark scenario.

9.4 Background estimation

The analysis is subject to several sources of background processes in the SRs. When considering the common SR preselection, the dominant processes arise from $Z \to \tau\tau$, fake, diboson, and top background. However, the tighter selections in the Low_{m_A} SR and High_{m_A} SR primarily suppress $Z \to \tau\tau$, with diboson becoming the dominant background in most bins. In the Low_{m_A} SR, diboson processes accounts for about 35% of the total background, followed by 28% from $Z \to \tau\tau$ processes, 20% from fake $\tau-$leptons, 10% from top processes (primarily from $t\bar{t}$), and 9% from Higgs processes. In the High_{m_A} SR, the main background component is also diboson processes, which constitutes 72% of the total background. Subdominant backgrounds include Higgs processes with 16% contribution and top processes with 9% contribution. Contributions from $Z \to \tau\tau$ and top are between 1-3%. Note that the relative contributions change and depends on which bin is considered.

Most background processes are estimated using MC simulations, with CRs defined for $Z \to \tau\tau$ and top processes to constrain their normalisation to data. Although diboson processes constitute the main background component, their kinematics resemble the signal too closely, making it challenging to define a diboson-enriched CR that is not signal contaminated. Instead, a VR is defined for diboson to validate the MC prediction to data. Additional VRs are also defined for $Z \to \tau\tau$ and top processes to validate the extrapolation of the modelling from the CRs to the SRs. The selection criteria for the VRs and CRs in this analysis is summarised in Table 9.7.

Finally, events with at least one fake τ-lepton are estimated from data. The approach is similar to what was described in Section 8.5.2 for the VBF CP analysis, but instead of misidentified electrons or muons, misidentified hadronic τ-leptons are now considered. Note that all regions shown in this section are binned and pre-fit, meaning that no corrections have been applied from the CRs. Ultimately, the VRs and CRs are treated as single-bin, with the modelling validated only after the fitting procedure.

Variable	Z CR	Z VR	Fake Tau VR	Top CR	Comb VR	Diboson VR
Charge(τ_1, τ_2)	OS	OS	**SS**	OS	OS	OS
$N_{b\text{-jet}}$	0	0	0	**1**	0	0
$\Delta R_{\tau\tau}$	< 2	< 2	> 2	> 1	> 2	< 2
$m_{\text{vis}}(\tau_1, \tau_2)$	$<$ **40 GeV**	[40, 75] GeV	-	-	$>$ 125 GeV	**[40, 75] GeV**
$m_{\text{T}}^{\text{tot}}$	$>$ 50 GeV	$>$ 50 GeV	-	-	-	**[50, 400] GeV**
$m_{\text{T}}^{\tau_1}$	-	-	-	-	-	$>$ 60 GeV
$m_{\text{T}}^{\tau_2}$	-	-	-	-	-	$>$ 20 GeV
$m_{\text{T}}^{\tau_1} + m_{\text{T}}^{\tau_2}$	-	$<$ **100 GeV**	-	-	-	$>$ 140 *GeV*
$p_{\text{T}}^{\tau_1+\tau_2}$	-	-	-	-	$<$ 125 GeV	-

Table 9.7: Definitions of control and validation regions used by the analysis. Additionally events are required to have two τ-leptons that pass the the trigger threshold cuts and veto muons and electrons. Bold entries indicate selections ensuring orthogonality to other regions. Comb VR refers to an inclusive validation region containing several important backgrounds.

9.4.1 Fake background

Misidentified τ-leptons mainly originate from hadronic jets that mimic the signature of hadronic decays. As with the fake non-prompt electrons and muons described in Section 8.5.2, these are estimated using data-driven methods. However, instead of the Matrix Method, the so-called fake factor method is employed [236]. The two methods are related, and the the fake factor method can in fact be derived exactly from the matrix method [236]. Since the author was not involved in this procedure only a brief overview will be provided.

The fake factor method assumes that the probability of a non-τ-lepton object passing the τ-lepton identification criteria can be determined solely by the properties of the object itself, including its p_{T}, η, number of charged-particle tracks, and origin (quark/gluon), and not by event-level variables such as $E_{\mathrm{T}}^{\mathrm{miss}}$ or the number of τ-leptons. This probability is quantified by the fake factor, which is defined as the ratio of objects passing the `Medium` identification requirement to those passing the looser anti-ID τ-lepton selection. Anti-ID correspond to all τ-leptons that does pass the signal requirement on the τ-leptons. The fake factors are measured as a function of p_{T}, $|\eta|$, number of charged-particle tracks, and origin in regions enriched with fake τ-leptons and are subsequently applied to the analysis regions to estimate the contribution of fake τ-lepton background.

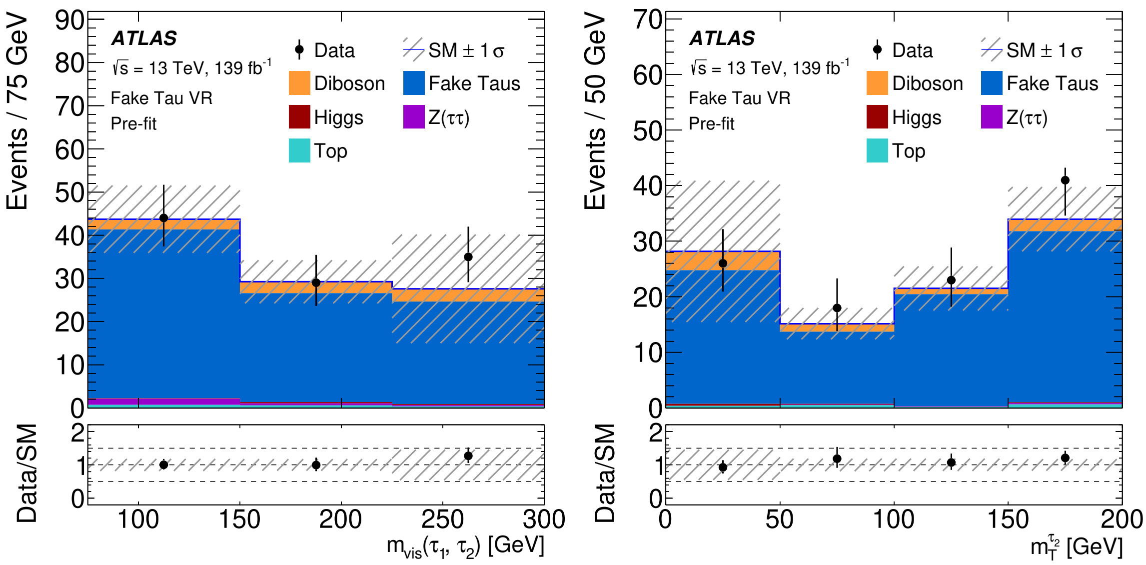

a) $m_{\tau\tau}^{\mathrm{vis}}$ b) $m_{\mathrm{T}}^{\tau_1}$

Figure 9.18: Distributions for $m_{\tau\tau}^{\mathrm{vis}}$ (left), $m_{\mathrm{T}}^{\tau_1}$ (right) in the same sign fake tau validation region. The uncertainty band includes both statistical and systematic uncertainties.

A fake tau VR is defined to validate the modelling from the fake estimate. Events in this region must pass the trigger thresholds and signal requirements, contain two τ-leptons, and veto electrons, muons, and b-jets. To improve the purity of fake τ-leptons in this region, the two τ-leptons are required to have the same charge.

Additionally, the condition $\Delta R_{\tau\tau} < 2$ is imposed to ensure the τ-leptons remain kinematically close to the common analysis phase space. Figure 9.18 shows distributions for $m_{\tau\tau}^{\text{vis}}$ and $m_{\text{T}}^{\tau_1}$ in the fake tau VR. The region has about 85% fake purity and demonstrates good agreement with data.

9.4.2 Z+jets background

The normalisation of the $Z \to \tau\tau$ + jets background is constrained by a normalisation factor derived from a dedicated $Z \to \tau\tau$ CR. Since this is the largest background in the general analysis phase space, defining an enriched region with sufficient statistics is relatively straightforward. In addition to the common CR/VR cuts, events are required to have $\Delta R_{\tau\tau} < 2$ to enrich the region in $Z \to \tau\tau$ event. An upper bound at 40 GeV is applied for the visible mass to keep the region orthogonal to the SRs and a lower bound of 50 GeV is applied for the total transverse mass to keep the region orthogonal to the region where trigger scale factors are derived.

This results in a CR with about 90% $Z \to \tau\tau$ purity. An additional VR is defined to validate the extrapolation of the $Z \to \tau\tau$ modelling from the $Z \to \tau\tau$ CR in the final fit. This region has a similar selection as the CR, but requires the visible mass to be in-between 40 and 75 GeV. To ensure orthogonality to the SRs, the sum $m_{\text{T}}^{\tau_1} + m_{\text{T}}^{\tau_2}$ is required to be less than 100 GeV. Distributions for $\Delta R_{\tau\tau}$ and $m_{\text{T}}^{\tau_1}$ in the $Z \to \tau\tau$ CR and $E_{\text{T}}^{\text{miss}}$ in the $Z \to \tau\tau$ VR can be seen in Figure 9.19.

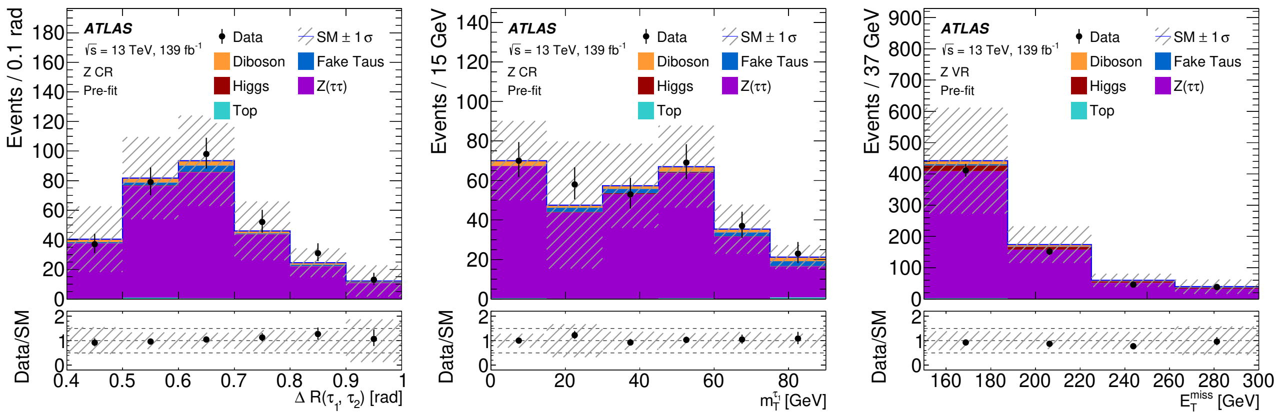

a) $m_{\tau\tau}^{\text{vis}}$ $Z \to \tau\tau$ CR   b) $m_{\text{T}}^{\tau_1}$ $Z \to \tau\tau$ CR   c) $E_{\text{T}}^{\text{miss}}$ $Z \to \tau\tau$ VR

Figure 9.19: Distributions for $\Delta R_{\tau\tau}$ (left), $m_{\text{T}}^{\tau_1}$ (middle) in the $Z \to \tau\tau$ CR and $E_{\text{T}}^{\text{miss}}$ in the $Z \to \tau\tau$ VR (right). The uncertainty band includes both statistical and systematic uncertainties.

9.4.3 Top background

The normalisation of the top background, primarily $t\bar{t}$, is constrained by a normalisation factor derived from a dedicated top CR. In addition to the common CR/VR selection criteria, the b-jet veto requirement is removed, and instead, exactly one b-jet is required.

The extrapolation across b-jet multiplicity is justified, as the majority of top-quark events entering the analysis phase space contain one true b-jet that fails the 77% b-tagging working point criteria. Similarly, events in the top CR with 1 b-jet that passes the working point criteria are also generally events with exactly one true b-jet. Hence the event composition is consistent between the region. To suppress contributions from other background processes, such as $Z \to \tau\tau$, events are required to satisfy $\Delta R_{\tau\tau} > 1$. This results in a CR with approximately 90% top purity. Distributions of $m_{\tau\tau}^{\mathrm{vis}}$ and $m_{\mathrm{T}}^{\tau_1}$ in the top CR are shown in Figure 9.20.

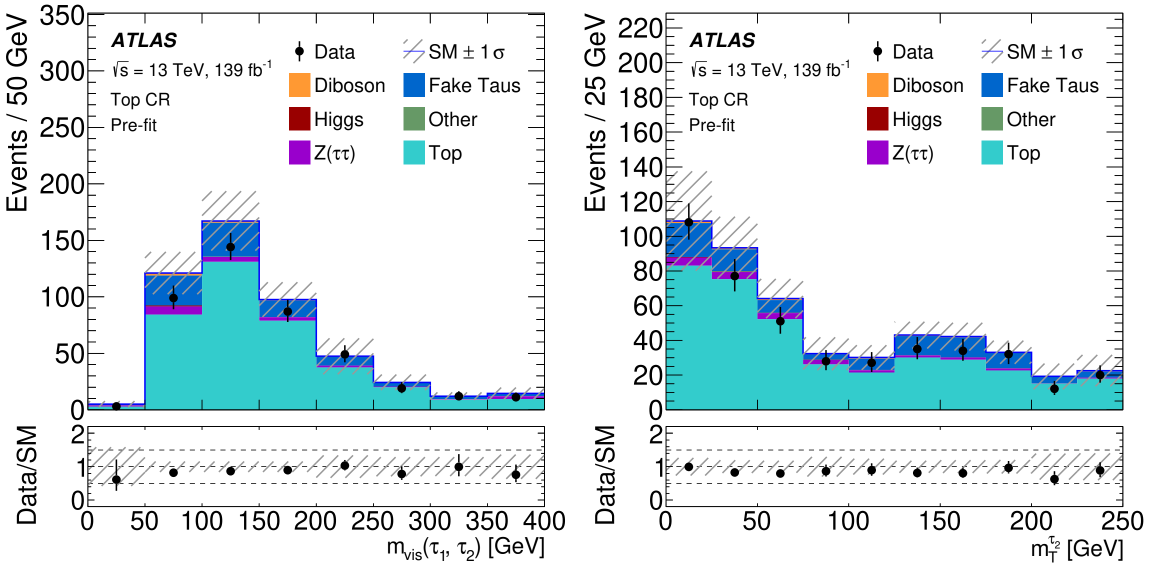

a) $m_{\tau\tau}^{\mathrm{vis}}$ b) $m_{\mathrm{T}}^{\tau_1}$

Figure 9.20: Distributions for $m_{\tau\tau}^{\mathrm{vis}}$ (left), $m_{\mathrm{T}}^{\tau_1}$ (right) in the top CR. The uncertainty band includes both statistical and systematic uncertainties.

9.4.4 Additional Validation Regions

An additional VR is defined to evaluate both the extrapolation of top modelling across b-jet multiplicity and the modelling of fake backgrounds. This region is defined at larger $\Delta R_{\tau\tau} > 2$, a phase space with reasonably large expected top and fake yields, along with contributions from $Z \to \tau\tau$ and diboson processes. Consequently, this serves as a combined VR for multiple processes. In addition to the angular cut, this region requires the common CR/VR selection criteria, two oppositely charged τ-leptons with a visible mass above 125 GeV and a di-τ transverse momentum below 125 GeV to suppress signal contamination.

Diboson processes constitute the main background in both SRs. However, the overall event yield in the analysis phase space is too low to construct a statistically enriched CR without significant signal contamination. Instead, a VR is defined to assess the modelling of diboson processes. The events in the diboson VR follow the general VR/CR selection, with additional upper bounds on $m_{\mathrm{T}}^{\tau_1}$ and $m_{\mathrm{T}}^{\tau_2}$ at 60 GeV and 20 GeV, respectively, as well as their sum $m_{\mathrm{T}}^{\tau_1} + m_{\mathrm{T}}^{\tau_2} < 140$ GeV to enhance diboson purity. To ensure orthogonality to the SRs, the requirements $m_{\tau\tau}^{\mathrm{vis}} < 75$ GeV and $m_T^{\mathrm{tot}} < 400$ GeV are imposed. Distribution for m_T^{tot} in the combined VR and $m_{\mathrm{T}}^{\tau_1} + m_{\mathrm{T}}^{\tau_2}$ in the diboson VR are shown in Figure 9.21.

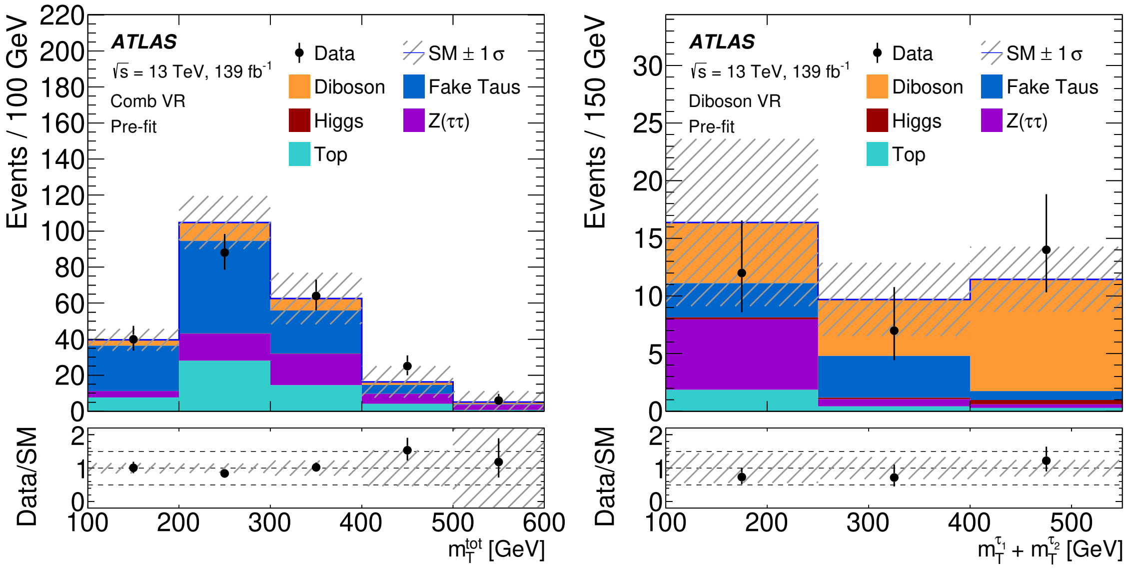

a) m_T^{tot} Comb VR

b) $m_{\mathrm{T}}^{\tau_1} + m_{\mathrm{T}}^{\tau_2}$ Diboson VR

Figure 9.21: Distributions for m_T^{tot} in the Comb validation region (left) and the sum $m_{\mathrm{T}}^{\tau_1} + m_{\mathrm{T}}^{\tau_2}$ (right) in the diboson validation region. The uncertainty band includes both statistical and systematic uncertainties.

9.5 Systematic uncertainties

The same set of experimental systematic uncertainty sources and a similar set of theoretical systematic uncertainties that was included in the VBF CP analysis are also included in this analysis. Additional sources include systematic uncertainties from the data-driven fake factor method and theory uncertainties on the 2HDM+a signal and relevant background samples.

9.5.1 Background theory uncertainties

This analysis use the prescription for assigning uncertainties to Top and $Z \to \tau\tau$ background processes as was described in Section 8.6. Since diboson processes are among the dominant backgrounds in both SRs, the same uncertainty prescription as was implemented for $Z \to \tau\tau$ are also included for these samples. Additionally a generator uncertainty is assigned to the theory prediction for both $Z \to \tau\tau$ and diboson processes.

Diboson and $Z \to \tau\tau$ generator uncertainties are estimated by comparing the nominal SHERPA produced samples with alternative MADGRAPH5_aMC@NLO + PYTHIA samples. The variation between the two samples is taken as the uncertainty. It should be noted that comparing the samples this way does not allow for separating the effects from the matrix element and parton shower in the generation chain. This was the reason it was dropped in the VBF CP analysis, since it resulted in noisy template histograms that overestimated uncertainties. In this analysis however, the templates are more reasonable. Figure 9.22 shows a comparison of the two generators for the diboson background in the High$_{m_A}$ SR and for the $Z \to \tau\tau$ background in the Low$_{m_A}$ SR.

Uncertainties related to the cross-section normalisation of diboson and Higgs background processes, arising from the theoretical cross-section predictions, are evaluated as a 15% overall uncertainty. This uncertainty is included since these processes are among the dominant background processes in the SRs, but not constrained by data.

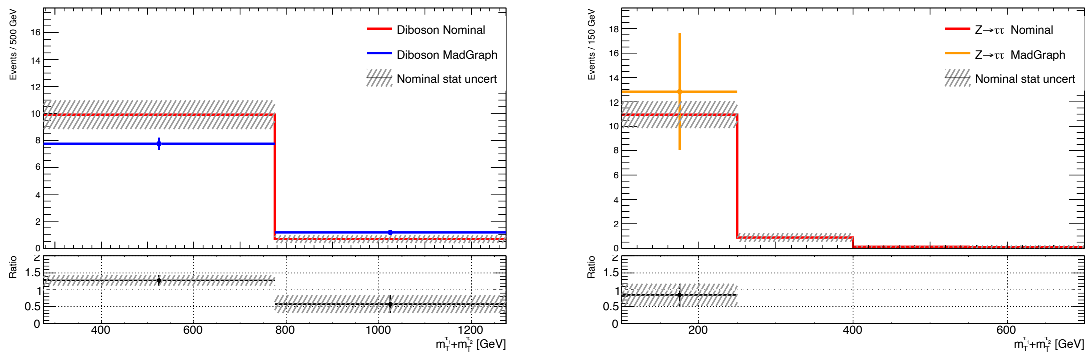

a) Diboson High$_{m_A}$ SR

b) $Z \to \tau\tau$ Low$_{m_A}$ SR

Figure 9.22: Histogram templates showing the nominal SHERPA distributions for the diboson background in the High$_{m_A}$ SR (left) and $Z \to \tau\tau$ in the Low$_{m_A}$ SR (right).

9.5.2 Signal theory uncertainties

The generated reco-level signal samples were not produced with the set of event weights needed to compute the scale variations for μ_R and μ_F. To avoid regenerating the full detector chain for the signal grids, which is very computationally expensive, a truth-level implementation is used instead. The nominal MADGRAPH5_aMC@NLO +PYTHIA setup is tuned to to generate samples with weights corresponding the different theory variations. These samples are further processed in the ATLAS SimpleAnalysis framework [237]. Within this framework an analysis-specific selection is implemented that selects objects with similar kinematic properties as those used in the analysis as well as performing a simple overlap-removal procedure. A comparison between the truth-level and reco-level distributions in the Low$_{m_A}$ SR and High$_{m_A}$ SR for three representative signal points in the $m_A - m_a$ grid is shown in Figure 9.23. Good agreement is observed in all bins, validating the extrapolation of theory uncertainties from truth-level.

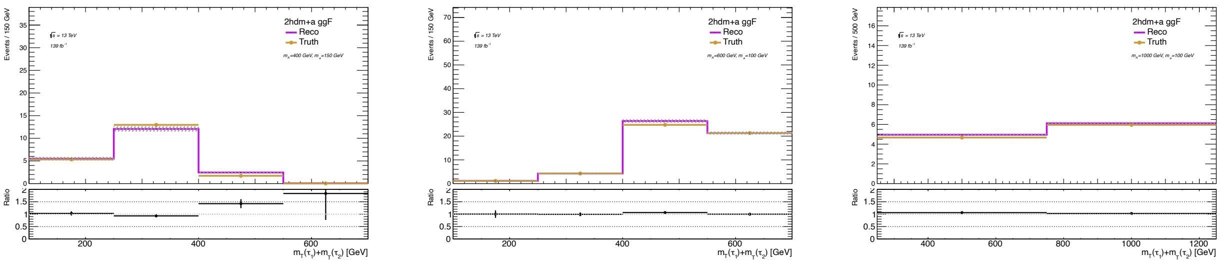

a) m_A = 400 GeV, m_a = 150 GeV b) m_A = 600 GeV, m_a = 100 GeV c) m_A = 1000 GeV, m_a = 100 GeV

Figure 9.23: Comparison of reco-level and truth-level distributions for $[m_A, m_a] \in [400, 150]$ GeV in (left) and $[m_A, m_a] \in [600, 100]$ GeV (middle) in the Low$_{m_A}$ SR and $[m_A, m_a] \in [600, 100]$ GeV (right) in the High$_{m_A}$ SR.

The theory uncertainty due to scale variations is estimated at truth-level like before by taking the envelope of the seven up/down variations. The resulting uncertainty is generally small for most signal points, with larger uncertainties being correlated with larger values of m_A. A conservative overall uncertainty of 10% is assigned to each signal point. This is well above the largest observed variation, but also reflects the uncertainty on the extrapolation from truth- to reco-level. Uncertainties on the cross-section is provided by MadGraph5_aMC@NLO during event generation. The largest uncertainty is found to be at 1.7% and is applied as an overall uncertainty for all signal samples. The PDF and α_s variations are included as weights at reco-level and the uncertainty is evaluated using a similar prescription as was discussed in the VBF CP analysis.

9.5.3 Data-driven fake uncertainties

Systematic uncertainties related to the fake-factor modelling include uncertainties in the number of events in the regions used to measure and apply the fake factors, the statistical and systematic uncertainties of the MC samples in the application regions, and uncertainties arising from the extrapolation and application of the fake factors.

9.6 Fit model

The goal of the analysis is to search for associated DM production in the 2HDM+a model based on the defined regions. The SRs used in the analysis are defined in Section 9.3 and the treatment of backgrounds is detailed in Section 9.4.

The analysis considers three types of fits, all implemented in the ATLAS HistFitter framework [238]. Firstly, a background-only fit performed in order to obtain normalisation factors from data and correct the background prediction for Top and $Z \to \tau\tau$ processes. The fit is performed simultaneously in both CRs defined in Section 9.4 with no SRs participating in the fit. No signal assumption is made and no signal models are included. The fitted normalisations are propagated to the SRs and VRs. The post-fit modelling in the VRs is then used to validate the extrapolation. The purpose of the fit is to check the quality of the modelling, obtain normalisation factors and evaluate the compatibility between prediction and data. A schematic of the general workflow for background-only fits in HistFitter is shown in Figure 9.24. The normalisation factors used in the fit and corresponding samples/regions are summarised in Table 9.8.

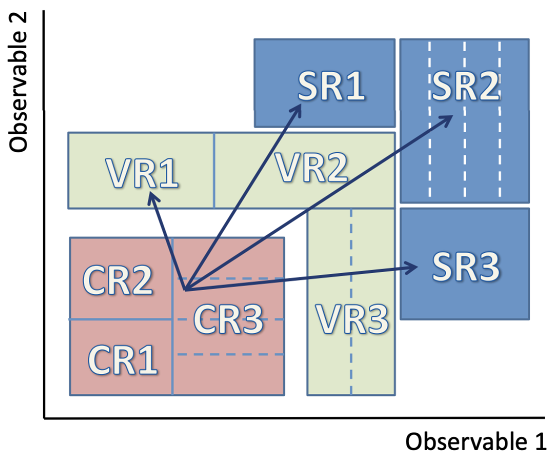

Figure 9.24: Illustration of the the typical HistFitter workflow for background-only fits where modelling is checked in the CRs and normalisation factors are propagated to the SRs/VRs [238].

Normalisation factor	Region	Sample
$NF_{Z\tau\tau}$	$Z \to \tau\tau$ CR	$Z \to \tau\tau$
NF_{Top}	Top CR	$t\bar{t}$ and single-top

Table 9.8: Normalisation factors used in the fits, the regions where they are obtained and the samples they are applied to.

Following the background-only fit, model dependent exclusion fits are performed with the purpose of setting limits on the 2HDM+a model. These fits are performed simultaneously in both CRs and individual SRs for each of the considered signal points in both the $m_A - m_a$ grid and the $m_A - \tan\beta$ grid. The normalisation factors obtained by the background-only fit are applied. The signal strength μ is treated as a free parameter in the fit, and the compatibility of the observed yields in the Low_{m_A} SR and High_{m_A} SR with respect to the signal predictions is evaluated. The results are obtained using the CL_s method introduced in Section 7.3. The CL_s value is computed for each signal point and interpolated to form 95% confidence level exclusion contours. This is done in both the $m_A - m_a$ grid and $m_A - \tan\beta$ grid. Since the two SRs are not statistically independent, the exclusion contours are computed separately and then combined according to the most sensitive expected CL_s result for each signal point in each region. In the $m_A - \tan\beta$ grid the CL_s values are only computed in the Low_{m_A} SR.

Finally, model independent upper limits on the visible cross-section of BSM physics are set by testing the compatibility of the background prediction and data. Fits are performed simultaneously in both CRs and separately for each SR bin. A generic signal model with signal strength μ is considered to be present in each SR bin.

9.6.1 Results from the background-only fit

The background-only fit is performed simultaneously in both CRs where normalisation factors are propagated to the VRs and SRs. The observed and predicted yields after the background-only fit in the CRs and VRs used in the analysis are shown in Figure 9.25. The statistical significance is computed according to the recommendations in Ref. [239] to quantify any deviations when observing n events given the prediction $b \pm \sigma$:

$$Z = \begin{cases} +\sqrt{2\left(n\ln\left[\frac{n(b+\sigma^2)}{b^2+n\sigma^2}\right] - \frac{b^2}{\sigma^2}\ln\left[1+\frac{\sigma^2(n-b)}{b(b+\sigma^2)}\right]\right)} & \text{if } n \geq b \\ -\sqrt{2\left(n\ln\left[\frac{n(b+\sigma^2)}{b^2+n\sigma^2}\right] - \frac{b^2}{\sigma^2}\ln\left[1+\frac{\sigma^2(n-b)}{b(b+\sigma^2)}\right]\right)} & \text{if } n < b. \end{cases} \tag{9.3}$$

The observed statistical significance is small (< 0.5) in each region, indicating good agreement between prediction and data. The normalisation factors obtained from the fit are summarised in Table 9.9. Both normalisation factors are consistent with one within uncertainties.

Normalisation factor	Value
$NF_{Z\tau\tau}$	$1.04^{+0.22}_{-0.22}$
NF_{Top}	$0.82^{+0.15}_{-0.15}$

Table 9.9: Normalisation factors from the background-only fit.

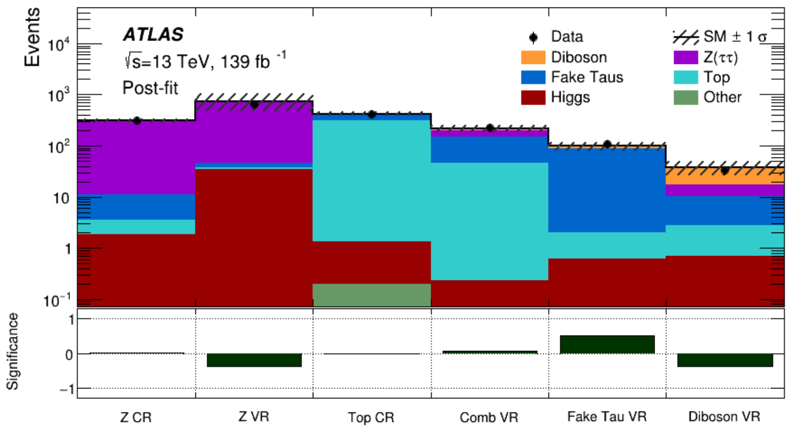

Figure 9.25: Expected and observed yields after the background-only fit in all VRs and CRs used in the analysis. The lower panel shows the estimated statistical significance in each region.

These normalisation factors are also propagated to the SRs to check for any excess. The resulting SR distributions in $m_{\mathrm{T}}^{\tau_1} + m_{\mathrm{T}}^{\tau_2}$ after the background-only fit can be seen in Figure 9.26.

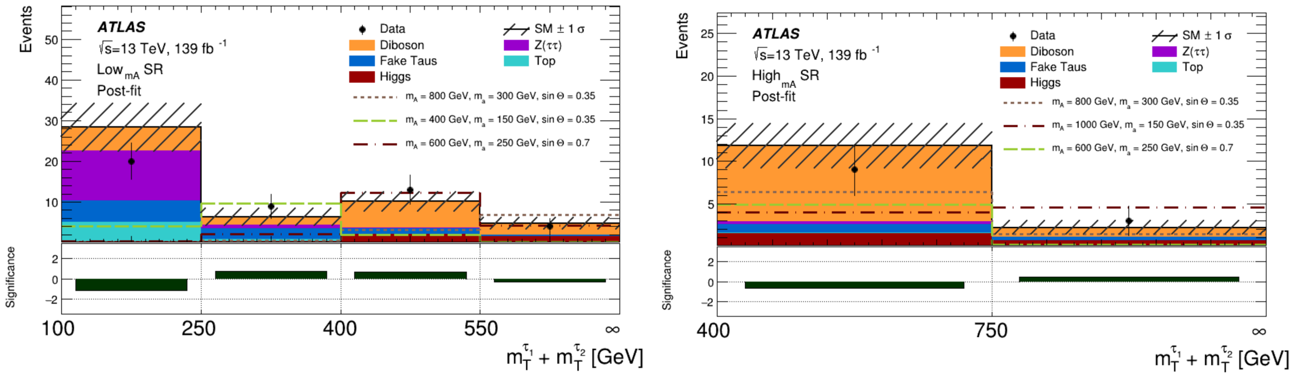

a) Low$_{m_A}$ SR

b) High$_{m_A}$ SR

Figure 9.26: Distributions of $m_{\mathrm{T}}^{\tau_1} + m_{\mathrm{T}}^{\tau_2}$ in the Low$_{m_A}$ SR (left) and High$_{m_A}$ SR (right) after the background-only fit. The lower panel shows the computed significance based on the observed and predicted yields in each bin. Three representative signal points are also shown.

No statistical significant deviation between prediction and data is observed and the results are consistent with the SM. The largest deviations comes from a slight under-prediction in the first bin in the Low$_{m_A}$ SR.

The corresponding event yields per bin are summarised in Table 9.10 and Table 9.11 for the Low$_{m_A}$ SR and High$_{m_A}$ SR, respectively. The quoted uncertainties include both statistical and systematic uncertainties. The grouped impact of the systematic uncertainties on the yields in all SR bins is summarised in Table 9.12. The largest sources of uncertainty in all bins come from background theory uncertainties, with dominating contributions including diboson and $Z \to \tau\tau$ generator uncertainties and scale variations. The uncertainties from the fake-factor method have especially large impact in the second bin of the Low$_{m_A}$ SR. This is driven by a higher contribution of fake τ-leptons in that bin, which has a large associated uncertainty due to limited statistics in the anti-ID region. Other significant sources of uncertainties are the limited number of MC events in the SRs and the uncertainty on the $Z \to \tau\tau$ normalisation factor.

$m_T^{\tau_1} + m_T^{\tau_2}$	$\in [100, 250]$ GeV	$\in [250, 400]$ GeV	$\in [400, 550]$ GeV	> 550 GeV
Observed events	20	9	13	4
Fitted background events	28.3 ± 5.9	6.3 ± 2.1	10.1 ± 2.4	4.8 ± 1.3
Diboson	5.7 ± 2.4	2.0 ± 0.7	6.5 ± 2.1	2.8 ± 1.1
$Z \to \tau\tau$	12.3 ± 3.8	$0.8^{+1.0}_{-0.8}$	$0.1^{+0.2}_{-0.1}$	$0.1^{+0.2}_{-0.1}$
$t\bar{t}$	4.4 ± 2.7	$0.3^{+0.8}_{-0.3}$	0.0 ± 0.0	0.0 ± 0.0
Single-top	$0.2^{+0.4}_{-0.2}$	$0.2^{+0.3}_{-0.2}$	0.0 ± 0.0	0.0 ± 0.0
$t\bar{t}V$	0.1 ± 0.0	0.1 ± 0.1	0.1 ± 0.0	0.1 ± 0.0
Higgs	0.4 ± 0.1	0.4 ± 0.1	2.0 ± 0.4	1.5 ± 0.4
Fake tau	5.3 ± 1.8	2.6 ± 1.3	1.4 ± 0.6	0.3 ± 0.2
$m_a = 150$ GeV, $\sin\theta = 0.35$ $m_A = 400$ GeV, $\tan\beta = 1$	4.1 ± 0.6	9.6 ± 1.2	1.9 ± 0.4	0.1 ± 0.0
$m_a = 250$ GeV, $\sin\theta = 0.7$ $m_A = 600$ GeV, $\tan\beta = 1$	0.4 ± 0.1	2.0 ± 0.3	12.3 ± 1.3	4.3 ± 0.6
$m_a = 300$ GeV, $\sin\theta = 0.35$ $m_A = 800$ GeV, $\tan\beta = 1$	0.2 ± 0.0	0.5 ± 0.1	3.1 ± 0.4	6.8 ± 0.9

Table 9.10: Observed and expected yields in the Low$_{m_A}$ SR bins after the background-only fit. The upper part of the table describes the breakdown of predicted SM backgrounds. The lower part of the table shows predicted yields of three signal model benchmark parameter configurations.

$m_T^{\tau_1} + m_T^{\tau_2}$	$\in [400, 750]$ GeV	> 750 GeV
Observed events	9	3
Fitted background events	11.8 ± 2.6	2.2 ± 0.8
Diboson	8.9 ± 2.4	1.1 ± 0.6
$Z \to \tau\tau$	$0.4^{+0.5}_{-0.4}$	$0.0^{+0.1}_{-0.0}$
$t\bar{t}V$	0.1 ± 0.0	0.1 ± 0.0
Higgs	1.5 ± 0.3	0.7 ± 0.2
Fake tau	0.9 ± 0.5	0.4 ± 0.3
$m_a = 150$ GeV, $\sin\theta = 0.35$ $m_A = 1000$ GeV, $\tan\beta = 1$	4.0 ± 0.5	4.6 ± 0.6
$m_a = 250$ GeV, $\sin\theta = 0.7$ $m_A = 600$ GeV, $\tan\beta = 1$	4.9 ± 0.7	0.2 ± 0.1
$m_a = 300$ GeV, $\sin\theta = 0.35$ $m_A = 800$ GeV, $\tan\beta = 1$	6.4 ± 0.8	1.4 ± 0.3

Table 9.11: Observed and expected yields in the High$_{m_A}$ SR bins after the background-only fit. The upper part of the table describes the breakdown of predicted SM backgrounds. The lower part of the table shows predicted yields of three signal model benchmark parameter configurations.

Region $m_T^{\tau_1} + m_T^{\tau_2}$ [GeV]	Low_{m_A} $\in [100, 250]$	Low_{m_A} $\in [250, 400]$	Low_{m_A} $\in [400, 550]$	Low_{m_A} > 550	High_{m_A} $\in [400, 750]$	High_{m_A} > 750
Theoretical	15.9%	20.9%	15.4%	13.3%	14.2%	21.7%
Fake τ-leptons	6.2%	19.1%	6.0%	3.0%	4.0%	13.2%
Jets	6.2%	7.9%	5.2%	11.0%	3.4%	7.9%
True τ-leptons	1.6%	3.1%	7.0%	10.6%	4.8%	5.0%
Normalisation	4.5%	4.0%	4.8%	8.1%	4.8%	6.1%
MC statistical	7.6%	13.2%	9.3%	15.6%	9.2%	22.2%
Other	4.1%	2.7%	5.3%	6.3%	4.9%	4.5%
Total	20.8%	32.8%	23.8%	28.3%	22.2%	36.3%

Table 9.12: Systematic uncertainties on the post-fit SM background predictions in the six bins in the Low_{m_A} SR after the background-only fit. The normalisation uncertainty includes the effect of keeping the normalisation factors as free-floating parameters in the fit. The individual sources of uncertainty can be correlated and do not necessarily add in quadrature to equal the total uncertainty. Other includes electron and muon uncertainties.

9.6.2 Limits on the 2HDM+a model

A signal-plus-background fit is performed for each considered signal point. The fit include the same CRs used in background-only fit and is performed separately for each SR since they are not statistically independent. The signal strength μ is treated as a free floating parameter. The 25 NPs with the largest impact on the fitted signal strength is shown in Figure 9.27 for $[m_A, m_a] = [800, 400]$ GeV in both the Low_{m_A} SR and High_{m_A} SR.

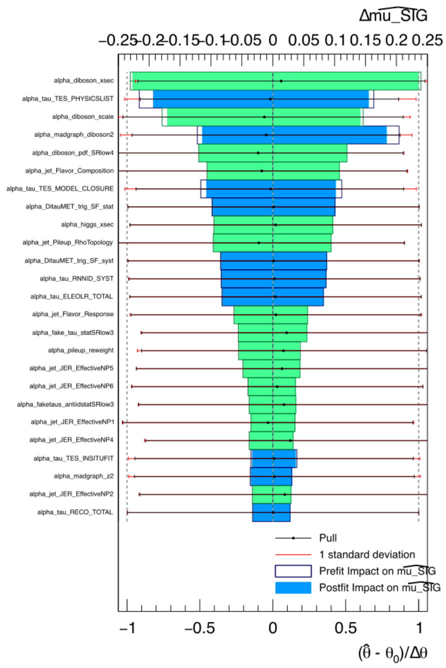

a) Low_{m_A} SR

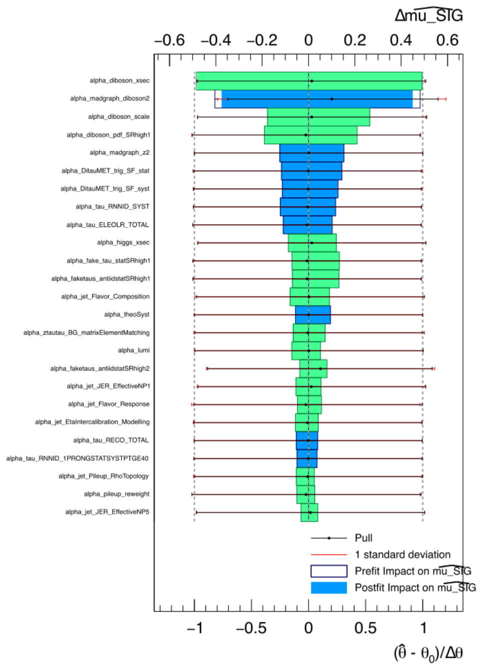

b) High_{m_A} SR

Figure 9.27: The top 25 ranked nuisance parameter based on their impact on the signal strength μ for the signal point $[m_A, m_a] = [800, 400]$ GeV with $\tan\beta = 1$ and $\sin\theta = 0.35$ in both Low_{m_A} SR (left) and High_{m_A} SR (right).

The ranking of the NPs is defined in the same way as was described in Section 8.7. The NPs with the largest impact mainly come from theoretical uncertainties related to the diboson background. Relevant contributions also include uncertainties related to the energy scale and identification of the reconstructed τ-leptons. It should be noted that the highest ranked NPs depends on the kinematics of the considered signal point and hence also on the corresponding background composition in relevant bins. This results in differences in the relative impact of certain NPs for different signal points, with diboson theory uncertainties generally having the largest impact across the signal grids.

The CL_s value for each signal point is calculated according to Eq. 7.12 in both SRs to form two separate exclusion contours. All points with $\mathrm{CL_s} \leq 0.05$ are excluded at 95% confidence level. This is first done for the $m_A - m_a$ parameter space, where the considered values are within $m_a \in [100, 400]$ GeV and $m_A \in [300, 1200]$ GeV. The Low_{m_A} SR is sensitive to values of $m_A \leq 800$ GeV, while the High_{m_A} SR has a bit higher reach with sensitivity up to 1000 GeV. The two contours are shown in Figure 9.28. The contours are combined using the expected CL_s value obtained with Asimov pseudodata as a figure of merit. The combined contour can be seen in Figure 9.29.

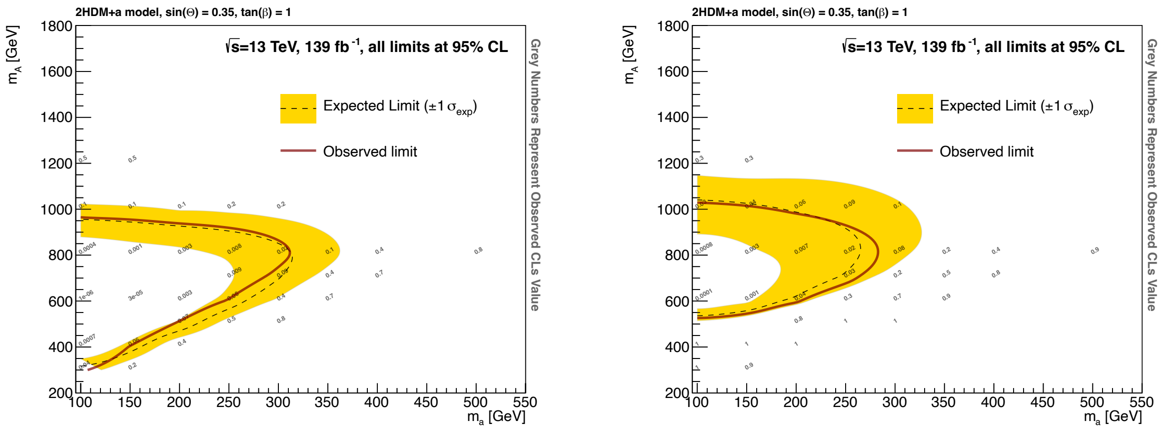

a) Low_{m_A} SR   b) High_{m_A} SR

Figure 9.28: Exclusion contours for the 2HDM+a in the $m_A - m_a$ grid in the Low_{m_A} SR (left) and High_{m_A} SR (right). All points to the left of the solid line are excluded at 95% confidence level with the $\pm 1\sigma$ uncertainty on the contour indicated by the yellow band. The dashed line is the expected contour obtained Asimov pseudodata.

The second parameter space considered by the analysis is based on signal points with $m_A \in [500, 1300]$ GeV and $\tan\beta \in [0.3, 20]$ with the parameters m_a and $\sin\theta$ fixed to the values of 250 GeV and 0.7 respectively. Only the Low_{m_A} SR has significant sensitivity to signal points with these parameter values. The resulting exclusion contour can be seen in Figure 9.30. Signal points with $\tan\beta \leq 1$ are excluded for m_A up to 900 GeV.

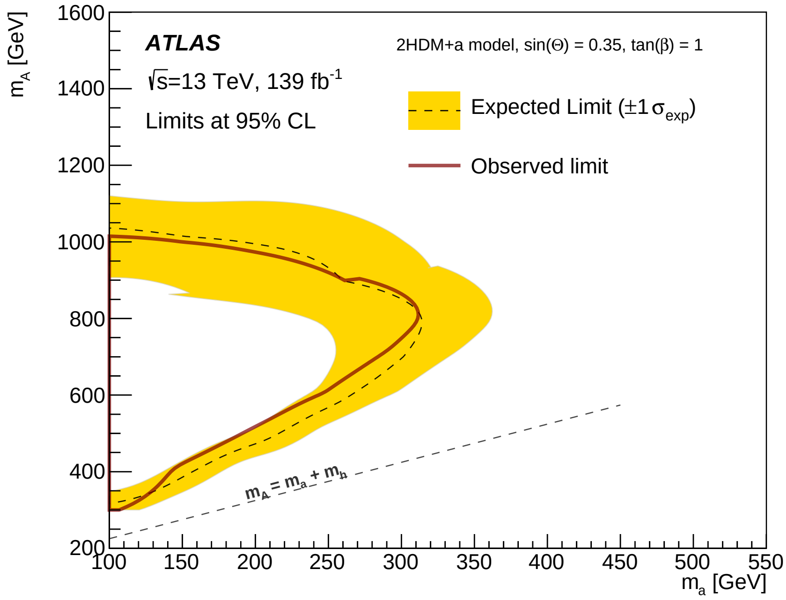

Figure 9.29: Observed and expected combined exclusion contours at 95% confidence level as function of m_a and m_A with $\tan\beta = 1$ and $\sin\theta = 0.35$. All points to the left of the solid line are excluded at 95% confidence level with the $\pm 1\sigma$ uncertainty on the contour indicated by the yellow band. The dashed line is the expected contour obtained Asimov pseudodata.

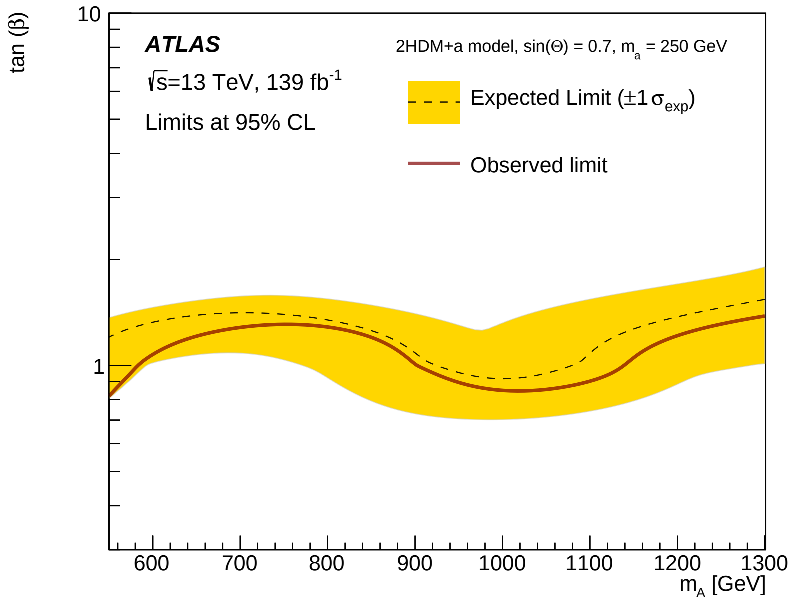

Figure 9.30: Observed and expected exclusion contours at 95% confidence level as function of m_A and $\tan\beta$ with $m_a = 250$ GeV and $\sin\theta = 0.7$ in the Low$_{m_A}$ SR. All points bellow the solid line are excluded at 95% confidence level with the $\pm 1\sigma$ uncertainty on the contour indicated by the yellow band. The dashed line is the expected contour obtained Asimov pseudodata.

The 2HDM+a model has been probed in a wide range of physics analyses in ATLAS. A summary from various Run 2 results can be found in Ref. [113]. The summary plots in the $m_A - m_a$ and $m_A - \tan\beta$ parameter spaces can be seen in Figure 9.31 and Figure 9.32, respectively. The sensitivity is mainly driven by the $E_T^{\mathrm{miss}} + h(b\bar{b})$ [116] and the $E_T^{\mathrm{miss}} + Z(\ell\ell)$ [117] searches in both parameter grids, with the former providing the strongest constraints for high m_A in the $m_A - m_a$ grid. The green filled regions are obtained by a statistical combination of the $E_T^{\mathrm{miss}} + h(b\bar{b})$, $E_T^{\mathrm{miss}} + Z(\ell\ell)$ and $tbH^{\pm}(tb)$ searches, and covers most of the considered parameter space. The sensitivity from the $h(\tau\tau) + E_T^{\mathrm{miss}}$ search discussed in this thesis is indicated in pale pink and exclude parts of the $m_A - m_a$ parameter space also previously excluded by $h(b\bar{b})$. Due to the lower branching fraction of the Higgs decay to τ-leptons the constraints are weaker for larger values of m_A. This analysis is however more sensitive than the $E_T^{\mathrm{miss}} + h(\gamma\gamma)$ search [240], which can only exclude values of m_A up to 800 GeV and values of m_a up to 250 GeV.

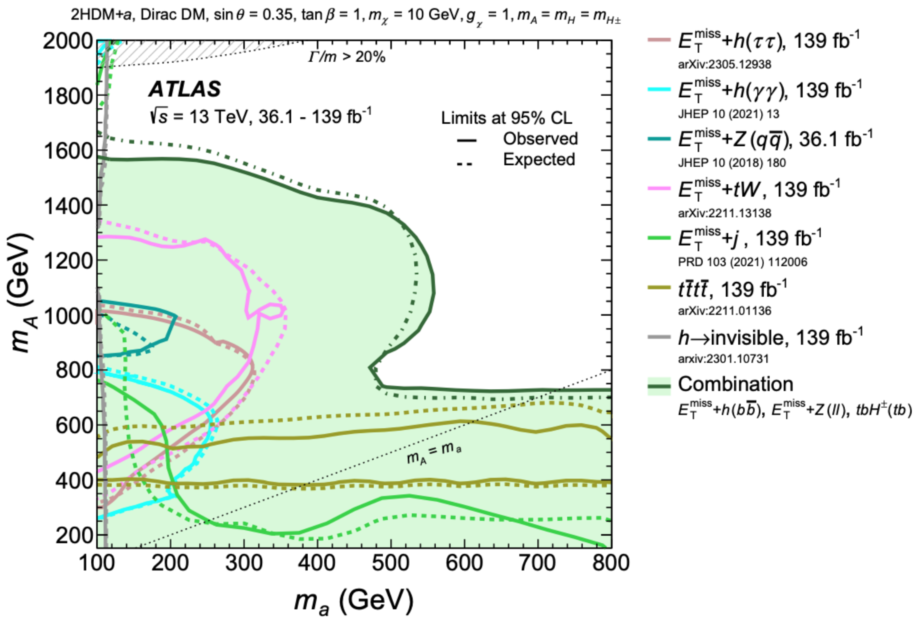

Figure 9.31: Observed (solid lines and filled area) and expected (dashed lines) exclusion regions at 95% CL in the $m_A - m_a$ space for different ATLAS Run 2 searches. The green filled area is the exclusion region coming from the the statistical combination of the $E_T^{\mathrm{miss}} + h(b\bar{b}), E_T^{\mathrm{miss}} + Z(\ell\ell)$, and $tbH^{\pm}(tb)$ searches. The exclusion contour from this analysis is indicated in pale pink. The dashed grey regions indicate the region where the width any Higgs bosons exceed 20% of its mass. Taken from [113].

In the $m_A - \tan\beta$ parameter space, this analysis offers complimentary sensitivity for low $\tan\beta$ values, compared to the $h(b\bar{b}) + E_T^{\mathrm{miss}}$ analysis. However, also in this parameter configuration, $h(b\bar{b}) + E_T^{\mathrm{miss}}$ generally have stronger constraints due to the larger branching ratio. Nevertheless, this analysis is the first search in the $E_T^{\mathrm{miss}} + h(\tau\tau)$ final state, and is defined to be statistically independent from other searches. It can therefore be included in future statistical combinations.

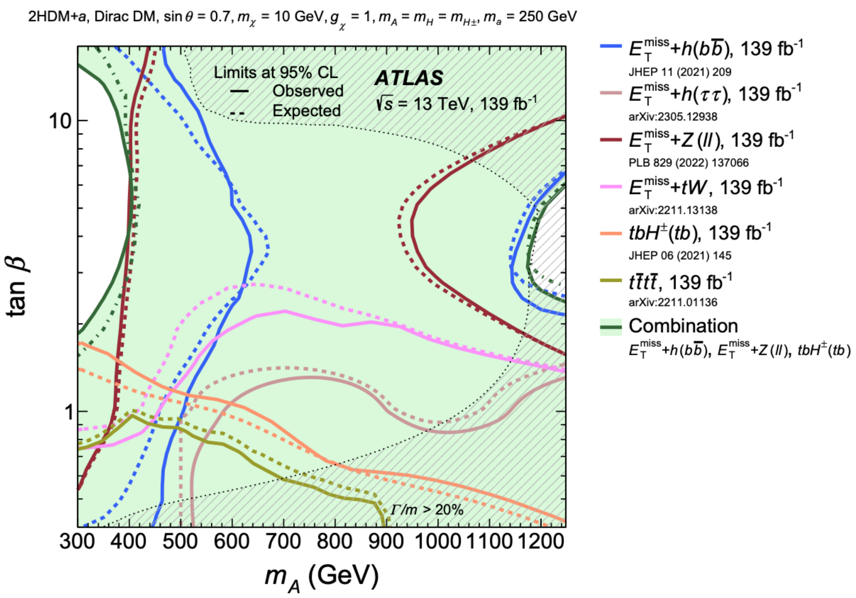

Figure 9.32: Observed (solid lines and filled area) and expected (dashed lines) exclusion regions at 95% CL in the $m_A - \tan\beta$ parameter space for different ATLAS Run 2 searches. The green filled area is the exclusion region coming from the the statistical combination of the $E_{\mathrm{T}}^{\mathrm{miss}} + h(b\bar{b})$, $E_{\mathrm{T}}^{\mathrm{miss}} + Z(\ell\ell)$, and $tbH^{\pm}(tb)$ searches. The exclusion contour from this analysis is indicated in pale pink. The dashed grey regions indicate the region where the width any Higgs bosons exceed 20% of its mass [113].

9.6.3 Model independent fits

The model-independent (or discovery) fit is used to set a limit on the number of events in the SRs above the SM background prediction. This way the analysis sets general upper limit on the visible cross-section of new physics in the $h(\tau\tau) + E_{\mathrm{T}}^{\mathrm{miss}}$ topology.

No specific signal model is assumed. However, a dummy signal model is introduced for each SR bin, assigned a bin value of one. A corresponding free floating signal strength parameter is included in the fit. The fit is performed simultaneously across both CRs and each SR bin individually, with the post-fit normalisation factors propagated to each bin. The following parameters are computed:

$\boldsymbol{\langle\epsilon\sigma\rangle^{95}_{obs}}$: 95% CL upper limit on the visible cross-section for new physics.

$\boldsymbol{S^{95}_{exp}}$: 95% CL upper limit on the number of signal events.

$\boldsymbol{S^{95}_{exp}}$: 95% CL upper limit on the number of signal events, given the number of SM predicted background events.

$\mathbf{CL}_b$: Confidence level for the background only (SM) hypothesis.

$\boldsymbol{p(s=0)}$: Discovery p-value for new physics.

The observed values for these parameters are summarised in Table 9.13. No evidence for new physics is observed, with the upper limit on the visible cross-section at 95% confidence level ranging between 0.04 and 0.08 depending on the fitted bin.

Signal channel	$\langle\epsilon\sigma\rangle_{obs}^{95}$[fb]	S_{obs}^{95}	S_{exp}^{95}	$\mathrm{CL_b}$	$p(s=0)$ (Z)
Low_{m_A} SR					
$m_\mathrm{T}^{\tau_1}+m_\mathrm{T}^{\tau_2}\in[100,250]$ GeV	0.08	10.7	$12.5^{+5.2}_{-3.5}$	0.27	0.86 (−1.07)
$m_\mathrm{T}^{\tau_1}+m_\mathrm{T}^{\tau_2}\in[250,400]$ GeV	0.07	9.1	$7.6^{+3.1}_{-1.6}$	0.72	0.30 (0.53)
$m_\mathrm{T}^{\tau_1}+m_\mathrm{T}^{\tau_2}\in[400,550]$ GeV	0.08	10.8	$8.9^{+3.4}_{-2.3}$	0.75	0.26 (0.65)
$m_\mathrm{T}^{\tau_1}+m_\mathrm{T}^{\tau_2}>550$ GeV	0.04	5.8	$6.0^{+2.6}_{-1.6}$	0.42	0.61 (−0.29)
High_{m_A} SR					
$m_\mathrm{T}^{\tau_1}+m_\mathrm{T}^{\tau_2}\in[400,750]$ GeV	0.05	7.6	$8.8^{+3.1}_{-2.4}$	0.34	0.85 (−1.03)
$m_\mathrm{T}^{\tau_1}+m_\mathrm{T}^{\tau_2}>750$ GeV	0.04	5.4	$4.6^{+1.8}_{-0.8}$	0.67	0.34 (0.42)

Table 9.13: Left to right: 95% CL upper limits on the visible cross-section ($\langle\epsilon\sigma\rangle_{obs}^{95}$) and on the number of signal events (S_{obs}^{95}). The third column (S_{exp}^{95}) shows the 95% CL upper limit on the number of signal events, given the expected number (and $\pm1\sigma$ excursions on the expectation) of background events. The last two columns indicate the $\mathrm{CL_b}$ value, i.e. the confidence level observed for the background-only hypothesis, and the discovery p-value ($p(s=0)$).

Chapter **10**

Conclucion

In this thesis, two independent analyses have been presented, both exploiting the full Run 2 dataset of proton–proton collisions at $\sqrt{s} = 13$ TeV recorded by the ATLAS experiment, corresponding to an integrated luminosity of 140 fb^{-1}. While both analyses investigate Higgs boson production in final states with τ-leptons, they focus on different physical phenomena.

The measurement of Higgs CP properties in VBF HVV couplings is covered in Chapter 8. The analysis is motivated by the Shakarov conditions which state that new source of CP violation are needed, beyond those in the SM, to explain the observed baryon asymmetry in the universe. The analysis targets the VBF production mode and use NNs to separate signal from backgrounds. Two SRs are defined from the corresponding NN output score, and are binned in the Optimal Observable to measure and constrain EFT parameters that induce CP-violating couplings in the HVV vertex. No sign of CP violation is observed, and the results are consistent with the SM prediction. The best fit value and associated uncertainties in the HISZ basis is obtained by maximum likelihood fits to data via $\tilde{d}$, and is measured to be:

$$\tilde{d} = 0.003^{+0.032}_{-0.032}\,(1\sigma)^{+0.088}_{-0.081}\,(2\sigma)\ (\tau_\ell\tau_\ell \text{ only}),$$
$$\tilde{d} = 0.014^{+0.014}_{-0.013}\,(1\sigma)^{+0.030}_{-0.025}\,(2\sigma)\ (\text{combined}).$$

This measurement is a sizeable improvement with respect to the partial Run 2 measurement [51], with $\tau_\ell\tau_\ell$ alone providing more sensitivity. Additional new interpretations in the Warsaw basis are also added via measurements of the CP-odd Wilson coefficients $c_{H\tilde{W}}$, $c_{H\tilde{B}}$ and $c_{H\tilde{W}B}$. The analysis is mainly sensitivity to $c_{H\tilde{W}}$ due to the coupling structure of the HVV vertex in VBF production. The best fit value and associated uncertainties for $c_{H\tilde{W}}$ is measured to be:

$$c_{H\tilde{W}} = 0.05^{+0.64}_{-0.61}\,(1\sigma)^{+1.66}_{-1.43}\,(2\sigma)\ (\tau_\ell\tau_\ell \text{ only}),$$

$$c_{H\tilde{W}} = 0.25^{+0.27}_{-0.25}\,(1\sigma)^{+0.57}_{-0.51}\,(2\sigma)\ \text{(combined)}.$$

These measurements represent some of the most stringent constraints to date in ATLAS, and will contribute to a broader combination effort with measurements in the $H \to \gamma\gamma$ [53] and $H \to ZZ \to 4\ell$ [52] channels. The combined results will conclude the ATLAS Run 2 program of measurements of the CP properties in VBF Higgs production, thereby establishing a benchmark for future precision studies of the CP nature of the Higgs boson.

The search for DM produced in association with a Higgs boson decaying into a pair of hadronically decaying τ-leptons is covered in Chapter 9. The analysis uses the same full Run 2 dataset and targets final states with large $E_{\mathrm{T}}^{\mathrm{miss}}$. Two SRs are defined, each subdivided into bins of $m_{\mathrm{T}}^{\tau_1} + m_{\mathrm{T}}^{\tau_2}$ to probe different parts of parameter space. No significant excess over the SM background is observed.

The results are interpreted in the context of the 2HDM+a model, setting 95% confidence level limits in both the m_a–m_A and m_A–$\tan\beta$ parameter grids. Model-independent upper limits are also placed on the visible cross-section, σ_{vis}, for BSM processes involving large $E_{\mathrm{T}}^{\mathrm{miss}}$ and a Higgs boson decaying to τ-leptons. These limits range from 0.04 to 0.08 fb, depending on the considered SR bin. This work represents the first ATLAS exploration of the mono-Higgs signature with $E_{\mathrm{T}}^{\mathrm{miss}} + h(\tau\tau)$, and offers complementary sensitivity to the existing $E_{\mathrm{T}}^{\mathrm{miss}} + h(b\bar{b})$ mono-Higgs search [116], particularly in the low $\tan\beta$ region of the m_A–$\tan\beta$ plane. In both considered benchmark scenarios, the analysis is defined with an orthogonal event selection with respect to other searches, which allows for future combinations.

Bibliography

[1] Georges Aad et al. Observation of a new particle in the search for the Standard Model Higgs boson with the ATLAS detector at the LHC. *Phys. Lett. B*, 716:1–29, 2012. doi:10.1016/j.physletb.2012.08.020.

[2] Serguei Chatrchyan et al. Observation of a New Boson at a Mass of 125 GeV with the CMS Experiment at the LHC. *Phys. Lett. B*, 716:30–61, 2012. doi:10.1016/j.physletb.2012.08.021.

[3] Patrick Huet and Eric Sather. Electroweak baryogenesis and standard model cp violation. *Phys. Rev. D*, 51:379–394, Jan 1995. doi:10.1103/PhysRevD.51.379. URL `https://link.aps.org/doi/10.1103/PhysRevD.51.379`.

[4] M. B. Gavela, P. Hernandez, J. Orloff, and O. Pene. Standard model CP violation and baryon asymmetry. *Mod. Phys. Lett. A*, 9:795–810, 1994. doi:10.1142/S0217732394000629.

[5] A G Cohen, D B Kaplan, and A E Nelson. Progress in electroweak baryogenesis. *Annual Review of Nuclear and Particle Science*, 43(1):27–70, December 1993. ISSN 1545-4134. doi:10.1146/annurev.ns.43.120193.000331. URL `http://dx.doi.org/10.1146/annurev.ns.43.120193.000331`.

[6] A. D. Sakharov. Violation of CP Invariance, C asymmetry, and baryon asymmetry of the universe. *Pisma Zh. Eksp. Teor. Fiz.*, 5:32–35, 1967. doi:10.1070/PU1991v034n05ABEH002497.

[7] Nicola Cabibbo. Unitary symmetry and leptonic decays. *Phys. Rev. Lett.*, 10:531–533, Jun 1963. doi:10.1103/PhysRevLett.10.531. URL `https://link.aps.org/doi/10.1103/PhysRevLett.10.531`.

[8] Makoto Kobayashi and Toshihide Maskawa. CP Violation in the Renormalizable Theory of Weak Interaction. *Prog. Theor. Phys.*, 49:652–657, 1973. doi:10.1143/PTP.49.652.

[9] G. Hinshaw et al. Five-Year Wilkinson Microwave Anisotropy Probe (WMAP) Observations: Data Processing, Sky Maps, and Basic Results. *Astrophys. J. Suppl.*, 180:225–245, 2009. doi:10.1088/0067-0049/180/2/225.

[10] P. A. R. Ade et al. Planck 2015 results. XIII. Cosmological parameters. *Astron. Astrophys.*, 594:A13, 2016. doi:10.1051/0004-6361/201525830.

[11] Martin Bauer, Ulrich Haisch, and Felix Kahlhoefer. Simplified dark matter models with two higgs doublets: I. pseudoscalar mediators. *Journal of High Energy Physics*, 2017(5), May 2017. ISSN 1029-8479. doi:10.1007/jhep05(2017)138. URL `http://dx.doi.org/10.1007/JHEP05(2017)138`.

[12] T. Nakano and K. Nishijima. Charge Independence for V-particles. *Prog. Theor. Phys.*, 10:581–582, 1953. doi:10.1143/PTP.10.581.

[13] S. Navas et al. Review of particle physics. *Phys. Rev. D*, 110(3):030001, 2024. doi:10.1103/PhysRevD.110.030001.

[14] S. L. Glashow. Partial Symmetries of Weak Interactions. *Nucl. Phys.*, 22:579–588, 1961. doi:10.1016/0029-5582(61)90469-2.

[15] Steven Weinberg. A Model of Leptons. *Phys. Rev. Lett.*, 19:1264–1266, 1967. doi:10.1103/PhysRevLett.19.1264.

[16] Abdus Salam. Weak and Electromagnetic Interactions. *Conf. Proc. C*, 680519:367–377, 1968. doi:10.1142/9789812795915_0034.

[17] G. Arnison et al. Experimental Observation of Isolated Large Transverse Energy Electrons with Associated Missing Energy at $\sqrt{s} = 540$ GeV. *Phys. Lett. B*, 122:103–116, 1983. doi:10.1016/0370-2693(83)91177-2.

[18] M. Banner et al. Observation of Single Isolated Electrons of High Transverse Momentum in Events with Missing Transverse Energy at the CERN anti-p p Collider. *Phys. Lett. B*, 122:476–485, 1983. doi:10.1016/0370-2693(83)91605-2.

[19] G. S. Guralnik, C. R. Hagen, and T. W. B. Kibble. Global Conservation Laws and Massless Particles. *Phys. Rev. Lett.*, 13:585–587, 1964. doi:10.1103/PhysRevLett.13.585.

[20] F. Englert and R. Brout. Broken Symmetry and the Mass of Gauge Vector Mesons. *Phys. Rev. Lett.*, 13: 321–323, 1964. doi:10.1103/PhysRevLett.13.321.

[21] Peter W. Higgs. Broken Symmetries and the Masses of Gauge Bosons. *Phys. Rev. Lett.*, 13:508–509, 1964. doi:10.1103/PhysRevLett.13.508.

[22] Christoph Berger et al. Jet Analysis of the Υ (9.46) Decay Into Charged Hadrons. *Phys. Lett. B*, 82: 449–455, 1979. doi:10.1016/0370-2693(79)90265-X.

[23] Christoph Berger et al. Evidence for Gluon Bremsstrahlung in e+ e- Annihilations at High-Energies. *Phys. Lett. B*, 86:418–425, 1979. doi:10.1016/0370-2693(79)90869-4.

[24] R. Brandelik et al. Evidence for Planar Events in e+ e- Annihilation at High-Energies. *Phys. Lett. B*, 86: 243–249, 1979. doi:10.1016/0370-2693(79)90830-X.

[25] D. P. Barber et al. Discovery of Three Jet Events and a Test of Quantum Chromodynamics at PETRA Energies. *Phys. Rev. Lett.*, 43:830, 1979. doi:10.1103/PhysRevLett.43.830.

[26] S. Abachi et al. Search for high mass top quark production in $p\bar{p}$ collisions at $\sqrt{s} = 1.8$ TeV. *Phys. Rev. Lett.*, 74:2422–2426, 1995. doi:10.1103/PhysRevLett.74.2422.

[27] F. Abe et al. Observation of top quark production in $\bar{p}p$ collisions. *Phys. Rev. Lett.*, 74:2626–2631, 1995. doi:10.1103/PhysRevLett.74.2626.

[28] S. W. Herb et al. Observation of a Dimuon Resonance at 9.5-GeV in 400-GeV Proton-Nucleus Collisions. *Phys. Rev. Lett.*, 39:252–255, 1977. doi:10.1103/PhysRevLett.39.252.

[29] Standard Model Summary Plots June 2024. Technical report, CERN, Geneva, 2024. URL `https://cds.cern.ch/record/2903866`. All figures including auxiliary figures are available at https://atlas.web.cern.ch/Atlas/GROUPS/PHYSICS/PUBNOTES/ATL-PHYS-PUB-2024-011.

[30] Z. Bern, J. J. Carrasco, Lance J. Dixon, H. Johansson, and R. Roiban. The Ultraviolet Behavior of N=8 Supergravity at Four Loops. *Phys. Rev. Lett.*, 103:081301, 2009. doi:10.1103/PhysRevLett.103.081301.

[31] T. Yoneya. Connection of Dual Models to Electrodynamics and Gravidynamics. *Prog. Theor. Phys.*, 51: 1907–1920, 1974. doi:10.1143/PTP.51.1907.

[32] Joel Scherk and John H. Schwarz. Dual Models and the Geometry of Space-Time. *Phys. Lett. B*, 52: 347–350, 1974. doi:10.1016/0370-2693(74)90059-8.

[33] Carlo Rovelli and Lee Smolin. Loop Space Representation of Quantum General Relativity. *Nucl. Phys. B*, 331:80–152, 1990. doi:10.1016/0550-3213(90)90019-A.

[34] Y. Ashie et al. Evidence for an oscillatory signature in atmospheric neutrino oscillation. *Phys. Rev. Lett.*, 93:101801, 2004. doi:10.1103/PhysRevLett.93.101801.

[35] Q. R. Ahmad et al. Measurement of the rate of $\nu_e + d \to p + p + e^-$ interactions produced by ^{8}B solar neutrinos at the Sudbury Neutrino Observatory. *Phys. Rev. Lett.*, 87:071301, 2001. doi:10.1103/PhysRevLett.87.071301.

[36] A. B. McDonald et al. Direct evidence for neutrino flavor transformation from neutral-current interactions in SNO. *AIP Conf. Proc.*, 646(1):43–58, 2002. doi:10.1063/1.1524553.

[37] Ziro Maki, Masami Nakagawa, and Shoichi Sakata. Remarks on the unified model of elementary particles. *Prog. Theor. Phys.*, 28:870–880, 1962. doi:10.1143/PTP.28.870.

[38] B. Pontecorvo. Neutrino Experiments and the Problem of Conservation of Leptonic Charge. *Zh. Eksp. Teor. Fiz.*, 53:1717–1725, 1967.

[39] Vera C. Rubin and W. Kent Ford, Jr. Rotation of the Andromeda Nebula from a Spectroscopic Survey of Emission Regions. *Astrophys. J.*, 159:379–403, 1970. doi:10.1086/150317.

[40] H. Tananbaum, M. C. Weisskopf, W. Tucker, B. Wilkes, and P. Edmonds. Highlights and Discoveries from the Chandra X-ray Observatory. *Rept. Prog. Phys.*, 77:066902, 2014. doi:10.1088/0034-4885/77/6/066902.

[41] Adam G. Riess et al. Observational evidence from supernovae for an accelerating universe and a cosmological constant. *Astron. J.*, 116:1009–1038, 1998. doi:10.1086/300499.

[42] S. Perlmutter et al. Measurements of Ω and Λ from 42 High Redshift Supernovae. *Astrophys. J.*, 517: 565–586, 1999. doi:10.1086/307221.

[43] P. J. E. Peebles and Bharat Ratra. The Cosmological Constant and Dark Energy. *Rev. Mod. Phys.*, 75: 559–606, 2003. doi:10.1103/RevModPhys.75.559.

[44] D. de Florian et al. Handbook of LHC Higgs Cross Sections: 4. Deciphering the Nature of the Higgs Sector. 2/2017, 10 2016. doi:10.23731/CYRM-2017-002.

[45] A. Bredenstein, Ansgar Denner, S. Dittmaier, and M. M. Weber. Precise predictions for the Higgs-boson decay $H \to WW/ZZ \to 4$ leptons. *Phys. Rev. D*, 74:013004, 2006. doi:10.1103/PhysRevD.74.013004.

[46] A. Bredenstein, Ansgar Denner, S. Dittmaier, and M. M. Weber. Precision calculations for the Higgs decays $H \to ZZ/WW \to 4$ leptons. *Nucl. Phys. Proc. Suppl.*, 160:131–135, 2006. doi:10.1016/j.nuclphysbps.2006.09.104.

[47] A. Djouadi, J. Kalinowski, and M. Spira. HDECAY: A program for Higgs boson decays in the Standard Model and its supersymmetric extension. *Comput. Phys. Commun.*, 108:56, 1998. doi:10.1016/S0010-4655(97)00123-9.

[48] L. D. Landau. On the angular momentum of a system of two photons. *Dokl. Akad. Nauk SSSR*, 60(2): 207–209, 1948. doi:10.1016/B978-0-08-010586-4.50070-5.

[49] Georges Aad et al. Study of the spin and parity of the Higgs boson in diboson decays with the ATLAS detector. *Eur. Phys. J. C*, 75(10):476, 2015. doi:10.1140/epjc/s10052-015-3685-1. [Erratum: Eur.Phys.J.C 76, 152 (2016)].

[50] Georges Aad et al. Test of CP Invariance in vector-boson fusion production of the Higgs boson using the Optimal Observable method in the ditau decay channel with the ATLAS detector. *Eur. Phys. J. C*, 76 (12):658, 2016. doi:10.1140/epjc/s10052-016-4499-5.

[51] Georges Aad et al. Test of CP invariance in vector-boson fusion production of the Higgs boson in the H$\rightarrow\tau\tau$ channel in proton–proton collisions at s=13TeV with the ATLAS detector. *Phys. Lett. B*, 805: 135426, 2020. doi:10.1016/j.physletb.2020.135426.

[52] Georges Aad et al. Test of CP-invariance of the Higgs boson in vector-boson fusion production and in its decay into four leptons. *JHEP*, 05:105, 2024. doi:10.1007/JHEP05(2024)105.

[53] Georges Aad et al. Test of CP Invariance in Higgs Boson Vector-Boson-Fusion Production Using the H$\rightarrow\gamma\gamma$ Channel with the ATLAS Detector. *Phys. Rev. Lett.*, 131(6):061802, 2023. doi:10.1103/PhysRevLett.131.061802.

[54] ATLAS Collaboration. ATLAS Combined Summary Plots for Higgs Physics. `https://atlas.web.cern.ch/Atlas/GROUPS/PHYSICS/CombinedSummaryPlots/HIGGS/`.

[55] C. D. Anderson. The Positive Electron. *Phys. Rev.*, 43:491–494, 1933. doi:10.1103/PhysRev.43.491.

[56] J. H. Christenson, J. W. Cronin, V. L. Fitch, and R. Turlay. Evidence for the 2π decay of the k_2^0 meson. *Phys. Rev. Lett.*, 13:138–140, Jul 1964. doi:10.1103/PhysRevLett.13.138. URL `https://link.aps.org/doi/10.1103/PhysRevLett.13.138`.

[57] Wenbin Qian. Recent CKMfitter updates on global fits of the CKM matrix. *PoS*, CKM2021:074, 2023. doi:10.22323/1.411.0074.

[58] Marcella Bona et al. New UTfit Analysis of the Unitarity Triangle in the Cabibbo-Kobayashi-Maskawa scheme. *Rend. Lincei Sci. Fis. Nat.*, 34:37–57, 2023. doi:10.1007/s12210-023-01137-5.

[59] C. Jarlskog. Commutator of the Quark Mass Matrices in the Standard Electroweak Model and a Measure of Maximal CP Nonconservation. *Phys. Rev. Lett.*, 55:1039, 1985. doi:10.1103/PhysRevLett.55.1039.

[60] N. Aghanim et al. Planck 2018 results. VI. Cosmological parameters. *Astron. Astrophys.*, 641:A6, 2020. doi:10.1051/0004-6361/201833910. [Erratum: Astron.Astrophys. 652, C4 (2021)].

[61] Antonio Riotto and Mark Trodden. Recent progress in baryogenesis. *Ann. Rev. Nucl. Part. Sci.*, 49: 35–75, 1999. doi:10.1146/annurev.nucl.49.1.35.

[62] Thomas Appelquist and J. Carazzone. Infrared Singularities and Massive Fields. *Phys. Rev. D*, 11:2856, 1975. doi:10.1103/PhysRevD.11.2856.

[63] E. Fermi. An attempt of a theory of beta radiation. 1. *Z. Phys.*, 88:161–177, 1934. doi:10.1007/BF01351864.

[64] W. Buchmuller and D. Wyler. Effective Lagrangian Analysis of New Interactions and Flavor Conservation. *Nucl. Phys. B*, 268:621–653, 1986. doi:10.1016/0550-3213(86)90262-2.

[65] Andrew Kobach. Baryon Number, Lepton Number, and Operator Dimension in the Standard Model. *Phys. Lett. B*, 758:455–457, 2016. doi:10.1016/j.physletb.2016.05.050.

[66] B. Grzadkowski, M. Iskrzyński, M. Misiak, and J. Rosiek. Dimension-six terms in the standard model lagrangian. *Journal of High Energy Physics*, 2010(10), October 2010. ISSN 1029-8479. doi:10.1007/jhep10(2010)085. URL `http://dx.doi.org/10.1007/JHEP10(2010)085`.

[67] Kaoru Hagiwara, S. Ishihara, R. Szalapski, and D. Zeppenfeld. Low-energy effects of new interactions in the electroweak boson sector. *Phys. Rev. D*, 48:2182–2203, 1993. doi:10.1103/PhysRevD.48.2182.

[68] G. F. Giudice, C. Grojean, A. Pomarol, and R. Rattazzi. The Strongly-Interacting Light Higgs. *JHEP*, 06:045, 2007. doi:10.1088/1126-6708/2007/06/045.

[69] Upalaparna Banerjee, Joydeep Chakrabortty, Suraj Prakash, Shakeel Ur Rahaman, and Michael Spannowsky. Effective Operator Bases for Beyond Standard Model Scenarios: An EFT compendium for discoveries. *JHEP*, 01:028, 2021. doi:10.1007/JHEP01(2021)028.

[70] V. Hankele, G. Klamke, D. Zeppenfeld, and T. Figy. Anomalous Higgs boson couplings in vector boson fusion at the CERN LHC. *Phys. Rev. D*, 74:095001, 2006. doi:10.1103/PhysRevD.74.095001.

[71] S. Schael et al. Improved measurement of the triple gauge-boson couplings gamma W W and Z W W in e+ e- collisions. *Phys. Lett. B*, 614:7–26, 2005. doi:10.1016/j.physletb.2005.03.058.

[72] G. Abbiendi et al. Measurement of W boson polarizations and CP violating triple gauge couplings from W^+W^- production at LEP. *Eur. Phys. J. C*, 19:229–240, 2001. doi:10.1007/s100520100602.

[73] P. Achard et al. Search for anomalous couplings in the Higgs sector at LEP. *Phys. Lett. B*, 589:89–102, 2004. doi:10.1016/j.physletb.2004.03.048.

[74] Johann Brehmer, Felix Kling, Tilman Plehn, and Tim M. P. Tait. Better Higgs-CP Tests Through Information Geometry. *Phys. Rev. D*, 97(9):095017, 2018. doi:10.1103/PhysRevD.97.095017.

[75] Tao Han and Yingchuan Li. Genuine CP-odd Observables at the LHC. *Phys. Lett. B*, 683:278–281, 2010. doi:10.1016/j.physletb.2009.12.047.

[76] David Atwood, Shaouly Bar-Shalom, Gad Eilam, and Amarjit Soni. CP violation in top physics. *Phys. Rept.*, 347:1–222, 2001. doi:10.1016/S0370-1573(00)00112-5.

[77] Tilman Plehn, David L. Rainwater, and Dieter Zeppenfeld. Determining the Structure of Higgs Couplings at the LHC. *Phys. Rev. Lett.*, 88:051801, 2002. doi:10.1103/PhysRevLett.88.051801.

[78] Anja Butter, Tilman Plehn, Nathalie Soybelman, and Johann Brehmer. Back to the formula - LHC edition. *SciPost Phys.*, 16(1):037, 2024. doi:10.21468/SciPostPhys.16.1.037.

[79] D. Atwood and A. Soni. Analysis for magnetic moment and electric dipole moment form factors of the top quark via $e^+e^-\to$tt$^-$. *Phys. Rev. D*, 45:2405–2413, Apr 1992. doi:10.1103/PhysRevD.45.2405. URL `https://link.aps.org/doi/10.1103/PhysRevD.45.2405`.

[80] M. Davier, L. Duflot, F. Le Diberder, and A. Rougé. The optimal method for the measurement of tau polarization. *Physics Letters B*, 306(3):411–417, 1993. ISSN 0370-2693. doi:https://doi.org/10.1016/0370-2693(93)90101-M. URL `https://www.sciencedirect.com/science/article/pii/037026939390101M`.

[81] M. Diehl and O. Nachtmann. Optimal observables for measuring three gauge boson couplings in e+ e- —> W+ W-. In *Physics with e+ e- Linear Colliders (The European Working Groups 4 Feb - 1 Sep 1995: Session 2)*, pages 301–304, 3 1996.

[82] Ansgar Denner, Stefan Dittmaier, Stefan Kallweit, and Alexander Mück. HAWK 2.0: A monte carlo program for higgs production in vector-boson fusion and higgs strahlung at hadron colliders. *Computer Physics Communications*, 195:161–171, 10 2015. doi:10.1016/j.cpc.2015.04.021. URL `https://doi.org/10.1016%2Fj.cpc.2015.04.021`.

[83] M. Ciccolini, A. Denner, and S. Dittmaier. Strong and electroweak corrections to the production of a higgs boson + 2 jets via weak interactions at the large hadron collider. *Phys. Rev. Lett.*, 99:161803, 10

2007. doi:10.1103/PhysRevLett.99.161803. URL https://link.aps.org/doi/10.1103/PhysRevLett.99.161803.

[84] M. Ciccolini, Denner A., and Dittmaier S. Electroweak and qcd corrections to higgs production via vector-boson fusion at the cern lhc. *Phys. Rev. D*, 77:013002, 1 2008. doi:10.1103/PhysRevD.77.013002. URL https://link.aps.org/doi/10.1103/PhysRevD.77.013002.

[85] A. Elagin, P. Murat, A. Pranko, and A. Safonov. A New Mass Reconstruction Technique for Resonances Decaying to di-tau. *Nucl. Instrum. Meth. A*, 654:481–489, 2011. doi:10.1016/j.nima.2011.07.009.

[86] Hung-Liang Lai, Marco Guzzi, Joey Huston, Zhao Li, Pavel M. Nadolsky, Jon Pumplin, and C. P. Yuan. New parton distributions for collider physics. *Phys. Rev. D*, 82:074024, 2010. doi:10.1103/PhysRevD.82.074024.

[87] R. Akers et al. A Test of CP invariance in Z0 —> tau+ tau- using optimal observables. *Z. Phys. C*, 66: 31–44, 1995. doi:10.1007/BF01496578.

[88] K. Ackerstaff et al. Search for CP violation in Z0 —> tau+ tau- and an upper limit on the weak dipole moment of the tau lepton. *Z. Phys. C*, 74:403–412, 1997. doi:10.1007/s002880050403.

[89] F. Zwicky. Die Rotverschiebung von extragalaktischen Nebeln. *Helv. Phys. Acta*, 6:110–127, 1933. doi:10.1007/s10714-008-0707-4.

[90] F. Zwicky. On the Masses of Nebulae and of Clusters of Nebulae. *Astrophys. J.*, 86:217–246, 1937. doi:10.1086/143864.

[91] V. C. Rubin, N. Thonnard, and W. K. Ford, Jr. Rotational properties of 21 SC galaxies with a large range of luminosities and radii, from NGC 4605 /R = 4kpc/ to UGC 2885 /R = 122 kpc/. *Astrophys. J.*, 238:471, 1980. doi:10.1086/158003.

[92] T. S. van Albada, John N. Bahcall, K. Begeman, and R. Sancisi. The Distribution of Dark Matter in the Spiral Galaxy NGC-3198. *Astrophys. J.*, 295:305–313, 1985. doi:10.1086/163375.

[93] Timothy Clifton, Pedro G. Ferreira, Antonio Padilla, and Constantinos Skordis. Modified Gravity and Cosmology. *Phys. Rept.*, 513:1–189, 2012. doi:10.1016/j.physrep.2012.01.001.

[94] Carnegie Institution for Science. Magellan telescopes at las campanas observatory. https://obs.carnegiescience.edu/magellan, 2000. Located at Las Campanas Observatory, Chile.

[95] Joel R. Primack. Dark matter and structure formation. In *Midrasha Mathematicae in Jerusalem: Winter School in Dynamical Systems*, 7 1997.

[96] Howard Baer, Ki-Young Choi, Jihn E. Kim, and Leszek Roszkowski. Dark matter production in the early Universe: beyond the thermal WIMP paradigm. *Phys. Rept.*, 555:1–60, 2015. doi:10.1016/j.physrep.2014.10.002.

[97] Gary Steigman and Michael S. Turner. Cosmological Constraints on the Properties of Weakly Interacting Massive Particles. *Nucl. Phys. B*, 253:375–386, 1985. doi:10.1016/0550-3213(85)90537-1.

[98] Gerard Jungman, Marc Kamionkowski, and Kim Griest. Supersymmetric dark matter. *Phys. Rept.*, 267: 195–373, 1996. doi:10.1016/0370-1573(95)00058-5.

[99] Particle Data Group, P.A. Zyla, et al. Review of Particle Physics. *PTEP*, 2020(8):083C01, 2020. doi:10.1093/ptep/ptaa104.

[100] Francesca Chadha-Day, John Ellis, and David J. E. Marsh. Axion dark matter: What is it and why now? *Sci. Adv.*, 8(8):abj3618, 2022. doi:10.1126/sciadv.abj3618.

[101] A. Boyarsky, M. Drewes, T. Lasserre, S. Mertens, and O. Ruchayskiy. Sterile neutrino Dark Matter. *Prog. Part. Nucl. Phys.*, 104:1–45, 2019. doi:10.1016/j.ppnp.2018.07.004.

[102] Nicolás Bernal, Matti Heikinheimo, Tommi Tenkanen, Kimmo Tuominen, and Ville Vaskonen. The Dawn of FIMP Dark Matter: A Review of Models and Constraints. *Int. J. Mod. Phys. A*, 32(27):1730023, 2017. doi:10.1142/S0217751X1730023X.

[103] Stefano Giagu. Dark Matter Searches at Colliders. *Riv. Nuovo Cim.*, 42(10):497–550, 2019. doi:10.1393/ncr/i2019-10161-4.

[104] Michael Klasen, Martin Pohl, and Guenter Sigl. Indirect and Direct Search for Dark Matter. *Prog. Part. Nucl. Phys.*, 85:1–32, 2015. doi:10.1016/j.ppnp.2015.07.001.

[105] Farinaldo S. Queiroz. Dark Matter Overview: Collider, Direct and Indirect Detection Searches. *PoS*, ICHEP2016:1185, 2016.

[106] Linda M. Carpenter, Anthony DiFranzo, Michael Mulhearn, Chase Shimmin, Sean Tulin, and Daniel Whiteson. Mono-Higgs: A New Collider Probe of Dark Matter. *Phys. Rev. D*, 89(7):075017, 2014. doi:10.1103/PhysRevD.89.075017.

[107] Giorgio Busoni, Andrea De Simone, Enrico Morgante, and Antonio Riotto. On the Validity of the Effective Field Theory for Dark Matter Searches at the LHC. *Phys. Lett. B*, 728:412–421, 2014. doi:10.1016/j.physletb.2013.11.069.

[108] Jalal Abdallah et al. Simplified Models for Dark Matter Searches at the LHC. *Phys. Dark Univ.*, 9-10: 8–23, 2015. doi:10.1016/j.dark.2015.08.001.

[109] John F. Gunion, Howard E. Haber, Gordon L. Kane, and Sally Dawson. *The Higgs Hunter's Guide*, volume 80. 2000. ISBN 978-0-429-49644-8. doi:10.1201/9780429496448.

[110] Heather E. Logan. TASI 2013 lectures on Higgs physics within and beyond the Standard Model. 6 2014.

[111] G. C. Branco, P. M. Ferreira, L. Lavoura, M. N. Rebelo, Marc Sher, and Joao P. Silva. Theory and phenomenology of two-Higgs-doublet models. *Phys. Rept.*, 516:1–102, 2012. doi:10.1016/j.physrep.2012.02.002.

[112] Tomohiro Abe et al. LHC Dark Matter Working Group: Next-generation spin-0 dark matter models. *Phys. Dark Univ.*, 27:100351, 2020. doi:10.1016/j.dark.2019.100351.

[113] Georges Aad et al. Combination and summary of ATLAS dark matter searches interpreted in a 2HDM with a pseudo-scalar mediator using 139 fb−1 of s=13 TeV pp collision data. *Sci. Bull.*, 69(19):3005–3035, 2024. doi:10.1016/j.scib.2024.06.003.

[114] Albert M Sirunyan et al. Search for dark matter particles produced in association with a Higgs boson in proton-proton collisions at $\sqrt{\mathrm{s}} = 13$ TeV. *JHEP*, 03:025, 2020. doi:10.1007/JHEP03(2020)025.

[115] Albert M Sirunyan et al. Search for dark matter produced in association with a leptonically decaying Z boson in proton-proton collisions at $\sqrt{s} = 13$ TeV. *Eur. Phys. J. C*, 81(1):13, 2021. doi:10.1140/epjc/s10052-020-08739-5. [Erratum: Eur.Phys.J.C 81, 333 (2021)].

[116] Georges Aad et al. Search for dark matter produced in association with a Standard Model Higgs boson decaying into b-quarks using the full Run 2 dataset from the ATLAS detector. *JHEP*, 11:209, 2021. doi:10.1007/JHEP11(2021)209.

[117] Georges Aad et al. Search for associated production of a Z boson with an invisibly decaying Higgs boson or dark matter candidates at s=13 TeV with the ATLAS detector. *Phys. Lett. B*, 829:137066, 2022. doi:10.1016/j.physletb.2022.137066.

[118] R. Assmann, M. Lamont, and S. Myers. A brief history of the LEP collider. *Nucl. Phys. B Proc. Suppl.*, 109:17–31, 2002. doi:10.1016/S0920-5632(02)90005-8.

[119] ALEPH collaboration. Observation of an Excess in the Search for the Standard Model Higgs Boson at ALEPH. *Phys. Lett. B*, 495(1-2):1–17, 2000. doi:10.1016/S0370-2693(00)01269-7. URL `https://cds.cern.ch/record/476830`. 16 pages, 13 figures Report-no: CERN-EP/2000-138.

[120] Oliver Sim Brüning, Paul Collier, P Lebrun, Stephen Myers, Ranko Ostojic, John Poole, and Paul Proudlock. *LHC Design Report*. CERN Yellow Reports: Monographs. CERN, Geneva, 2004. doi:10.5170/CERN-2004-003-V-1. URL `https://cds.cern.ch/record/782076`.

[121] Oliver Sim Brüning, Paul Collier, P Lebrun, Stephen Myers, Ranko Ostojic, John Poole, and Paul Proudlock. *LHC Design Report*. CERN Yellow Reports: Monographs. CERN, Geneva, 2004. doi:10.5170/CERN-2004-003-V-2. URL `https://cds.cern.ch/record/815187`.

[122] Armen Tumasyan et al. A portrait of the Higgs boson by the CMS experiment ten years after the discovery. *Nature*, 607(7917):60–68, 2022. doi:10.1038/s41586-022-04892-x. [Erratum: Nature 623, (2023)].

[123] CERN. High-luminosity lhc project. `https://hilumilhc.web.cern.ch/content/hl-lhc-project`, 2025.

[124] Hannes Bartosik and Giovanni Rumolo. Performance of the LHC injector chain after the upgrade and potential development. In *Snowmass 2021*, 3 2022.

[125] Esma Mobs. The CERN accelerator complex in 2019. Complexe des accélérateurs du CERN en 2019. 2019. URL `https://cds.cern.ch/record/2684277`. General Photo.

[126] The ATLAS Collaboration. The atlas experiment at the cern large hadron collider. *Journal of Instrumentation*, 3(08):S08003, aug 2008. doi:10.1088/1748-0221/3/08/S08003. URL `https://dx.doi.org/10.1088/1748-0221/3/08/S08003`.

[127] S. Chatrchyan et al. The cms experiment at the cern lhc. *JINST*, 3:S08004, 2008. doi:10.1088/1748-0221/3/08/S08004.

[128] K. Aamodt et al. The alice experiment at the cern lhc. *JINST*, 3:S08002, 2008. doi:10.1088/1748-0221/3/08/S08002.

[129] A. Augusto Alves et al. The lhcb detector at the lhc. *JINST*, 3:S08005, 2008. doi:10.1088/1748-0221/3/08/S08005.

[130] G. Anelli et al. The totem experiment at the cern large hadron collider. *JINST*, 3:S08007, 2008. doi:10.1088/1748-0221/3/08/S08007.

[131] O. Adriani et al. The lhcf detector at the cern large hadron collider. *JINST*, 3:S08006, 2008. doi:10.1088/1748-0221/3/08/S08006.

[132] Akitaka Ariga et al. Faser: Forward search experiment at the lhc. *Phys. Rev. D*, 99(9):095011, 2019. doi:10.1103/PhysRevD.99.095011.

[133] B. Acharya et al. The physics programme of the moedal experiment at the lhc. *Int. J. Mod. Phys. A*, 29: 1430050, 2014. doi:10.1142/S0217751X14300506.

[134] ATLAS Collaboration. Luminosity Public Results Run 2, 2025. URL `https://twiki.cern.ch/twiki/bin/view/AtlasPublic/LuminosityPublicResultsRun2`. Accessed: 11 March 2025.

[135] Joao Pequenao. Computer generated image of the whole ATLAS detector. 2008. URL `https://cds.cern.ch/record/1095924`.

[136] TikZ.net. Tikz and pgf: graphics for latex, 2024. URL `https://tikz.net/`.

[137] *ATLAS inner detector: Technical Design Report, 1.* Technical design report. ATLAS. CERN, Geneva, 1997. URL `https://cds.cern.ch/record/331063`.

[138] S Haywood, L Rossi, R Nickerson, and A Romaniouk. *ATLAS inner detector: Technical Design Report, 2.* Technical design report. ATLAS. CERN, Geneva, 1997. URL `https://cds.cern.ch/record/331064`.

[139] Joao Pequenao. Computer generated image of the ATLAS inner detector. 2008. URL `https://cds.cern.ch/record/1095926`.

[140] Aad G. et al. Atlas pixel detector electronics and sensors. 3(07):P07007, jul 2008. doi:10.1088/1748-0221/3/07/P07007. URL `https://dx.doi.org/10.1088/1748-0221/3/07/P07007`.

[141] Abbott B. et al. Production and integration of the atlas insertable b-layer. 13(05):T05008, may 2018. doi:10.1088/1748-0221/13/05/T05008. URL `https://dx.doi.org/10.1088/1748-0221/13/05/T05008`.

[142] The ATLAS collaboration. Operation and performance of the atlas semiconductor tracker. *Journal of Instrumentation*, 9(08):P08009–P08009, August 2014. ISSN 1748-0221. doi:10.1088/1748-0221/9/08/p08009. URL `http://dx.doi.org/10.1088/1748-0221/9/08/P08009`.

[143] Vasiliki A. Mitsou. The ATLAS transition radiation tracker. In *8th International Conference on Advanced Technology and Particle Physics (ICATPP 2003): Astroparticle, Particle, Space Physics, Detectors and Medical Physics Applications*, pages 497–501, 11 2003. doi:10.1142/9789812702708_0073.

[144] E. Abat et al. The ATLAS Transition Radiation Tracker (TRT) proportional drift tube: Design and performance. *JINST*, 3:P02013, 2008. doi:10.1088/1748-0221/3/02/P02013.

[145] Joao Pequenao. Computer Generated image of the ATLAS calorimeter. 2008. URL `https://cds.cern.ch/record/1095927`.

[146] ATLAS liquid argon calorimeter: Technical design report. 12 1996.

[147] ATLAS tile calorimeter: Technical design report. 12 1996.

[148] ATLAS muon spectrometer: Technical design report. 6 1997.

[149] Joao Pequenao. Computer generated image of the ATLAS Muons subsystem. 2008. URL `https://cds.cern.ch/record/1095929`.

[150] Georges Aad et al. Operation of the ATLAS trigger system in Run 2. *JINST*, 15(10):P10004, 2020. doi:10.1088/1748-0221/15/10/P10004.

[151] John C. Collins, Davison E. Soper, and George F. Sterman. Factorization of Hard Processes in QCD. *Adv. Ser. Direct. High Energy Phys.*, 5:1–91, 1989. doi:10.1142/9789814503266_0001.

[152] G. M. Prosperi, M. Raciti, and C. Simolo. On the running coupling constant in QCD. *Prog. Part. Nucl. Phys.*, 58:387–438, 2007. doi:10.1016/j.ppnp.2006.09.001.

[153] Andy Buckley et al. General-purpose event generators for LHC physics. *Phys. Rept.*, 504:145–233, 2011. doi:10.1016/j.physrep.2011.03.005.

[154] Bo Andersson, G. Gustafson, G. Ingelman, and T. Sjöstrand. Parton fragmentation and string dynamics. *Phys. Rept.*, 97:31–145, 1983. doi:10.1016/0370-1573(83)90080-7.

[155] B. R. Webber. A QCD Model for Jet Fragmentation Including Soft Gluon Interference. *Nucl. Phys. B*, 238:492–528, 1984. doi:10.1016/0550-3213(84)90333-X.

[156] Stefan Höche. Introduction to parton-shower event generators. In *Theoretical Advanced Study Institute in Elementary Particle Physics: Journeys Through the Precision Frontier: Amplitudes for Colliders*, pages 235–295, 2015. doi:10.1142/9789814678766_0005.

[157] Zachary Marshall. Simulation of Pile-up in the ATLAS Experiment. *J. Phys. Conf. Ser.*, 513:022024, 2014. doi:10.1088/1742-6596/513/2/022024.

[158] G. Aad et al. The ATLAS Simulation Infrastructure. *Eur. Phys. J. C*, 70:823–874, 2010. doi:10.1140/epjc/s10052-010-1429-9.

[159] S. Agostinelli et al. GEANT4 – a simulation toolkit. *Nucl. Instrum. Meth. A*, 506:250, 2003. doi:10.1016/S0168-9002(03)01368-8.

[160] Coll ATLAS, M Beckingham, M Duehrssen, E Schmidt, M Shapiro, M Venturi, J Virzi, I Vivarelli, M Werner, S Yamamoto, and T Yamanaka. The simulation principle and performance of the ATLAS fast calorimeter simulation FastCaloSim. Technical report, CERN, Geneva, 2010. URL `https://cds.cern.ch/record/1300517`. All figures including auxiliary figures are available at https://atlas.web.cern.ch/Atlas/GROUPS/PHYSICS/PUBNOTES/ATL-PHYS-PUB-2010-013.

[161] K. Edmonds, S. Fleischmann, T. Lenz, C. Magass, J. Mechnich, and A. Salzburger. The fast ATLAS track simulation (FATRAS). 3 2008.

[162] T. G. Cornelissen, N Van Eldik, M. Elsing, W. Liebig, E. Moyse, N. Piacquadio, K. Prokofiev, A. Salzburger, and A. Wildauer. Updates of the ATLAS Tracking Event Data Model (Release 13). 6 2007.

[163] M. Aaboud et al. Performance of the ATLAS Track Reconstruction Algorithms in Dense Environments in LHC Run 2. *Eur. Phys. J. C*, 77(10):673, 2017. doi:10.1140/epjc/s10052-017-5225-7.

[164] R. Fruhwirth. Application of Kalman filtering to track and vertex fitting. *Nucl. Instrum. Meth. A*, 262: 444–450, 1987. doi:10.1016/0168-9002(87)90887-4.

[165] Morad Aaboud et al. Reconstruction of primary vertices at the ATLAS experiment in Run 1 proton–proton collisions at the LHC. *Eur. Phys. J. C*, 77(5):332, 2017. doi:10.1140/epjc/s10052-017-4887-5.

[166] Vertex Reconstruction Performance of the ATLAS Detector at "\sqrts = 13~\textrmTeV". 2015.

[167] ATLAS Collaboration. Electron and photon reconstruction and performance in ATLAS using a dynamical, topological cell clustering-based approach. ATL-PHYS-PUB-2017-022, 2017. URL `https://cds.cern.ch/record/2298955`.

[168] Georges Aad et al. Electron and photon performance measurements with the ATLAS detector using the 2015–2017 LHC proton-proton collision data. *JINST*, 14(12):P12006, 2019. doi:10.1088/1748-0221/14/12/P12006.

[169] Georges Aad et al. Topological cell clustering in the ATLAS calorimeters and its performance in LHC Run 1. *Eur. Phys. J. C*, 77:490, 2017. doi:10.1140/epjc/s10052-017-5004-5.

[170] Improved electron reconstruction in ATLAS using the Gaussian Sum Filter-based model for bremsstrahlung. 5 2012.

[171] Morad Aaboud et al. Electron reconstruction and identification in the ATLAS experiment using the 2015 and 2016 LHC proton-proton collision data at $\sqrt{s}$ = 13 TeV. *Eur. Phys. J. C*, 79(8):639, 2019. doi:10.1140/epjc/s10052-019-7140-6.

[172] Georges Aad et al. Electron and photon efficiencies in LHC Run 2 with the ATLAS experiment. *JHEP*, 05:162, 2024. doi:10.1007/JHEP05(2024)162.

[173] Georges Aad et al. Muon reconstruction performance of the ATLAS detector in proton–proton collision data at $\sqrt{s}$ =13 TeV. *Eur. Phys. J. C*, 76(5):292, 2016. doi:10.1140/epjc/s10052-016-4120-y.

[174] Georges Aad et al. Muon reconstruction and identification efficiency in ATLAS using the full Run 2 pp collision data set at $\sqrt{s} = 13$ TeV. *Eur. Phys. J. C*, 81(7):578, 2021. doi:10.1140/epjc/s10052-021-09233-2.

[175] Matteo Cacciari, Gavin P. Salam, and Gregory Soyez. The anti-k_t jet clustering algorithm. *JHEP*, 04:063, 2008. doi:10.1088/1126-6708/2008/04/063.

[176] Morad Aaboud et al. Jet reconstruction and performance using particle flow with the ATLAS Detector. *Eur. Phys. J. C*, 77(7):466, 2017. doi:10.1140/epjc/s10052-017-5031-2.

[177] Georges Aad et al. Jet energy scale and resolution measured in proton–proton collisions at $\sqrt{s} = 13$ TeV with the ATLAS detector. *Eur. Phys. J. C*, 81(8):689, 2021. doi:10.1140/epjc/s10052-021-09402-3.

[178] M. Aaboud et al. Jet energy scale measurements and their systematic uncertainties in proton-proton collisions at $\sqrt{s} = 13$ TeV with the ATLAS detector. *Phys. Rev. D*, 96(7):072002, 2017. doi:10.1103/PhysRevD.96.072002.

[179] Tagging and suppression of pileup jets. 2014.

[180] Morad Aaboud et al. Identification and rejection of pile-up jets at high pseudorapidity with the ATLAS detector. *Eur. Phys. J. C*, 77(9):580, 2017. doi:10.1140/epjc/s10052-017-5081-5. [Erratum: Eur.Phys.J.C 77, 712 (2017)].

[181] Georges Aad et al. ATLAS flavour-tagging algorithms for the LHC Run 2 pp collision dataset. *Eur. Phys. J. C*, 83(7):681, 2023. doi:10.1140/epjc/s10052-023-11699-1.

[182] Georges Aad et al. ATLAS b-jet identification performance and efficiency measurement with $t\bar{t}$ events in pp collisions at $\sqrt{s} = 13$ TeV. *Eur. Phys. J. C*, 79(11):970, 2019. doi:10.1140/epjc/s10052-019-7450-8.

[183] Reconstruction, Energy Calibration, and Identification of Hadronically Decaying Tau Leptons in the ATLAS Experiment for Run-2 of the LHC. 2015.

[184] Measurement of the tau lepton reconstruction and identification performance in the ATLAS experiment using pp collisions at $\sqrt{s} = 13\ TeV$. 5 2017.

[185] T. Barillari et al. Local hadronic calibration. 2009.

[186] Identification of hadronic tau lepton decays using neural networks in the ATLAS experiment. 2019.

[187] ATLAS Collaboration. A Guide to the ABCD Method in ATLAS. `https://indico.cern.ch/event/1122790/contributions/4713580/attachments/2381493/4270369/ABCDGuide_draft18Oct18.pdf`, 2018. Draft version dated 18 Oct 2018.

[188] Erlend Aakvaag. Measurment of Tau ID efficiencies using $W \to \tau\nu$ events with the ATLAS detector in LHC Run 2. Technical report, CERN, Geneva, 2023. URL `https://cds.cern.ch/record/2866467`.

[189] $E_{\mathrm{T}}^{\mathrm{miss}}$ performance in the ATLAS detector using 2015-2016 LHC pp collisions. 6 2018.

[190] Georges Aad et al. The performance of missing transverse momentum reconstruction and its significance with the ATLAS detector using 140 fb^{-1} of $\sqrt{s} = 13$ TeV pp collisions. 2 2024.

[191] Glen Cowan, Kyle Cranmer, Eilam Gross, and Ofer Vitells. Asymptotic formulae for likelihood-based tests of new physics. *Eur. Phys. J. C*, 71:1554, 2011. doi:10.1140/epjc/s10052-011-1554-0.

[192] Kyle Cranmer, George Lewis, Lorenzo Moneta, Akira Shibata, and Wouter Verkerke. HistFactory: A tool for creating statistical models for use with RooFit and RooStats. Technical report, New York U., New York, 2012. URL `https://cds.cern.ch/record/1456844`.

[193] Lorenzo Moneta, Kevin Belasco, Kyle S. Cranmer, S. Kreiss, Alfio Lazzaro, Danilo Piparo, Gregory Schott, Wouter Verkerke, and Matthias Wolf. The RooStats Project. *PoS*, ACAT2010:057, 2010. doi:10.22323/1.093.0057.

[194] Wouter Verkerke and David Kirkby. The RooFit toolkit for data modeling, 2003.

[195] F. James and M. Roos. Minuit: A System for Function Minimization and Analysis of the Parameter Errors and Correlations. *Comput. Phys. Commun.*, 10:343–367, 1975. doi:10.1016/0010-4655(75)90039-9.

[196] S. S. Wilks. The Large-Sample Distribution of the Likelihood Ratio for Testing Composite Hypotheses. *Annals Math. Statist.*, 9(1):60–62, 1938. doi:10.1214/aoms/1177732360.

[197] Georges Aad et al. Combined Measurement of the Higgs Boson Mass in pp Collisions at $\sqrt{s} = 7$ and 8 TeV with the ATLAS and CMS Experiments. *Phys. Rev. Lett.*, 114:191803, 2015. doi:10.1103/PhysRevLett.114.191803.

[198] Alexander L. Read. Presentation of search results: The CL_s technique. *J. Phys. G*, 28:2693–2704, 2002. doi:10.1088/0954-3899/28/10/313.

[199] ATLAS Collaboration. ATLAS data quality operations and performance for 2015–2018 data-taking. *JINST*, 15:P04003, 2020. doi:10.1088/1748-0221/15/04/P04003.

[200] Georges Aad et al. Luminosity determination in *pp* collisions at $\sqrt{s} = 13$ TeV using the ATLAS detector at the LHC. *Eur. Phys. J. C*, 83(10):982, 2023. doi:10.1140/epjc/s10052-023-11747-w.

[201] Georges Aad et al. Measurement of the properties of Higgs boson production at $\sqrt{s} = 13$ TeV in the $H \to \gamma\gamma$ channel using 139 fb^{-1} of *pp* collision data with the ATLAS experiment. *JHEP*, 07:088, 2023. doi:10.1007/JHEP07(2023)088.

[202] Georges Aad et al. Differential cross-section measurements of Higgs boson production in the $H \to \tau^+\tau^-$ decay channel in *pp* collisions at $\sqrt{s} = 13$ TeV with the ATLAS detector. 7 2024.

[203] Enrico Bothmann et al. Event generation with Sherpa 2.2. *SciPost Phys.*, 7(3):034, 2019. doi:10.21468/SciPostPhys.7.3.034.

[204] Steffen Schumann and Frank Krauss. A parton shower algorithm based on Catani–Seymour dipole factorisation. *JHEP*, 03:038, 2008. doi:10.1088/1126-6708/2008/03/038.

[205] The NNPDF Collaboration, Richard D. Ball, et al. Parton distributions for the LHC run II. *JHEP*, 04: 040, 2015. doi:10.1007/JHEP04(2015)040.

[206] Simone Alioli, Paolo Nason, Carlo Oleari, and Emanuele Re. A general framework for implementing NLO calculations in shower Monte Carlo programs: the POWHEG BOX. *JHEP*, 06:043, 2010. doi:10.1007/JHEP06(2010)043.

[207] Torbjörn Sjöstrand, Stefan Ask, Jesper R. Christiansen, Richard Corke, Nishita Desai, Philip Ilten, Stephen Mrenna, Stefan Prestel, Christine O. Rasmussen, and Peter Z. Skands. An introduction to PYTHIA 8.2. *Comput. Phys. Commun.*, 191:159, 2015. doi:10.1016/j.cpc.2015.01.024.

[208] ATLAS Collaboration. The Pythia 8 A3 tune description of ATLAS minimum bias and inelastic measurements incorporating the Donnachie–Landshoff diffractive model. ATL-PHYS-PUB-2016-017, 2016. URL `https://cds.cern.ch/record/2206965`.

[209] Jon Butterworth et al. PDF4LHC recommendations for LHC Run II. *J. Phys. G*, 43:023001, 2016. doi:10.1088/0954-3899/43/2/023001.

[210] A. Djouadi, M. M. Mühlleitner, and M. Spira. Decays of Supersymmetric particles: The Program SUSY-HIT (SUspect-SdecaY-Hdecay-InTerface). *Acta Phys. Polon. B*, 38:635–644, 2007.

[211] Fabio Maltoni, Kentarou Mawatari, and Marco Zaro. Higgs characterisation via vector-boson fusion and associated production: NLO and parton-shower effects. *Eur. Phys. J. C*, 74(1):2710, 2014. doi:10.1140/epjc/s10052-013-2710-5.

[212] Ilaria Brivio, Yun Jiang, and Michael Trott. The SMEFTsim package, theory and tools. *JHEP*, 12:070, 2017. doi:10.1007/JHEP12(2017)070.

[213] Georges Aad et al. Measurements of Higgs boson production cross-sections in the $H \to \tau^+\tau^-$ decay channel in pp collisions at $\sqrt{s} = 13$ TeV with the ATLAS detector. *JHEP*, 08:175, 2022. doi:10.1007/JHEP08(2022)175.

[214] R. Keith Ellis, I. Hinchliffe, M. Soldate, and J. J. van der Bij. Higgs Decay to tau+ tau-: A Possible Signature of Intermediate Mass Higgs Bosons at high energy hadron colliders. *Nucl. Phys. B*, 297:221–243, 1988. doi:10.1016/0550-3213(88)90019-3.

[215] Georges Aad et al. Measurements of Higgs boson production cross-sections in the $H \to \tau^+\tau^-$ decay channel in pp collisions at $\sqrt{s} = 13$ TeV with the ATLAS detector. *JHEP*, 08:175, 2022. doi:10.1007/JHEP08(2022)175.

[216] Diederik P. Kingma and Jimmy Ba. Adam: A method for stochastic optimization, 2017. URL `https://arxiv.org/abs/1412.6980`.

[217] Frank Sauerburger. Freeforestml, 2023. URL `https://gitlab.cern.ch/fsauerbu/freeforestml`.

[218] François Chollet et al. Keras, 2015. URL `https://keras.io`.

[219] Martin Abadi et al. TensorFlow: Large-scale machine learning on heterogeneous systems, 2015. URL `http://tensorflow.org/`. Software available from tensorflow.org.

[220] Takuya Akiba, Shotaro Sano, Toshihiko Yanase, Takeru Ohta, and Masanori Koyama. Optuna: A next-generation hyperparameter optimization framework, 2019. URL `https://arxiv.org/abs/1907.10902`.

[221] Shuhei Watanabe. Tree-structured parzen estimator: Understanding its algorithm components and their roles for better empirical performance, 2023. URL `https://arxiv.org/abs/2304.11127`.

[222] Lukas Heinrich, Matthew Feickert, Giordon Stark, and Kyle Cranmer. pyhf: pure-python implementation of histfactory statistical models. *Journal of Open Source Software*, 6(58):2823, 2021. doi:10.21105/joss.02823. URL `https://doi.org/10.21105/joss.02823`.

[223] The ATLAS collaboration. Modelling z → processes in atlas with -embedded z → data. *Journal of Instrumentation*, 10(09):P09018–P09018, September 2015. ISSN 1748-0221. doi:10.1088/1748-0221/10/09/p09018. URL `http://dx.doi.org/10.1088/1748-0221/10/09/P09018`.

[224] Georges Aad et al. Tools for estimating fake/non-prompt lepton backgrounds with the ATLAS detector at the LHC. *JINST*, 18(11):T11004, 2023. doi:10.1088/1748-0221/18/11/T11004.

[225] J R Andersen et al. Handbook of LHC Higgs Cross Sections: 3. Higgs Properties. 7 2013. doi:10.5170/CERN-2013-004.

[226] L. A. Harland-Lang, R. Nathvani, R. S. Thorne, and A. D. Martin. MMHT PDFs: updates and outlook. *Acta Phys. Polon. B*, 48:1011–1024, 2017. doi:10.5506/APhysPolB.48.1011.

[227] Sayipjamal Dulat, Tie-Jiun Hou, Jun Gao, Marco Guzzi, Joey Huston, Pavel Nadolsky, Jon Pumplin, Carl Schmidt, Daniel Stump, and C. P. Yuan. New parton distribution functions from a global analysis of quantum chromodynamics. *Phys. Rev. D*, 93(3):033006, 2016. doi:10.1103/PhysRevD.93.033006.

[228] TRExFitter Collaboration. Trexfitter documentation. `https://trexfitter-docs.web.cern.ch/trexfitter-docs/latest/`. Accessed: 2025-05-01.

[229] Georges Aad et al. Measurements of Higgs boson production via gluon-gluon fusion and vector-boson fusion using $H \to WW^* \to \ell\nu\ell\nu$ decays in pp collisions with the ATLAS detector and their effective field theory interpretations. 4 2025.

[230] Akanksha Bhardwaj, Christoph Englert, Robert Hankache, and Andrew D. Pilkington. Machine-enhanced CP-asymmetries in the Higgs sector. *Phys. Lett. B*, 832:137246, 2022. doi:10.1016/j.physletb.2022.137246.

[231] Georges Aad et al. Search for dark matter produced in association with a Higgs boson decaying to tau leptons at $\sqrt{s} = 13$ TeV with the ATLAS detector. *JHEP*, 09:189, 2023. doi:10.1007/JHEP09(2023)189.

[232] Luminosity determination in pp collisions at $\sqrt{s} = 13$ TeV using the ATLAS detector at the LHC. 6 2019.

[233] Stefan Höche, Frank Krauss, Marek Schönherr, and Frank Siegert. QCD matrix elements + parton showers. The NLO case. *JHEP*, 04:027, 2013. doi:10.1007/JHEP04(2013)027.

[234] J. Alwall, R. Frederix, S. Frixione, V. Hirschi, F. Maltoni, O. Mattelaer, H. S. Shao, T. Stelzer, P. Torrielli, and M. Zaro. The automated computation of tree-level and next-to-leading order differential cross sections, and their matching to parton shower simulations. *JHEP*, 07:079, 2014. doi:10.1007/JHEP07(2014)079.

[235] Tanju Gleisberg and Stefan Höche. Comix, a new matrix element generator. *JHEP*, 12:039, 2008. doi:10.1088/1126-6708/2008/12/039.

[236] Konstantin Lehmann and Bernd Stelzer. The Fake Factor Method and its relation to the Matrix Method. *Nucl. Instrum. Meth. A*, 1054:168376, 2023. doi:10.1016/j.nima.2023.168376.

[237] SimpleAnalysis: Truth-level Analysis Framework. 2022.

[238] J. M. Lorenz, M. Baak, G. J. Besjes, D. Côté, A. Koutsman, and D. Short. HistFitter - A flexible framework for statistical data analysis. *J. Phys. Conf. Ser.*, 608:012049, 2015. doi:10.1088/1742-6596/608/1/012049.

[239] ATLAS Collaboration. Formulae for Estimating Significance. ATL-PHYS-PUB-2020-025, 2020. URL `https://cds.cern.ch/record/2736148`.

[240] Georges Aad et al. Search for dark matter in events with missing transverse momentum and a Higgs boson decaying into two photons in pp collisions at $\sqrt{s} = 13$ TeV with the ATLAS detector. *JHEP*, 10:013, 2021. doi:10.1007/JHEP10(2021)013.

List of Figures

List of Tables